CHARACTERISATION OF COHERENT RADIATION IN SHORT-BUNCH LINAC-DRIVEN FELS

A thesis submitted to The University of Manchester
for the degree of Doctor of Philosophy
in the Faculty of Science and Engineering

September 2019

Billy S Kyle

Department of Physics and Astronomy

Contents

List of Tables

List of Figures

Abstract

A new CSR model implemented in the General Particle Tracer [1] proposes the possibility of incorporating effects often ignored by other CSR models, such as effects arising from the transverse beam size and computation of CSR effects in the fringe region of a dipole field. Presented in this thesis are start-to-end simulations for both the CLARA Phase 1 beamline and the MAX IV linac. A reduction in the r.m.s energy spread of the electron bunch has been predicted in simulations arising from the velocity term of the Liènard-Wiechert field. This energy spread reduction occurs in the drift immediately following a dipole bend, and the effect has been shown to almost mitigate the energy spread induced by CSR in the dipole bend by $\sim$20%. Further energy spread reductions have been shown in simulation by employing a scheme using strong focusing optics prior to a dipole bend in the presence of non-zero dispersion. A reduction in the r.m.s energy spread of 10 keV is observed across the first $\sim$150 mm of the dipole bend.

Measurements of fringe-field CSR emitted from a bunch compressor dipole on the MAX IV linac are compared to GPT CSR simulations. These measurements were collected using a photonic approach of inferring the energy loss of the bunch centroid from pyroelectric detection of THz radiation. Scans of several machine parameters, were carried out in order to provide several quantitative comparisons to the GPT CSR model. Two of the scans performed demonstrated very good agreement with the energy loss predicted by GPT simulations providing confidence in the novel effects observed in GPT simulations of the CLARA Phase 1 beamline. This study also presents the first comparison to the GPT CSR model carried out using direct measurements of the radiation.

Declaration

No portion of the work referred to in this thesis has been submitted in support of an application for another degree or qualification of this or any other university or other institute of learning.

Copyright

i. The author of this thesis (including any appendices and/or schedules to this thesis) owns certain copyright or related rights in it (the "Copyright") and s/he has given The University of Manchester certain rights to use such Copyright, including for administrative purposes.

ii. Copies of this thesis, either in full or in extracts and whether in hard or electronic copy, may be made **only** in accordance with the Copyright, Designs and Patents Act 1988 (as amended) and regulations issued under it or, where appropriate, in accordance with licensing agreements which the University has from time to time. This page must form part of any such copies made.

iii. The ownership of certain Copyright, patents, designs, trade marks and other intellectual property (the "Intellectual Property") and any reproductions of copyright works in the thesis, for example graphs and tables ("Reproductions"), which may be described in this thesis, may not be owned by the author and may be owned by third parties. Such Intellectual Property and Reproductions cannot and must not be made available for use without the prior written permission of the owner(s) of the relevant Intellectual Property and/or Reproductions.

iv. Further information on the conditions under which disclosure, publication and commercialisation of this thesis, the Copyright and any Intellectual Property and/or Reproductions described in it may take place is available in the University IP Policy (see `http://documents.manchester.ac.uk/`

DocuInfo.aspx?DocID=24420), in any relevant Thesis restriction declarations deposited in the University Library, The University Library's regulations (see http://www.library.manchester.ac.uk/about/regulations/) and in The University's policy on presentation of Theses

Acknowledgements

I would like to thank my supervisors Dr Robert Appleby and Dr Peter Williams for their continued moral, technical, and practical support throughout the course of this project. They have provided me with many hours of their time, thrashing out difficult concepts both scientific and computational, and their patience with me know no bounds. Furthermore, I would like to thank Rob for providing me the opportunity to be involved in the Tactile Collider project, which was one of the most enriching experiences of my postgraduate study. I also would like to thank Dr James Jones who, as a member of the ASTeC staff, has provided me with so much help on the topics of programming and general computational tools. I would like to thank Dr Sara Thorin and Dr Erik Mansten from the MAX IV Facility for giving me the tremendous opportunity to work on the MAX IV accelerator. My time spent working on the MAX IV linac was truly the most enjoyable part of my postgraduate study, not to mention that it's provided me with all of the experimental results featured in this thesis.

I would like to express my sincerest thanks Thomas Pacey and Joseph Wolfenden for their patience and advice on experimental physics, as well as getting me involved in practical coherent radiation studies in the first place. It's been a privilege to be able to work alongside them on experiments at CLARA and MAX IV, and I'm very grateful to be able to consider them my friends. I would also like to thank other members of the postgraduate cohort at the Cockcroft Institute, with special mention to Dr. Paolo Pizzol and Andrew Vint, who along with Tom Pacey, have provided me with hours of fun playing board games.

Special thanks go out to Jory Bahra, John Maksymiw, Jake Harrison, and Bradley West, all of whom I have had the pleasure of living with at one time or another for the past four years, and in some cases longer still. They have always been incredibly supportive friends, and living with them has comprised the most enjoyable time of my life thus far. I would also like to thank my mum and dad, for their support, both emotional and material, over the last four years and especially in the tumultuous final months of the write up of this thesis. Their continued belief in me, and at times constant nagging, has kept me on task for this write-up and I cannot thank them enough.

Last, and most importantly, I'd like to thank my girlfriend and the love of my life, Abi Himan. No-one has been more supportive and encouraging than her during the time we have been together, and her patience in the face of constant delays and extensions has been nothing short of saintly. She is the perfect partner and my best friend, and I cannot wait for us to spend the rest of our lives together, wherever that may be!

Chapter 1

Introduction

Since the construction of the Tantalus beamline at the University of Wisconsin in 1968 [2, 3], synchrotron radiation has been the primary source of X-rays for use in scientific endeavours. Presenting orders of magnitude greater photon fluxes than the previous standard of X-ray tubes, they are a vital experimental tool in a wide range of disciplines including solid-state physics, biochemistry, and materials science [4, 5]. Synchrotron radiation is typically broadband, though the spectrum is in principle tunable with respect to the electron beam energy, and it is this tunability of the spectrum that makes synchrotron light so useful for a wide range of applications involving the microstructure of matter.

Initially synchrotron light sources simply used the emission that comes as a by-product of constraining electrons on circular storage ring orbits, a fundamental process that previously had been viewed as a hindrance in synchrotron operation. The synchrotron emission was exploited through the installation of X-ray beamlines at the dipole magnets of the accelerator. Later, the development of beamline elements known as insertion devices heralded accelerators whose sole

purpose was the generation of synchrotron light, such as the SRS at Daresbury Laboratory [6]. Insertion devices, such as wigglers and undulators, force electrons to move along tight oscillatory paths through a series of closely-packed, alternating-field magnetic poles, thus generating a large radiating path length within a relatively small length of the storage ring beamline, and increasing the overall photon output. More recently still, accelerators known as "free electron lasers" (FELs) have been developed, which exploit coupling between the electron beam and co-propagating radiation to stimulate increased emission from the electron beam [7] beyond the usual coherent undulator radiation. This demands careful design of both the undulators and the driving beamline, and in many cases requires electron beams with a large peak-current generated through bunch compression. The amplification of emitted radiation can be further increased by introducing short-wavelength modulations in the electron bunch current profile, known as microbunches [8, 9].

FEL light possesses narrower bandwidth, better spatial coherence, narrower collimation angle and greater-yet brilliance [10] than periodic-lattice light sources, and these parameters are typically used as an assessment of the FEL beam quality. Further to these advantages, the FEL central frequency is tunable through variation of parameters within the radiating section, such as the undulator pole gap and the electron beam energy [11].

The brilliance of a light source is typically defined as the photon flux density within a certain spectral fraction[12]. While the FEL process leads to a significant increase in the overall brilliance of the photon beam when compared to that of a single undulator, the qualitative arguments surrounding the basis of

the brightness of an undulator and its relation to the electron beam still apply to the case of FELs. The brilliance of an undulator depends upon the electron bunch distribution but can be broadly categorised into two-regimes: diffraction limited and emittance-dominated [13]. In the emittance-dominated case the photon beam's brilliance is heavily modified by the electron beam emittance, such that at the centre of the photon beam

$$B_{Und,\epsilon} = \frac{F_\gamma(\omega)}{4\pi^2 \epsilon_x \epsilon_y},$$

where $B_{Und,\epsilon}$ is the brilliance (or brightness) of the undulator in the emittance-dominated regime, $F_\gamma(\omega)$ is the spectral photon flux, typically defined as within 0.1% of the central frequency, and ϵ_x, y are the transverse (geometric) beam emittances. Conversely, when the beam emittance is sufficiently low and thus the electron beam's r.m.s size and divergence is small, the photon beam's brilliance is limited solely by the diffraction-limit for a particular wavelength. It follows then, that the demand for ever higher quality FEL photon beams is tied to a demand for lower emittance electron beams [14]; the diffraction limited case is not typical of FEL beamlines given the lack of radiation damping like that seen in storage rings [15].

The energy spread of the electron beam is another key parameter in refining the FEL beam quality. Correlated energy spreads present within the electron beam lead to individual longitudinal slices following different orbits within the undulator. This leads to each slice exciting a different mode frequency within the FEL, thus diluting the overall spectrum [16]. This is not necessarily an undesirable effect, but does result in a lower current exciting a given FEL resonant

mode, and thus lowering the brilliance at a given resonant frequency. In the case of uncorrelated energy spreads, the effect is to smear out the electron trajectories, such that it further dilutes the peak current contributing to a given resonant frequency. In the case of both of these effects, the energy spread serves to continually dilute the transverse beam emittance throughout the lasing section [17].

Upstream collective effects such as space charge, wakefields, and coherent synchrotron radiation (CSR) can serve to degrade the electron beam by driving increases in the electron beam energy spread, transverse emittances, and through microbunching gain at adverse modulation wavenumbers. As such, the characterisation and quantitative assessment of these processes on FEL beam quality is of great importance to the on-going development and optimisation of modern FEL beamlines. This thesis will focus on the modelling of the process of CSR in the context of linac-driven single-pass FEL beamlines, with the aim of determining effects hereto uncharacterised by current methodologies.

In this introductory chapter, the typical layout and components of an FEL beamline will be touched upon with reference to the machines covered in the work presented herein, as well the status of beam dynamics simulations for FEL design will be summarised. The theoretical foundations behind the CSR process will then be covered in the following chapter, with simple analytic theories compared to more complex adaptations. In Chapter 3, an overview of the computational tools currently available for the modelling of the CSR process is presented, along with experimental comparisons to these computational tools. Chapter 3 will also cover the implementation of the beamlines considered within simulation codes. Following this, simulations carried out for the CLARA Phase 1 beamline are then

presented, along with an experimental plan for characterisation of CSR outside the limit of applicability for conventional analytical models. Finally, simulations and experimental comparisons carried out for the MAX IV linac are presented.

1.1 Free-Electron Lasers

The fundamental difference between FELs and other light sources arises from the exploitation of the coupling between the drive beam and the already existing radiation field within the lasing section. As an electron travels through an undulator it not only emits conventional undulator radiation, but also interacts with the electric field from previously-emitted radiation contained within the FEL. If the electron interacts with the electric field at a decelerative phase additional radiative emission is induced as the electron does work against the electric field [18]. The amplification occurs at a preferential wavelength, namely that which is matched to the periodicity of the bunch trajectory within undulator. This arises from resonance, wherein a given particle observes the FEL field at the same phase along it's trajectory through the undulator. In this way, the electron beam acts as the gain medium for the FEL, with the laser operating wavelength being determined by the undulator and electron beam properties.

FELs can be realised in a variety of ways depending upon the requirements for the FEL output and performance. The fundamental resonant wavelength of an undulator, λ, is expressed as [19]

$$\lambda = \lambda_u \frac{1 + K^2/2}{2\gamma^2}, \tag{1.1}$$

where λ_u is the undulator period, K is the undulator parameter, and γ is the

relativistic Lorentz factor. Radiation emitted from an electron within an undulator overtakes the electron by λ over an undulator period [18] . The undulator parameter is given by

$$K = \frac{eB_0\lambda_u}{2\pi m_e c^2},$$

where B_0 is the magnetic field on the central axis of the undulator, and m_e and e are the electron mass and charge respectively. It follows that there is some degree of tunability in the undulator radiation, either by variation of the undulator period [20], or most commonly through variation of the axial magnetic field strength. Because the rate-of-change of the resonant wavelength with respect to the axial magnetic field is a cubic function of the undulator period, this tunability is more easily realised for FELs operating in longer wavelength regimes, such as IR-FELS, where the undulator period is typically larger.

1.1.1 FEL Oscillators

FELs operating within the spectral range between infra-red (IR) and ultra-violet (UV) typically employ a FEL oscillator scheme. This configuration uses high-reflectivity mirrors at either end of the undulator (or undulator chain) in combination with a high repetition rate electron current (Figure 1.1). The separation between the two mirrors is set to support the resonant modes of the undulator radiation [18], with the mirror spacing being often variable to facilitate a tunable FEL output [21].

FEL oscillators use a long electron bunch train to amplify the radiation field

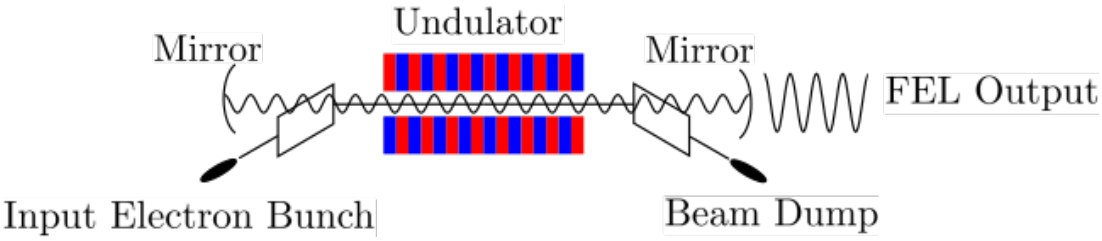

Figure 1.1: A FEL Oscillator. A resonant FEL mode is contained by high-reflectivity mirrors, and is amplified by each fresh electron bunch traversing the undulator. Low amplitude modulation of the electron bunch occurs as the electron bunch passes through, further increasing the emission stimulated by the FEL mode.

to saturation. Radiation emitted from the first electron bunch makes one round trip in the oscillator before interacting with the "fresh" electron current provided by the second electron bunch. The radiation within the resonator stimulates greater emission of radiation within the second electron bunch [18]. This process continues, with each subsequent electron bunch in the train adding more energy until saturation of the oscillator is achieved.

FEL oscillators typically operate in the low gain regime, wherein the electron bunch distribution is modulated by the laser field but not to full saturation. This is permitted by the continually refreshed electron current, and so FEL oscillators have relatively relaxed requirements upon the electron beam quality when compared to high-gain FEL modes [22].

Energy recovery linacs (ERLs) are commonly used as drivers for FEL oscillators. An ERL generates a long bunch train either through a high repitition-rate photoinjector [23–25] or through a thermionic cathode in combination with a buncher cavity [26], with initial acceleration often achieved using high-voltage DC electron guns. ERLs are, broadly speaking, single-pass machines; the current

profile of a given bunch within the bunch train is significantly degraded by the FEL section, rendering re-circulation of the current of little benefit. A notable exception to this is the Novosibirsk ERL [27], in which electron bunches travel up to three passes before being dumped. However, this consists of three distinct orbits rather than a singular orbit, and is employed for the purpose of operating at several different beam energies on a single ERL lattice rather than reusing a spent electron bunch in the FEL sections. The key feature of an ERL beamline is the introduction of the spent electron bunch to the accelerating cavity at the decelerative phase of the field, whereupon the spent electron beam transfers it's energy to the structure before being dumped, thus improving the efficiency of the ERL operation [28].

1.1.2 Linac-Driven FELs

For FELs operating in the extreme UV (XUV) and X-ray spectra, where suitably reflective mirrors that are durable to high radiation intensities are not as commonplace, lasing occurs in a single pass and typically uses a longer chain of undulators [29]. These beamlines thus employ conventional linac drivers, and it is this context that the work in this thesis is carried out. As the driving current consists of a singular electron bunch an X-ray FEL operates in the high gain regime [30], which poses greater demands upon the electron peak current, emittance and energy spread. Although there are numerous operating modes employed for linac-driven FELs, the two predominant modes are externally seeded and self-amplified spontaneous emission (SASE).

Externally-seeded FELs often employ a two stage FEL (Figure 1.2). In the

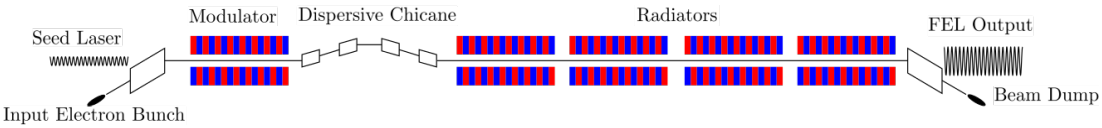

Figure 1.2: The seeded FEL operating principle. The seed laser and modulator impart an energy modulation in the input electron bunch. The dispersive chicane maps this modulation to a longitudinal density modulation, which grows into a microbunched structure as the bunch travels through the radiator section. The radiative output of the electron bunch increases as the electron beam becomes more tightly bunched.

first stage a high-power laser pulse enters the first undulator, typically known as the modulator, in synchronicity with the electron bunch [31]. The coupling between the electron bunch and the seed laser pulse induces an energy modulation along the electron bunch. The electron beam then passes through a dispersive structure, which maps the energy modulation to a density modulation [32]. The beam then enters the second undulator section, wherein the density modulation is of a wavelength equivalent to the FEL wavelength. The modulated beam thus couples strongly to it's emitted field, with electrons in a given modulation peak interacting with the radiation emitted one undulator period prior from the modulation peak immediately behind it. Alongside stimulating increased emission, this coupling amplifies the modulation, which in turn leads to further increased emission as the microbunched structure becomes more tightly confined into thin slices spaced at the resonant FEL wavelength [29]. This process repeats until the saturation point of the FEL, whereupon the drive beam is fully microbunched at the fundamental harmonic of the FEL. With further propagation the electron beam continues to become more bunched until the dissolution of the microbunch structure occurs [30].

The primary limitation of an externally seeded FEL lies in the availability

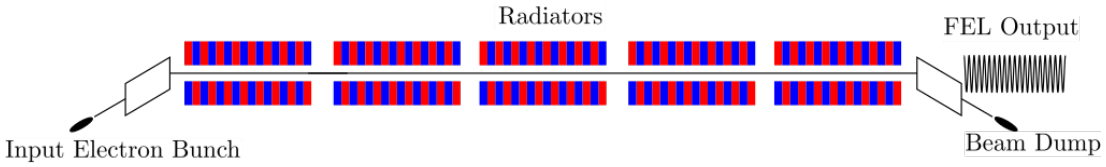

Figure 1.3: The SASE FEL. The undulator radiation emitted at the start of the radiator chain is incoherent, echoing the shot-noise derived initial bunch spectrum. As the electron bunch travels along the FEL, the resonant wavelength of radiation begins to dominate as it induces microbunching at the corresponding modulation wavelength.

of seed lasers of the appropriate wavelength. For hard X-ray applications the SASE mode is commonly employed [33], which uses the initial statistical modulations arising from the discrete nature of the electron bunch to act as a seed for the FEL (Figure 1.3). Here, the initial emission is significantly less coherent than that in an externally seeded FEL, as the electron current spectrum modulation consists of shot noise and collective effect modulations generated upstream (e.g. resistive-wall wakefields, CSR, longitudinal space charge) [34]. As the beam travels through the undulators, the resonant wavelength of the FEL is preferentially amplified and a longitudinal energy modulation once again forms within the bunch at this wavelength. The resultant density modulation and microbunching emerges from the dispersion within the periodic magnetic field rather than a dedicated chicane or dogleg as is found in seeded FELs [35]. As with a seeded scheme, the high gain regime that SASE FELs operate in results in a completely microbunched beam at the start of saturation, beyond which the microbunched structure breaks up and the gain reduces rapidly. More so than the seeded FEL, SASE modes require extremely high peak current and beam quality to generate sufficient radiation at the start of the FEL to appreciably induce an energy modulation within the electron bunch [36].

In order to meet the low-emittance requirements of a SASE FEL in the absence

of the emittance damping found in storage rings, the beam is typically sourced from a photoinjector rather than a thermionic electron source [37]. Photoinjectors exploit the photoelectric effect [38] to generate charge from a conducting cathode surface using ultra-short laser pulses, typically on the order of a few ps. This in-turn generates an electron bunch with a short longitudinal extent, which facilitates achieving the high peak currents commonly required for effective FEL gain.

The ultra-short photon pulses are produced using a mode-locked laser system. In such a system, the resonant modes of the laser cavity possess well-defined phase relationships between one another, as opposed to the randomly distributed relative phases found between the cavity modes in conventional laser systems [39]. The coherence of the cavity modes in a mode-locked system thus permits constructive and destructive interference of the individual modes, through which the resultant electric field produces a short, high power pulse with a broad bandwidth rather than a pseudo-continuous output with a very well defined spectrum [40]. Such intense photon pulses can cause damage to the laser cavity through non-linear self-focusing within the gain medium, and so the total pulse energy must be initially restricted to prevent such consequences from occurring.

In order to liberate the required amount of charge from the photocathode surface amplification of the short laser pulse must be carried out. In order to perform this amplification without incurring non-linear effects, a process called chirped pulse amplification is carried out. The ultra-short, low amplitude pulse is first directed towards a series of dispersive gratings, that separate out the spectral components and create a path-length difference between them. This lengthens the pulse, imparting a correlated spectral-temporal relationship, and lowers the

peak power. The arrangement of the gratings is such that no additional temporal dispersion of the pulse's spectral components occurs upon exiting. The lengthened pulse is then safe to amplify due to it's reduced peak power after which, the chirped bunch is then re-compressed through another system of dispersive gratings.

The liberated electrons are then accelerated to semi-relativistic energies (typically less than 10 MeV) in an RF electron gun. At the low energies at the start of the linac, the electron beam is in the space charge dominated regime. Here, the emittance of the bunch is a non-constant quantity as transverse space charge results in non-linear correlations in the beam phase space [41]. In order to minimise the emittance growth, a solenoid and booster cavity are used to match the beam through the rest of the injector. This matching technique will be covered in greater detail at a later point in this thesis. The booster cavity is used to accelerate the beam to ultra-relativistic energies ($\sim$100 MeV). Subsequent accelerating cavities are then used to increase the energy up to the nominal beam energy, which partly determines the FEL output wavelength (Equation 1.1).

Alongside accelerating the electron beam the linac RF system is used to facilitate bunch compression, which results in the high peak current required for effective lasing in the FEL. The RF phase is set such that the electron beam enters a cavity offset from the peak of the RF wave. This imparts a correlation in the longitudinal phase space, which generates a correspondingly correlated path-length difference when the beam passes through a dispersive beamline section [42]. By correctly selecting the value of the correlation, this path length difference can be exploited to compress the electron bunch. The dispersive structures

used for this bunch compression are broadly categorised as doglegs or chicanes [43]. Higher-order magnetic optics are used in these structures to compensate for the effects of non-linear collective effects (e.g. CSR), as well as higher-order correlations imparted on the bunch from the off-crest RF cavity field [44]. Alternatively, higher frequency X-band cavities are used to compensate for curvature in the longitudinal phase space [45], which would otherwise hamper the FEL performance by both limiting the peak current achievable, and by diluting the bunch coherence in the FEL section. After bunch compression, the electron beam enters the FEL section for lasing.

1.1.3 CLARA

The CLARA project is an FEL currently under construction at Daresbury Laboratory (DL). Its purpose is to serve as a test facility for the development of FEL schemes, beam dynamics techniques, and accelerator technologies for use in the planned UK-XFEL. It will deliver 250 pC [46] electron bunches to a lasing section, comprised of seven planar undulator radiators [47], at a rate of 400 Hz. Electrons will be accelerated to 250 MeV by four S-band linacs. Bunch compression will occur in a variable chicane bunch compressor [48], allowing a range of electron bunch lengths to be used for lasing and thus enabling a tunable output FEL gain and bandwidth [49]. Prior to this bunch compressor, an X-band cavity will be installed to function as a linearizer (Figure 1.4), removing longitudinal phase space (LPS) curvature brought about by preceding linacs in order to minimise emittance gain due to higher order dispersive terms in the bunch compressor.

Both seeded and self-amplified spontaneous emission (SASE) operational modes are planned, and several beam modes are planned with various energies, bunch

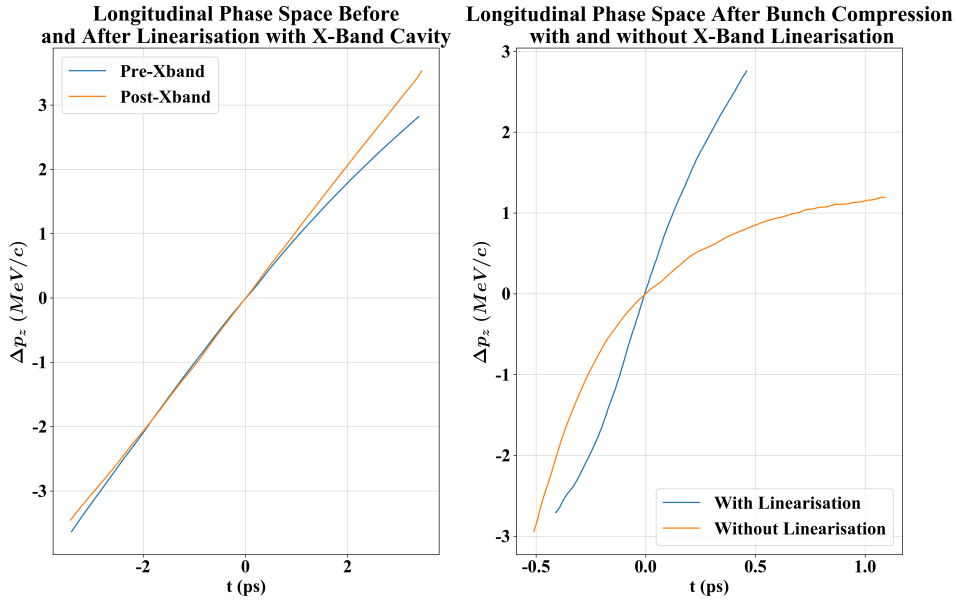

Figure 1.4: X-band cavities are used to linearise the longitudinal phase space. Without this linearisation, the compression of the electron bunch is hampered. The effect of the linearisation is most clearly seen after bunch compression has occured. Image generated using data taken from [45].

charges, and bunch lengths. The FEL central frequency will be in the visible-UV region, facilitating easy inspection of the characteristics of the FEL output. The variability of the CLARA FEL is central to its utility; by being able to perform in a wide range of regimes, it will allow for the effects of beam characteristic on the FEL output to be characterised and help to inform the development of the UK-XFEL.

The first phase of the CLARA installation was completed in 2018. Phase 1 consists of the CLARA injector and a quadrupole telescope arrangement, which transfers electron beams to the pre-existing VELA beamline via a dogleg structure. The CLARA injector currently accelerates 100 pC electron bunches to 45 MeV, with a machine repetition rate of 10 Hz. Bunch compression can be

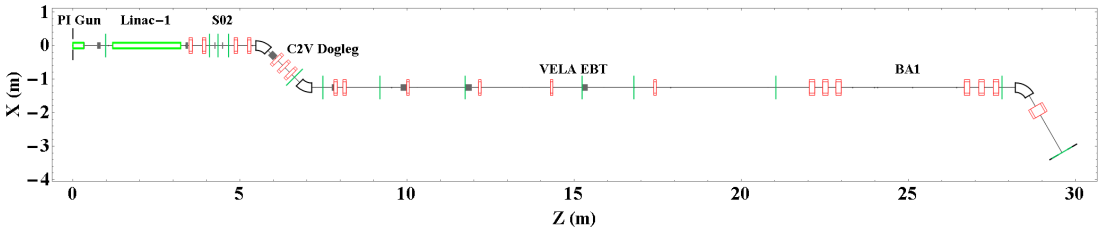

Figure 1.5: Schematic Diagram of the CLARA Phase 1 Lattice with key beamline sections labelled. Dipoles are shown in white, quadrupole magnets in red, orbit-correction magnets in grey, accelerating structures in light green, and YAG screen locations are displayed as green markers.

achieved through the CLARA dogleg (Figure 1.5) due to the structure's non-zero R_{56}, allowing sub-ps bunches to be delivered along the VELA transport line to one of two experimental areas, Beam Areas 1 and 2. Beam Area 1 houses a dedicated user testing chamber, which can be isolated from the rest of the machine vacuum allowing for easy insertion and removal of components for testing. Downstream from the testing chamber is a spectrometer line terminated by a Faraday cup.

The Phase 1 beamline is currently used for development of technologies for use in the future CLARA project, as well as commissioning of existing beamline components such as the 400 Hz DC Photoinjector Gun [50]. Subsequent phases of the CLARA installation will see the removal of the VELA beamline, and so Phase 1 is a crucial period in the larger context of CLARA development.

1.1.4 MAX IV

The MAX IV facility is a synchrotron radiation laboratory situated in Lund, Sweden, which is home to three particle accelerators used for production of synchrotron light. The MAX IV linac acts as a driver for two storage rings, at

1.5 GeV and 3 GeV, as well as the single-pass Short Pulse Facility (SPF) [51] (Figure 1.6). The function of the MAX IV storage rings is to act as an X-ray light source for experiments in a range of fields, such as nano-materials [52] to macromolecular X-ray [53] crystallography. The SPF currently houses a single experimental beamline, FemtoMAX, which uses the short electron pulses provided by the MAX IV linac to produce ultra-short photon pulses generated in a 10 m undulator. These photon pulses are then used to produce time-resolved data of chemical and biological processes, as well as investigating substructure on the scale of ∼Å [54].

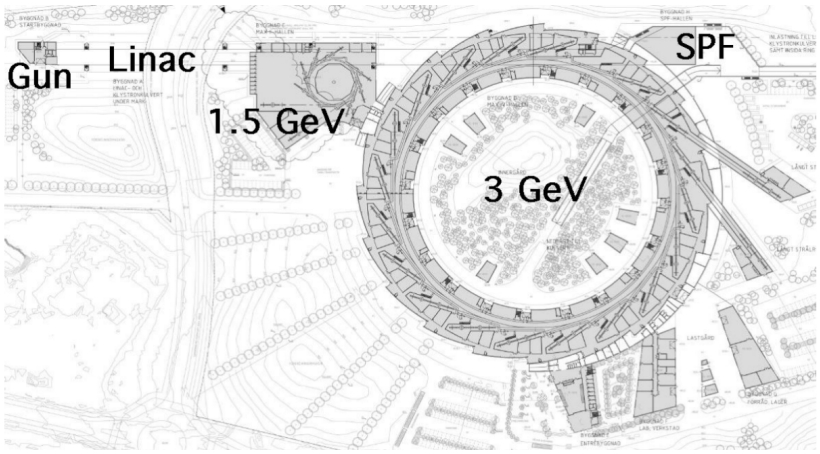

Figure 1.6: The MAX IV synchrotron radiation facility. The total length of the Linac section is ∼300 m, with the diameters of the 1.5 GeV and 3 GeV rings being ∼30 m and ∼170 m respectively. Image sourced from [51].

The MAX IV linac has two injectors, a thermionic gun used for top-up and injection to the storage rings, and a photoinjector for bunches delivered to the SPF. The injected bunch is passed through an injector linac, K00, which accelerates bunches to ∼ 100 MeV. The MAX IV linac consists of two separate accelerating structures, K01 and K02, which are separated by the first bunch compressor BC1 [55] (Figure 1.7). The accelerating gradients of both K01 and

K02 are ∼14.5 MeV m^{-1} at nominal operation. Electron bunches exit BC1 at a typical energy of ∼ 250 MeV in SPF operation, with a linear chirp applied to the electron bunch by a phase offset of the accelerating field. BC1 is a dogleg structure consisting of two double bend achromats separated by a 37.89 m dispersion free section, in which is situated a quadrupole triplet. Each achromat comprises four dipoles, two quadrupoles and a sextupole. The dogleg is designed such that the natural T_{566} compensates curvature in the longitudinal phase space of the beam imparted by the far off-crest K01 field. The T transfer matrix of a beamline section defines the 2$^{\text{nd}}$-order dependence of the final particle coordinates (at the end of the beamline section) on the initial particle coordinates (at the start of the beamline section), with the T_{566} element describing the path-length difference incurred as a result of the square of the momentum deviation. The linear dependence on the initial particle coordinates is given by the R-matrix. The total transfer map (up to 2$^{\text{nd}}$-order) of a particle travelling through a given lattice is described in index notation as [56]

$$x_i^{(1)} = \sum_j R_{i,j} x_j^{(0)} + \sum_{j,k} T_{i,j,k} x_j^{(0)} x_k^{(0)}, \tag{1.2}$$

where $i, j, k \in [1...6]$, with $x_i = (x, x', y, y', z, \delta)_i$. Here, the superscripts $^{(0)}$ and $^{(1)}$ refer to the initial and final coordinates respectively, and the spatial-momentum deviation (z-δ) convention has been used to represent the longitudinal phase space. This linearisation is further aided by the sextupole optics, which also aid in minimisation of the 2$^{\text{nd}}$-order dispersion of the bunch [44]. Bunches are compressed from around 1.8 ps to between 0.7 ps-0.1 ps over BC1 before being accelerated to 3 GeV in K02. From there, the electron bunch is further compressed in BC2, which shares a similar double bend achromat structure to BC1, albeit

with different dimensions. The r.m.s electron bunch length at the exit of BC2 is typically between ∼0.1 ps-∼10 fs. The future plans for the SPF include installation of a transverse deflecting cavity (TDC) [57], for detailed characterisation of the bunch current profile, and a FEL beamline.

Figure 1.7: The MAX IV Linac and SPF, with relevant beamline sections have been highlighted for visibility purposes. The SPF comprises the last portion of the beamline, from BC2 onward. Extensions to the SPF are planned, including a TDC diagnostic beamline and an X-ray FEL, but only SP02 is currently installed.

1.2 Simulations in FEL Development

It has been demonstrated that start-to-end (S2E) simulations [58], where an electron bunch is simulated through an entire beamline typically passing between multiple codes, are key to determining potential sources of emittance and energy-spread growth in a beamline that would otherwise be missed and/or ignored if FEL simulations are conducted in isolation. It stands to reason then that these S2E simulations should be able to capture as many dynamical effects as possible, including but not limited to those of space charge, wakefields, and CSR.

CSR defines the coherent amplification of the conventional single particle synchrotron emission within a bunched electron beam. It typically occurs at short bunch lengths, where wavelengths greater than the electron bunch length are amplified due to being emitted at approximately the same phase and thus constructively interfering (Figure 1.8). The effects of CSR are a potentially significant limiting factor in the performance of FELs. Due to the requirement of

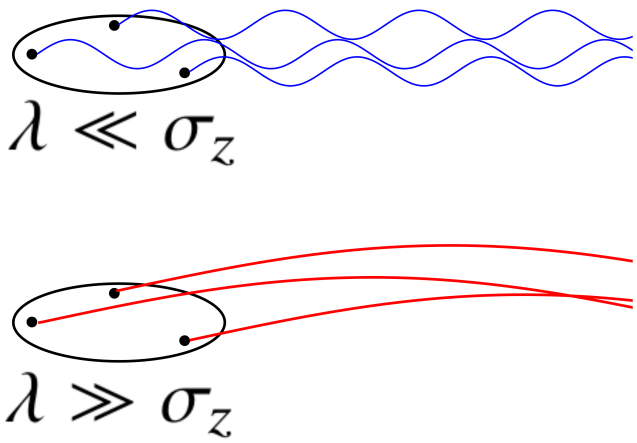

Figure 1.8: Coherent amplification of the electron bunch's synchrotron emission occurs at wavelengths greater than the electron bunch length. The radiation field of the individual electrons are at a similar phase and thus constructively interfere.

ever-greater peak electron current in the radiating portion of the FEL beamline, magnetic bunch compression schemes are used to achieve ultra-short bunch lengths. In doing so, the emission of synchrotron radiation in the bending magnets of these structures can be coherently amplified [59, 60]. This process not only drives energy loss within the beam but also redistributes energy within the beam, which increases the overall beam energy-spread [60]. This energy redistribution also drives emittance gain in the compressing structures due to the variation of electron trajectories within the bunch [61, 62].

Microbunching is a fundamental requirement of the FEL lasing process, wherein the electron current profile is modulated with a wavenumber $k = \frac{2\pi}{\lambda_{Und.}}$, where $\lambda_{Und.}$ is the central FEL output wavelength [35, 63]. This modulation can either be self-seeded in the case of SASE operation, or can be externally seeded via an input laser. Interaction of the electron beam with the FEL photon beam further drives the amplitude of the modulation, which in turn amplifies the emission at the desired wavelength. Thus, through the microbunching process the electron

beam becomes the lasing medium of the FEL.

Despite its integral role in the operation of an FEL, microbunching poses a significant issue to FEL optimisation. Initial high-frequency density modulations of the electron current profile are typically brought about by shot-noise at a photoinjector and amplified by longitudinal space charge in the low-energy section of the accelerator [64]. Shot-noise is a natural consequence of Poisson statistics in photoinjectors, and is akin to white-noise in the electron current profile [65]. This white-noise essentially consists of high-frequency modulations of the longitudinal electron density. Alongside these density modulations are modulations of a similar wavenumber generated in the longitudinal bunch energy spectrum, which continue to be amplified after the low-energy injector. When passing through a bunch compressor, these energy modulations undergo a mapping to the spatial distribution of the bunch via the bunch compressor's R_{56} (Equation 1.2), further amplifying the spatial modulation within the bunch current profile [66]. The R_{56} is only non-trivial across dispersive structures where particles of different momenta take different trajectories as they travel through dipole magnetic fields. While this geometric effect occurs, further modulation of the bunch energy spectrum can then occur in tandem from the emission of CSR [67, 68]. The amplification of a density modulation with a wavenumber different to the desired undulator wavenumber results in a loss of FEL gain and resultant FEL brightness.

Modelling of the CSR process is typically limited by numerous approximations and assumptions. One such assumption is the effect of the omission of the transverse extent of the electron bunch, which becomes more significant for highly compressed electron bunches. When these transverse effects are accounted

for, it typically is carried out in isolation; as such it is desirable in the context of FEL design to have simulation tools available for the modelling of CSR in concert with other collective effects such as space charge. The effects of dipole fringes and the evolution of the CSR wake in drift sections downstream from dipole magnets is another area of the CSR process that is less understood. This thesis strives to characterise the CSR process in bending magnets on CLARA Phase 1 and the MAX IV Linac in regimes outside of conventional analytical models, while also incorporating the effects of space charge. This characterisation will focus on analysing energy-spread and emittance growth across dipole magnets and downstream drift sections for electron bunches of large transverse sizes, as well as the effects of the velocity term of the Liènard-Wiechert field [69] in subsequent drift sections of compression structures. This work has implications for the design of bunch compression systems wherein the energy spread and emittance growth due to CSR may be self-cancelling. Also presented is a quantitative assessment of a novel numerical model of the CSR process using measurements carried out on the MAX IV beamline. These measurements assess the model's ability to capture the effects of radiation emitted in dipole fringe fields.

Chapter 2

Literature Review and Theory

In this chapter, the theoretical fundamentals of synchrotron radiation will be discussed including its spectral and polarisation characteristics. From there, the 1-dimensional analytical limit of CSR will be derived along with its implications on the spectral properties and spatial distribution of the radiation. This framework will then be expanded to cover the effects of a variable bunch length and the full 3-dimensional electron bunch distribution. The effects of the transient regime of the CSR process, occurring close to the entrance and exit faces of bending magnets, will be established, and a framework to describe the radiation emitted in these regions will be discussed.

2.1 Synchrotron Radiation

The invention of the betatron can be regarded as a key moment in the development of electron accelerator technology. No longer limited by the relativistic de-phasing of the electron beam found in cyclotrons, particle accelerators could now reliably accelerate electrons to relativistic energies. But in doing so, a new

limitation to a particle accelerator's energy would be discovered, that of synchrotron radiation [70]. First observed at the General Electric Synchrotron in 1946 [71], it is the predominant barrier in the construction of high-energy periodic electron accelerators, however it also forms the fundamental basis for modern high brightness light sources such as storage rings.

Synchrotron radiation arises naturally from the Liénard-Wiechert Fields when applied to the case of an electron constrained to a circular orbit. In an unpublished report [59], Julian Schwinger set about a thorough treatment of the nature of synchrotron radiation, specifically in the context of radiative losses within a betatron accelerator. He also set out the first analysis of the coherent effects of synchrotron radiation within this report. Therein Schwinger demonstrated that a homogeneous, continuous electron current would effectively suppress any radiative losses due to synchrotron radiation. Conversely, his treatment of a bunched electron beam, as had become common with the advent of synchrotrons, demonstrated that harmonics of the synchrotron radiation with wavelengths longer than the electron bunch length may be coherently amplified.

Analytical representations of synchrotron radiation, both coherent and incoherent, are only possible in certain idealised regimes for example, periodic motion around a circular orbit. While these analytical regimes are useful from a qualitative perspective when understanding the processes involved in synchrotron radiation emission, they fall short when a quantitative appraisal is required, save for providing back-of-the-envelope first approximations. Typically numerical modelling is used to make up for this shortfall, with various models each working within a set of limitations and assumptions. Typically the fewer assumptions

made in these models the more computationally intensive they become, especially so when modelling coherent processes.

This chapter will discuss the fundamental physics behind synchrotron radiation, both incoherent and coherent, focusing on the key features of the emission processes which are relevant for the research featured in subsequent sections of this thesis. It will also aim to address and explain the numerous approximations made in the analytical understanding of incoherent and coherent synchrotron radiation and their limitations, as well as discussing generalisations and additions to the modelling methods made and adopted over the years of research.

2.1.1 The Liénard-Wiechert Fields of a Moving Electron

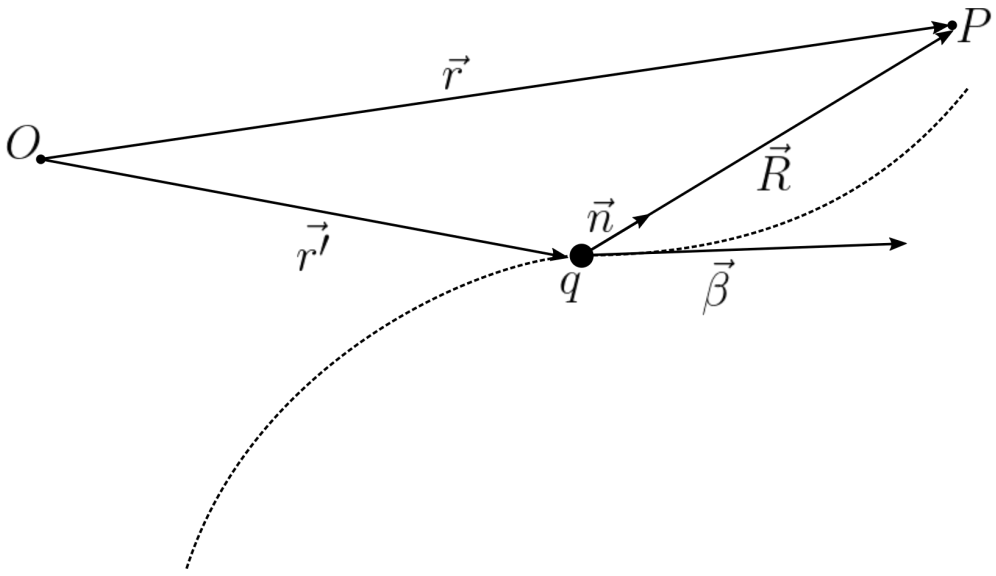

Figure 2.1: Geometry of a charge, q moving along an arbitrary trajectory (dashed), with relevant vectors labelled along with the origin, O, and observation point, P.

The fields of a moving charge, q, differ from those of a static charge due to the finite speed of information transfer. This modifies the electromagnetic fields

seen at an observation point, P, at time t and position $\vec{r}$, such that the field seen is that of the charge at some previous time, t_{ret}, known as the retarded time. These two times are related as [69]

$$t = t_{ret} + \frac{R(t_{ret})}{c}, \tag{2.1}$$

where R is the separation distance, $|\vec{r}-\vec{r'}|$, between the charge and P (Figure 2.1). The 4-potential, $A^\mu = (V/c, \vec{A})$ where V and $\vec{A}$ are the scalar and vector potentials respectively, at the observation point at t for an arbitrary 4-current density, $J^\mu = (c\rho, \vec{j})$ where ρ and $\vec{j}$ are the charge and current densities respectively, is thus given by [72]

$$A^\mu(\vec{r}, t) = \frac{\mu_0}{4\pi} \int \frac{J^\mu(\vec{x'}, t')}{R(\vec{x'})} \delta\left(t - \frac{R(t')}{c} - t'\right) d^3\vec{x'}dt'. \tag{2.2}$$

In the case of a single electron moving with speed $\vec{v} = c\vec{\beta}$ along the trajectory $\vec{r'}(t)$, the 4-current density may be expressed as

$$J^\mu(\vec{r}, t) = qc\beta^\mu \delta\left(\vec{r} - \vec{r'}(t)\right) = qc\delta\left(\vec{r} - \vec{r'}(t)\right)(1, \vec{\beta}(t)),$$

whereupon Equation 2.2 becomes [73]

$$A^\mu(\vec{r}, t) = \frac{\mu_0}{4\pi} \int \frac{qc\beta^\mu(t')}{R(\vec{r'}(t'))} \delta\left(t - \frac{R(\vec{r'}(t'))}{c} - t'\right) dt'. \tag{2.3}$$

The remaining delta function in the integrand of Equation 2.3 contains a function of the integration variable, and so the following relationship is used to calculate the integral [73]:

$$\int h(x)\delta(f(x) - x_0)dx = \left[\frac{h(x)}{df/dx}\right]\Bigg|_{f(x)=x_0}.$$

Here we use the retardation condition in place of $f(x)$, which yields the derivative

$$\frac{d}{dt'}\left(t' + \frac{R(t')}{c}\right) = 1 + \frac{1}{c}\frac{dR(t')}{dt'} = 1 - \frac{\vec{R}\cdot\vec{\beta}}{R} = 1 - \vec{n}\cdot\vec{\beta} = \kappa, \tag{2.4}$$

which when applied to Equation 2.3 produces the well-known expression for the generalised 4-potential (also known as the Liènard-Wiechert potentials) of a single particle moving along an arbitrary trajectory:

$$A^{\mu}(\vec{r},t) = \frac{\mu_0}{4\pi}\left[\frac{qc\beta^{\mu}}{R\kappa}\right]\Bigg|_{t_r}. \tag{2.5}$$

Here, the symbol t_r is used to represent the retarded time such that Equation 2.1 is satisfied. This 4-potential can be then used to calculate the corresponding electromagnetic fields, which when written in tensor-notation is given by the antisymmetric tensor [72]

$$F^{\mu\nu} = \partial_{\mu}A^{\nu} - \partial_{\nu}A^{\mu} = \begin{bmatrix} 0 & E_x/c & E_y/c & E_z/c \\ -E_x/c & 0 & B_z & -B_y \\ -E_y/c & -B_z & 0 & B_x \\ -E_z/c & B_y & -B_x & 0 \end{bmatrix}, \tag{2.6}$$

where ∂_{μ} is the covariant, 4-dimensional divergence operator. It is worth noting that this operator is differentiating with respect to the observer coordinates t and $\vec{r}$. As such, it is useful to perform a change of variables to the more convenient coordinates t_r and $\vec{R}$. Transformation to the former of these is relatively straightforward, simply requiring a change of variables as defined by Equation 2.4; the

latter is made more complex by the fact that any change in the observer coordinate will result in a corresponding change in the retarded time. Hoffman[69] asserts this latter transformation can be split into two contributions, the first corresponding to the absolute shift in the coordinate $\vec{R}$ with respect to a change in the observer position $\vec{r}$, and the second due to the aforementioned change in the retarded time. Formally, this is described in the Einstein index convention by [69]

$$dR^i = dr^i - dr'^i = dr^i - c\beta^i dt_r, \tag{2.7}$$

where the Roman index i denotes the non-zero, space-like components. Here it is recognised that the infinitesimal shift in the particle's retarded position $dr^i = c\beta^i dt_r$. The electric field is described by the first row of the tensor given in Equation 2.6, such that

$$E^i = cF^{0i} = c(\partial_0 A^i - \partial_i A^0). \tag{2.8}$$

Application of Eq 2.4 to the first term of Equation 2.8 yields [69]

$$\begin{aligned} \partial_0 A^i = -\frac{1}{\kappa c}\partial_{t_r} A^i &= -\frac{\mu_0}{4\pi}\frac{q}{\kappa}\left[\frac{\dot{\beta}^i}{R\kappa} - \frac{\beta^i}{R^2\kappa^2}\partial_{t_r}(R\kappa)\right]\Bigg|_{t_r} \\ &= -\frac{\mu_0 q}{4\pi}\left[\frac{(n^j\beta^j - \beta^2)c\beta^i}{R^2\kappa^3} + \frac{\kappa\dot{\beta}^i + n^j\dot{\beta}^j\beta^i}{R\kappa^3}\right]\Bigg|_{t_r}, \end{aligned} \tag{2.9}$$

where $\dot{\beta}^i = \frac{d\beta^i}{dt_r}$ is the particle's acceleration normalised to the speed of light in free space. In order to arrive at the final expression shown in Equation 2.9, the observation has been made that $r^i = r'^i + R^i$ is a constant vector, and so it follows

that $\partial_{t_r} R^i = -\partial_{t_r} r'^i = -c\beta^i$. The second term of Equation 2.8 corresponds to the divergence of the scalar potential,

$$\partial_i A^0 = \frac{\mu_0 qc}{4\pi}\left[\partial_i\left(\frac{1}{R\kappa}\right)\right]\Bigg|_{t_r} = -\frac{\mu_0 qc}{4\pi}\left[\frac{\partial_i\left(R\kappa\right)}{R^2\kappa^2}\right]\Bigg|_{t_r}, \tag{2.10}$$

which requires the more complex change of variables detailed by Equation 2.7 to solve. An infinitesimal change in the distance between the observation and emission points, $dR = n^i dR^i$, yields a variation in the path length travelled by photons. If it is enforced that these photons arrive at the same time, dR may be equated to an equivalent change in the path length for photons emitted $-cdt_r$, which alongside Equation 2.7 produces the expression[69]

$$dt_r(t = const.) = -\frac{n^i dr^i}{c\kappa} = \partial_i t_r dr^i. \tag{2.11}$$

Equations 2.7 and 2.11 can then be used to determine the expression for an infinitesimal change in the quantity $\kappa R = R - R^i\beta^i$ with respect to an infinitesimal change in the observer position dr^i:

$$\begin{aligned} dR - \beta^i dR^i - R^i d\beta^i &= -cdt_r - \beta^i(dr^i - c\beta^i dt_r) - R^i\dot{\beta}^i dt_r \\ &= -\beta^i dr^i - \left(c\left(1-\beta^2\right) + R^i\dot{\beta}^i\right)dt_r \\ &= \left(-\beta^i + \frac{c\left(1-\beta^2\right) + R^j\dot{\beta}^j}{c\kappa}n^i\right)dr^i. \end{aligned} \tag{2.12}$$

Equation 2.12 can then be related to the numerator of Equation 2.10 simply as $d(\kappa R) = \partial_i(\kappa R)dr^i$. Equations 2.8, 2.9, 2.10, and 2.12 can then be combined to find an expression for the electric field [69],

$$
\begin{aligned}
E^i &= -\frac{\mu_0 q c}{4\pi}\left(\left[\frac{(n^j\beta^j-\beta^2)c\beta^i}{R^2\kappa^3}+\frac{\kappa\dot{\beta}^i+n^j\dot{\beta}^j\beta^i}{R\kappa^3}\right]\Bigg|_{t_r}-\left[\frac{-c\beta^i+\frac{c\left(1-\beta^2\right)+R^j\dot{\beta}^j}{\kappa}n^i}{\kappa^2R^2}\right]\Bigg|_{t_r}\right)\\
&= \frac{q}{4\pi\epsilon_0}\left[\frac{\left(1-\beta^2\right)\left(n^i-\beta^i\right)}{R^2\kappa^3}+\frac{n^j\dot{\beta}^j\left(n^i-\beta^i\right)-\left(1-n^j\beta^j\right)\dot{\beta}^i}{cR\kappa^3}\right]\Bigg|_{t_r}\\
&= \frac{q}{4\pi\epsilon_0}\left[\frac{\left(1-\beta^2\right)\left(n^i-\beta^i\right)}{R^2\kappa^3}+\frac{n^j\dot{\beta}^j\left(n^i-\beta^i\right)-n^j\left(n^j-\beta^j\right)\dot{\beta}^i}{cR\kappa^3}\right]\Bigg|_{t_r}\\
&= \frac{q}{4\pi\epsilon_0}\left[\frac{\left(1-\beta^2\right)\left(n^i-\beta^i\right)}{R^2\kappa^3}+\frac{\varepsilon_{ijk}n^j\varepsilon_{klm}\left(n^l-\beta^l\right)\dot{\beta}^m}{cR\kappa^3}\right]\Bigg|_{t_r}.
\end{aligned}
\tag{2.13}
$$

Here, ε_{ijk} and ε_{klm} are rank-3 Levi-Civita tensors, and the vector triple product rule has been used to obtain the final expression. Similarly to Equation 2.8, the magnetic field can be represented as

$$
B^i = \frac{1}{2}\varepsilon_{ijk}F^{jk} = \frac{1}{2}\varepsilon_{ijk}\left(\partial_j A^k - \partial_k A^j\right) = \varepsilon_{ijk}\partial_j A^k,
$$

which results in

$$
B^i = \frac{\mu_0 q c}{4\pi}\left[\varepsilon_{ijk}\partial_j\left(\frac{\beta^k}{R\kappa}\right)\right]\Bigg|_{t_r} = \frac{\mu_0 q c}{4\pi}\left[\varepsilon_{ijk}\left(\frac{\partial_j\beta^k}{R\kappa}-\frac{\partial_j\left(R\kappa\right)\beta^k}{R^2\kappa^2}\right)\right]\Bigg|_{t_r}. \tag{2.14}
$$

In order to solve the first term in Equation 2.14 the curl of the normalised velocity must be calculated. This is done using the chain rule alongside Equation 2.11 such that

$$
\varepsilon_{ijk}\partial_j\beta^k = \varepsilon_{ijk}\partial_j t_r\partial_{t_r}\beta^k = \varepsilon_{ijk}\frac{\dot{\beta}^j n^k}{c\kappa},
$$

which can then be used alongside the result calculated in Equation 2.12 to find the final expression for the Liènard-Wiechert magnetic field [69];

$$B^i = -\frac{\mu_0 q c}{4\pi}\left[\frac{\varepsilon_{ijk}n^j\left(\kappa\dot{\beta}^k + n^l\dot{\beta}^l\beta^k\right)}{cR\kappa^3} + \frac{\varepsilon_{ijk}n^j\left(1-\beta^2\right)\beta^k}{R^2\kappa^3}\right]\Bigg|_{t_r}. \tag{2.15}$$

2.1.2 Synchrotron Radiation: Electromagnetic Fields of an Electron Constrained to a Circular Orbit

Synchrotron radiation arises when the Liènard-Wiechert fields are contextualised to a relativistic electron moving along a circular trajectory. In this section, the equations governing synchrotron radiation will be derived from the Liènard-Wiechert fields previously defined, with the angular distribution and polarisation characteristics extracted from calculation of the Poynting vector. The spectrum of the synchrotron emission will then be gleaned from a Fourier analysis of the electric field.

Using the expressions derived for the Liènard-Wiechert fields it is possible to derive the power radiated by a moving electron. The Poynting vector, S^i, defines the power density flux of an electromagnetic field, and is related to the Liènard-Wiechert fields by[73]

$$S^i = \frac{\varepsilon_{ijk}E^jB^k}{\mu_0}. \tag{2.16}$$

Comparison of Equations 2.13 and 2.15 shows that it is possible to write the magnetic field solely in terms of the electric field and the vector n^i:

$$B^i = \frac{\varepsilon_{ijk} n_r^j E^k}{c},$$

where the subscript r denotes evaluation at the retarded time. With this relationship, the Poynting vector is now

$$S^i = \frac{\varepsilon_{ijk} E^j \varepsilon_{klm} n_r^l E^m}{\mu_0 c} = \frac{\left(\delta_{il}\delta_{jm} - \delta_{im}\delta_{jl}\right) E^j n_r^l E^m}{\mu_0 c} = \frac{E^2 n_r^i - n_r^j E^j E^i}{\mu_0 c}. \quad (2.17)$$

Here, δ_{ij} is the Krönecker delta, and the identity

$$\varepsilon_{ijk}\varepsilon_{klm} = \varepsilon_{kij}\varepsilon_{klm} = \left(\delta_{il}\delta_{jm} - \delta_{im}\delta_{jl}\right) \quad (2.18)$$

has been used. This identity has already been implicitly used albeit reversed, namely in the application of the vector triple product rule in Equation 2.13. In order for a non-zero energy loss to occur the integral

$$\lim_{r\to\infty} \int_{\mathbf{S}} S^i dA^i = \lim_{r\to\infty} \int_{\mathbf{S}} S^i n_{\mathbf{S}}^i r^2 \sin\theta d\theta d\phi, \quad (2.19)$$

where $\mathbf{S}$ defines the surface of a sphere of radius r and unit normal $n_{\mathbf{S}}^i$, must be finite. As shown in Equation 2.17, the Poynting vector is quadratic in terms of the electric field. The term in the electric field $\propto r^{-2}$ will vanish to zero in this integral, as will the cross terms in E^2. It follows that only the term $\propto r^{-1}$ contributes to radiation in the far-field, and from Equation 2.13 it can be asserted that this term is perpendicular to n^i, resulting in only the first term in 2.17 being present in the effective far-field Poynting vector

$$S^i = \frac{1}{\mu_0 c} E_{acc}^2 n_r^i, \quad (2.20)$$

where E_{acc} is the term in the Liènard-Wiechert electric field dependent on the normalised acceleration of the electron, and the subscript r denotes evaluation at the retarded time. This expression has no loss in generality, save that it only holds true in the far-field regime. The near-field interaction has no effect for a solitary free electron but becomes more relevant in the context of an ensemble of particles, wherein it plays the role of redistributing energy within the ensemble.

There are two distinct scenarios that arise when considering radiative losses of an electron under acceleration: the case in which acceleration is parallel to the electron's velocity, and the case where it is perpendicular. The former of these would arise in the accelerating structures of a particle accelerator, but in reality are so small as to be negligible in all practical situations [74]. In the case of a relativistic electron, the latter defines synchrotron radiation.

The radiative part of 2.13 for an electron constrained to a circular orbit becomes

$$E^i_{acc} = -\frac{q}{4\pi\epsilon_0}\left[\frac{\dot{\beta}\sin\theta\cos\phi\,(n^i-\beta^i)+(1-\beta\cos\theta)\,\dot{\beta}^i}{cR\,(1-\beta\cos\theta)^3}\right]\Bigg|_{t_r}, \tag{2.21}$$

where θ and ϕ are the polar and azimuthal angles about the axis parallel to the particle's velocity. Using Equations 2.19 and 2.20, the angular distribution of the radiated power is [59, 75, 76]

$$\frac{dP}{d\Omega} = R_r^2 S^i n_r^i = \frac{1}{\mu_0 c}\left(\frac{q\beta^2}{4\pi\epsilon_0\rho}\right)^2\left[\frac{(1-\beta\cos\theta)^2-\gamma^{-2}\sin^2\theta\cos^2\phi}{(1-\beta\cos\theta)^6}\right]\Bigg|_{t_r}, \tag{2.22}$$

where ρ is the orbit radius and γ is the Lorentz factor. Here, it has been asserted that the magnitude of the reduced acceleration $\dot{\beta} = \frac{\beta^2 c}{\rho}$. Equation 2.22 represents the radiative power density received by the observer with respect to the observer time, t, such that $P = \frac{dU}{dt}$ where U is the radiated energy. In order to instead calculate the radiative losses of the electron it is necessary to express the radiated energy distribution with respect to the retarded time. Once again using the Jacobian element defined in Equation 2.11, Equation 2.22 becomes

$$\frac{dP_r}{d\Omega} = \frac{d}{d\Omega}\left(\frac{dU}{dt_r}\right) = \kappa_r \frac{dP}{d\Omega}. \tag{2.23}$$

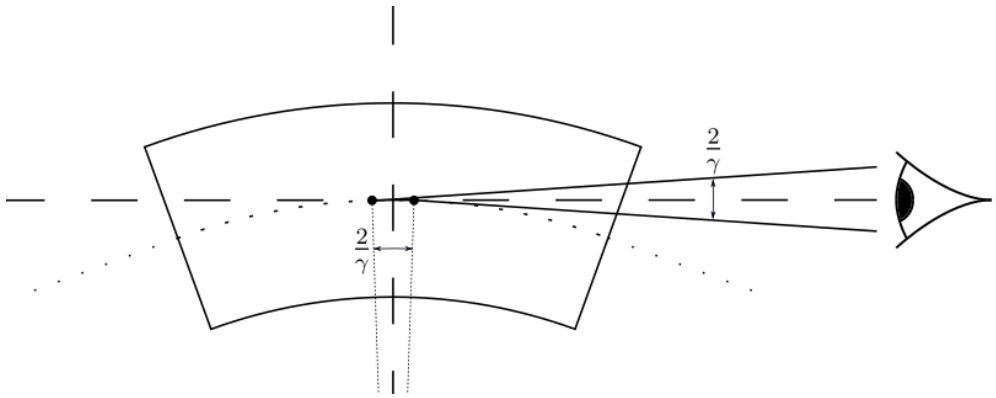

Figure 2.2: As an electron passes through a dipole bend, it generates a cone of synchrotron radiation with opening angle $\frac{1}{\gamma}$. As such, an observer of the electric field at a fixed location only sees a radiation pulse corresponding to an angular portion of the trajectory $\frac{2}{\gamma}$ long.

There are regions of the single-particle synchrotron radiation distribution where the radiative far-field power is exactly zero. At observations within the bending plane ($\phi = 0, \pi$), this corresponds to $\cos\theta_0 = \beta$, which has the consequence of constraining the emitted radiation to an ever-tighter cone with increasing particle momentum. In the relativistic limit, this cone has an opening angle of $\theta_0 \approx \frac{1}{\gamma}$.

A consequence of the distinction between the instantaneous power observed at t versus the power emitted at t_r shown in Equation 2.23 is a compression of the observed radiation pulse with respect to its emission time from the perspective of the emitting electron. For an observer located tangentially to the orbit of the electron, as shown in Figure 2.2, only radiation emitted over an angle of $2\theta_0 \approx \frac{2}{\gamma}$ is observed. In the frame of an ultra-relativistic electron, this radiation is emitted over a time interval Δt_r. In the observer frame, the difference in velocities between the emitting electron and the radiation are small leading to a pile-up of the emitted photons.

This essentially creates a Doppler shift of the radiation, wherein the instantaneous power is raised by the near-equal velocities of the emitted radiation and the emitting electron, and the frequency of the radiation received by the observer is blue-shifted [77]. This Doppler shift is strongest for radiation emitted directly along the tangent, i.e. at the centre of the synchrotron source from the point of view of the observer. Here the compressed pulse duration at the observer is received over a duration $\Delta t = \frac{\Delta t_r}{2\gamma^2}$.

The total instantaneous power radiated by the electron is found through integration of Equation 2.23 over 4π sr solid angle;

$$\begin{aligned} P_r &= \frac{1}{\mu_0 c}\left(\frac{q\beta^2}{4\pi\epsilon_0\rho}\right)^2 \int_0^{2\pi}\int_0^{\pi}\left[\frac{\left(1-\beta\cos\theta\right)^2 - \gamma^{-2}\sin^2\theta\cos^2\phi}{\left(1-\beta\cos\theta\right)^5}\right]\sin\theta d\theta d\phi \\ &= \frac{q^2}{4\pi\epsilon_0}\frac{2c}{3\rho^2}\left(\gamma\beta\right)^4, \end{aligned} \tag{2.24}$$

where p is the particle momentum. This is the well-known result indicating the strong dependence of the emitted power to the normalised particle momentum, whereby the total instantaneous power emitted by the electron scales as $\propto (\gamma\beta)^4$.

The Fourier Transformed Field

In order to derive the spectral dependence of synchrotron radiation it is necessary to consider the Fourier-transform of the radiation field given in Equation 2.21, which enables the spectral properties of the radiation to be determined. The generalised Fourier transform of a time-varying electric field is given by

$$\tilde{E}^i(\omega) = \frac{1}{\sqrt{2\pi}} \int_{-\infty}^{\infty} E^i(t) e^{-i\omega t} dt,$$

where $\omega = 2\pi\nu$ is the angular frequency. For the radiation field of the electron, this integral becomes [78]

$$\begin{aligned} \tilde{E}^i_{acc}(\omega) &= \frac{1}{\sqrt{2\pi}} \frac{q}{4\pi\epsilon_0 c} \int_{-\infty}^{\infty} \left[\frac{\varepsilon_{ijk} n^j \left(\varepsilon_{klm} \left(n^l - \beta^l \right) \dot{\beta}^m \right)}{R\kappa^3} \right] \Bigg|_{t_r} e^{-i\omega t} dt \\ &= \frac{1}{\sqrt{2\pi}} \frac{q}{4\pi\epsilon_0 c} \int_{-\infty}^{\infty} \frac{\varepsilon_{ijk} n^j \left(\varepsilon_{klm} \left(n^l - \beta^l \right) \dot{\beta}^m \right)}{R\kappa^2} e^{-i\omega(t_r + R/c)} dt_r. \end{aligned} \tag{2.25}$$

In the ultra-relativistic limit, the electron only radiates energy towards the observer for a small portion of its trajectory. For an observer sufficiently far enough away, the vector R^i changes very little over the course of the motion and both n^i and R can be assumed approximately constant [79]. This assumption does not extend to the quantity in the exponent arising from the retardation condition however. Given these approximations, evaluation of the integral in Equation 2.25 can be carried out by integration by parts. The complex exponential term is easily

accounted for in the calculation, but the first term is calculated by recognising that [78]

$$\begin{aligned}
\frac{d}{dt_r}\left(\frac{\varepsilon_{ijk}n^j\varepsilon_{klm}n^l\beta^m}{R\kappa}\right) &= \frac{\varepsilon_{ijk}n^j\varepsilon_{klm}n^l}{R\kappa^2}\left(\kappa\dot{\beta}^m - \beta^m\frac{d\kappa}{dt_r}\right) \\
&= \frac{\varepsilon_{ijk}n^j\varepsilon_{klm}n^l}{R\kappa^2}\left(\dot{\beta}^m + n^u\dot{\beta}^u\beta^m - n^u\beta^u\dot{\beta}^m\right) \\
&= \frac{\varepsilon_{ijk}n^j\varepsilon_{klm}n^l}{R\kappa^2}\left(\dot{\beta}^m + \varepsilon_{mpq}n^p\varepsilon_{qrs}\beta^r\dot{\beta}^s\right) \\
&= \frac{\varepsilon_{ijk}n^j}{R\kappa^2}\left(\varepsilon_{klm}n^l\dot{\beta}^m + (\delta_{kp}\delta_{lq} - \delta_{kq}\delta_{lp})n^ln^p\varepsilon_{qrs}\beta^r\dot{\beta}^s\right) \\
&= \frac{\varepsilon_{ijk}n^j}{R\kappa^2}\left(\varepsilon_{klm}n^l\dot{\beta}^m + n^kn^l\varepsilon_{lrs}\beta^r\dot{\beta}^s - n^ln^l\varepsilon_{krs}\beta^r\dot{\beta}^s\right) \\
&= \frac{1}{R\kappa^2}\left(\varepsilon_{ijk}n^j\varepsilon_{klm}n^l\dot{\beta}^m - \varepsilon_{ijk}n^j\varepsilon_{krs}\beta^r\dot{\beta}^s\right) \\
&= \frac{\varepsilon_{ijk}n^j\varepsilon_{klm}(n^l-\beta^l)\dot{\beta}^m}{R\kappa^2},
\end{aligned}$$

where once again the identity given in Equation 2.18 has been used. It follows that the Fourier transform of the radiative electric field is given by

$$\begin{aligned}
\tilde{E}^i_{acc} =& \frac{1}{\sqrt{2\pi}}\frac{q}{4\pi\epsilon_0 c}\left(\left[\frac{\varepsilon_{ijk}n^j\varepsilon_{klm}n^l\beta^m}{R\kappa}e^{-i\omega(t_r+R/c)}\right]_{-\infty}^{\infty}\right. \\
&\left. + i\omega\int_{-\infty}^{\infty}\frac{\varepsilon_{ijk}n^j\varepsilon_{klm}n^l\beta^m}{R}e^{-i\omega(t_r+R/c)}dt_r\right).
\end{aligned} \tag{2.26}$$

The motion is periodic, and the behaviour exhibited over the infinite time interval is equivalent to that over a single revolution; the lowest harmonic of the electric field is equivalent to the revolution frequency of the electron along the circular orbit. As such, it is illustrative to change the limits of the first term in Equation 2.26 can be altered accordingly to become

$$\begin{aligned}\tilde{E}^i_{acc} =& \frac{1}{\sqrt{2\pi}}\frac{q}{4\pi\epsilon_0 c}\left(\left[\frac{\varepsilon_{ijk}n^j\varepsilon_{klm}n^l\beta^m}{R\kappa}e^{-i\omega(t_r+R/c)}\right]_0^{T_{rev}}\right.\\ &\left.+i\omega\int_{-\infty}^{\infty}\frac{\varepsilon_{ijk}n^j\varepsilon_{klm}n^l\beta^m}{R}e^{-i\omega(t_r+R/c)}dt_r\right)\\ =& \frac{1}{\sqrt{2\pi}}\frac{i\omega q}{4\pi\epsilon_0 cR}\int_{-\infty}^{\infty}\varepsilon_{ijk}n^j\varepsilon_{klm}n^l\beta^m e^{-i\omega(t_r+R/c)}dt_r,\end{aligned} \tag{2.27}$$

where it has been noted that, assuming negligible energy losses per revolution, the first term has the same value at $t_r = 0$ and $t_r = T_{rev}$.

The Single-Particle Synchrotron Radiation Spectrum

Calculation of the single-particle synchrotron radiation spectrum requires consideration of the steady-state particle motion, i.e. the electric field evolution at the observer location, P, across an entire revolution of the particle orbit. In order to do so it is first helpful to identify a corrected observation time,

$$t_P = t - \frac{r}{c}, \tag{2.28}$$

which accounts for the delay arising from the distance between the centre of the synchrotron radiation source and P [77], meaning that the centre of the received radiation signal arrives at $t_P = 0$. Here, as before, r is the magnitude of the position vector of P, and it has been asserted that the origin coincides with the centre of the synchrotron radiation source (Figure 2.2).

Because t_P is simply a translation applied to t the variable of integration in Equation 2.27 can be changed from t to t_P without any consequence, and the Fourier transform of the radiation field becomes [77]

$$\tilde{E}^i_{acc} = \frac{1}{\sqrt{2\pi}} \frac{i\omega q}{4\pi\epsilon_0 cR} \int_{-\infty}^{\infty} \varepsilon_{ijk} n^j \varepsilon_{klm} n^l \beta^m e^{-i\omega(t_r + (R-r)/c)} dt_r. \tag{2.29}$$

Similarly, the time-dependent electric field can be represented in terms of an inverse Fourier transform

$$E^i(t_P) = \frac{1}{\sqrt{2\pi}} \int_{-\infty}^{\infty} \tilde{E}^i(\omega) e^{i\omega t_P} d\omega. \tag{2.30}$$

Because $E^i(t_P)$ is a real-valued function, $\tilde{E}^i(\omega) = \tilde{E}^{i*}(-\omega)$. Using Parseval's theorem one can then write the angular dependence of the emitted power found in Equation 2.22 as [75]

$$\frac{dU}{d\Omega} = \int_{-\infty}^{\infty} \frac{dP}{d\Omega} dt_P = \frac{R^2}{\mu_0 c} \int_{-\infty}^{\infty} E^i_{acc} E^i_{acc} dtr = \frac{R^2}{\mu_0 c} \int_{-\infty}^{\infty} \tilde{E}^i_{acc} \tilde{E}^{i*}_{acc} d\omega, \tag{2.31}$$

where once again the value of R is assumed to be approximately constant over the portion of the trajectory which radiates towards the observer at P. As the integrand in Equation 2.31 is a symmetric function, the limits of the integration may be changed and, using Equation 2.29, the angular energy distribution becomes [75, 80]

$$\frac{dU}{d\Omega} = \frac{\omega^2 q^2}{16\pi^3 \epsilon_0 c} \int_0^{\infty} \left| \int_{-\infty}^{\infty} \varepsilon_{ijk} n^j \varepsilon_{klm} n^l \beta^m e^{-i\omega(t_r + (R-r)/c)} dt_r \right|^2 d\omega. \tag{2.32}$$

Because of the implicit symmetry in the motion of the electron, the observer coordinate can be considered as located at a declination angle of ψ with the

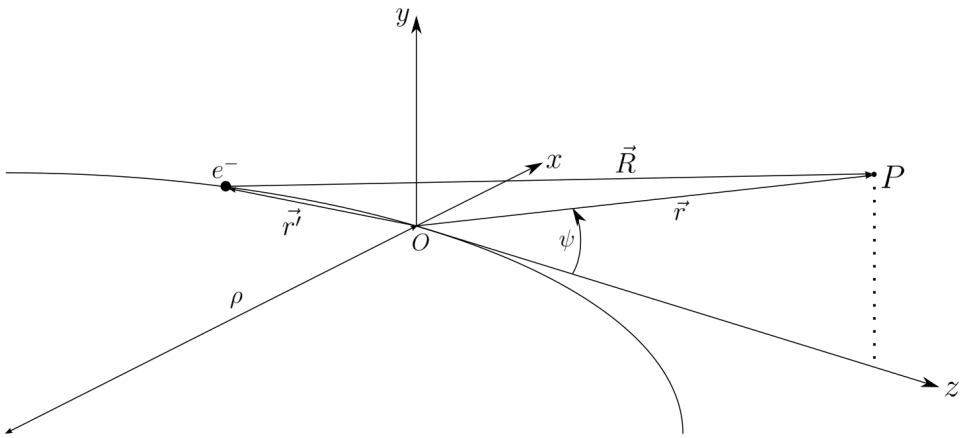

Figure 2.3: Geometry for synchrotron motion, with relevant coordinates. The observation point P is located in the $x = 0$ plane and can thus be described in terms of a vertical declination angle ψ.

orbital plane, and tangentially to the orbit within the orbital plane. The point of tangency on the orbit is chosen to be the origin, through which the electron passes at $t_r = 0$ (Figure 2.3) [77]. Because the relevant motion only concerns a total angle of $\omega_0 \Delta t_r \approx 2/\gamma$, where $\omega_0 = \beta c/\rho$ is the revolution frequency of the electron, the small angle approximation may be made. In this limit, the vectors n^i and β^i are given by

$$\vec{n} = \sin\psi \vec{e_y} + \cos\psi \vec{e_z}$$

$$\vec{\beta}(t_r) = \beta(-\sin\omega_0 t_r \vec{e_x} + \cos\omega_0 t_r \vec{e_z}),$$

where conventional vector notation has been adopted for the less-general case. Once again, the vector $\vec{n}$ has been assumed constant across the relevant portion of the trajectory. In this coordinate system, the quantity R becomes

$$R(t_r) = r\sqrt{1 + \frac{2\rho}{r}(\frac{\rho}{r}(1 - \cos\omega_0 t_r) - \cos\psi \sin\omega_0 t_r)}. \tag{2.33}$$

Expansion of this expression to first order depends upon the fact that $\omega_0 \Delta t_r \approx 2/\gamma$ and that the angle out of the orbital plane $\psi \lesssim 1/\gamma$. The trigonometric functions within this expression can then be expanded to find the typical maximal value of R over the relevant trajectory,

$$R_{max} \approx r\sqrt{1 - \frac{2\rho}{r\gamma} + \frac{\rho^2}{r^2\gamma^2} + \mathcal{O}(\gamma^{-3})},$$

at which non-trivial radiation is received by the observer [77]. Expansion then relies upon the condition that

$$\frac{\rho}{r\gamma} \ll 1,$$

and the expansion of R to first order is given by

$$R(t_r) \approx r\left(1 - \frac{\rho}{r}\cos\psi \sin\omega_0 t_r\right).$$

Once again because of the small opening angle of the radiation, a Taylor expansion of this expression can be used to simplify the exponent in Equation 2.32. Using the further ultra-relativistic approximations that $1 - \beta \approx 1/2\gamma^2$ and $\beta \approx 1$, the expression for the corrected observation time then becomes [75, 77]

$$\begin{aligned} t_P &= t_r + \frac{R-r}{c} \\ &= t_r - \frac{\rho}{c}\cos\psi \sin\omega_0 t_r \\ &\approx t_r - \frac{\rho}{c}(1-\psi^2/2)(\omega_0 t_r - (\omega_0 t_r)^3/6) \\ &= t_r(1-\beta(1-\psi^2/2-(\omega_0 t_r)^2/6)) \\ &\approx t_r(1/2\gamma^2 + \psi^2/2 + (\omega_0 t_r)^2/6) \\ &= \frac{(1+\gamma^2\psi^2)t_r}{2\gamma^2}\left(1+\frac{(\gamma\omega_0 t_r)^2}{3(1+\gamma^2\psi^2)}\right). \end{aligned} \tag{2.34}$$

This expansion for t_P is kept to third order in $\omega_0 t_r$ due to the suppression of the first term by a factor of γ^{-2}, hence keeping the two contributions of a similar magnitude. In contrast, the vector triple product in Equation 2.32 can be expanded to first order only given the terms' similar magnitude which is of the order γ^{-1}, giving

$$\sum_{i=1}^{3} \varepsilon_{ijk} n^j \varepsilon_{klm} n^l \beta^m \vec{e_i} = \vec{n} \times (\vec{n} \times \vec{\beta}) \approx \omega_0 t_r \vec{e_x} + \psi \vec{e_y}. \tag{2.35}$$

Differentiation of Equation 2.32 with respect to ω yields the angular spectral energy distribution, $\frac{d^2U}{d\Omega d\omega}$, of the emitted synchrotron radiation. It is important to note that ω denotes the angular frequency as measured at the observation point P, rather than from the point of view of the radiating electron. This distinction is made explicit in Equation 2.25 where the change of variables from $dt \to dt_r$ is accounted for. Because the change of variables $dt_P \to dt$ is a simple translation, the Jacobian for $dt_P \to dt_r$ is equivalent to that for $dt \to dt_r$. As such, the single-particle synchrotron angular spectral distribution is given by

$$\frac{d^2U}{d\Omega d\omega} = \frac{\omega^2 q^2}{16\pi^3\epsilon_0 c}\left|\int_{-\infty}^{\infty}(\omega_0 t_r \vec{e_x} + \psi\vec{e_y})e^{-i\omega\frac{(1+\gamma^2\psi^2)t_r}{2\gamma^2}\left(1+\frac{(\gamma\omega_0 t_r)^2}{3(1+\gamma^2\psi^2)}\right)}dt_r\right|^2. \quad (2.36)$$

The infinite limits of the integration over t_r in this expression may at first seem contrary to the approximations made in the simplification of the corrected observation time (Equation 2.34) in the exponent. This contradiction is rationalised by the fact that the frequencies present in the overall spectrum are harmonics of the fundamental revolution frequency [59], with the energy radiated into each harmonic increasing incrementally up to a critical harmonic defined by the particle energy. As such, the majority of this radiation is emitted into high frequency harmonics, which oscillate over time scales small enough for the approximations made in 2.34 to remain valid [78].

Expansion of the exponent in Equation 2.36 into trigonometric functions allows for further simplification, with the angular spectral energy distribution expressed as two transverse amplitude components. By recognising that integration of an odd integrand over symmetric limits yields a null result, these amplitudes can be expressed as

$$\frac{d^2U}{d\Omega d\omega} = \frac{\omega^2 q^2}{16\pi^3\epsilon_0 c}\left(|A_x(\omega,\psi)|^2 + |A_y(\omega,\psi)|^2\right),$$

where

$$A_x(\omega,\psi) = i\int_{-\infty}^{\infty} \omega_0 t_r \sin\left(\omega\frac{(1+\gamma^2\psi^2)t_r}{2\gamma^2}\left(1+\frac{(\gamma\omega_0 t_r)^2}{3(1+\gamma^2\psi^2)}\right)\right)dt_r, \tag{2.37}$$

$$A_y(\omega,\psi) = \int_{-\infty}^{\infty} \psi\cos\left(\omega\frac{(1+\gamma^2\psi^2)t_r}{2\gamma^2}\left(1+\frac{(\gamma\omega_0 t_r)^2}{3(1+\gamma^2\psi^2)}\right)\right)dt_r. \tag{2.38}$$

The Airy function and its derivative,

$$\mathrm{Ai}(\xi) = \frac{1}{\pi}\int_0^{\infty}\cos\left(\xi\tau\left(1+\frac{\tau^2}{3\xi}\right)\right)d\tau, \tag{2.39}$$

$$\mathrm{Ai}'(\xi) = -\frac{1}{\pi}\int_0^{\infty}\tau\sin\left(\xi\tau\left(1+\frac{\tau^2}{3\xi}\right)\right)d\tau, \tag{2.40}$$

can then be compared to this result. Using the substitutions $\tau = \frac{1}{2^{1/3}}\left(\frac{\omega_0}{\omega}\right)^{2/3}\omega t_r$ and $\xi = \left(\frac{\omega}{2\omega_0}\right)^{2/3}\frac{1+\gamma^2\psi^2}{\gamma^2}$, the angular spectral density can be expressed as

$$\frac{d^2U}{d\Omega d\omega} = \frac{q^2}{4\pi\epsilon_0 c}\left(\left(\frac{\omega}{2\omega_0}\right)^{2/3}\mathrm{Ai}'^2(\xi) + \psi^2\left(\frac{\omega}{2\omega_0}\right)^{4/3}\mathrm{Ai}^2(\xi)\right). \tag{2.41}$$

This expression should be compared to that shown in Equation 2.24; the strong dependence seen on the particle energy in the total power is absent in the expression of the power emitted into a particular frequency interval $d\omega$. Schwinger concludes in [59] that a large number of harmonics of the fundamental frequency must contribute to the overall power, with that number dependent on the particle energy. The critical frequency of synchrotron radiation,

$$\omega_c = \frac{3}{2}\gamma^3\omega_0,$$

defines the median of the synchrotron radiation spectrum, i.e. the frequency up

to which 50% of the radiated power is emitted [81], and demonstrates this energy dependence.

The value of the Airy function argument ξ in Equation 2.41 is always positive, and as such these can then be expressed in terms of modified Bessel functions of the second kind [78]:

$$\frac{d^2U}{d\Omega d\omega} = \frac{3\gamma^2 q^2}{4\pi^3 \epsilon_0 c}\left(\frac{\omega}{2\omega_c}\right)^2 \left(\left(1+\gamma^2\psi^2\right)^2 K_{2/3}^2\left(\frac{\omega}{2\omega_c}\left(1+\gamma^2\psi^2\right)^{3/2}\right) + \gamma^2\psi^2\left(1+\gamma^2\psi^2\right) K_{1/3}^2\left(\frac{\omega}{2\omega_c}\left(1+\gamma^2\psi^2\right)^{3/2}\right)\right). \tag{2.42}$$

The spectral distribution of the single-particle synchrotron radiation can then be obtained by integration over the full solid angle:

$$\begin{aligned}\frac{dU}{d\omega} &= \int_0^{2\pi}\int_{-\infty}^{\infty} \frac{d^2U}{d\Omega d\omega} d\psi d\phi \\ &= 2\pi \int_{-\infty}^{\infty} \frac{d^2U}{d\Omega d\omega} d\psi.\end{aligned} \tag{2.43}$$

In this case, ϕ is equivalent to the angular position around the particles orbit; as the motion is assumed periodic and the rate of emission assumed constant there is no dependence on this coordinate. The limits of the integration over ψ can be taken as infinite due to the fact that the radiation is emitted into a small cone. The evaluation and final result of this integral is convoluted and will not be included here, but the resulting spectrum can be qualitatively described. It increases rapidly with respect to frequency, up to close to the critical frequency beyond which it sharply decreases (Figure 2.4). The spectral power at a given

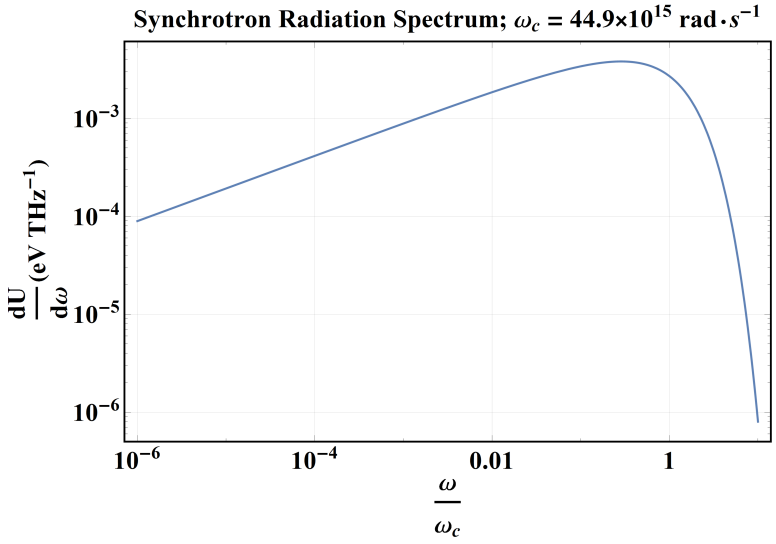

Figure 2.4: Spectrum of single-particle synchrotron radiation ($\gamma = 10^3$, $\rho = 10$ m). The spectrum peaks just before the critical frequency ω_c before rapidly falling off in intensity.

frequency is roughly independent of energy, especially at low frequencies [81]. However since the width of the distribution is defined by the critical frequency, which is itself $\propto \gamma^3$, the total radiated power is strongly energy dependent [59].

The amplitudes defined in Equations 2.37 and 2.38 imply that there exists two orthogonal polarisation states given by the first and second terms in Equation 2.42, respectively known as the σ-mode (x, in orbit plane) and π-mode (y, out of plane). The dominant contribution to the total synchrotron power always arises from the σ-mode, which overall constitutes $\frac{7}{8}$ of the total power. This is especially the case at high frequencies ($\omega \gg \omega_c$) where $\gamma\psi \ll 1$. In this case, the $\gamma^2\psi^2$ term in the π-mode suppresses the vertical polarisation almost entirely, contributing only $\approx 2.5\%$ of the total power. At low frequencies, the π mode becomes more significant, with $\approx 22\%$ of the power up to $0.1\omega_c$. At these frequencies, the opening angle of the radiation is significantly greater than $1/\gamma$ (Figure 2.5).

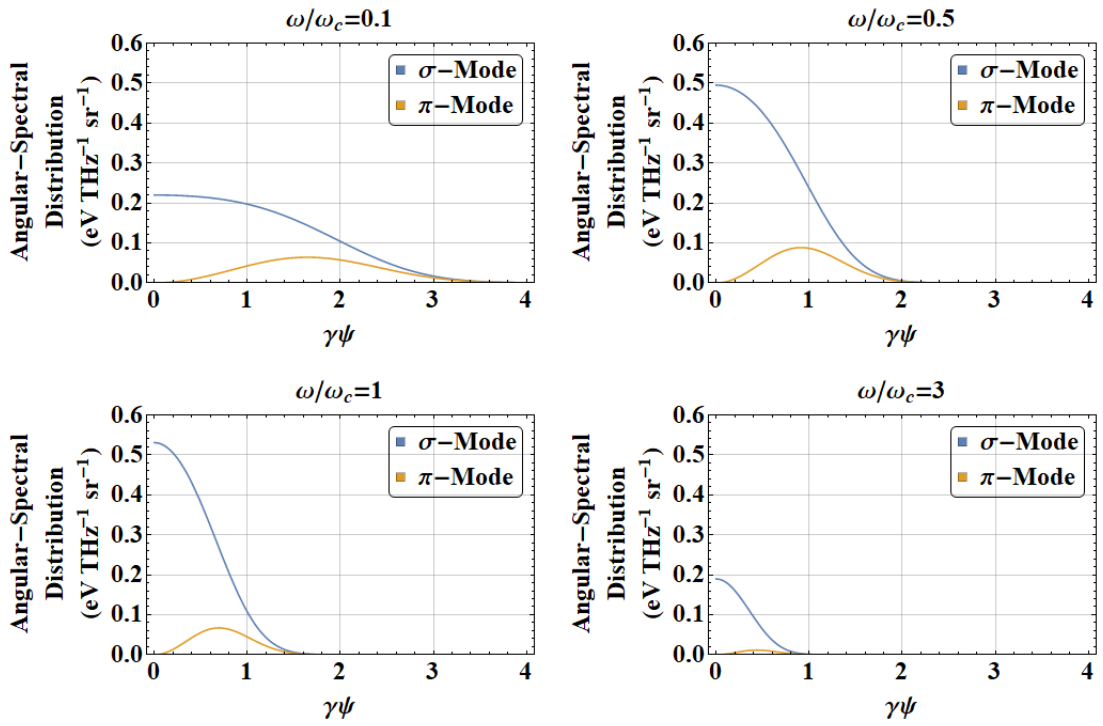

Figure 2.5: Angular dependence of σ- and π-modes for single-particle synchrotron radiation ($\gamma = 10^3$) at different frequencies. At higher frequencies, the σ-mode becomes considerably more dominant, and the radiation distribution narrows. Beyond the critical frequency synchrotron radiation is significantly suppressed.

2.2 Coherent Synchrotron Radiation: Steady State Regime

This section will now discuss the effects of a coherent amplification of synchrotron radiation emission for an ensemble of particles. This treatment will both examine the resultant changes to the emitted radiation, as well as the energy redistribution which occurs within the electron bunch due to the near-field interaction. To this end, the "steady-state" regime is defined to be one where all electrons within the ensemble experience a constant magnetic field, e.g. in the central portion of a

bending magnet.

2.2.1 Synchrotron Interaction Between Two Electrons

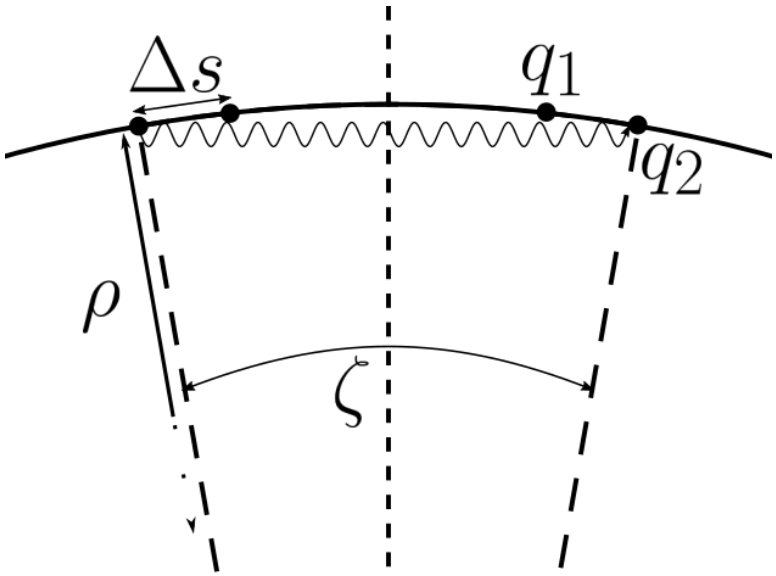

Figure 2.6: Geometry of the Liènard-Wiechert interaction between two electrons constrained to a circular orbit. The rear electron emits radiation that moves along the chord and interacts with the front electron at a later time. The electrons are separated in space by the distance Δs, with the angle between the front electron's position and the retarded read electron position being ζ.

The Liènard-Wiechert interaction between two electrons constrained on the same circular orbit separated by distance Δs (Figure 2.6) is asymmetric insomuch as the force felt on the front electron due to the rear electron is larger than that felt by the rear electron due to the front. That is not to say that the interaction does not obey Newton's 3$^{\text{rd}}$ law; each electron will feel an opposite radiative reaction force. The work done on the front electron due to the rear electron is given by [60]

$$\frac{dU_{21}}{dt} = q_2 \beta_2^i c E_{21}^i.$$

Here, the subscripts $._1$ and $._2$ denote the rear and front electrons respectively, and the subscript $._{ij}$ refers to some effect occurring on electron i due to electron j. Although not technically evaluated at the retarded time β_2^i may be brought inside the square brackets in the expression for the electric field (Equation 2.13) as the two electrons are co-moving, assumed to be at the same speed with any changes to particle velocities assumed negligible (ultra-relativistic limit). As such, differentiation with respect to the time at which the front electron receives radiation, t, is equivalent to that with respect to t_r. Given these assumptions, the energy change of the front electron is then given by

$$\frac{dU_{21}}{dt} = \frac{q^2 c\beta}{16\pi\epsilon_0\rho^2}\left[\frac{\cos\left(\frac{\zeta}{2}\right) - \beta\cos\zeta}{\gamma^2\sin\left(\frac{\zeta}{2}\right)^2\left(1-\beta\cos\left(\frac{\zeta}{2}\right)\right)^3} + \frac{2\beta^2\left(\sin\left(\frac{\zeta}{2}\right)\left(\cos\left(\frac{\zeta}{2}\right) - \beta\cos\zeta\right) - \left(1-\beta\cos\left(\frac{\zeta}{2}\right)\right)\sin\zeta\right)}{\sin\left(\frac{\zeta}{2}\right)\left(1-\beta\cos\left(\frac{\zeta}{2}\right)\right)^3}\right]. \tag{2.44}$$

Here, ζ refers to the angular separation between the emitting electron at t_r and the receiving electron at t. Given the ultra-relativistic approximation has been made, this angle can be assumed to once again be very small, and expansion of the trigonometric functions in Equation 2.44 to 2^{nd} order in ζ, as well as asserting $1-\beta \approx \frac{1}{2\gamma^2}$ and $\beta \approx 1$ yields

$$\frac{dU_{21}}{dt} \approx \frac{\gamma^4 q^2 c}{\pi\epsilon_0\rho^2}\left[\frac{1+\frac{3\gamma^2\zeta^2}{4}}{\gamma^2\zeta^2\left(1+\frac{\gamma^2\zeta^2}{4}\right)^3} + \frac{\frac{\gamma^2\zeta^2}{4}-1}{2\left(1+\frac{\gamma^2\zeta^2}{4}\right)^3}\right]. \tag{2.45}$$

This expression describes both the dissipative radiation interaction between the electrons and the non-dissipative Coulomb repulsion. In [60], Saldin separates out these two contributions to isolate the radiative interaction only. In doing so,

it is useful to define the particle separation along the orbit, Δs in terms of the retarded angle ζ. Radiation emitted from the rear electron will traverse the chord defined by ζ over the same time interval that the electron bunch will traverse the arc, minus the slippage which is equivalent to Δs. As such, Δs is given by

$$\Delta s = \rho\left(\zeta - 2\beta\sin\left(\zeta/2\right)\right) \approx \rho\zeta\left((1-\beta) + \frac{\zeta^2}{24}\right). \tag{2.46}$$

The Liènard-Wiechert field for two electrons in linear motion at the same velocity, separated by Δs, can be found from the first term in Equation 2.13, such that

$$E^i_{Coul.} = \frac{q}{4\pi\epsilon_0}\left[\frac{n^i-\beta^i}{\gamma^2 R^2\kappa^3}\right]\Bigg|_{t_r} = \frac{q}{4\pi\epsilon_0\gamma^2\Delta s^2}\left[\frac{n^i-\beta^i}{1-\beta}\right]\Bigg|_{t_r}.$$

When this expression is combined with Equation 2.46 and subtracted from Equation 2.45, the dissipative interaction [60, 82, 83]

$$\left(\frac{dU_{21}}{dt}\right)_{CSR} = \frac{\gamma^4 q^2 c}{\pi\epsilon_0\rho^2}\left[\frac{1}{\gamma^2\zeta^2}\left(\frac{1+\frac{3\gamma^2\zeta^2}{4}}{\left(1+\frac{\gamma^2\zeta^2}{4}\right)^3} - \frac{1}{\left(1+\frac{\gamma^2\zeta^2}{12}\right)^2}\right) - \frac{1-\frac{\gamma^2\zeta^2}{4}}{2\left(1+\frac{\gamma^2\zeta^2}{4}\right)^3}\right] \tag{2.47}$$

can be determined. As Saldin asserts in [60], this expression is useful as it is not singular at $\zeta = 0$ (Figure 2.7), unlike Equation 2.45. An interesting feature of the interaction is that it is not monotonic, nor is it entirely repulsive (Figure 2.7), becoming positive at $\gamma\zeta \approx 1.612$ or at a separation

$$\Delta s \approx 1.786 \frac{\rho}{\gamma^3}.$$

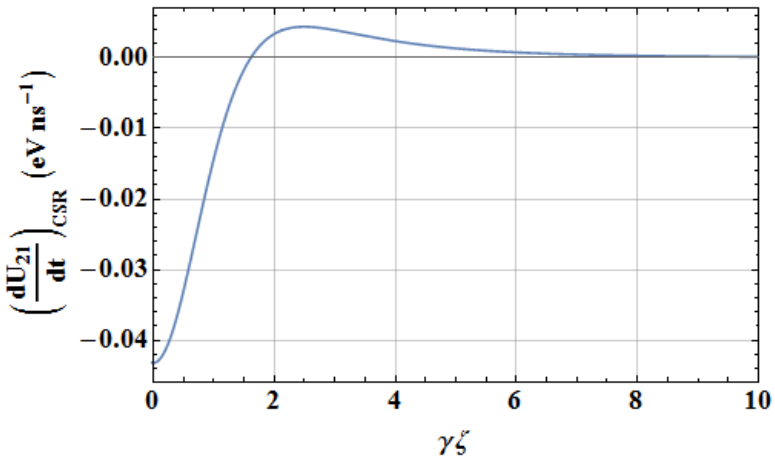

Figure 2.7: Energy change imparted upon the front electron due to the rear electron as a function of retarded angle. Here $\gamma = 10^3$ and $\rho = 10$ m

The force acting of the rear electron due to the front is purely Coulomb in nature and is thus not dissipative for the two particle system. Because of this, Equation 2.47 describes the coherent radiative losses of the combined two-electron system. From this it can be shown, as Saldin does in [60], that the two-electron system effectively radiates as a single particle of twice the elementary charge in the limit that their separation approaches zero. In the scenario where the electron separation is large, i.e. $\zeta \gg \frac{1}{\gamma}$, the term proportional to $(\gamma\zeta)^{-2}$ in Equation 2.47 is negligible and can be safely ignored. In this regime the dissipative interaction,

$$\left(\frac{dU_{21}}{dt}\right)_{CSR} = \frac{1}{4\pi\epsilon_0}\frac{32q^2c}{\rho^2\zeta^4}, \tag{2.48}$$

is no longer strongly energy dependent, and the retarded angle may be approximated as [60]

$$\zeta = \left(\frac{24\Delta s}{\rho}\right)^{1/3}. \tag{2.49}$$

It follows that the longer range interaction, defined by Saldin in [60] as where $\Delta s \gg \frac{\rho}{\gamma^3}$, can be written as

$$\left(\frac{dU_{21}}{dt}\right)_{CSR} = \frac{1}{4\pi\epsilon_0}\frac{2q^2c}{(9\rho\Delta s^2)^{2/3}}. \tag{2.50}$$

2.2.2 1-Dimensional Charge Distribution

The 2-particle interaction can then be generalised to an ensemble of particles. In this section, the ensemble will be considered as constrained upon the same orbit, i.e. a 1-dimensional charge distribution. The total force acting on a particle i at angular position ϕ_i due to the ensemble is given by

$$\left(\frac{dU_i}{dt}\right)_{CSR} = \frac{\gamma^4 q^2 c}{\pi\epsilon_0\rho^2}\sum_{j=1}^{j<i}\left[\frac{1}{\gamma^2(\Delta\phi)_{ij}^2}\left(\frac{1+\frac{3\gamma^2(\Delta\phi)_{ij}^2}{4}}{\left(1+\frac{\gamma^2(\Delta\phi)_{ij}^2}{4}\right)^3}-\frac{1}{\left(1+\frac{\gamma^2(\Delta\phi)_{ij}^2}{12}\right)^2}\right)-\frac{1-\frac{\gamma^2(\Delta\phi)_{ij}^2}{4}}{2\left(1+\frac{\gamma^2(\Delta\phi)_{ij}^2}{4}\right)^3}\right],$$

where $(\Delta\phi)_{ij} = \phi_i - \phi_j$ and it is assumed that for $j < i$, $\phi_j < \phi_i$, thus recognising that only electrons behind electron i result in coherent interaction. This is expressed more simply by assuming a continuous 1-dimensional charge distribution $\lambda(s)$:

$$\left(\frac{dU(s)}{dt}\right)_{CSR} = \int_{-\infty}^{s}\left(\frac{dU_1(s-s')}{dt}\right)_{CSR}\lambda(s')ds', \tag{2.51}$$

where $\left(\frac{dU_1(s-s')}{dt}\right)_{CSR}$ is the rate of energy change experienced at s due to a single electron at s', and $s-s' = \Delta s$ is defined as in Equation 2.46. If a constant charge density, $\lambda(s) = \lambda_0 = const.$, is selected this integral becomes

$$\left(\frac{dU}{dt}\right)_{CSR} = \frac{-\lambda_0 \rho}{2\gamma^3} \int_{-\infty}^{0} \left(1 + \frac{(\gamma\zeta)^2}{4}\right) \left(\frac{dU_1(\gamma\zeta)}{dt}\right)_{CSR} d(\gamma\zeta), \tag{2.52}$$

where the variable of integration has been changed to the retarded angle $\gamma\psi$ using a Jacobian element calculated from Equation 2.46, and where $\left(\frac{dU_1(\gamma\zeta)}{dt}\right)_{CSR}$ is the rate of energy change described by Equation 2.47. This integral evaluates to zero, which demonstrates the well know result found by Schwinger in [59] that a uniform ring of charge does not radiate. It is useful in the analysis for non-uniform charge distributions however, by showing that

$$\int_{-\infty}^{s} \left(\frac{dU_1(s-s')}{dt}\right)_{CSR} ds' = 0. \tag{2.53}$$

The integral in Equation 2.51 can be calculated by parts, with the boundary term evaluating to zero because of the relation given in Equation 2.53. Using the limit of the individual interaction strength given in Equation 2.50, where $\frac{R}{\gamma^3} \ll \sigma_z$ and σ_z is some characteristic length describing the arbitrary 1-dimensional distribution $\lambda(s)$, the coherent interaction as a function of the position within the electron bunch can be approximated as [8, 60, 84]

$$\left(\frac{dU(s)}{dt}\right)_{CSR} = -\frac{1}{4\pi\epsilon_0} \frac{2q^2 c}{(3\rho^2)^{1/3}} \int_{-\infty}^{s} \frac{1}{(s-s')^{1/3}} \frac{d\lambda(s')}{ds'} ds'. \tag{2.54}$$

A Gaussian bunch is an appropriate rough approximation to the current profile found in modern bunched-beam accelerators, and the resultant intra-bunch

energy redistribution for a Gaussian bunch is shown in Figure 2.8. The predominant feature is the asymmetry of the bunch, with only a small fraction of the energy lost by the bunch tail being imparted upon the head.

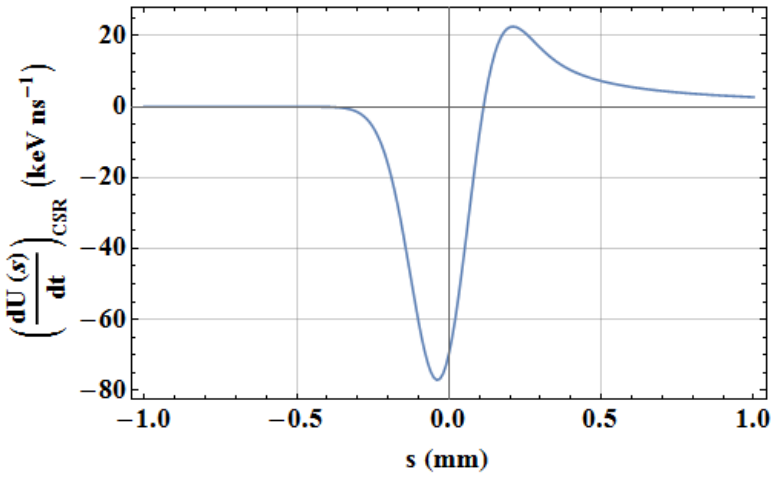

Figure 2.8: Rate of energy change due to CSR as a function of coordinate within the bunch. The electron bunch distribution is considered as 1-dimensional and mono-energetic, with a Gaussian distribution of $\sigma = 0.1$ mm. The total charge, $Q = 1$ nC, $\gamma = 10^3$, and $\rho = 10$ m.

The total coherent radiation emission for periodic motion is given by

$$P_{CSR} = \int_{-\infty}^{\infty} \lambda(s) \left(\frac{dU(s)}{dt}\right)_{CSR} ds, \tag{2.55}$$

where N is the total number of particles in the electron bunch. For a 1-dimensional Gaussian distribution propagated along a curved trajectory in free-space, this radiated power is equivalent to [82]

$$P_{CSR} = \frac{Q^2 c}{8\pi^2 \epsilon_0} \frac{3^{1/6}\Gamma^2(2/3)}{(\rho\sigma_z^2)^{2/3}}, \tag{2.56}$$

where σ_z is the r.m.s bunch length, and Q is the total bunch charge.

Far-field Steady-state Coherent Spectral Distribution

The total electric field for an arbitrary ensemble of electrons at an observation point P located at r from the origin is

$$\vec{E}(\vec{r},t) = \sum_{j=1}^{N} \vec{E}_j(\vec{r},t),$$

where N is the total number of electrons in the ensemble. It follows then that the Fourier Transform of this field [85],

$$\vec{\tilde{E}}(\vec{r},\omega) = \frac{1}{\sqrt{2\pi}} \sum_{j=1}^{N} \int_{-\infty}^{\infty} \vec{E}_j(\vec{r},t) e^{-i\omega t} dt.$$

In the scenario where a 1-dimensional, mono-energetic, ultra-relativistic bunch distribution can be assumed, the electric field contributions from the individual electrons in the ensemble are equivalent save for an offset in time, Δt_j [59, 85, 86], i.e. $\vec{E}_j(t) = \vec{E}_1(t + \Delta t_j)$, where $\vec{E}_1$ is the single particle electric field given in the previous section (Equation 2.13). In such a case, the Fourier transformed field becomes

$$\begin{aligned} \vec{\tilde{E}}(\vec{r},\omega) &= \frac{1}{\sqrt{2\pi}} \sum_{j=1}^{N} \int_{-\infty}^{\infty} \vec{E}_1(\vec{r}, t + \Delta t_j) e^{-i\omega t} dt \\ &= \frac{1}{\sqrt{2\pi}} \sum_{j=1}^{N} \int_{-\infty}^{\infty} \vec{E}_1(\vec{r}, \tilde{t}) e^{-i\omega(\tilde{t} - \Delta t_j)} d\tilde{t} \\ &= \vec{\tilde{E}}_1(\vec{r},\omega) \sum_{j=1}^{N} e^{i\omega \Delta t_j}, \end{aligned} \tag{2.57}$$

where $\vec{\tilde{E}}_1$ is the single-particle Fourier-transformed synchrotron radiation field (Equation 2.29). This can then be used alongside Equation 2.31 to define an

angular spectral energy distribution for the radiation field of the whole bunch [86],

$$\begin{aligned}\left(\frac{d^2U}{d\Omega d\omega}\right)_{Total} &= \frac{1}{\mu_0 c}|R\tilde{\vec{E}}|^2 = \frac{1}{\mu_0 c}\left(R\,\tilde{\vec{E}}_1\sum_{j=1}^{N} e^{i\omega\Delta t_j}\right)\left(R\,\tilde{\vec{E}}_1^{*}\sum_{k=1}^{N} e^{-i\omega\Delta t_k}\right) \\ &= \left(\frac{d^2U}{d\Omega d\omega}\right)_1\left(N + \sum_{j=1}^{N} e^{i\omega\Delta t_j}\sum_{\substack{k=1\\k\neq j}}^{N} e^{-i\omega\Delta t_k}\right),\end{aligned} \tag{2.58}$$

where $\left(\frac{d^2U}{d\Omega d\omega}\right)_1$ is the single particle angular spectral density (Equation 2.42). The mono-energetic, 1-dimensional, ultra-relativistic bunch distribution can be represented as a temporal density distribution,

$$\lambda(t) = \frac{1}{N}\sum_{j=1}^{N}\delta(t-\Delta t_j). \tag{2.59}$$

A subset of this density distribution can be defined as

$$\lambda_j(t) = \frac{1}{N-1}\sum_{\substack{k=1\\k\neq j}}^{N}\delta(t-\Delta t_k) \approx \lambda(t),$$

allowing Equation 2.58 to be written as

$$\begin{aligned}\left(\frac{d^2U}{d\Omega d\omega}\right)_{Total} &\approx \left(\frac{d^2U}{d\Omega d\omega}\right)_1\left(N + N(N-1)\int_{-\infty}^{\infty}\lambda(t)e^{i\omega t}dt\int_{-\infty}^{\infty}\lambda(t)e^{-i\omega t}dt\right) \\ &= \left(\frac{d^2U}{d\Omega d\omega}\right)_1\left(N + N(N-1)|F(\omega)|^2\right),\end{aligned} \tag{2.60}$$

where $F(\omega)$ is the form-factor corresponding to the electron distribution density

function $\lambda(t)$. This expression is common for many types of coherent radiation besides CSR, where a form-factor dependent on the bunch distribution modulates an amplified coherent term proportional to Q^2, where Q is the total electron bunch charge. The modulation essentially defines the region of the incoherent spectrum which is amplified, with wavelengths longer than the electron bunch length amplified coherently (Figure 2.9).

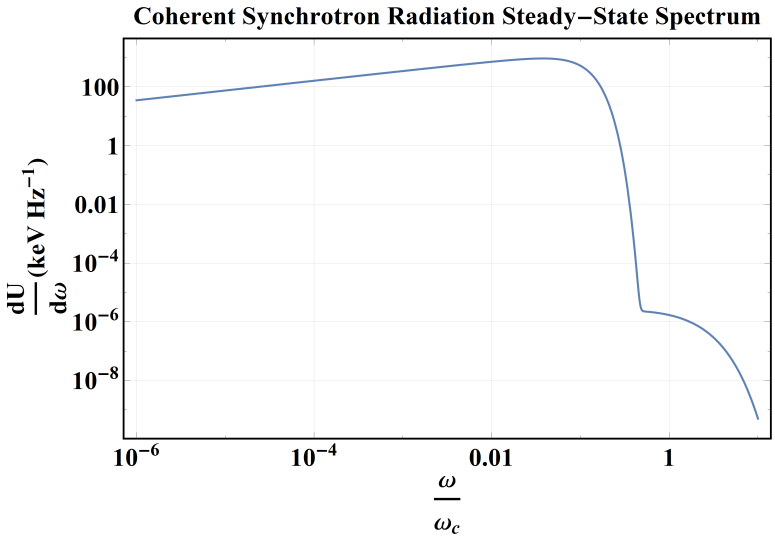

Figure 2.9: Spectrum of combined coherent and incoherent synchrotron emission of a 100 fs, 35 MeV, 100 pC Gaussian electron bunch using the 1-dimensional analytical model. At this low energy and short bunch length the emission is almost completely coherent.

Because coherent amplification only occurs for the longer wavelength (lower frequency) part of the synchrotron radiation spectrum, the typical coherent radiation distribution is much broader than the incoherent portion (Figure 2.10). This is most noticeable in lower-energy machines, where the coherent component dominates the overall synchrotron power due to the critical harmonic wavelength being closer to the electron bunch length. A further consequence of this is that

the vertical (π) polarisation mode comprises a larger proportion of the total coherent emission. This allows the orthogonal polarisation modes to be a useful indicator of the presence of coherent radiation (Figure 2.11), through the use of a suitable polariser rated for the necessary bandwidth expected for the coherent radiation.

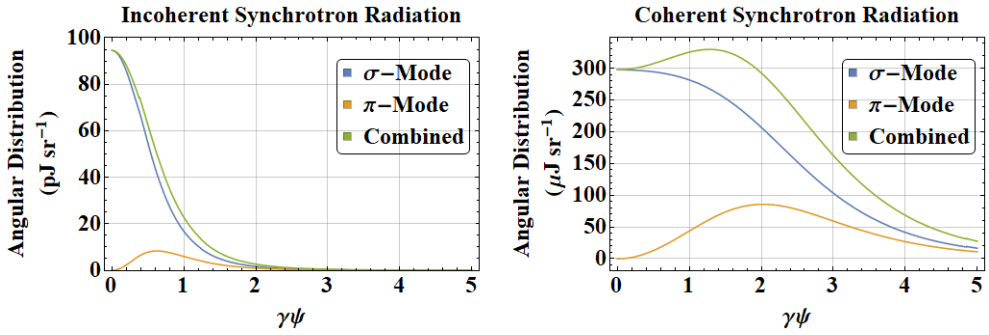

Figure 2.10: Angular distribution of incoherent and coherent synchrotron radiation distributions for an ideal 1-dimensional Gaussian electron bunch. $Q = 100$ pC, $\langle U \rangle = 35$ MeV, $\sigma_t = 100$ fs, and $\rho = 1$ m. At this energy the coherent radiation dominates the total emission, and the width of the distribution is orders of magnitude larger.

Again, it is illustrative to look at the common approximation to a bunched electron beam current profile, the Gaussian distribution. In such a case, the angular spectral distribution is given by

$$\left(\frac{d^2U}{d\Omega d\omega}\right)_{Total} = \left(\frac{d^2U}{d\Omega d\omega}\right)_1 \left(N + N(N-1)e^{-\omega^2\sigma_t^2}\right),$$

where σ_t is the characteristic electron pulse length. When integrated with respect to the solid angle Ω, this distribution yields the characteristic "double-hump" of CSR (Figure 2.9).

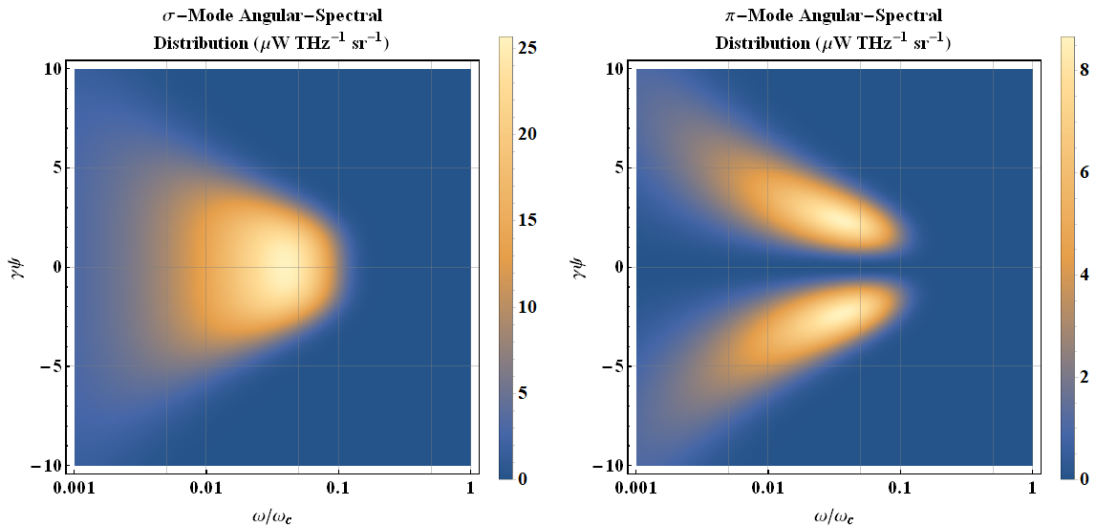

Figure 2.11: Orthogonal polarisation modes of a 100 fs, 35 MeV, 100 pC Gaussian electron bunch in the 1-dimensional analytical limit of CSR. Both the incoherent and coherent contributions to the radiation distribution are shown, but the coherent contribution dominates at this low energy.

2.3 CSR: Beyond Steady-State

The model for coherent radiation outlined in the previous section is useful for a qualitative view on the processes underlying CSR, and can also provide good quantitative approximations to the impacts of the CSR process, such as the total beam energy loss and the growth in energy spread, however it comes with important caveats. In this section many of the limitations regarding analytical modelling of CSR will be addressed.

2.3.1 CSR in the Presence of Bunch Compression

The first of these limitations arises from the ultra-relativistic approximation, which is used to justify expansion up to second order in ψ or $\omega_0 t_r$ of trigonometric functions as well as omitting powers of β. In most electron accelerators, especially high-energy synchrotrons, this is a reasonable assumption to make due

to the high γ. A more significant caveat is the assumption of a mono-energetic beam, which enforces that particles follow the same trajectory curvature through the magnetic field. Once again this is an appropriate assumption to make for synchrotrons, in particular storage-rings, where the energy spread is minimised within the equilibrium beam to maintain the beam's longitudinal stability. For linac-driven FELs, this constraint is not so valid given the use of dispersive compression to achieve very short electron pulse lengths. In a bunch-compressor dipole, not only do the particles within a bunch propagate along different trajectories, the overall bunch length varies, changing the strength of the coherent interaction. Analysis carried out in [83] demonstrates a 1-dimensional formulation of the CSR interaction, which accounts for bunch compression. This is carried out using the Jefimenko electromagetic equations [87]

$$\vec{E}(\vec{r},t) = \frac{1}{4\pi\epsilon_0}\int\left(\frac{\rho(\vec{r'},t_r)}{R^2}\vec{n} + \frac{\dot{\rho}(\vec{r'},t_r)}{cR}\vec{n} - \frac{\dot{\vec{J}}(\vec{r'},t_r)}{c^2R}\right)d^3r', \tag{2.61}$$

$$\vec{B}(\vec{r},t) = \frac{\mu_0}{4\pi}\int\left(\frac{\vec{J}(\vec{r'},t_r)}{R^2} + \frac{\dot{\vec{J}}(\vec{r'},t_r)}{cR}\right)\times\vec{n}\;d^3r', \tag{2.62}$$

which allows the retarded field calculation to be carried out using generalised, time-dependent, charge ($\rho(\vec{r},t)$) and current ($\vec{J}(\vec{r},t)$) densities. Here $\dot{\rho}(\vec{r},t) = \frac{\partial\rho}{\partial t}$ and $\dot{\vec{J}}(\vec{r},t) = \frac{\partial\vec{J}}{\partial t}$ are the respective rates of change of these distributions. Consider a one-dimensional ultra-relativistic normalised bunch distribution, λ, with the distribution centred on $s = 0$ at $t = 0$, such that

$$\rho(s,t) = Q\lambda(s-\beta ct),$$
$$\vec{j}(s,t) = Qc\vec{\beta}(s)\lambda(s-\beta ct),$$

where Q is the total bunch charge and s defines the position along the bunch trajectory. In [83] the component of the wake due to CSR is calculated in a similar manner to that outlined here previously (from [60]), where the space charge component is subtracted from the total wake, removing the singularity of the wake as the separation between the witness and source, R, tends towards 0. It is established by Mayes and Hoffstaetter in [83] that the 1-dimensional CSR wake induced on the electron bunch due to passing through a dipole bend is given by

$$\begin{aligned}\left(\frac{dU(s,t)}{dt}\right)_{CSR} = \frac{Nq^2c}{4\pi\epsilon_0}\Bigg(&\left[\frac{\lambda(s_\alpha(\alpha,s,t))}{\rho\sqrt{2-2\cos\alpha}}\right]_{\alpha=-(\theta_D-\theta(s))}^{\alpha=\theta(s)} \\ &+\int_{-(\theta_D-\theta(s))}^{\theta(s)}\Bigg[\frac{\beta^2\cos\alpha-1}{\sqrt{2-2\alpha}} \\ &+\frac{\mathrm{sgn}(\alpha)}{\gamma^2}\frac{1-\frac{\beta\sin\alpha}{\sqrt{2-2\cos\alpha}}}{\alpha-\beta\sqrt{2-2\cos\alpha}}\Bigg]\lambda'(s_\alpha(\alpha,s,t))d\alpha \\ &-\int_{-\infty}^{-(\theta_D-\theta(s))} I_{SC}(\alpha,s,t)d\alpha-\int_{\theta(s)}^{\infty} I_{SC}(\alpha,s,t)d\alpha\Bigg),\end{aligned} \tag{2.63}$$

where $s_\alpha = \rho(\theta(s)-\theta_0(t)-\alpha)+\beta\rho\sqrt{2-2\cos\alpha}$, $\theta(s) = s/\rho$, $\theta_0(t) = \beta ct/\rho$, and θ_D is the total bend angle of the magnet. Here, α is used as a variable integration related to the angular separation of the source and witness positions, $\lambda'(s_\alpha) = d\lambda/ds_\alpha$, and $I_{SC}(\alpha,s,t)$ describes the contribution to the wake arising

from space charge and takes the form shown in [83]. By allowing an explicit time dependence for the linear density λ, the effect of a changing bunch length can be included.

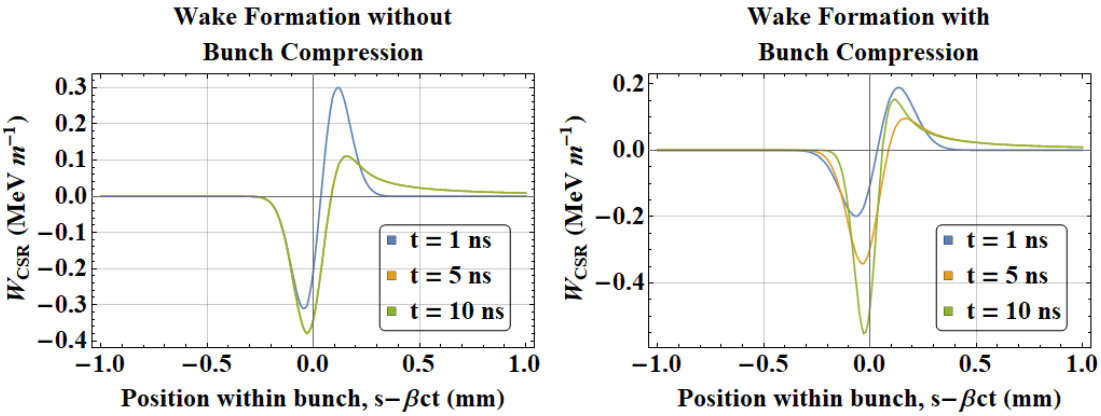

Figure 2.12: Evolution of the CSR wake for 1-dimensional Gaussian electron bunches passing through a dipole with constant bunch length and a linearly varying bunch length respectively. Here $\gamma = 10^3$, $Q = 1$ nC, $\rho = 10$ m, and $\theta_D = \pi/10$ rad. In constant bunch length case, $\sigma = 0.075$ mm, and in the variable bunch length case σ varies linearly between 0.1 mm and 0.05 mm. In the case of constant bunch length, after the initial formation of the wake it remains constant with respect to the bunch's position within the dipole (i.e steady-state), as is shown by the complete overlap of the 5 ns and 10 ns curves.

This expression eliminates another caveat of the previously defined 1-dimensional theory, by considering a finite dipole. Equation 2.63 is only strictly valid for an isolated dipole, however it establishes a framework from which to perform an analytical calculation for more complex bending magnet configurations. Numerical evaluation of Equation 2.63 is shown in Figure 2.12 for Gaussian bunches in the cases where the bunch length is constant and where the bunch length varies linearly as the bunch propagates through the bending magnet. This effect is of importance to the work in this thesis, wherein simulations of the CLARA Phase 1 accelerator are carried out in the regime of rapid bunch compression through

dipole bends. As such, this expression will provide an analytical comparison of the total energy loss and redistribution across the dipoles.

2.3.2 Generalised Charge Distribution

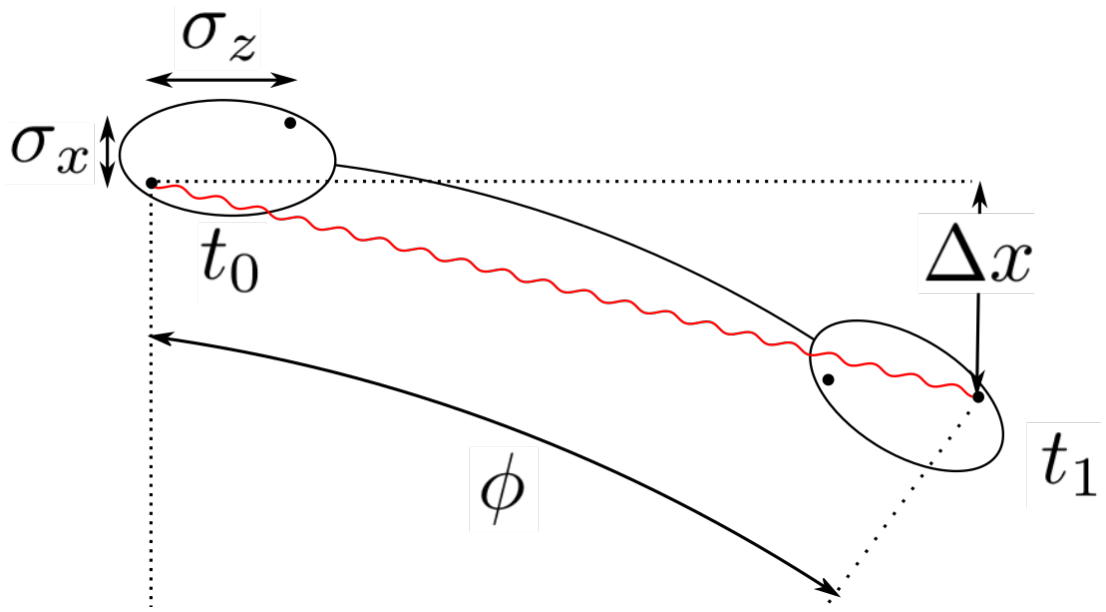

Figure 2.13: Diagram showing the geometry involved in evaluating the 1-dimensional limit of CSR modelling. Two electrons is an electron bunch travelling on a curved trajectory are separated by σ_x transversely and σ_z longitudinally. At time t_0, radiation (in red) is emitted from the rearward electron, and then overtakes the electron bunch and interacts with the headward electron at t_1. Over this time frame, the electron bunch travels a slippage length (defined by the angle ϕ), the transverse projection of which is given by Δx.

So far, all models for CSR that have been considered have all relied upon a 1-dimensional approximation. The validity of this approximation will naturally be dependent in some way upon the bunch aspect ratio. Consider an electron bunch traversing an arc in the x-z plane. At t_0, radiation from an electron towards the back of the bunch is emitted and received at a later time, t_1 (Figure 2.13). For simplicity, it will be assumed that the bunch velocity $\vec{\beta}(t_1)c = \beta c\vec{e_z}$, i.e. the bunch is parallel with the z-axis at t_1, and at t_0 the bunch is located at an angular

displacement ϕ. The projection along the x-axis of the bunch trajectory between t_0 and t_1 is described by

$$\Delta x = 2\rho \sin^2\left(\frac{\phi}{2}\right) \approx \frac{\rho\phi^2}{2}. \tag{2.64}$$

A reasonable criterion for the validity of a 1-dimensional model of CSR would be that $\sigma_x \ll \Delta x$. Violation of this would imply that the extra path length distance between off-axis particles was non-negligible with regards to the overall path length of the radiation. For radiation emitted from a source particle σ_z behind the witness particle, the retarded angle is found by equating the travel times for the radiation and the electrons, i.e.

$$\Delta t = \frac{2\rho \sin\left(\frac{\phi}{2}\right)}{c} = \frac{\rho\phi - \sigma_z}{\beta c},$$

which, when a small angle approximation is made, corresponds to a retarded angle of

$$\phi \approx 2\left(\frac{3\sigma_z}{\rho}\right)^{1/3}.$$

Inserting this expression into Equation 2.64, and applying the condition previously stated on the transverse bunch extent gives the so-called"Derbenev Criterion" [8]

$$\sigma_x \ll 2\left(9\rho\sigma_z^2\right)^{1/3},$$

or as it is more commonly expressed [88]

$$\frac{\sigma_x}{(\rho\sigma_z^2)^{1/3}} \ll 1. \tag{2.65}$$

Henceforth, the quantity $\frac{\sigma_x}{(\rho\sigma_z^2)^{1/3}}$ will be referred to as the Derbenev parameter. A similar condition can be made for the vertical (out-of-plane) beam size, this time by enforcing that the vertical displacement of emitted radiation is far smaller than the length the chord traversed in the bending plane. In this way, the 1-dimensional limit for the vertical beam size is that

$$\frac{\sigma_y}{(\rho^2\sigma_z)^{1/3}} \ll 1, \tag{2.66}$$

which is notably a far more relaxed condition than that given in Equation 2.65.

Modelling coherent radiation outside this regime is carried out using a variety of numerical methods. Possibly the most simplistic formulation in 3-dimensions is found in [86, 89], whereby a 3-dimensional form factor is generated in a manner similar to Equations 2.58, 2.59, and 2.60. This analysis operates under the assumption that the far-field condition is met, wherein the unit vectors from all points within the source distribution to the observer position can be considered approximately parallel. For a given source electron located at $\vec{r_j}$, the corresponding field contribution witnessed at the observation point located at $\vec{R_P}$ is equivalent to that emitted from the bunch centre, located at the origin, save for a time delay. This time delay is given by

$$\Delta t_j = \frac{1}{c}(R_j - R_P),$$

where $R_j = |\vec{R_j}|$ is the distance from the source electron to the observer, and $R_P = |\vec{R_P}|$. Using the aforementioned far-field (or paraxial) assumption, the distance $R_j = (\vec{R_P} - \vec{r_j}) \cdot \vec{n_j} \approx R_P - \vec{n} \cdot \vec{r_j}$, where $\vec{n_j}$ and $\vec{n}$ are the unit vectors pointing towards the observer from the source electron and the bunch centre

respectively, and have been approximated as equivalent. As such the time delay is then written as

$$\Delta t_j = -\frac{\vec{n}\cdot\vec{r_j}}{c} = -\frac{\vec{k}\cdot\vec{r_j}}{\omega},$$

where the wave-vector $\vec{k} = \frac{\omega}{c}\vec{n}$. Replacing the expressions for Δt_j in Equation 2.58 with this expression and recognising that the bunch distribution

$$\rho(\vec{r}) = \frac{1}{N}\sum_{j=1}^{N}\delta(\vec{r}-\vec{r_j})$$

yields a modified form of 2.60:

$$\begin{aligned}\left(\frac{d^2U}{d\Omega d\omega}\right)_{Total} &\approx \left(\frac{d^2U}{d\Omega d\omega}\right)_1 \left(N + N(N-1)\int \rho(\vec{r'})e^{i\vec{k}\cdot\vec{r'}}d^3r' \int \rho(\vec{r'})e^{-i\vec{k}\cdot\vec{r'}}d^3r'\right) \\ &= \left(\frac{d^2U}{d\Omega d\omega}\right)_1 \left(N + N(N-1)|F_{3D}(\Omega,\omega)|^2\right).\end{aligned} \tag{2.67}$$

It should be noted that this expression for the angular spectral distribution is limited to the steady state regime, as analytical calculation of the spectral dependence of the radiation requires this assumption (periodic motion). As such, it is not applicable to situations where the charge density is changing with respect to time, as is common in bunch compressor dipoles. In order to calculate the coherent emission in such a scenario, dedicated numerical methods must be employed in simulations. Nevertheless, this generalisation is a useful method for estimating the angular-spectral distribution of emitted radiation for electron bunches which do not reduce down to a 1-dimensional Gaussian current profile.

2.3.3 Transient Regime

A fundamental issue with employing the steady state regime is that a majority of accelerators consist of finite dipole arcs joined with long drift sections. For a given dipole bend, the steady state regime is only valid from the location where the radiation interacting with the front of the bunch was emitted from the rear of the bunch as it entered the dipole. As such, this distance is approximately equivalent to the overtaking length for the whole bunch length, i.e. [60, 88]

$$(\Delta s)_{SS} \approx \left(24\rho^2\sigma_z\right)^{1/3}. \tag{2.68}$$

This is typically not a small quantity for many bending magnet configurations. For example, an electron bunch passing through a 10° bend of radius $\rho = 10$ m with an r.m.s bunch length of 0.15 mm (approximately 0.5 ps) will only enter the steady state regime at a distance of 0.711 m into the dipole, which is 40% of the entire magnet length. Only in situations where either the bunch is very short, the bending radius is very small, or the dipole is very long can the transient regime be considered negligible. As such, proper modelling of the transient regime is necessary for confidence when evaluating the impact of CSR on the longitudinal phase space of the bunch during bunch compression.

While the entrance transient has been discussed briefly in the previous section it will be analysed more closely here with a different formalism. In order to understand the effect of the entrance transient, it is necessary to reformulate the 2-particle interaction for the case when the rear electron's retarded position is outside of the bending magnet. It should be evident that because the source electron propagating in free space, then the field felt by the front electron is

purely Coulomb in nature. The work done by a witness particle within a dipole field against the electric field generated from a particle at a retarded positioned outside of the dipole field is given by [88]

$$\left(\frac{dU_{21}}{dt}\right)_{Entrance} = \frac{q^2 c\beta}{4\pi\epsilon_0\gamma^2}\frac{(\delta - \beta R)\cos\phi + \rho\sin\phi}{(R - \beta(\delta + \rho\sin\phi))^3}, \tag{2.69}$$

where a similar labelling scheme has been used as in Section 2.2.1, δ is the distance between the retarded source position and the magnet entrance, and ϕ is the angular position within the bend of the witness electron. Extending this to a 1-dimensional charge distribution $\lambda(s)$, requires combination of the steady-state interaction arising from Equation 2.47, and of Equation 2.69 for the parts of the distribution that are also witnessing the field of electrons outside of the magnet. The resultant wake takes the form of [8, 60, 88]

$$\begin{aligned}\left(\frac{dU(\tilde{s},t)}{dt}\right)_{Entrance} =& \frac{Nq^2\beta^2 c}{8\pi\epsilon_0\rho}\int_0^{\phi(\tilde{s},t)}\frac{\beta - \cos(\zeta/2)}{(1-\beta\cos(\zeta/2))^2}\lambda(\tilde{s_r})d\zeta \\ &+ \frac{Nq^2 c}{4\pi\epsilon_0\gamma^2}\int_0^D \frac{(\delta - \beta R(\delta))\cos\phi + \rho\sin\phi}{\left(R(\delta) - \beta(\delta + \rho\sin\phi)\right)^2 R(\delta)}d\delta,\end{aligned} \tag{2.70}$$

where $\tilde{s}$ is the longitudinal position within the bunch (relative to the bunch centroid), t is the observation time measured relative to the bunch centroid passing through the entrance of the magnet, $\phi = \phi(\tilde{s},t) = (\tilde{s} + \beta ct)/\rho$ is the angular position of the observer position with respect to the dipole entrance, and ζ is the retarded angle as used previously. The coordinate $\tilde{s}_r = \tilde{s} - \rho\zeta + 2\rho\beta\sin(\zeta/2)$ is the retarded position within the bunch, D is the total length of the drift preceding the dipole, the variable of integration δ refers to the distance to the magnet entrance from the downstream position in the drift of length D, and the quantity $R(\delta) = \sqrt{\delta^2 + 2\rho\delta\sin\phi + 4\rho^2\sin^2(\phi/2)}$ is the distance between the observer

within the dipole and the source without. The first term in this expression is due to the radiative interaction in the steady state alone, being equivalent to the expression in 2.47 albeit for a linear charge distribution rather than due to a singular electron. The latter term is a velocity term arising from electrons outside of the dipole magnet, which has the effect of reducing the net CSR force in the entrance transient regime. As is observed in [88], the partial cancelling effect due to the velocity term in Equation 2.70 implies that the CSR entrance transient is dependent upon the drift length preceding the dipole. For a given angular position within the bend, ϕ, there is a critical value of δ below which there is negligible reduction of the radiation field due to the velocity term contribution, and this is given by [88]

$$\delta_c \approx \frac{\gamma\rho\phi}{\sqrt{2}}. \tag{2.71}$$

In the case of the exit transient, the situation is somewhat reversed. Particles in the bunch continue to witness radiation emitted from retarded positions within the dipole after they have left the dipole themselves. Using a similar treatment to that when deriving the entrance transient 2-particle system, the exit transient wake is given by

$$\begin{aligned}\left(\frac{dU_{21}}{dt}\right)_{Exit} =& \frac{q^2c\beta^2}{4\pi\epsilon_0\gamma^2}\frac{\delta+\rho\sin\phi-\beta R\cos\phi}{(R-\beta(\delta\cos\phi+\rho\sin\phi))^3} \\ &+\frac{q^2c\beta^3}{4\pi\epsilon_0\rho}\left(\frac{2\sin(\phi/2)(\delta+\rho\sin\phi-\beta R\cos\phi)(\rho\sin(\phi/2)+\delta\cos(\phi/2)}{(R-\beta(\delta\cos\phi+\rho\sin\phi))^3}\right. \\ &\left.-\frac{R\sin\phi}{(R-\beta(\delta\cos\phi+\rho\sin\phi))^2}\right),\end{aligned} \tag{2.72}$$

where once again δ refers to the distance away from the dipole face, though in this case it is the distance of the witness particle from the exit face. The angle ϕ defines the retarded position of the source electron, with R the distance between the source and the witness, which is equivalent to its stated definition in the entrance transient case. When applied to a 1-dimensional line charge profile, $\lambda(s)$, in the ultra-relativistic limit such that the opening angle of the radiation cone $\Delta\phi \lesssim 1/\gamma$, the dipole exit wake takes the form [88]

$$\begin{aligned}\left(\frac{dU(\tilde{s},t)}{dt}\right)_{Exit} =& \frac{Nq^2c}{\pi\epsilon_0}\left(\frac{\lambda(\tilde{s}-\Delta s_{max})}{\phi_0\rho+2\delta}\right. \\ &\left. + \int_{\tilde{s}-\Delta s_{max}}^{\tilde{s}} \frac{\partial\lambda(\tilde{s}')}{\partial\tilde{s}'}\frac{1}{\phi(\tilde{s}')\rho+2\delta}d\tilde{s}'\right).\end{aligned} \tag{2.73}$$

Here ϕ_0 is the total dipole bend angle, and $\phi(\tilde{s})$ is defined by the equation

$$\tilde{s}-\tilde{s}' = \frac{\rho^2\phi^4+4\delta\rho\phi^3}{24(\rho\phi+\delta)}.$$

The value Δs_{max} is equivalent to the right hand side of this expression in the case that $\phi = \phi_0$. This theory is laid out in [88] in order to stress the importance of the velocity term when calculating transient effects in CSR emission. Experimental results of emittance growth were compared to GPT simulations with and without the Coulomb term included in the CSR calculation, and successfully demonstrated the importance of this effect. Fundamentally, analytical CSR calculation are always limited in terms of their applicability, with numerical and simulation methods becoming necessary in order to accurately simulate the effects due to a realistic beam, and such simulations will form the basis of this thesis.

2.3.4 Radiation Emitted from a Dipole Fringe

Alongside the transient effects upon the steady-state CSR wake discussed previously, a second process occurs in the fringe field region of a dipole. The inhomogeneous magnetic field typical of a dipole fringe gives rise to a form of radiation qualitatively different to that emitted in the steady-state. This radiation essentially arises from sudden changes to the velocity field of the Liènard-Wiechert field, i.e. the "Coulomb" term, resulting in a non-vanishing contribution to the Poynting vector at large distances. In this thesis, measurements of this variant of coherent synchrotron are carried out at the MAX IV beamline and compared to CSR simulations which include the effect of the velocity field.

First observed as the interference of background incoherent synchrotron radiation sources in wiggler experiments on the "Sirius" electron synchrotron [90], the first experimental study of the process was carried out by Nikitin *et al.* in [91]. A foundational analysis of such radiation was described by Geloni *et al.* in [92, 93], wherein the behaviour of the incoherent emission was analysed in several qualitative regimes. Of particular relevance to this thesis are the cases which deal with the interference of the emission between two neighbouring dipole edges, and where the radiation from a single edge is captured by a mirror in the downstream drift section. The analysis set out in [92] argues that the qualitative description of synchrotron radiation depends upon two dimensionless intensive variables,

$$\tilde{\delta} \equiv \frac{(\rho^2 \lambda\!\!\!^{-})^{1/3}}{L}, \qquad \tilde{\phi} \equiv \frac{L}{\gamma^2 \lambda\!\!\!^{-}}, \tag{2.74}$$

where $\lambda\!\!\!^{-} = \frac{\lambda}{2\pi}$ is the reduced wavelength, and L is the length of a drift section. The first of these parameters essentially defines the ratio between the formation

length of conventional synchrotron radiation at a given wavelength and the length of the straight section, and as such serves to define the relative contribution between conventional synchrotron radiation and fringe-field synchrotron radiation, with solely conventional synchrotron radiation being corresponding to $\tilde{\delta} \geq 1$. The second parameter defines the ratio between the straight section length and what is termed the "critical length of interest". This defines the distance separating two points over which it is impossible to map the temporal behaviour of the observed electric field to an equivalent source position.

The analysis continues by providing a general expression for the Fourier-transformed field of a single electron travelling along an arbitrary trajectory. This is done via solution of the Helmholtz equation using a Green's function method, where the paraxial approximation is made. This assumption establishes that the methodology presented in [92] is only valid in an ultra-relativistic regime, such that $\gamma^2 \gg 1$, and at an observer distance much greater than the reduced wavelength of the radiation. Further to this, the analysis is carried out in the long–wavelength limit $\lambda\!\!\!^{-}/\lambda\!\!\!^{-}_c \gg 1$, where $\lambda\!\!\!^{-}_c \sim \rho/\gamma^3$ is the critical wavelength of the synchrotron emission within the magnets. It is asserted then that edge radiation should be considered only in the case where $\tilde{\delta} \ll 1$ and $\tilde{\delta}\tilde{\phi} \ll 1$. In the context of this thesis, wherein the focus is specifically upon coherent emission processes, the relevant wavelength range is further restricted to those larger than the electron bunch dimensions.

This treatment is then applied to a range of beamline geometries to obtain the Fourier components of the electric field in a given case. Of the cases considered

in [92], the most relevant to this thesis is that which deals with the fringe radiation generated from a single dipole bend edge observed in the near field. This corresponds to the geometry which will be discussed in a later section regarding photonic detection upon the CLARA Phase 1 beamline. In this scenario, detection of fringe field CSR emitted from the exit of a dogleg transfer line and the entrance to a spectrometer line (separated by a long straight section) is considered as a method of indirectly corroborating GPT simulations of CSR. Because of spatial constraints in the proposed detection location, this imaging of radiation in the context of the closer downstream dipole fringe will be both near-field and far-field depending upon the expected electron bunch dimensions. As the experimental context of this application of fringe-field radiation involves variation of the electron bunch compression, both regimes would need to be considered. In both scenarios however, the further upstream dipole is significantly far away that the field contribution arising from it has vanishing impact upon the electric field at the measurement point when compared to that of the closer fringe. Close to maximum compression the electron bunch length in CLARA Phase 1 is typically of the order ∼200 fs, and the angular-spectral energy density of the incoherent fringe radiation is given by the far-field expression,

$$\frac{d^2U}{d\Omega d\omega} = \frac{q^2}{4\pi^3\epsilon_0 c}\frac{\gamma^4 r_\perp^2 d^2}{(\gamma^2 r_\perp^2 + d^2)^2}, \tag{2.75}$$

where $r_\perp$ is the transverse distance from the central beam axis (incoming relative to the dipole fringe) of the observer, and d is the longitudinal distance. This single particle angular-spectral energy density can be used in Equation 2.67 to determine the corresponding coherent energy density [93]. While the presented single-particle energy density is frequency-independent, coherent effects will of

course show spectral variation. The domain of applicability specified for this expression is stated as when $\gamma^2\lambda \ll d$, which is observed for compressed bunches considering d ∼0.5 m and γ ≈70. For longer electron bunches, typically on the order of ∼ ps, $\gamma^2\lambda_{\min}$ approaches approximately 2 m, where $\lambda_{\min}$ corresponds to the shortest coherently amplified wavelength (on the order of the electron bunch length), meaning that the near-field analysis must be applied. In this regime, the electric field (in the frequency domain) due to a single electron passing through the fringe is given by

$$\tilde{\vec{E}}(\omega, d, \vec{r}_\perp) = \frac{i}{4\pi\epsilon_0 r_\perp^2} \frac{2q\vec{r}_\perp}{c\left(1-\frac{L}{2d}\right)} e^{\frac{i\omega L}{4c\gamma^2}} e^{\frac{i\omega r_\perp^2}{4c(d-L/2)}} \sin\left(\frac{\omega r_\perp^2}{4c(d-L/2)}\right). \tag{2.76}$$

Here, similarly to the scalar distance $r_\perp$, the vector $\vec{r}_\perp$ describes the transverse position of the observer relative to the central beam axis. This expression can then be used in Equation 2.31 to obtain the angular-spectral energy distribution in the near-field regime.

The second context of relevance to radiation emitted in the fringe field are measurements made on the MAX IV linac presented in this thesis. Here, a mirror 1.678 m downstream from the final dipole of a bunch compressor is used to extract fringe-field radiation. This geometry is specifically analysed in the context of coherent emission in [93]. Here it is stated that in the situation where $\tilde{\phi} \gg 1$, the fringe field emission can be accurately represented as transition radiation, and as such can be modelled with the Ginzburg-Frank formula [94]. However given the high energy of the MAX IV beam (3 GeV), only wavelengths $\lambda \ll 48.7$ nm can be treated in this manner, far smaller than the wavelengths of interest to

the experimental work within this thesis. Instead, the radiation is described by $\phi \ll 1$, and the electric field is given by

$$\tilde{\vec{E}}(\omega, L/2, \vec{r}_\perp) = \frac{-1}{4\pi\epsilon_0 r_\perp^2} \frac{2q\vec{r}_\perp}{c\left(1 - \frac{L}{2d}\right)} e^{\frac{i\omega r_\perp^2}{2cL}}. \tag{2.77}$$

Here, $L/2$ is equivalent to the distance from the fringe to the target. When applied to Equation 2.31, this yields a spectral density that is singular at $r_\perp = 0$; this is a result of a sharp edge approximation that has been used in the analysis. All expressions featured in [92, 93] incorporate a sharp-edge model of the dipole fringe, and have limited applicability in situations where the dipole fringe has significant extent. The simulations in this thesis all incorporate fringes of a finite width and so the quantitative conclusions of this theory are not necessarily applicable, although the qualitative arguments help understand the nature of emission processes in some of the regimes studied herein. Evaluation of the radiation energy density featured herein will be carried out through numerical simulations.

Chapter 3

Computational Tools

In this chapter, a survey of the computational tools currently available for the calculation of CSR effects is presented. The different ways from which these tools approach the CSR problem, and their respective advantages and limitations, will be discussed. Experimental comparisons to the numerical methods found in the literature will also be covered where applicable. Further to this, the implementation in simulation tools of the beamlines covered in this thesis is explained.

3.1 Simulation Tools for Collective Effects

Because of its importance when considering the dynamics of short electron pulse accelerators, many simulation codes are either capable of or dedicated to the modelling of collective effects such as CSR. In the case of CSR, there is a significant requirement for accurate modelling of the process without incurring too large a computational cost. Due to it being a coherent process, the execution time of any point-wise calculation of the CSR wake scales as $\mathcal{O}(N^2)$, where N is the number of macroparticle sources used in the simulation. Further to this, exact calculation

has a significant computational overhead as it takes contributions from all of the particles which fulfil the retardation condition for the entire simulation (i.e. at every time step), which is both demanding on memory and processing capacities. As such many simulations make approximations and assumptions when calculating CSR. Many of the codes used for coherent radiation are with the specific goal of FEL design, while others adopt a more general approach to the coherent interaction. Only the latter will be covered in this summary due to their relevance to the work described in later chapters.

Another collective effect of relevance to the work outlined in this thesis is that of space charge, especially in the case of longitudinal space charge. This process can have significant impacts upon the longitudinal phase space (LPS) of an electron bunch, especially so in the case of short, low energy, or high charge electron bunches. Modelling of this process typically relies on either a wakefield methodology or a particle-in-cell (PIC) model.

While the process of centroid energy loss of a bunch due to CSR has been covered in the previous chapter, it is worthwhile to briefly summarise the mechanism by which CSR can induce a growth in both the slice and projected emittance of an electron bunch [95–98], as this is a common process used to identify and quantify the CSR interaction. The projected emittance of an electron bunch is akin to the entropy within the electron distribution. It has numerous definitions, but one of the most used is the r.m.s emittance

$$\epsilon_u = \sqrt{\langle u^2 \rangle \langle u'^2 \rangle - \langle u \cdot u' \rangle^2},$$

which roughly describes the area in the u-u' plane (also know as the u-u' phase space) occupied by the electron beam. Here u refers to a canonical coordinate of the electron bunch, typically the transverse coordinates x and y, and u' refers to the respective divergence along a given axis. The symbol $\langle\cdot\rangle$ refers to the arithmetic mean of a given function within the distribution. The r.m.s emittance can also be used to describe an energy-invariant form of the beam emittance, known as the normalised r.m.s emittance, whereby

$$\epsilon_n, u = \langle\gamma\beta\rangle\epsilon_u.$$

One can consider the electron bunch to be partitioned into longitudinal segments or "slices"; this is useful considering the majority of energy redistribution that occurs in high energy electron beamlines is typically correlated longitudinally. Furthermore, accelerating electric fields typically impart a correlation along the longitudinal energy-space distribution, also known as the longitudinal phase space. In the higher energy sections of an electron beamline, there is typically very little exchange of particles between slices due to the low velocity differences inherent at high energies. The slice emittance can be considered to be the r.m.s emittance of the electrons within a given slice.

In the case of the effects of CSR of the slice emittance, differences in the transverse phase space coordinates of particles in a given slice give rise to non-linear variation in momentum changes associated with the CSR wake within the slice, thus increasing the overall transverse slice emittance [99]; in the case of the projected emittance, a similar process drives an overall increase whereby the non-uniformity in individual slice centroids, including the longitudinal position in the

bunch, results once more in a non-linear correlated momentum variation across the bunch. An analytic model for the expected change in the bunch projected emittance due to CSR is found in work carried out by Yi Jiao *et al.* (excluded for brevity, Equation (2.12) in [100]). In this, the final beam emittance at the exit of an achromatic compression structure is considered to be a quadrature sum of the contribution arising from the transverse linear Courant-Snyder functions and the emittance at the achromat start, and the overall path and trajectory deviation accumulated from the energy spread gain due to CSR over the structure. This uses a matrix formalism of the CSR effect on the bunch by assuming the electron bunch distribution to be rigid as it traverses the bending magnet to then obtain these position and trajectory deviations. A simpler approximation for the emittance gain over a single bend is provided by Mitchell, Qiang and Emma in [101]:

$$\Delta\varepsilon_x \approx \varepsilon_{x,0}\left(1-\sqrt{1+\frac{\beta_x^{fin.}}{\varepsilon_{x,0}}\theta_D^2\sigma_\delta^2}\right), \tag{3.1}$$

where $\Delta\varepsilon_x$ and $\varepsilon_{x,0}$ are the change in and initial geometric beam emittances (in the bending plane), $\beta_x^{fin.}$ is the in-plane (horizontal) Courant-Snyder β-function at the bend exit, θ_D is the bend angle, and σ_δ is the r.m.s fractional energy-spread. This expression stems from a similar rationale as shown in [100], whereby a linear matrix formalism is adopted to calculated trajectory and position deviations from the ideal orbit arising from CSR-induced energy spread. The explicit dependence of the emittance growth on the transverse β function stems from cross terms in the quadratic sum used in the definition of the final beam emittance [100].

3.1.1 `elegant`

`elegant` [102] is a general-purpose accelerator code that uses transfer matrices and multipole kicks to enable tracking of macroparticles. This allows for fast simulation and optimisation of beamlines compared to time-domain codes. In terms of collective effects, `elegant` has methods for both longitudinal space charge (LSC) and CSR modelling among others [103]. The former of these is implemented only for drift spaces (LSCDRIFT) and accelerating structures (RFCW). It employs an ultra-relativistic approximation in the calculation of the LSC-impedance [104] from which the energy change is calculated. The electron distribution is sliced longitudinally to produce a histogram of the bunch current profile, from which a Fourier-transformed current profile $\tilde{I}(k)$ is developed. In the ultra-relativistic limit, assuming linear motion of the electron bunch (i.e. $\vec{\beta} = \beta\vec{e_z} \approx \vec{e_z}$), the LSC wake is given by

$$\left(\frac{dU(z)}{ds}\right)_{LSC} = qE_{LSC}(z) = \frac{q}{\sqrt{2\pi}}\int_{-\infty}^{\infty}\tilde{E}_{LSC}(k)e^{ikz}dk,$$

where $\tilde{E}_{LSC}(k) = \tilde{I}(k)Z_{LSC}(k)$, k is the wavenumber of a LSC perturbation, and z is the position within the electron bunch. The LSC impedance per unit length [103, 104]

$$Z_{LSC}(k) = \frac{iZ_0}{\pi k\left(\frac{1}{2}(\sigma_x+\sigma_y)\right)^2}\left(1 - K_1\left(\frac{k(\sigma_x+\sigma_y)}{2\gamma}\right)\right),$$

where $Z_0 = \sqrt{\mu_0/\epsilon_0}$ is the free-space impedance, $K_1()$ is a modified Bessel function, and σ_x and σ_y are the transverse r.m.s beam sizes. This expression is contingent on a uniform circular transverse beam cross-section, but can be approximated to a reasonable degree by the mean of the r.m.s transverse beam widths for a Gaussian cross section. It should be clear that this expression is thus

limited in its scope to electron bunches with appreciably symmetric transverse distributions. Nevertheless, the 1-dimensional model allows for fast calculation of the LSC wake in a drift in the limit of this assumption outlined. While other elements besides LSCDRIFT and RFCW in `elegant` do not allow for the calculation of LSC wakes, they can be applied providing the beam is within the ultra-relativistic limit (i.e. the variation in electron velocities are negligible). Because the simulations featured in this thesis will typically display a greater degree of detail in the transverse beam distribution, the applicability of the `elegant` model is limited save for fast optimisation solutions.

The CSR model used in `elegant` uses the analytical framework [105] laid out by Saldin *et al.* in [60] for modelling of steady-state CSR as well as the transition wake. The total wake is expressed as the sum of two components, the first of which corresponds to the steady state term outlined in Equation 2.54. The expression differs slightly insomuch as it recognises that only radiation emitted from electrons within a slippage length will be felt by the test location at any given time, and as such with the lower limit on the integral is alters from $-\infty$ to $s - s_L$, where $s_L = \rho\phi^3/24$ is the slippage length and ϕ is the average angular position of the bunch within the dipole. The entrance transient term is also based on the analysis of Saldin *et al.* [60], and can be likened to the boundary term shown in Equation 2.63 [105]. The entrance transient wake

$$\left(\frac{dU}{cdt}\right)_{Entrance} = -\frac{q^2}{2\pi\epsilon_0}\frac{\lambda(s-s_L)-\lambda(s-4s_L)}{(3\rho^2 s_L)^{1/3}},$$

where λ is the normalised bunch profile and s is the position within the electron bunch (relative to the bunch centroid). `elegant` is further adapted to allow for

propagation of CSR from a dipole exit along a subsequent drift length (and from there into a subsequent dipole). For this calculation there a two options; the first is based upon the exit wake from the Saldin model used within the dipole proper, but with a decay with respect to the distance from the dipole exit applied to the overall strength of the wake; the second is based upon an extension to the Saldin model formulated by Stupakov [106], which operates in the ultra-relativistic limit ($\gamma \to \infty$). In this limit, the CSR wake in a subsequent drift section is

$$\left(\frac{dU}{cdt}\right)_{Drift} = -\frac{q^2}{\pi\epsilon_0\rho}\left(\frac{\lambda(s-\Delta s_{max})}{\theta_D + 2\delta} + \int_{s-\Delta s_{max}}^{s} \frac{1}{\psi + 2\delta}\frac{\partial\lambda}{\partial s'}ds'\right), \tag{3.2}$$

where δ is the distance of the witness from the dipole exit face, and θ_D is the total bend angle of the magnet. ψ is related to the source-witness separation $\Delta s = s - s'$, and is determined by solution of

$$\Delta s = \frac{\rho\psi^3}{24}\frac{\psi + 4\delta}{\psi + \delta}.$$

Δs_{max} is also defined by this expression, albeit in the case where $\psi \to \theta_D$. The limitations of these models should be evident, namely that they are all 1-dimensional and in the case of 3.2, only operate in the ultra-relativistic limit. For lower-energy machines, such as CLARA Phase 1 which operates around 40 MeV, this may prove problematic when attempting to properly characterise the coherent emission process and its effects upon the electron bunch during beam transport. The CSR and space charge models employed by `elegant` are computationally lean compared to most others available, but extra effort is required to achieve convergence of the settings used for the model, such as the number of CSR kicks calculated, the number of bins used for the current profile, and various

smoothing and high/low-frequency filters.

Experimental Comparisons

Because of its ubiquitous use in the field of beamline design, numerous experimental comparisons to the `elegant` CSR model exist. Here, some of the key comparative results will be discussed, largely based around emittance growth and energy loss of the electron bunch centroid. The `elegant` CSR model is shown to be a good approximation to the CSR force experienced within dipole magnets, and corresponds to measurement well within the 1-dimensional limit of CSR theory as would be expected.

`elegant` was initially developed to aid in the design of a bunch compressor for the LEUTL beamline at the Advanced Photon Source (APS), and was also used in the design of the LCLS beamline around the same period. During the design of the LCLS, the code predicted the presence of a microbunching instability driven by CSR in the bunch compressors [58]. This instability was determined to be a result of modulations in the initial beam distribution supplied to `elegant` simulations (generated in the Parmela code). It was further determined that the initial seed modulations arose from the full bunch distribution as opposed to solely the current profile [107].

Experimental studies into CSR-driven effects, namely emittance growth and energy loss, were carried out by Braun *et al.* at the second Compact Linear Collider Test Facility (CTF II). These measurements were compared to CSR simulations from both `elegant` and TraFiC^4. Emittance measurements at the exit of the dipole were carried out for a range of optics settings which served to

alter the horizontal β-function. According to theory laid out by Derbenev and Shiltsev in [108], the emittance growth across the structure should increase with respect to increasing horizontal β-function at the bunch compressor centre, due to varying (both focusing and defocusing) transverse CSR forces induced along the length of the electron bunch. CSR simulations in `elegant` and TraFiC^4 did not reflect the qualitative picture of this theory, predicting very little change in the transverse emittance with respect to the bunch's horizontal extent. However, experimental observations defied both theory and simulation, demonstrating a sharp increase in the transverse emittance at smaller values of β_x. This discrepancy has typically been attributed to poor knowledge of the initial 6-dimensional phase space at the entry of the bunch compressor, of which variations from idealised conditions may be responsible for significant changes in the intensity of the coherent emission process [107].

Energy-loss measurements were carried out on a "shielding chicane", downstream from the main bunch compressor. This "shielding chicane" was a purpose built beamline element used to investigate the shielding effect upon CSR emission. It consisted of four short dipoles encased within a vacuum chamber, that could itself be removed to provide variable shielding characteristics, and had a variable R_{56}. The linear energy correlation of the bunch was set to provide a fixed and desired bunch compression at the exit of the first chicane, after which the R_{56} of the shielding chicane was scanned to vary the strength of the CSR interaction. In contrast to the simulated effects of CSR on the bunch emittance, `elegant` simulations of the energy loss over the CTF II bunch compressor with respect to the structure's variable show very good agreement with measurements. However, best agreement is found when using the Saldin model for CSR in a drift,

rather than the Stupakov extension to the model [107]. It could be argued that this indicated the strength of the shielding effect was relatively small, especially when contrasted to simulations including shielding carried out in TraFiC^4, which will be covered later.

Similar experiments into energy loss and emittance changes due to CSR were carried out by Bane *et al.* on the LCLS bunch compressor BC1 and compared to multiple CSR codes, including `elegant` [109]. Energy loss measurements carried out from BPM readings at the bunch compressor whilst scanning the operating phase of a preceding cavity (in order to vary the momentum chirp imparted upon the bunch and thus alter the overall compression), and are in generally good agreement to `elegant` simulations, although with a more marked discrepancy close to the phase of maximum compression is seen, with `elegant` overestimating the overall energy loss. This difference is likely due to the overestimation of the total bunch compression compared to measured bunch lengths, although there may be some error incurred due to the limitations of `elegant`'s 1-dimensional approach to CSR modelling, as the Derbenev parameter will take a larger value close to the maximal compression phase (assuming negligible change in the horizontal beam size). Changes in the horizontal emittance due to space charge are also well matched, though again exhibit the most discrepancy at maximal compression. The vertical emittance was not predicted to change in the `elegant` model, however measurements did report a change that was correlated with the overall compression, albeit less so than in the horizontal plane. It has been stated that a likely cause of this arises from space charge forces which were not precisely modelled by `elegant`.

3.1.2 TraFiC^4

TraFiC^4 is a dedicated CSR code that tracks electron bunches in the time-domain, with the aim of reproducing macroscopic effects induced by CSR [110]. The electron bunch is modelled as an ensemble of macroparticles, which themselves are "smeared" out into Gaussian sub-bunches. Field calculations are facilitated through storage of a history of macroparticle phase-space coordinates. Unlike some CSR-modelling reliant upon particle histories, TraFiC^4 uses a Cartesian coordinate system rather than coordinates localised to individual time steps. TraFiC^4 has a facility to include the CSR shielding effect due to conducting beam pipe walls.

At its core, the TraFiC^4 tracking algorithm is an iterative one. For a given beamline, which may consist of any number of standard magnetic accelerator elements, tracking is discretised into a set of equal time steps [111], t_i. The bunch is initially tracked for the entire beamline in the absence of CSR, with the particle phase-space coordinates stored at each t_i. Following this, the effect of CSR is treated as a series of kicks, originating and evaluated at midway points between time steps ($t_{i+1/2}$). The discretisation of the particle trajectories allows for easy and computationally efficient selection of the contributing retarded sources for a given witness position. The smearing of Gaussian sub-bunches allows for a relaxation of the retardation condition by providing a retarded time interval as opposed to a singular time as would be required from point-to-point evaluation of the retarded field. The overall CSR kick calculated at $t_{i+1/2}$ is split equally between t_i and t_{i+1}.

TraFiC^4 has two methods for incorporating the effect of CSR fields onto the

overall bunch evolution. In the first method, the "macroscopic" trajectory is recalculated [111] for every kick applied. Because the change in trajectories due to the kick may significantly alter the total bunch distribution, the process of recalculation of the CSR field can be iteratively computed for a given t_i. The number of iterations is specified by the user, and so it is important that this be optimised to provide convergence of the algorithm without excessive use of computational resources [110]. This process is carried out for every time step until the entire beamline has been tracked. The second method uses two initially identical electron bunches, whose trajectories evolve as a result of the fields of the other [112]. Once again, the number of iterations by which the trajectories are re-evaluated is provided by the user, requiring careful selection in order to result in convergence.

When carrying out a 2- or 3-dimensional field calculation, TraFiC^4 adopts a convolution method to speed up computation [113]. Instead of performing calculations for 3-dimensional source or witness density distributions, the charge density is modelled as the convolution between a line charge density and a transverse density distribution. Naturally, the assumption of a separable spatial bunch distribution results in limited applicability to lattice regions where large correlations occur between the spatial planes, for example in regions of dispersion in compression structures, or beamlines with large residual higher-order dispersion. Nevertheless, this approach effectively reduces the dimensionality of the integration down to 1-dimension.

1-dimensional approaches to modelling CSR always encounter the issue of a singularity for observer positions on-axis, and numerical methods for calculating

in this regime must take this into account. For example in the Saldin model [60] described in Section 2.2.1, the typical Coulomb repulsion term is subtracted from the total interaction in order to remove the singularity and only analyse the dissipative interaction. TraFiC^4 adopts a similar method, insomuch as the total force on a given sub-bunch is separated into a short range singular and a longer range non-singular contribution. Dohlus *et al.* assert that the asymptotic behaviour of the former of these is analytically known, allowing for swift integration over the source distribution [114]. The longer range interaction must be solved numerically, though due to the comparative length scale it may be treated as a 1-dimensional interaction, wherein the fields due to a 3-dimensional sub-bunch may be approximated as those of a 1-dimensional line charge. This approximation is only valid for sources within the Derbenev limit (Equation 2.65).

Experimental Comparisons

TraFiC^4 has been compared against experimental data gathered on the CTF II beamline, alongside `elegant` [115]. Similarly to `elegant`, little emittance growth across the bunch compressor chicane was predicted with respect to variation of the transverse beam size at the chicane centre, in contrast to the clear inverse dependence upon β_x of the measured emittance change . Energy loss measurements were in comparably better agreement with simulations, although where `elegant`'s modelling of CSR in free space mirrored the experimental measurement almost completely, TraFiC^4 typically over-estimated the energy loss in the presence of no-shielding, and under-estimated the energy loss when shielding was included in the simulation.

Later experiments carried out at CTF II [112], made measurements of transverse emittance growth at the bunch compressor exit as a function of the LPS chirp (controlled via the operating phase offset of the preceding accelerating structure). These measurements showed a marked improvement in the agreement with TraFiC^4 simulations than the aforementioned experiment, however this agreement was largely qualitative as opposed to quantitative in the case of the horizontal emittance. The vertical emittance growth showed some degree of quantitative agreement with simulations, although due to its overall lack of correlation with respect to variable linac phase offset and qualitative comparison should be treated sceptically.

Observations of longitudinal de-bunching observed at the TESLA Test Facility were analysed using TraFiC^4 simulations by Limberg, Piot, and Schneidmiller [116]. Under maximal compression, the energy spectra of electron bunches fractionated into two distinct peaks. TraFiC^4 qualitatively echoed this effect, including capturing the asymmetry of the two peaks after passing through the spectrometer dipole downstream from the bunch compressor, effectively confirming the coherent interaction being as the main driver of these unusual longitudinal dynamics at very short bunch lengths. This goes some way towards further validating the TraFic^4 CSR algorithm.

3.1.3 CSRTrack

Developed by authors of TraFiC^4, Dohlus and Limberg, CSRTrack aims to build upon the framework set out in TraFiC^4. It incorporates two distinct modelling methods for CSR, a 1-dimensional approach similar to that employed in `elegant`, and a 3-dimensional sub-bunch method [114]. The 1-dimensional methodology

uses a fast Fourier transform (FFT) method to quickly evaluate the longitudinal field evolution within a certain time interval. A mesh is used to facilitate interpolation of the longitudinal field to future particle positions.

The three-dimensional approach bears many similarities to that used in TraFiC^4, in that it employs finite time-independent sub-bunches (c.f. "smeared-out" macroparticles) as opposed to point particles to model a time-dependent macroscopic bunch distribution. Each sub-bunch source is associated with a witness bunch, which tests the generated field and determines the overall trajectory of the source bunch. Further witness bunches can be used to test transverse field effects [114].

Sub-bunch tracking can make use of several distinct methods for electromagnetic field evaluation [117]. One of these is equivalent to the convolution method employed in TraFiC^4, wherein each source bunch is modelled as the convolution of a 1-dimensional line-charge distribution with a 2-dimensional transverse density distribution. Alternatively, a "pseudo-Green's function" method is available [114], which uses a single "reference" sub-bunch to approximate the retarded fields of the whole bunch. The reference bunch travels along its trajectory, with the fields calculated and interpolated over a 2-dimensional mesh at each time step for a pseudo-Green's function. The individual fields of the source bunches are then calculated via a shift-rotation-transformation (see [114]) of the Green's function. There is also an explicit meshed method which uses an interpolation over a mesh of the fields for all source sub-bunches as opposed to a single reference bunch, along with a combined method which uses both the pseudo-Green's function method in combination with the meshed method. Tracking is carried

out in a similar iterative method to that prescribed by TraFiC^4 to ensure self-consistency of sub-bunch trajectories.

Each of the methods stated has a different applicability dependent upon the requirements of the user. The fastest method is naturally the 1-dimensional FFT method, which is in turn the least accurate, neglecting any transverse dependence or transverse forces. In the case of the 3-dimensional methods, the computational effort depends entirely upon the requested number of source and witness bunches. If vertical (out of the bending plane) forces are expected be significant, the only method which is applicable is the convolution method. Typically this method has the largest computational overhead, particularly in the case of large numbers of source and witness sub-bunches. As such, the pseudo-Green's function and mesh methods are faster at large particle numbers and have similar regions of applicability in terms of the forces calculated, though the overall speed of the calculation depends entirely upon the particular simulation scenario [118].

Experimental Comparisons

CSRTrack was also used (alongside `elegant`) in comparison to data in the experiments of Bane *et al.* on the LCLS [109]. However, the number of simulation points carried out in CSRTrack compared to other codes is low, with only 2-3 simulations carried out for a particular measurement compared to 10-20 measurement points and $\sim$10 simulation points in `elegant`. The 2-dimensional (neglecting vertical forces) combined Green's function and mesh method was used and agrees well with measurements for the linac phases simulated, with a clear improvement for the predicted energy loss at maximal compression when compared to `elegant`

simulations. In terms of predicted emittance growth CSRTrack performed comparably to `elegant` simulations.

Prior to its removal for the installation of a longitudinal emittance exchange beamline, a study into the effects of CSR in the bunch compressor of the A0 photoinjector was used conducted by Fliller *et al.* [119]. The data gathered is compared against CSRTrack simulations of the full bunch compressor, with initial macroparticle distributions generated in the tracking code ASTRA [120]. Three regimes were investigated, namely a 16 MeV compressed beam, and 12.3 MeV compressed and uncompressed beams. Only the 16 MeV simulations showed a distinct variation between the cases with and without CSR, and simulations including CSR matched well to the observed beam energy spectrum in a downstream spectrometer. Of the lower-energy regimes, only the energy spectrum of the compressed case was convincingly recreated in CSRTrack simulations, albeit with no insight with regards to the role of CSR in the beam dynamics due to no visible distinction between the two simulations. The simulated uncompressed 12.3 MeV did not recreate the longitudinal phase space observed on the beamline.

3.1.4 SPECTRA

SPECTRA is a dedicated synchrotron radiation code developed by Tanaka and Kitamura [121], built with the view to quickly calculate radiation distributions and spectra for a variety of light sources. The program is predominantly geared towards incoherent SR distributions, however also has functionality for CSR calculations. Bending magnet fields can be modelled from both parametric built-in elements or generalised magnetic field maps. The radiation distribution may be calculated at any location, and both the radiation emitted from within both the

steady-state and transient edge regions can be simulated. Radiation sources can be modelled in 3 ways: an assumed Gaussian profile, where the beam dynamics are determined by values of the linear lattice functions at the start of the light source used in the SPECTRA simulation; generalised un-coupled distributions (except for $x - x'$ and $y - y'$)in the 6-dimensional phase space interpolated from file data; and full 6-dimensional macroparticle distributions. Various quantities can be extracted from simulations, such a total photon fluxes, angular and spatial distributions, spectra, and time-dependence of the photon flux. Furthermore, filters can be applied to the measurement, such as frequency filters to reduce the resultant spectrum to only that which will be resolved by a given measurement system.

Radiation calculation occurs from evaluation of the Liènard-Wiechert fields, but only radiative effects are considered; no effects regarding intra-bunch energy-redistribution are considered, meaning that SPECTRA is not ideal for light sources where the CSR-induced energy spread is large enough over the relevant trajectory that it significantly alters the individual trajectories and the overall coherent emission. Calculation of Fourier transforms are carried out using a recursive integration-by-parts method. For a function $g(t)$ that can be well approximated by an n^{th}-order polynomial, the Fourier transform [121]

$$\tilde{g}(\omega) = \left(-\frac{1}{i\omega}\right)^n \int \frac{d^n g}{dt^n} e^{i\omega t} dt - \sum_{k=1}^{n} \left(-\frac{1}{i\omega}\right)^k \left(\frac{d^{k-1} g}{dt^{k-1}} e^{i\omega t}\right).$$

The SPECTRA solver splits the Fourier integration into sections where the integrand is well-approximated by a cubic interpolation and applies this method, which enables very fast calculation of the Fourier transformed Liènard-Wiechert

fields. For calculation of the CSR spectrum, this is simply convolved with the Fourier-transformed bunch profile.

Few direct comparisons between SPECTRA and data exist, although SPECTRA simulations are used successfully to inform many experiments in fields such as X-ray diffraction [122, 123]. Further to this, comparisons have been presented between SPECTRA and the comparable radiation codes URGENT [124] and SRW [125] in [126], where the brightness of different undulator designs is compared using the codes. Overall brightness calculations do not compare well between URGENT and SPECTRA for the case of a linearly polarised wiggler, with SPECTRA predicting a far larger brightness than URGENT. However SPECTRA and URGENT do agree well for the case of a short-period undulator in terms of brightness, and SRW and SPECTRA predict comparable spectral photon fluxes.

SPECTRA has been used to model the expected radiation spectrum from the I18 spectroscopy beamline at Diamond Light Source [127]. Here, undulator radiation is transported to a sample over approximately 20 m of optical beamline. Measurements of the spectrum show great agreement in terms of the form of the spectrum, though the absolute intensities measured are typically lower than the theoretical intensities produced by the code. No direct comparison is available for SPECTRA modelling of bending magnet CSR.

3.1.5 General Particle Tracer

GPT is a multi-purpose time-domain accelerator code developed by S. B. van der Geer and M. J. de Loos of Pulsar Physics. In GPT electron bunches are

modelled as macroparticle distributions, with tracking carried out using a 5^{th}-order Runge-Kutta integrator with an adaptive time step [128]. One of the aims of the code is to ensure that all electromagnetic fields incorporated into the code are Maxwell-compliant, although this condition can be circumvented through user-supplied field maps and neglecting of magnetic fringe fields [129]. This is necessary given the implementation of complex electromagnetic fields within the code, be they space charge fields, wake fields, or magnetic and electric beamline elements, and ensures the electromagnetic fields encountered by particles within the code are smoothly varying-functions in space. This prevents computationally costly recursive shortening of the Runge-Kutta time step at discontinuous points in the field or field derivatives.

Space Charge Model

GPT has several space charge models available to the user. Two 2-dimensional models are available, one (spacecharge2Dcircle) which models each macroparticle as a uniformly charged disc, the other (spacecharge2Dline) which estimated space charge by considering the bunch to consist of infinitely long line charges. The applicability of these models is limited, the former notably being only suitable for cylindrically symmetric bunch geometries and the latter being useful for very long bunched beams or continuous beams. That being said, in situations where these conditions are met these models provide a fast method for approximation of space charge effects.

Four 3-dimensional space charge models are available, 3 of which are suitable for relativistic particle dynamics. The exception to this is spacecharge3Dclassic,

which models space charge as point-to-point classical Coulomb interactions between macroparticles. Another point-to-point algorithm exists, spacecharge3D, which is suitable for relativistic dynamics. Both of these models scale as $\mathcal{O}(N^2)$ and so are not ideal for simulations involving large numbers of macroparticles. The spacecharge3Dtree element is a model based around point-to-point interactions, where particles close to a witness particle are modelled in a conventional manner and distant particles are clumped together into a larger uniform charge. This model requires all macroparticles to have finite volume to avoid discontinuities. A Barnes-Hut algorithm is used to group particles in this model, resulting in a computational effort that scales as $\mathcal{O}(N \log N)$ [130]. The final algorithm available is a PIC model developed in collaboration with G. Pöplau, O. J. Luiten, and U. van Rienen [131, 132].

At each time step the spacecharge3Dmesh algorithm transforms the bunch into the rest frame of the bunch [133]. Because of this, the spacecharge3Dmesh model is not appropriate for use in particle beams with large relative energy spreads. A Cartesian mesh is then generated across the bunch. The mesh lines are non-equidistant, being based upon the local charge density within the bunch, which helps to reduce the effects of grid-heating of the electron bunch by ensuring sufficient resolution of the bunch distribution [134]. The charge is estimated at the mesh intersections and the potential is calculated through a discretisation of Poisson's equation according to a finite difference method. The space charge field is then derived from this potential. One advantage of this model is the fast Poisson solver, which is able to efficiently solve for the electrostatic potential in the presence of many degrees of freedom [133]. A further advantage is that re-initialisation of the 3-dimensional mesh results in fewer empty cells unnecessarily

using CPU time.

CSR Model

GPT's new CSR model comes in the wake of a user-created model implemented in the code by Bazarov [135], which itself is based upon a re-formulation of Saldin's method [60] carried out by David Sagan [136]. This model is still purely 1-dimensional, though overcomes the ultra-relativistic limit imposed by many 1-dimensional CSR codes, and it has been used in numerous beamline design studies [137, 138]. The newly created model aims to overcome a further limitation by incorporating the effect of the transverse bunch size as well as removing the assumption of particle trajectories. As part of the wider general purpose code it permits the simulation of CSR in concert with other collective effects such as space charge, wakefields, intra-beam and scattering as well as modelling of a wide range of accelerator elements including FEL radiators. In the context of FEL design, this is useful considering all of these effects can play a role in the typical parameter range of modern X-ray FELs, and would allow for start-to-end beam dynamics simulations to be conducted along the whole beamline within a single accelerator code. Additionally, multipole magnetic fringes have been implemented in the code allowing for better evaluation of coherent forces in this region.

GPT's CSR model takes a sub-bunch approach to calculating CSR in order to reduce the numerical effort of the calculation. At each step a local coordinate system is defined, with the longitudinal propagation axis defined along the direction of the average beam momentum, and the other two axes generated according to a right-handed coordinate system [1]. The beam is then binned into

sub-bunches along the longitudinal axis, with each sub-bunch's longitudinal extent being non-constant. The sub-bunch lengths are instead defined in terms of equal charge. For each sub-bunch, the mean momentum, position, and acceleration vectors are calculated with respect to the local coordinate system, along with the r.m.s transverse dimension of each sub-bunch. This information is then stored in a history manager, allowing the retarded fields due to each sub-bunch to be calculated at a later time step.

The CSR model allows for both the radiation term and Coulomb terms to be included or excluded as desired. As the fields are calculated directly from the Liènard-Wiechert fields there is not loss of generality in terms of the field evaluation, and both longitudinal and transverse fields components are included. When calculating the field, the electron bunch is once again sliced longitudinally according to charge quantiles [1] in a similar method to the binning of the bunch for storage in the history manager. For each witness slice, the field is evaluated at the slice centre. In discretised time the retardation condition can never be exactly fulfilled. Instead for each stored time step in the history manager, the two neighbouring slices for which the radiation of the first has already overtaken the witness and of the second has not yet arrived are found. The field contribution of these two neighbouring slices is calculated according to a weighted average, with the weighting based upon the distance from the source centres to the true retarded location. Each source slice is considered to radiate from four or sixteen source points (this is a user controlled option), located at an r.m.s distance from the slice centre (Figure 3.1).

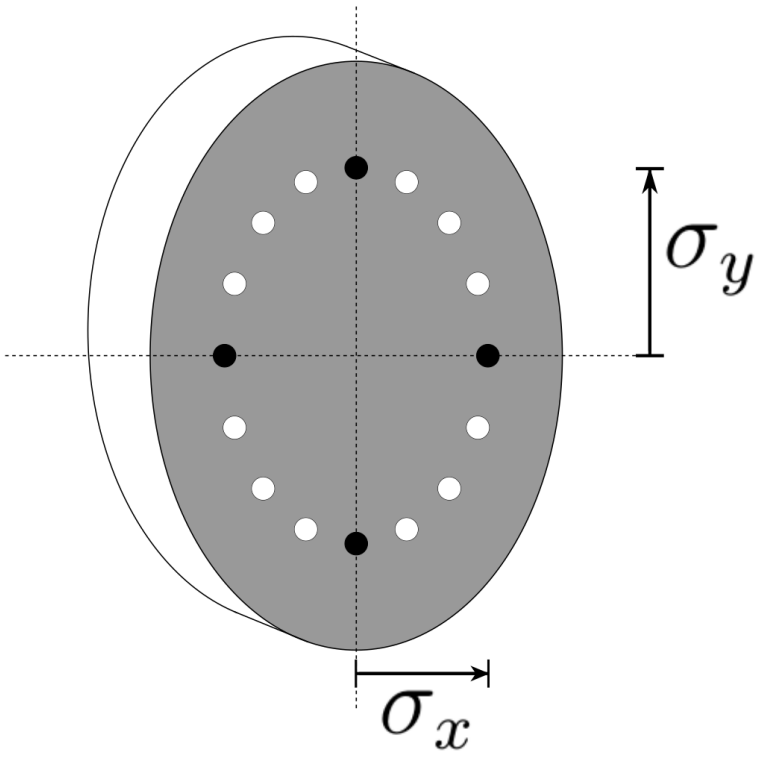

Figure 3.1: Arrangement of source points on each sub-bunch in GPT's CSR model. All points are used in the case where 16 are selected, but only the black points are used when 4 source points are used.

Simply summing contributions to the electric field directly can lead to a significant build-up of numerical noise in the simulation step due to the discretised nature of the sources. To account for this an interpolation of the electric field contributions at the witness with respect to the retarded time of the sources is generated. Numerical interference between subsequent contributing timestamps can lead to high frequency oscillatory changes to the field evaluated, and so a low-order interpolation is required [1]. This interpolation is then integrated with respect to the retarded time to reconstruct the field at the witness centre at the current simulation time.

A predominant limitation of this CSR model lies in the averaging of particle

phase-space coordinates in a given slice. Although an advantage of the GPT code is that the transverse extent of sources is taken into account, the compromise is that the transverse information of a given slice is reduced to its r.m.s size, and the effects of transverse substructure in the slice are neglected. Furthermore, in the case of an over-compressed "rolled-over" longitudinal phase space, particles at the same longitudinal position typically have considerably different momenta, with the overall momentum distribution being bimodal due to the two branches of the total phase-space occupying the same sub-bunch (Figure 3.2). In dispersive regions this bimodal momentum distribution will result in bimodal position and acceleration distributions within the slice, and simple calculation of the mean and r.m.s transverse sizes will lose this important information.

No noise filter is implemented in the integration procedure for the field of a given witness slice in the GPT CSR routine. As fewer macroparticles results in a more discretised electron distribution, high frequency components can enter into the temporal field evolution. This high frequency oscillation can lead to inaccuracies in the numerical integration of the field evolution, and thus affect the accuracy of the resultant CSR kick upon a given slice. As such convergence of the algorithm requires a large number of macroparticles, which has previously been established to be around 10^6 [1]. Further to this, sharp discontinuities in external electromagnetic fields result in recursive reduction of the time step, which slows down the calculation time of the simulation step. This is especially problematic in the case of long beamlines wherein either the Coulomb term of the Liènard-Wiechert fields are included (and as such the CSR algorithm operates continuously), or when a very low "MinCurvature" parameter is used when only the radiation term is considered. As such, inclusion of the effects of CSR in long

straight sections downstream from a bending magnet prove very computationally intensive.

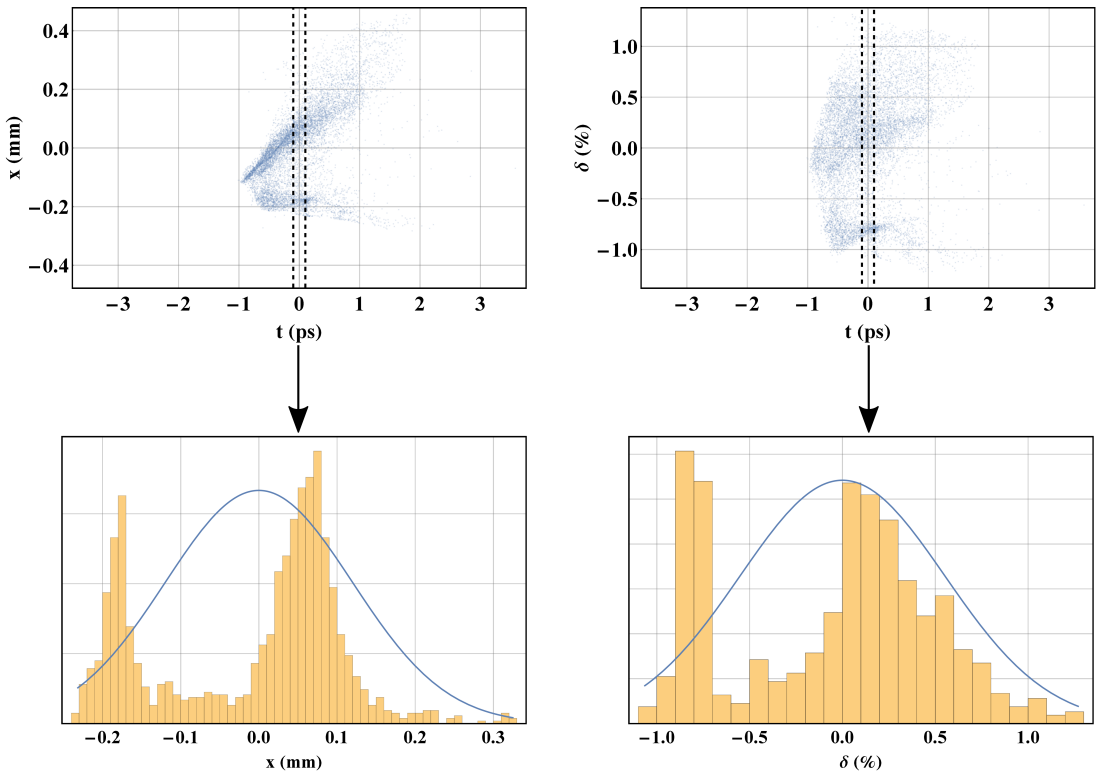

Figure 3.2: An example of a rolled over bunch which may prove problematic for GPT simulations. A slice is indicated by the dashed lines on the top row of plots, which display both x-t spatial distribution and the LPS. A histogram of the ordinate distribution within the displayed slice is shown below, with a Gaussian of the equivalent r.m.s size. As GPT does not consider the transverse distribution within a given slice outside of using radiating point offset by the r.m.s width from the centre, significant deviations from the realistic CSR interaction are likely to occur.

Experimental Comparisons

Given that GPT's CSR model has only been recently implemented there has only been one experimental comparison to the code produced so far. The work of Brynes *et al.* [88] on the FERMI FEL at ELETTRA in Trieste aimed to compare

the model in regimes operating outside of the conventional 1-dimensional analytical framework (i.e. for large values of the criterion in Equation 2.65). Emittance measurements were carried out via a quadrupole scanning technique over scans of three different parameters: the linac operating phase (and thus the LPS chirp), the dipole bending angle, and the strength of the final quadrupole preceding the bunch compressor. Each parameter was scanned independently, while the other two were maintained at their nominal values. The measurements were then compared to GPT, `elegant`, and CSRTrack simulations. The r.m.s bunch length for each of the parameter scans is approximated by the bunch length shown in `elegant` simulations.

There is good agreement between the data and both the 3-dimensional CSRTrack and GPT's CSR model, though GPT overestimates the emittance gain close to maximum compression. The measurement shows a decrease in the beam emittance gain close to maximum compression that goes against analytical and simulation predictions. Because OTR screens were used for measurement of the beam profile in the quadrupole scan, it is believed that the OTR signal is polluted by COTR generated in the presence of a highly compressed and microbunched beam, which has been observed previously [139]. A similar feature is observed for the linac phase scans, once again attributed to the generation of COTR. In this case the reduction is more significant, and neither of the 3-dimensional simulations compare well close to maximum compression. In both of these scans, the 3-dimensional CSR models outperformed the 1-dimensional analytical mode and the `elegant` model, especially close to maximum compression. This is expected as the value of the Derbenev parameter becomes very large in the third dipole of the bunch compressor at large compression ratios, thus making a 1-dimensional

model unsuitable. The quadrupole parameter scan was conducted to explicitly measure transverse dependence of the coherent emission, however simulation results did not show any quantitative agreement. The lattice mismatch brought about from the quadrupole scan resulted in a very diffuse transverse profile, and this is believed to be the cause of the quantitative discrepancy.

Also presented in [88] is a comparison between GPT simulations of the emittance growth over the FERMI bunch compressor with and without the inclusion of the Coulomb term of the Lièнard-Wiechert in the coherent field calculation. All three of the parameter scans are used in this comparison. Significantly larger increases are calculated by GPT simulations in the situation where the Coulomb term is included, especially when electron bunches are close to maximal compression, demonstrating its importance in the design of bunch compressor structures. The simulations featured in this thesis will all make use of the Coulomb term available in GPT, given its ability to highlight interesting effects downstream from radiating sections that are hereto not captured in conventional CSR simulations.

3.2 Implementation of CLARA Lattice

The first stage of the CLARA project installation, CLARA Phase 1, has been designed in order to commission and test the capabilities of the CLARA injector by using the pre-existing VELA beamline, along with having dedicated experimental periods for novel accelerator technology development. Electron beams are generated in a photoinjector (PI), consisting of a flat photocathode, a 10 Hz, 2.5-cell S-Band RF electron gun (previously used on as the VELA photoinjector),

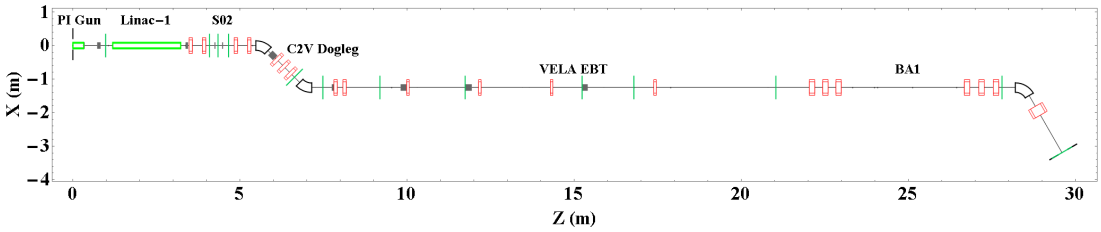

Figure 3.3: Schematic Diagram of the CLARA Phase 1 Lattice with key beamline sections labelled. Dipoles are shown in white, quadrupole magnets in red, orbit-correction magnets in grey, accelerating structures in light green, and YAG screen locations are displayed as green markers.

and a solenoid and bucking coil arrangement to control emittance compensation in the low-energy section. This emittance compensation exploits the low-energy space charge-dominated behaviour of the electron beam in the CLARA injector, whereby the electron beam behaves comparably to a plasma. When under the effects of both the ponderomotive RF focusing due to the electron gun and the focusing of the solenoid field the electron beam undergoes a plasma oscillation which is observed in the beam emittance. The principle of the emittance compensation employed lies in the variation of this focusing effect and the corresponding manipulation of the electron beam envelope. By tuning the focusing such that the electron beam undergoes a full plasma oscillation, the emittance growth from the first half of the oscillation is cancelled by the second half of the oscillation. The electron beam is then accelerated to relativistic energies, whereupon the plasma oscillation driven by space charge forces is damped by relativistic effects [140]. The function of the bucking coil is to modify the solenoid field close to the photocathode surface.

The PI laser (PIL) has a Gaussian design profile both transversely and longitudinally, though currently there are significant deviations between the intended and the actual transverse laser pulse profile (Figure 3.5). The hotspots seen in the

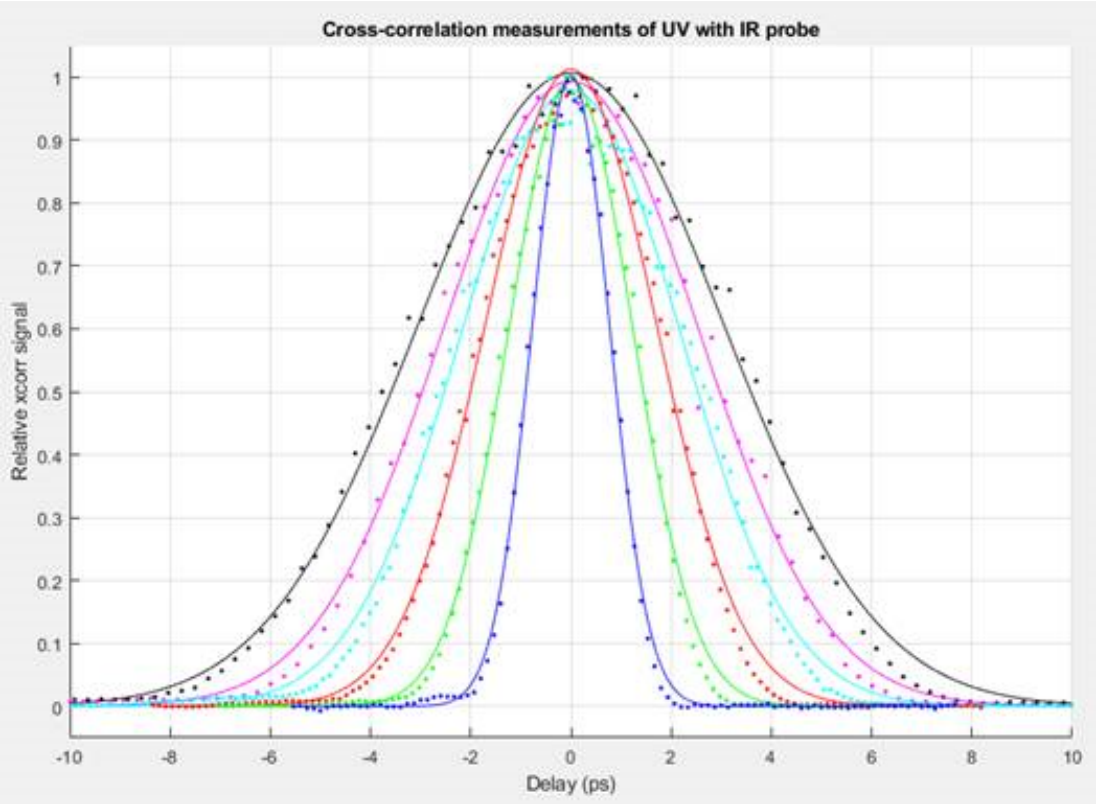

Figure 3.4: Measured laser pulse temporal profile for several pulse stretcher configurations. The profile clearly conforms to the "design" Gaussian distribution. Measurement carried out by and image courtesy of David Walsh (STFC Daresbury Laboratory) [141].

laser profile are expected to have both a significant impact upon the emittance growth of the electron bunch within the CLARA injector, as well as implications for the 3-dimensional form factor of the electron bunch when conducting CSR calculations. The transverse laser profile is monitored using a virtual cathode image, allowing steering of the laser spot on the cathode surface using mirrors along the laser transport line. The longitudinal profile is well-approximated as a Gaussian and has an adjustable pulse length via pulse-stretching optics [142] (Figure 3.4). The typical range of the pulse length is between 2-8 ps (FWHM).

Simulations of the CLARA Phase 1 lattice were carried out entirely in GPT.

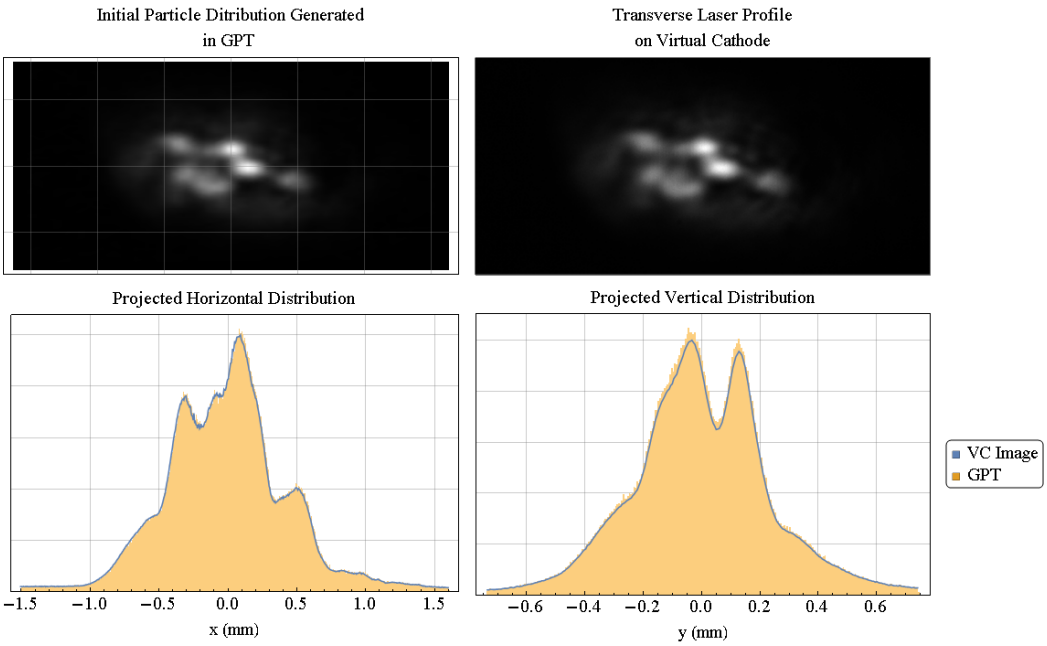

Figure 3.5: Comparison between VC image and initial transverse bunch distribution generated in GPT (10^6 macroparticles). The histograms and density plot shown use a bin size or bandwidth equivalent to the VC image pixel dimensions. The distributions match very well, with only the smallest scale density fluctuations being lost. A larger number of macroparticles would be expected to resolve this.

This decision was made because of the complexity of the initial transverse laser profile, as GPT has the ability to generate a bunch from a bitmap image. As such, an image taken from the virtual cathode was used in all GPT injector simulations. The generated particle distribution effectively captures all of the structure observed within the transverse laser profile (Figure 3.5). The operating longitudinal profile was set at 2 ps (FWHM) for the CLARA exploitation and commissioning period, and this was echoed in the initial GPT particle distribution. For the initial momentum distribution, particles were assumed to be emitted from the cathode surface with a well-defined energy equivalent to the laser photon energy less the photocathode work-function, which is taken to be 0.62 eV. The mono-energetic distribution is assumed to be emitted isotropically

away from the photocathode surface, resulting in a hemispherical shell being formed in the distribution's phase-space(Figure 3.6).

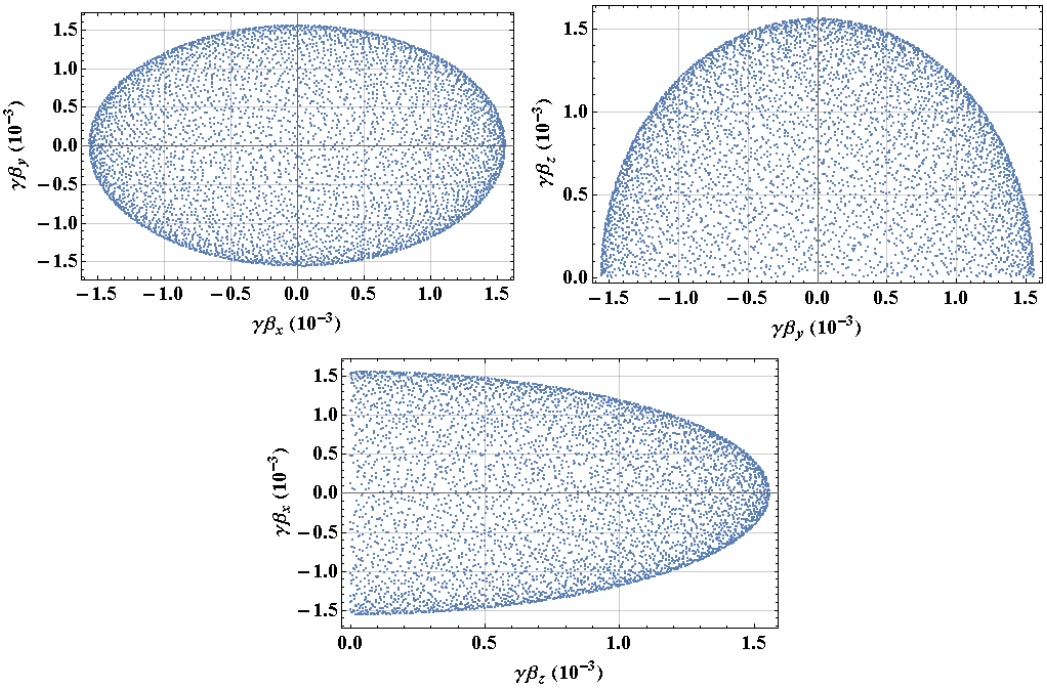

Figure 3.6: Initial momentum distribution of electrons emitted from the CLARA cathode in GPT in the absence of accelerating RF-fields and space charge. These plots are projections of the full 3-dimensional hemispherical shell in momentum space projected onto the (clockwise from top left) $\gamma\beta_x - \gamma\beta_y$, $\gamma\beta_y - \gamma\beta_z$, and $\gamma\beta_x - \gamma\beta_z$ planes. The lack of negative momenta in the $\gamma\beta_z$ direction is due to electrons only being emitted away from the planar cathode surface.

The fields of the current 10 Hz S-band electron gun are modelled using a 2-dimensional field map generated in Poisson Superfish courtesy of Bas van der Geer. This field map contains the spatial dependence of the longitudinal and radial fields, as well as the azimuthal magnetic field (Figure 3.7). This is used in conjunction with a 2.5-dimensional TM element ("map25D_TM") in GPT. The peak field of the electron gun is set to 71.5 MeV m^{-1} in all simulations, yielding a typical crest energy gain of ∼5 MeV. A 2-dimensional field of the combined

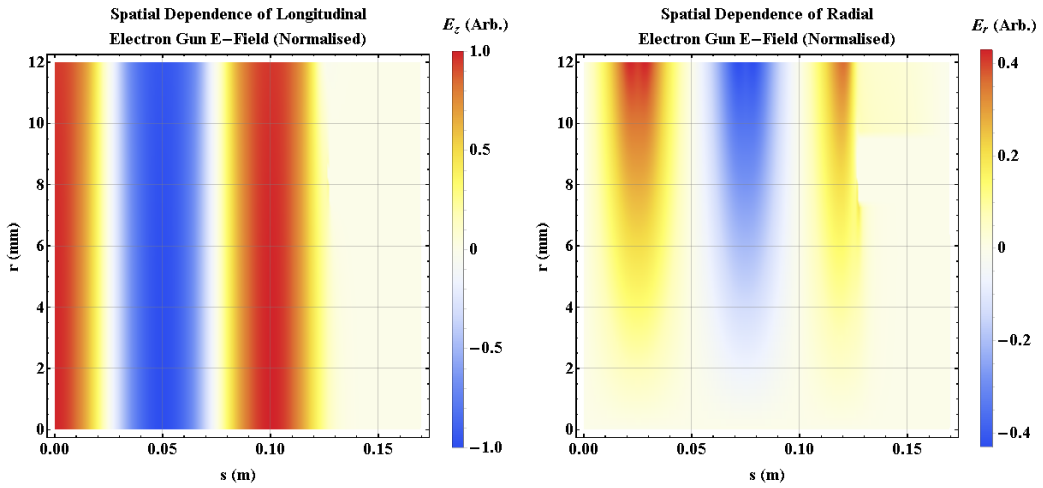

Figure 3.7: Radial and longitudinal electric field of the CLARA Phase 1 electron gun at $t = 0$ s, obtained from Poisson Superfish simulations. Both fields are normalised to the maximal value of the longitudinal field at the electron gun's centre.

solenoid and bucking coil arrangement is used with the map2D_B element in GPT (Figure 3.8). This field-map corresponds to the configuration of the coil current which reduce the longitudinal magnetic field to zero at the photocathode surface. Both of these field maps were created to model an electron gun designed by Strathclyde University, but because of similarities in the gun design this was deemed an acceptable model for the CLARA 10 Hz electron gun.

GPT's spacecharge3dmesh space charge routine is used in the injector, with image charges incorporated for when the beam is close to the photocathode surface. This model is chosen over point-to-point interactions for two reasons. The first of these is for computational efficiency, as CSR simulations will require 10^6 particles, and the second is in order to avoid overestimation of granularity effects due to the non-Gaussian initial transverse distribution used [128]. Because of the small relative size of the beam to the beam pipe diameter along with the

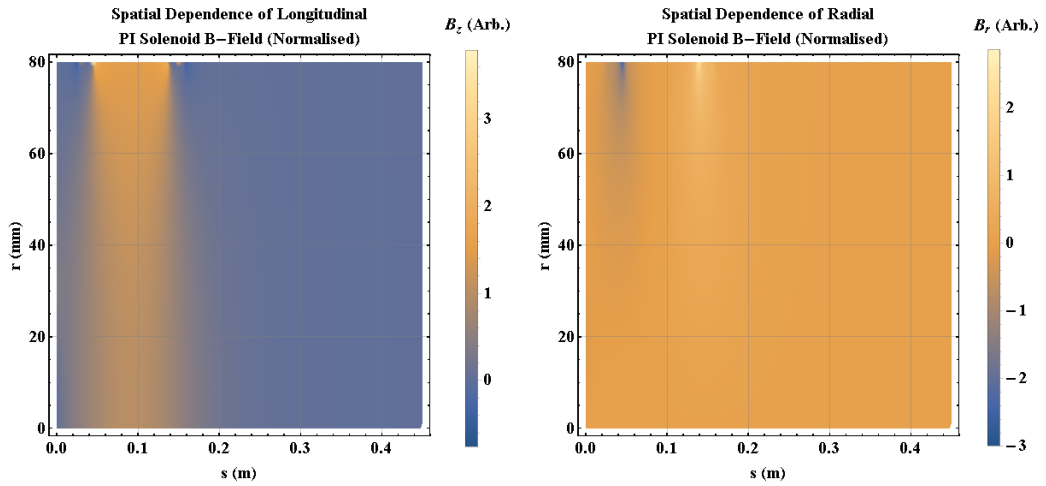

Figure 3.8: Radial and longitudinal magnetic field of the CLARA Phase 1 PI solenoid, obtained from Poisson Superfish Simulations. Both fields are normalised to the maximal value of the longitudinal field at the solenoid's centre. The solenoid field is scaled to a typical operating value of ∼0.25 T, although this is varied depending on the injector configuration in order to maximal compensate for the emittance growth in the injector.

reasonable approximation of perfectly conducting beam pipe walls, open boundary conditions would be appropriate for modelling the space charge forces of the bunch. However, convergence issues with the Poisson solver have been encountered when using these boundary conditions, and a boundary condition is used whereby the potential at the edge of the space charge grid is equivalent to that in the case of a uniformly charged brick of the same r.m.s dimensions as the electron bunch. While the mesh-based algorithm experiences issues when used to model electron beams of high energy spread, the generated electron pulse at the cathode is very short (on the order of ps, $\sim 0.1\%$ of the typical RF-period) and this problem is not assumed to apply in the context of the CLARA photoinjector.

The main accelerating cavity of the Phase 1 beamline, linac-1, is a 2 m-long, S-band, normal conducting, travelling wave structure. The structure is designed

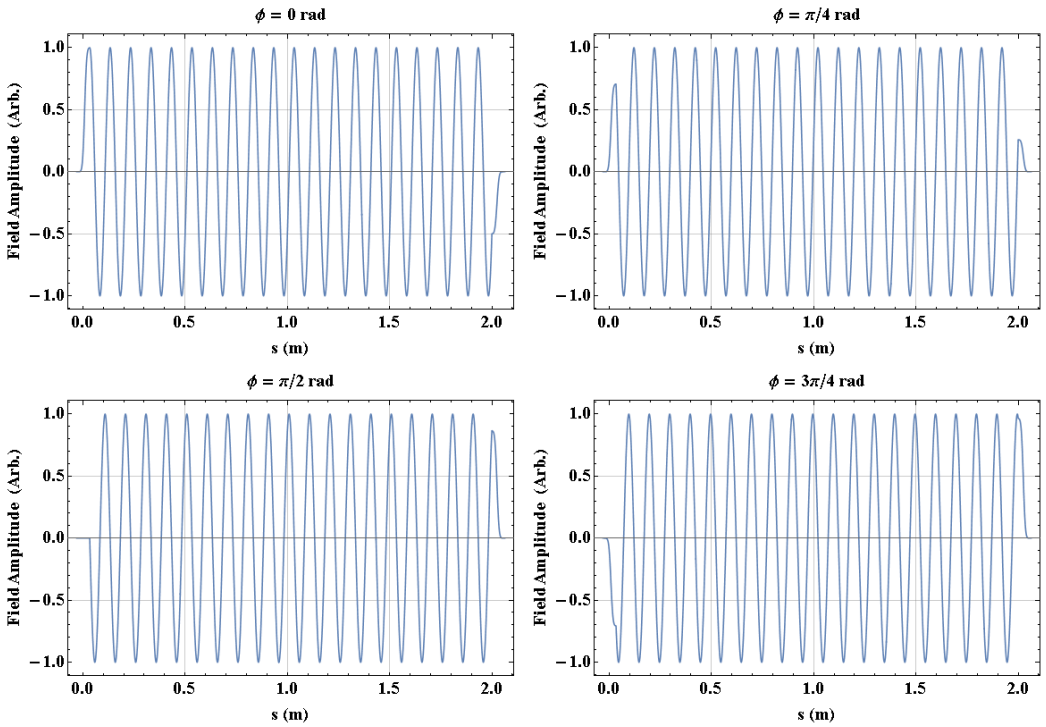

Figure 3.9: Linac-1 field model over a half oscillation period with normalised field amplitude. Note the discontinuity of the field gradient at the end cell boundary.

for constant power dissipation along it's length, in order to minimise structural deformation as a result of heating effects during 400 Hz operation [50], and consists of 60 regular cells of equal length along with 2 end cells. The RF-field's phase advances by $\frac{2\pi}{3}$ per cell. In order to properly model the travelling wave RF-field, two superimposed standing wave field-maps are used with the map1D_TM element, π out of phase of one another. Figure 3.9 shows the accelerating electric field in this model at four points in the RF cycle. The map1D_TM element assumes that the longitudinal field is dependent solely upon the longitudinal position and time, and extrapolates radial electric and azimuthal magnetic fields according to [128]

$$E_r(r,z,t) = -\frac{r}{2}\frac{dE_z(z,0)}{dz}\cos(\omega t + \phi),$$
$$B_\phi(r,z,t) = \frac{r\omega}{2c^2}E_z(z,0)\sin(\omega t + \phi),$$

where $E_z(z,0)$ is the longitudinal electric field interpolated from the supplied field map at $t = 0$, ω is the field's angular frequency and ϕ is the user-defined phase offset. The end cells are modelled as standing waves in order to ensure zero field at the structures entrance and exit. The cell boundary is matched such that there is no discontinuity in the longitudinal field's value, although the first derivative of the field is discontinuous at times other than $t = \frac{2n\pi}{\omega}$ for $n \in \mathbb{Z}$. This is believed to have a small impact upon the longitudinal phase space, namely in the form of additional curvature, though this will be minimal in comparison to the more linear contribution arising from the 60 regular accelerating cells.

Quadrupole and dipole magnets are implemented using the built-in "quadrupole" and "sectormagnet" elements in GPT. The magnetic fringe fields in these elements are modelled by Enge functions [128, 143]. The characteristic length of the fringe is controlled by the b_1 parameter, which is selected to have a value of 250 m^{-1} (Figure 3.10). This value was chosen to keep consistency with the fringe fields implemented in ASTRA simulations conducted by other members of the CLARA development team. The combined horizontal-vertical (H-V) correctors of the CLARA Phase 1 lattice are implemented using two superimposed "rectmagnet" elements at 90° to one another.

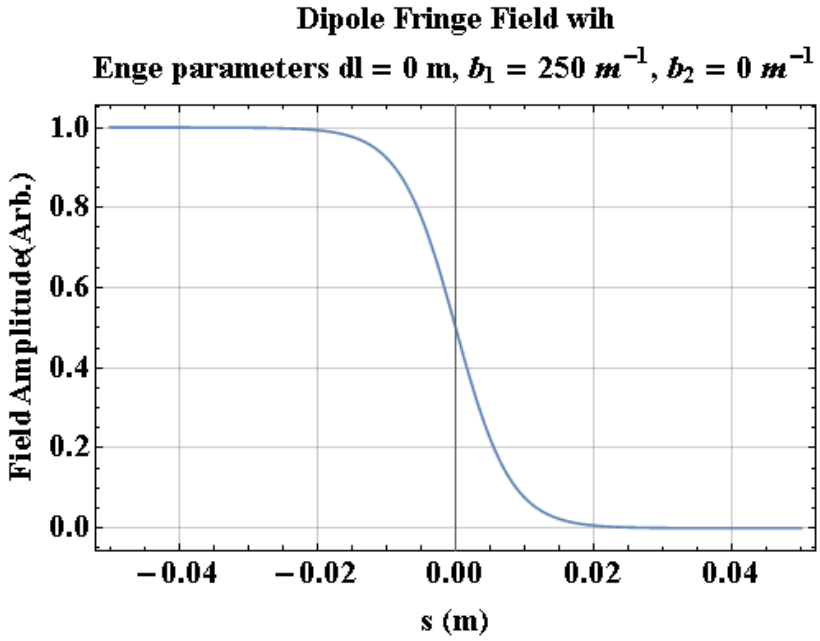

Figure 3.10: Dipole fringe field, with normalised field amplitude, as implemented in GPT model of CLARA Phase 1 bending magnets. The fringe model was developed by Bruno Muratori in [143], with the GPT implementation described in [128].

3.3 Implementation of MAX IV Lattice

Experiments at MAX IV occurred late into the course of this project, and the implementation of the lattice is largely built off of a pre-existing Elegant framework. The initial distribution is generated in ASTRA using ideal "matched" settings and corresponds to the bunch at the injector exit. These ASTRA simulations have been carried out previously, and simulations of the MAX IV injector will not be covered in this thesis. The electron bunch supplied to `elegant` as the initial macroparticle distribution exhibits cylindrical symmetry, which is likely a departure from the real injected bunch of the MAX IV Photoinjector. The electron bunch is then tracked in `elegant` using the pre-existing matched lattice (Figure 1.7). The phase offsets of two accelerating structures, K01 and K02, are varied as according to the setting used in experiments; these parameters were used

to control the compression in the two bunch compressors, BC1 and BC2, present on the MAX IV beamline. Alongside this, quadrupole optics in the beamline section downstream from the second accelerating structure are varied to provide control of the electron bunch distribution at the measurement location. A watch point is added in the drift length between the final two dipoles of the second bunch compressor (BC2), allowing for the electron distribution to be extracted at this location for use in GPT CSR simulations.

The BC2 dipoles are combined-function rectangular magnets. This element is modelled in `elegant` as the effect of multipoles and edge angles as kicks to the electron bunch; however in a time-domain code which complies with Maxwell's equations this is a more complicated problem. Currently GPT has an element capable of multipolar sector magnet fields with fringes, but it is currently only implemented as a sector magnet. This poses a limitation in the ability to model the MAX IV dipoles in GPT. The fringe field parameters used in GPT are based upon the measured profile of the magnetic field.

Chapter 4

Measurement of CSR at CLARA

Validation of CSR in GPT against measurement is desirable before its employment in the development of CLARA and the future UK-XFEL. In this chapter, several potential measurement techniques for the direct and indirect detection of CSR on the CLARA Phase 1 beamline will be presented and evaluated. A beam-based method which exploits the r.m.s energy spread increase due to CSR will be investigated in the context of a scan of the injector linac's phase offset. This will aim to show deviations from the analytic energy spread gain due to the constantly compressing bunch length as discussed in Section 2.3.1. Furthermore, deviations from the 1-dimensional model will be explored as dispersive effects drive transverse beam expansion while simultaneously longitudinally compressing the bunch.

A photonic method of CSR detection, wherein the energy loss of the electron bunch is inferred from the radiative THz emission extracted from a dipole, is also explored. Pyroelectric detectors will be proposed for the measurement of the relative signal strength and characterise the angular distribution of the

radiation. This method will use both a scan of the linac's phase to provide longitudinal control of the electron bunch, as well as use of transverse optics to control the transverse bunch distribution at the radiation location while maintaining the bunch length.

Insufficient growth in the r.m.s energy spread is observed in the beam-based investigation, resulting in the method being unsuitable for CSR detection on the CLARA Phase 1 beamline. However, an apparent reduction in the r.m.s energy spread is found in the drift section downstream from the dipole arising from the velocity term of the Liènard-Wiechert field. This echoes results reported in [88], and hints at a sign change in the longitudinal CSR field in the drift section. The implications of these results points towards novel bunch compressor design where the conventional energy spread growth arising from CSR is self-cancelling.

The photonic method is shown to be a viable method for CSR detection, with the expected detector irradiance well above the noise level for the pyroelectric detectors considered. While the transverse beam distribution can be controlled while maintaining the r.m.s bunch length at the measurement location, the degree to which this is possible is limited. While large values of the Derbenev parameter are achieved, these are shown to be insufficient in bringing about appreciable differences between the GT-calculated CSR emission and those predicted by a 1-dimensional analytical model. A novel effect has been hinted at however, whereby correlations in the x-δ plane due to residual 2^{nd}-order dispersion in combination with strong transverse focusing and short bunch length bring about energy spread reduction within the dipole itself. Once again, this has implications for compressor design, as well as transverse optics development in compressor systems.

4.1 Injector Optimisation

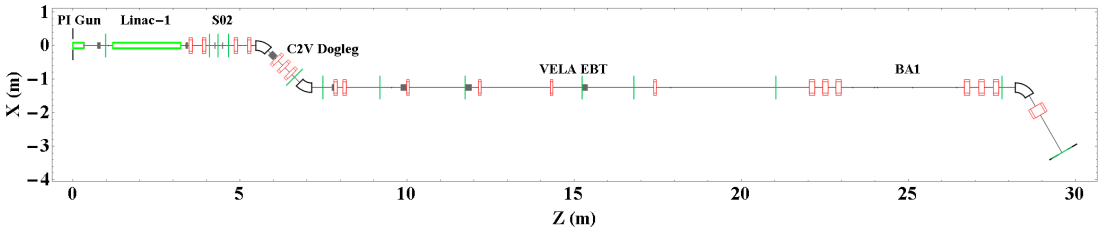

Figure 4.1: Schematic Diagram of the CLARA Phase 1 Lattice with key beamline sections labelled. Dipoles are shown in white, quadrupole magnets in red, orbit-correction magnets in grey, accelerating structures in light green, and YAG screen locations are displayed as green markers.

The crest phases of the RF photoinjector gun and linac-1 (Figure 4.1) are determined in such a way as to reflect the cavity cresting routine on the physical machine. This involves both a rough and fine scan of the phase for each cavity, with all preceding cavities set to their desired off-crest phase and peak accelerating gradient. In the case of the gun cresting, only in the region around the gun's crest phase is the electron bunch accelerated sufficiently quickly so as to remain in phase with the gun's electric field. This "acceptance window" is determined from charge measurements on a wall current monitor (WCM-01) in the straight section (S01) between the PI gun and linac-1 (Figure 4.2a). Space charge forces driving longitudinal expansion in the low-energy electron beam [144], and the energy gain with respect to the initial laser-gun phase difference is asymmetric about the crest phase (Figure 4.2a). However, despite this asymmetry the crest phase is approximately centrally located in this acceptance window, which allows an approximate range of the cavity phase to be defined for the finer scan.

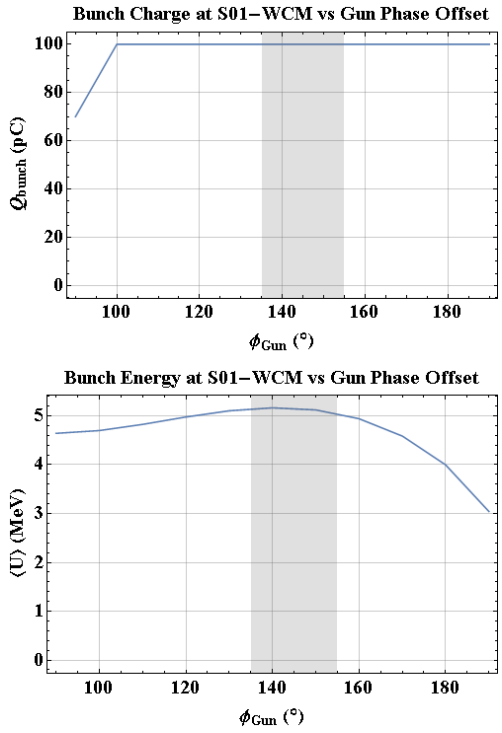

(a) Measurements of the charge at a wall current monitor close to the gun exit define a rough region in which the crest phase lies. The crest is assumed to be close to the centre of this region.

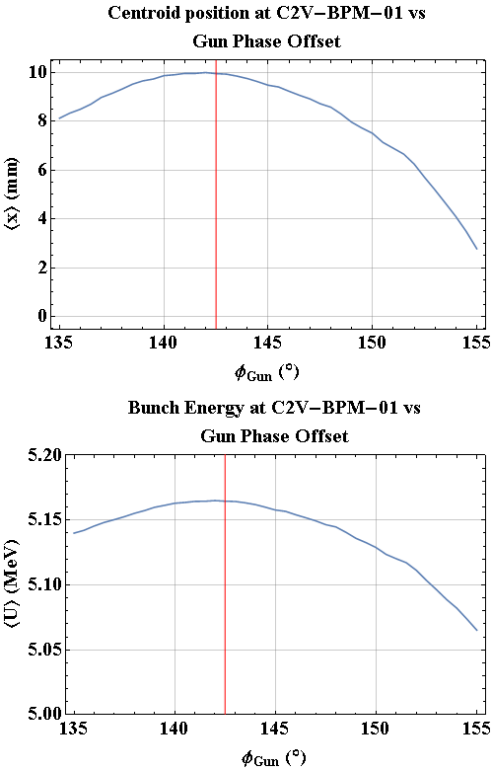

(b) Measurements of the beam momentum from a BPM downstream from a dipole magnet are used to precisely define the crest phase of the PI electron gun.

Figure 4.2: Determining the crest phase of the PI electron gun requires both a rough and a fine scan of the phase. The rough scan makes use of current measurements on a wall current monitor to define a region of the accelerating field phase offset applied to the photoinjector gun where the full bunch charge is accelerated away from the photocathode surface (indicated by the shaded region in Figure 4.2a). A fine scan then makes use of the variable centroid trajectory in a constant dipole field to determine the crest energy through BPM measurements (indicated by the red vertical line in Figure 4.2b).

The range of the fine scan is set to $\pm 10°$ from the central point of the "acceptance window". The design crest energy for the PI gun is 5 MeV, which is used as a target energy for the finer scan. A beam momentum measurement is carried out using a dipole downstream from the injector, with the applied current generating the correct magnetic field strength for a 5 MeV electron beam. Beam

position measurements are then taken on a further downstream beam position monitor (BPM-01) and screen (YAG-01) to determine the crest phase, whereby the excursion of the beam position is at a point of inflection with respect to the applied gun phase. The precision of this measurement on the CLARA beamline is limited by the energy jitter of the beam, which itself arises in part from timing jitters between the PIL and the RF system.

Due to the low-energy of the electron bunch in the injector, the time-of-flight between the PI gun and linac-1 at different gun phase offsets can vary significantly enough to shift the linac's crest phase by up to 5°. As such, the gun is set to its desired phase-offset before the crest phase of linac-1 is measured. This is also found via momentum measurement, with the dipole field set this time to the desired momentum of the beam. In simulations the accelerating field is scaled to the desired peak energy gain, while on CLARA this is done through the power supplied to the klystron driving the linac field. This is in turn set via an arbitrary amplitude parameter in the Libera RF control system, which controls the voltage of the klystron modulator. The phase of the linac field is set by altering the delay between the RF power supply and the photoinjector laser triggering system. An approximate momentum range is found via current measurements on BPM-01, essentially determining the phases at which the beam momentum is sufficient for successful transport through the dipole and further downstream.

The finer scan is carried out in a similar manner as with the PI gun, once again using BPM-01 and YAG-01 for momentum measurements. When simulating these scans in GPT, it is necessary to constrain the beam size in the case where the beam must pass through the first dipole of the CLARA→VELA dogleg

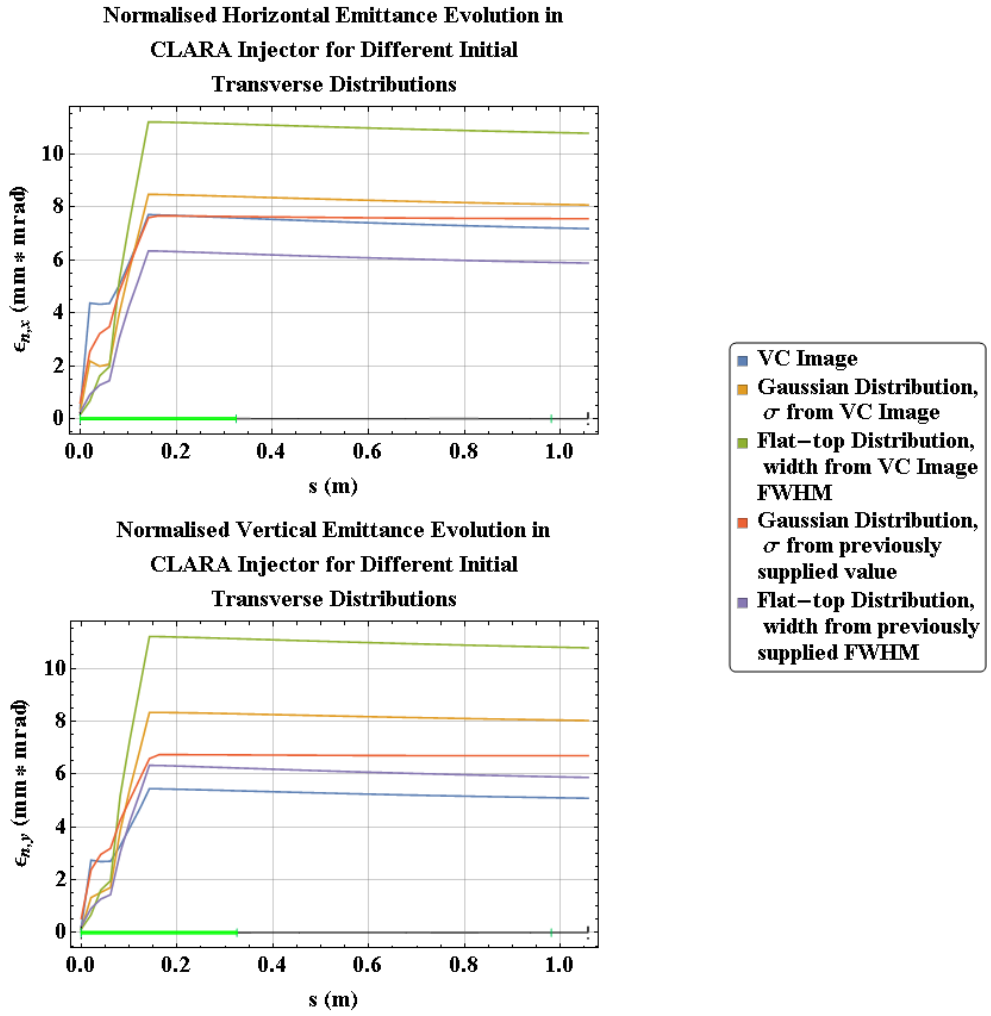

Figure 4.3: Transverse normalised r.m.s emittance evolution in the low energy section of the injector (up to injector linac entrance) for several initial bunch distributions. The superimposed lattice diagram on these o plots shows the location of the electron gun (green).

(C2V, Figure 4.1). The GPT tracking algorithm removes particles that would lie outside of the conventional magnet boundaries when they pass through the magnet, with particles at transverse offsets $r < \pi/b_1$ removed, where b_1 is the first-order Enge parameter describing the fringe field [128]. This is done in order to avoid effects arising from field singularities, but poses a problem when carrying out scans at low energy where space charge drives large blow-up of the beam's

transverse dimension. As such the PI solenoid field is set to have a different peak field than would conventionally be used for emittance compensation and quadrupole matching is carried out in `elegant` in order to prevent this erosion of the bunch charge from excessive transverse beam extent.

Despite the asymmetric transverse distribution of the VC image-generated bunch, it results in a smaller natural beam emittance at the injector exit than that of a Gaussian bunch of equivalent r.m.s size (Figure 4.3). This gives some assurance that there is no grid-heating in the spacecharge3dmesh algorithm due to the substructure in the VC image. Emittance compensation is carried out through the use of the solenoid positioned at the photocathode through invariant envelope matching. Emittance measurements in the CLARA injector are made using a quadrupole scanning technique, which is slow in the absence of an automated routine. As such, it is favourable to use envelope matching conditions for the transverse r.m.s beam size at the linac entrance, σ_i. Serafini and Rosenzweig demonstrate in [140] that there exists a set of conditions for the electron beam at the entrance of a standing wave accelerating structure which minimise the emittance at the structure exit (in the context of a low-energy injector section of beamline). In order to properly dampen the plasma oscillation at the correct phase, and thus minimise the beam's natural emittance, the beam divergence must be at a minimum at the linac entrance alongside the requirement that

$$\sigma_i = \frac{2}{\gamma'}\sqrt{\frac{I}{3I_0\gamma_i}}, \tag{4.1}$$

where γ_i is the normalised beam energy at the linac entrance, γ' is the normalised derivative of the beam energy with respect to the longitudinal coordinate, I is

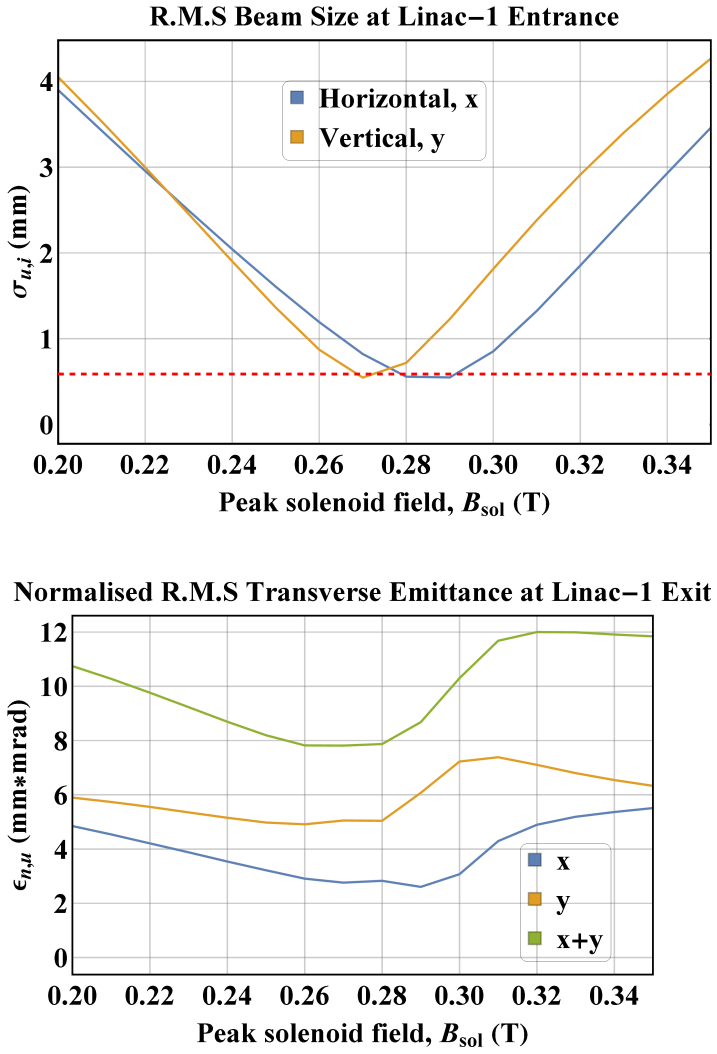

Figure 4.4: Transverse r.m.s beam sizes at the injector linac entrance for a range of solenoid peak field strengths, and the corresponding beam emittances at the linac exit as calculated in GPT simulations. The dashed line indicates the linac entrance condition calculated from Equation 4.1. Beam size measurements indicate that the minimum projected emittance occurs in the range 0.27-0.29 T, whereas the total combined emittance is minimised between 0.26-0.28 T.

the beam current, and $I_0 = \frac{ec}{r_e} \approxeq 17$ kA for electrons. In the case of a 5 MeV and 35 MeV electron beam at the entrance and exit of linac-1 respectively, the beam size at the linac entrance $\sigma_i \approx 0.6$ mm according to Equation 4.1, making the assumption that $I \approx Q/2\sigma_t$. As this value is only strictly true for standing

wave cavities in axisymmetric conditions, it does not provide an exact matching constraint for optimised emittance compensation given the complex nature of the transverse density distribution (Figure 3.5). It does however provide a good initial approximation for the travelling wave injector linac, as shown by GPT simulations (Figure 4.4).

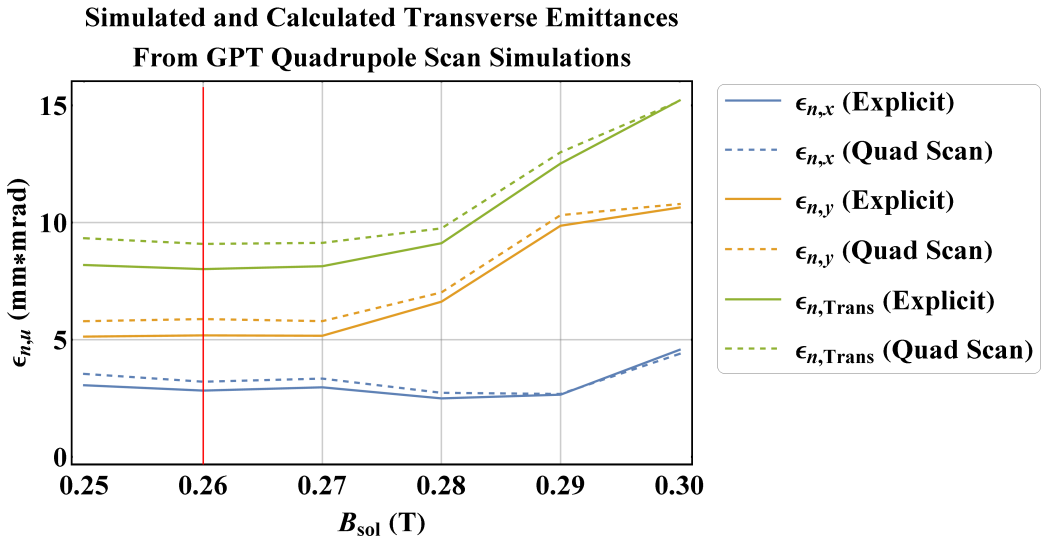

Figure 4.5: Quadrupole scanning technique for projected emittance measurement in GPT simulations. Calculation of the emittance from r.m.s beam sizes follows the procedure outlined in [145].

Following this approximation to the minimum emittance condition, a more thorough characterisation of the beam emittance is carried out via a quadrupole scanning technique (Figure 4.5). Of course, measurements using such a technique will still be limited in accuracy given the non-uniform transverse bunch distribution (Figure 3.5) and natural variation of slice Courant-Snyder parameters within the bunch (Figure 4.6), but they pose the best method currently available on the CLARA Phase 1 beamline which can be expediently carried out

from the control room. All measurement is carried out on-crest for linac-1, with the beam size monitored at S02-SCRN-01. The focusing strength, k_1, of the first quadrupole downstream from linac-1, S02-QUAD-01, is scanned around the value which minimises the bunch size (along one transverse axis) at the screen. This is then repeated for the other transverse axis. The resultant relationship between k_1 and the r.m.s size close to this minimum is pseudo-quadratic, as is predicted from the linear transfer map for a drift-quadrupole arrangement in the thin-lens approximation. A quadratic fit to the scan data can then be used to extract components of the initial σ-matrix describing the beam at the quadrupole, from which the emittance can then be calculated. When carried out in GPT simulations, this technique yields a good approximation for calculation of the CLARA beam emittance (Figure 4.5).

The substructure present in the initial distribution generated at the cathode results in the first moment of the bunch's transverse spatial distribution being displaced from the central axis. While defining the bunch centre in such a distribution is somewhat arbitrary given the number of hotspots present (Figure 3.5), the first moment of the distribution is chosen to conform with the commonly adopted convention. While the cylindrical symmetry of the injector is intrinsically broken by the "realistic" transverse distribution generated from the VC image, it is still preferable to have the bunch trajectory as close to the central axis as possible. Accordingly, two Horizontal-Vertical orbit-correction magnets in S01 are used to ensure the trajectory remains on-axis through linac-1. As with other facets of the injector optimisation, the corrector optimization is simulated to reflect the practical implementation of such optimization in the real accelerator. In this case, three screens are used, S01-SCRN-01, S02-SCRN-01,

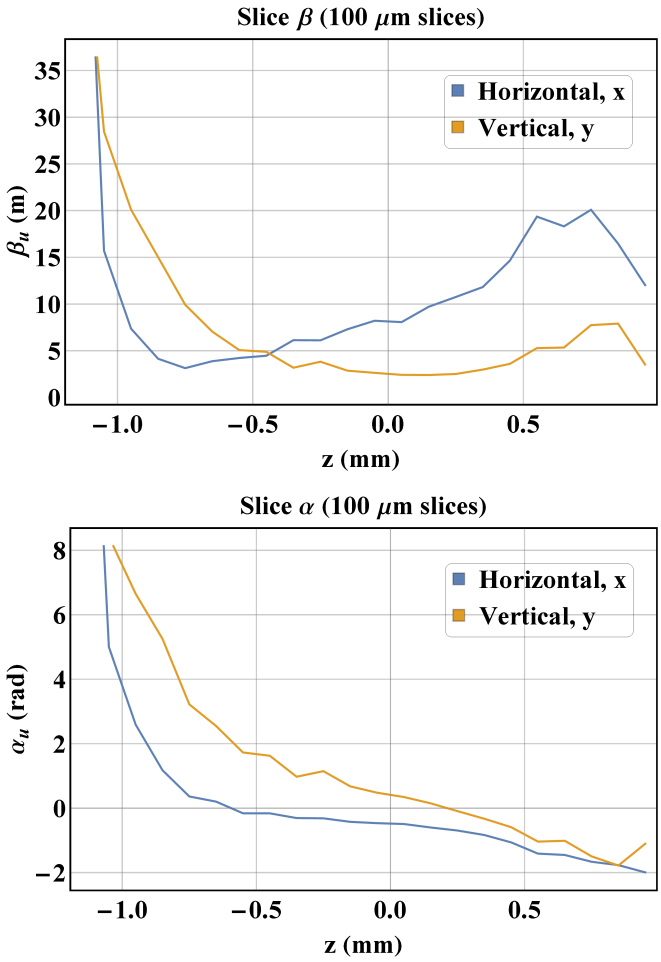

Figure 4.6: Slice Courant-Snyder parameters within the CLARA beam at the injector exit. The electron bunch shown has been accelerating at the linac-1 crest phase. The large spikes at the bunch tail can be attributed to low numbers of particles in the rear slices. The large variation shown demonstrates a limit in the validity of a quadrupole scanning technique.

and S02-SCRN-02. Initially, the correctors are tweaked with linac-1 switched off, with the aim of centring the beam on S01-SCRN-01 (positioned just prior to the linac) and S02-SCRN-01 (positioned just after the linac). This initial correction is carried out as the linac end-cells generate a kick to the bunch centroid in GPT simulations; this is possibly caused by the field discontinuity present in the travelling-wave field model used in the CLARA GPT model discussed in the previous chapter. Following this, an accelerating gradient is applied to the beam and

the orbit correction is adjusted once more, this time focusing upon S02-SCRN-01 and S02-SCRN-02. In all cases, the S02 quadrupoles have no current supplied to them. Following the corrector optimization, the entire injector optimization process is iterated over with new parameters until convergence.

4.2 Beam-based Detection

One method to demonstrate a correspondence between GPT's CSR model and physical observables on CLARA is to exploit the effects of the radiation-beam interaction. The CSR interaction generates a growth in the correlated energy spread of the beam through a redistribution of individual particle energies within the electron bunch (Figure 4.7). This energy spread growth could in principle be detected using a dispersive section of CLARA as a spectrometer. This section will detail a potential experimental study based on inferring the presence and characteristics of the coherent emission from such energy spread-growth, providing simulations which will pose quantitative and qualitative assessment of the method as it would be implemented on CLARA Phase 1. For a beam with a Gaussian transverse distribution, the r.m.s beam size is given by [146]

$$\sigma_u^2 = \epsilon_u \beta_u + \sum_i \left(\eta_u^{(i)} \sigma_\delta^i\right)^2, \tag{4.2}$$

where β_u is the transverse Courant-Snyder beta-function, ϵ_u is the transverse r.m.s emittance, $\eta_u^{(i)}$ is the i^{th}-order dispersion, σ_δ is the total (correlated and uncorrelated) r.m.s fractional momentum deviation, and $u = x, y$ is the transverse coordinate. Given knowledge of the machine lattice functions and the beam emittance it is therefore possible to determine the r.m.s energy spread of the beam. In practice however, this calculation is made simpler by minimising the first term,

attributed to the beta-function. If machine optics are designed such that β_x is minimised at a screen in a region of non-zero dispersion the beam size can be approximated as being solely composed of the dispersive contribution, removing the requirement of a well defined and measured beta-function and emittance.

The strength of the CSR interaction is inversely dependent on the bunch length. Saldin showed in [60] that for a Gaussian bunch passing through a long bending magnet (such that the trajectory within the arc is longer than the formation length of the radiation) in the ultra-relativistic limit, the radiative power due to the coherent interaction goes as $\propto \sigma_z^{-4/3}$. A similar argument can then be said about the near-field interaction, and the energy redistribution associated therein. A sharp increase in the r.m.s energy spread is therefore expected in the case where the bunch length is minimised and the CSR interaction is strongest (Figure 4.7), and this increase will be reflected in changes to the transverse beam size in regions of non-zero dispersion. In the case of CLARA Phase 1 the candidate dispersive sections are the dogleg transfer line connecting the CLARA front-end with the pre-existing VELA beamline, or a spectrometer line further downstream at the terminus of the VELA beamline. For the purpose of measurement of CSR-induced energy-spread, the former of these is the preferable choice as it allows the CSR interaction due to a single dipole to be measured, thus removing complexities arising from multiple sets of fringe fields. Furthermore, longitudinal space charge effects along the VELA beamline are likely to produce significant energy redistribution similarly inversely correlated with the bunch length.

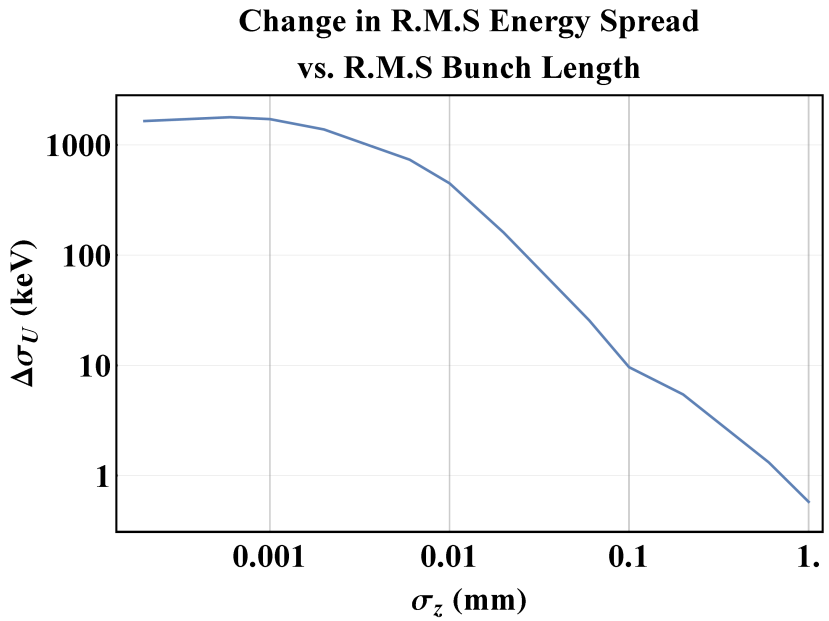

Figure 4.7: Simulated change in energy spread versus r.m.s bunch length for a 50 MeV, 100 pC electron beam passing through a $\pi/32$ rad bend of 10 m radius. The initial electron beam is "cold" i.e. it is mono-energetic and has zero emittance, is cylindrically symmetric, and has a Gaussian distribution in all dimensions. The transverse dimension is kept small at 0.1 mm so as to remain within the 1-dimensional limit described by 2.65.

Measurements of CSR-induced energy spread will require variable bunch dimensions to properly test the capabilities of the GPT CSR calculation. Transversely this will be carried out simply through manipulation of machine optics, whereas longitudinal control has several potential methods which will be discussed in the following sections. As has been stated previously, the pulse length of the CLARA photoinjector laser (PIL) is variable in the range of 2-8ps through the use of pulse stretching optics. A clear relationship can be seen between the PIL pulse length and the corresponding electron bunch length at the injector exit (Figure 4.8), with a shortest achievable bunch length at the injector exit of ∼1.3 ps. Discrepancies between the electron bunch length and the PIL pulse length can be attributed to the longitudinal expansion of the electron bunch in

the low-energy beamline of the CLARA injector. While the PIL pulse length does serve to provide a control for the resultant electron bunch length, this alone will be insufficient for producing the ultra-short bunch lengths required of the CLARA beam for CSR amplification. Furthermore, while the laser pulse length is variable, the overhead in time incurred from changing the laser pulse stretcher parameters and the subsequent adjustment of transport optics makes it an unsuitable experimental variable.

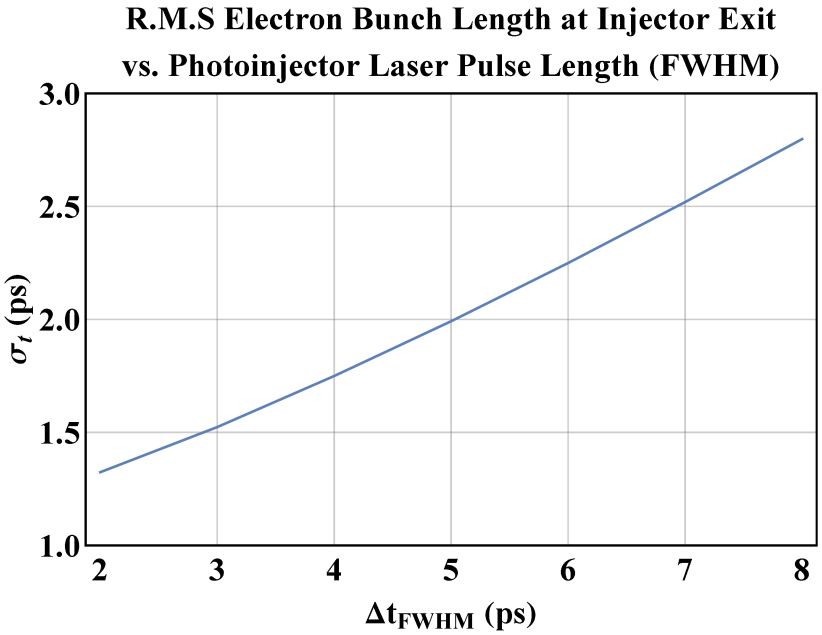

Figure 4.8: Simulated relationship between the PIL pulse length (FWHM) and the resultant r.m.s bunch length of the CLARA beam at the exit of the injector linac (linac-1). The relationship is pseudo-linear, with deviations arising from both space charge expansion and variation in the intrinsic energy spread of the bunch, the latter of these being derived from a greater spread in the witnesses PI gun phase observed within the bunch. In this simulation a -5° phase offset relative to the crest phase is applied to the PI gun corresponding to the typical operational setting of the CLARA injector. Linac-1 is operated on-crest, and the PI solenoid is switched off.

4.2.1 Velocity-bunching compression

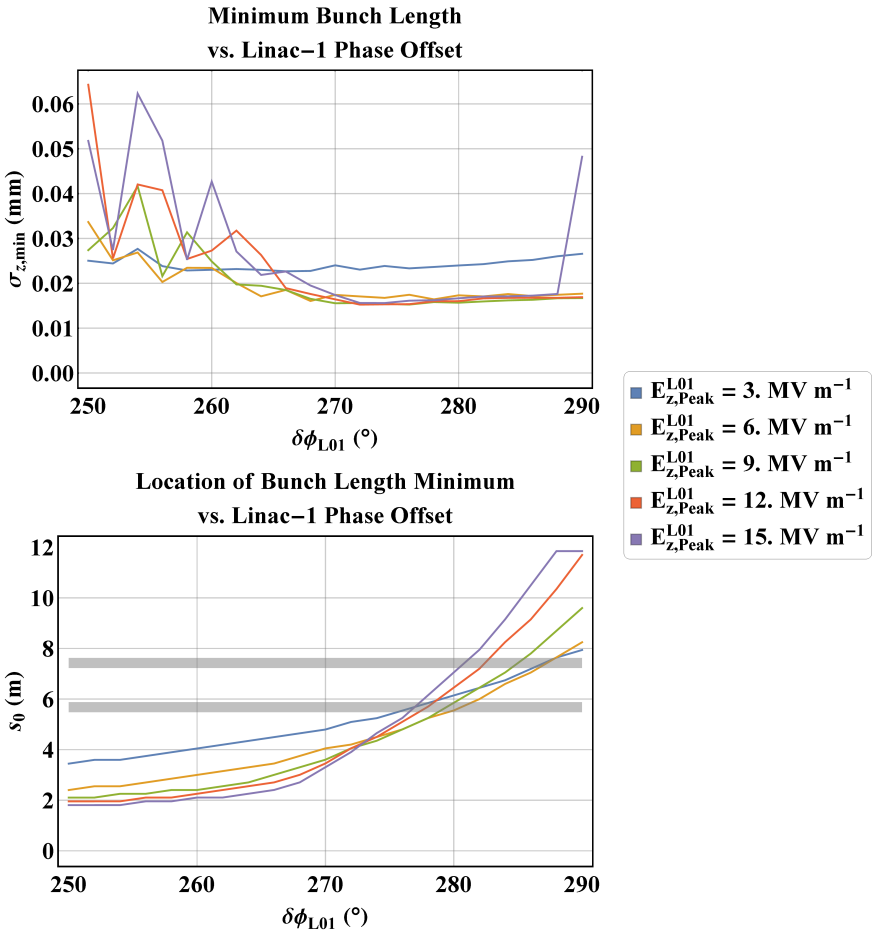

Figure 4.9: The minimum bunch length and its distance from the exit of the injector linac vs. linac phase offset and gradient in the velocity-bunching mode, as calculated in GPT simulations. The greyed out areas represent the equivalent distances of the two C2V dipoles.

One potential method of bunch compression is the velocity bunching mode of the CLARA injector. This mode relies on accelerating the bunch far off crest, close to the zero crossing of the injector linac field. As such, the electron bunch centroid gains very little energy while the correlated energy spread experiences a significant increase, resulting in a large increase in the correlated relative energy spread of the bunch. Due to relative low-energy of the bunch, this relative energy

spread results in a velocity spread within the bunch significant enough for particles at the tail of the bunch to catch up with the head of the bunch. Typically this mode is applied to the future phases of CLARA, where the bunch length is "frozen-in" by the energy gain in subsequent accelerating structures.

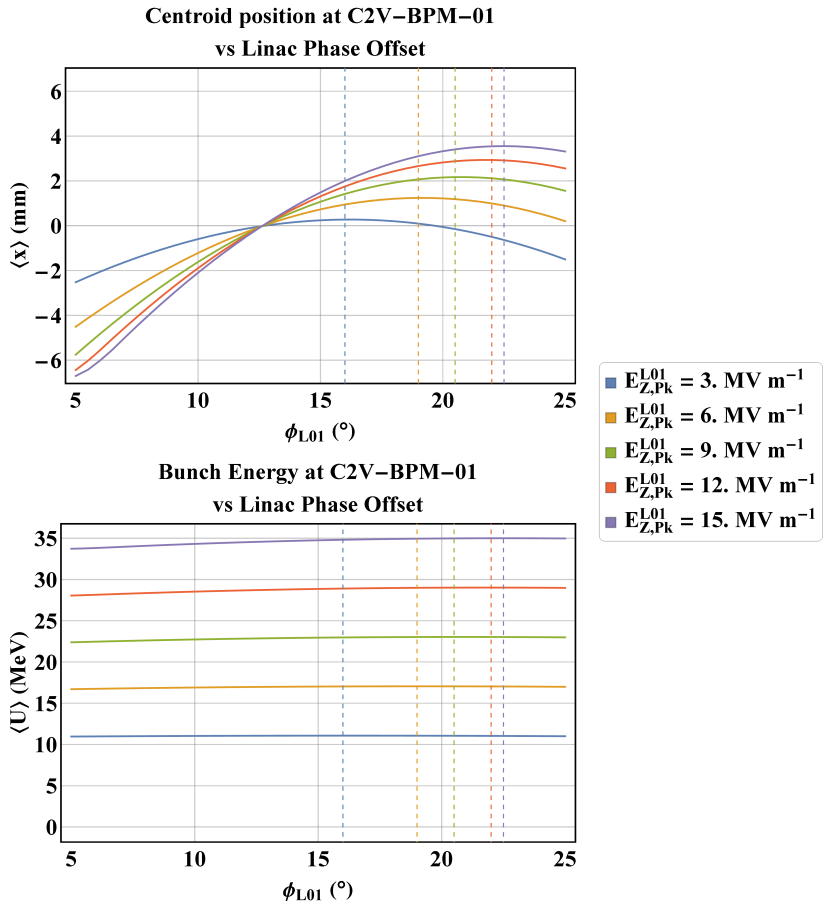

Figure 4.10: Summary of the fine cresting of linac-1 in the velocity bunching mode. Dashed lines indicate the respective crest phase for a given gradient.

Without an subsequent accelerating element in place to compensate the correlated velocity spread of the bunch downstream through an opposite electric field phase offset, the bunch will pass through a point of minimum compression and elongate. The location and sharpness of this minimum is determined by the

accelerating gradient and phase on the injector linac (Figure 4.9). Furthermore, a dependence on the bunch length evolution with respect to the PI solenoid peak field is seen, with the strongest variation observed for the lowest accelerating gradient.

In order to facilitate subsequent tracking of the electron bunch after the injector linac in GPT, the transverse beam size must once again be constrained. As such, the solenoid is adjusted to produce the minimum beam size at the injector exit, as opposed to minimum emittance. Furthermore, both solenoids surrounding linac-1 are enabled to further limit the expansion due to space charge. In principle, the linac-1 operating phase and gradient could be tuned to result in a bunch length minimum occurring within a dipole, resulting in a stronger CSR interaction. Variation of the injector linac's accelerating gradient requires the crest phase to be re-measured for each accelerating gradient (Figure 4.10).

Table 4.1: Summary of injector parameters used in GPT simulations of the velocity-bunching mode

Bunch Generation Parameters	
Laser Pulse Length (FWHM)	2 ps
Bunch Charge	100 pC
Number of macroparticles	10^4
Machine Parameters	
Gun Peak Field	71.5 MV m^{-1}
Gun On-Crest Phase	142.5°
Gun Off-Crest Phase Offset	-10°
Gun Solenoid Peak Field	0.288 T $\rightarrow$ 0.288 T
L01 Peak Field	3 MV m^{-1} $\rightarrow$ 15 MV m^{-1}
L01 On-Crest Phase	16° $\rightarrow$ 22.5°
L01 Off-Crest Phase Offset	260° $\rightarrow$ 280°
L01 Solenoid 1 Peak Field	-0.063 T $\rightarrow$ -0.046 T
L01 Solenoid 2 Peak Field	-0.549 T $\rightarrow$ -0.349 T

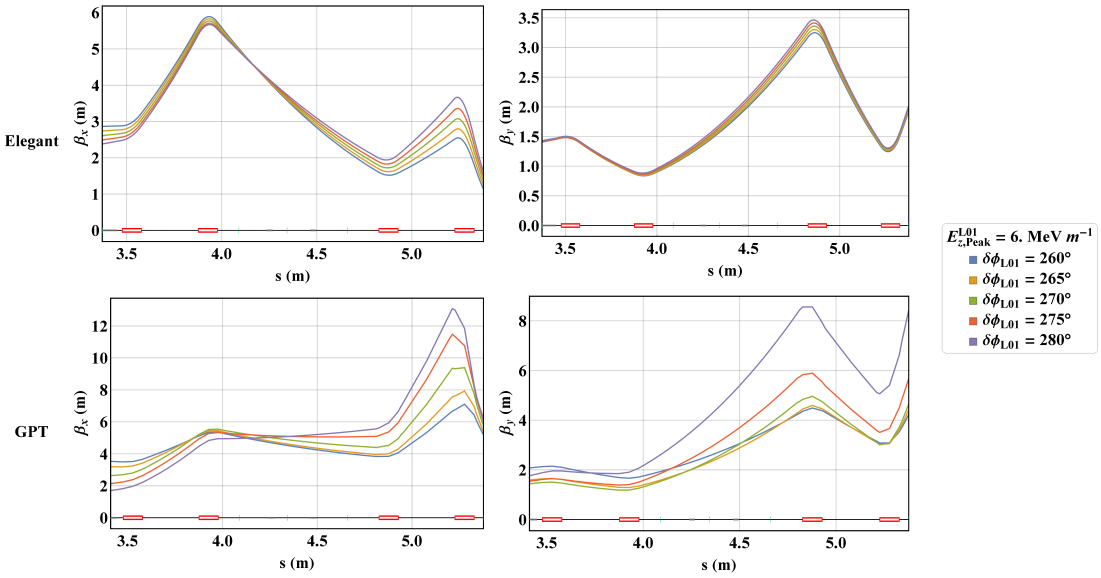

Figure 4.11: Beta-functions for `elegant` match of S02 for several electron bunches, with corresponding GPT β-functions. These lattice parameters correspond to the beam-based, statistical Courant-Snyder parameters. The significant discrepancies observed can be attributed to both removal of particles at large transverse offsets in GPT causing sharp discontinuities in the beam r.m.s size and emittance, and the higher-order chromatic effects not captured in `elegant` which bring about changes to the projected beam emittance.

The low energy of the bunch in this mode means that significant expansion due to space charge forces is expected. In the typical velocity-bunching mode investigated for the full CLARA beamline design, the photoinjector laser is attenuated to significantly reduce the bunch charge (down to 10 pC - 50 pC) and thus the transverse expansion of the bunch due to space charge. However, as CSR is a coherent process, such a reduction in the bunch charge is going to result in a equivalent quadratic reduction in the strength of the CSR interaction. Instead, machine optics will have to be used to constrain the bunch dimensions in the transport between the injector and the dogleg. The injector is simulated in GPT (Table 4.1) with the output then passed onto `elegant` for use in optimisation. The results of optimization in `elegant` are then re-simulated in GPT (Figure

4.11). Significant differences are observed between the `elegant` match and the corresponding re-simulation in GPT, which are believed to arise from higher-order chromaticity not captured in `elegant` simulations as well as quadrupole fringe-field effects.

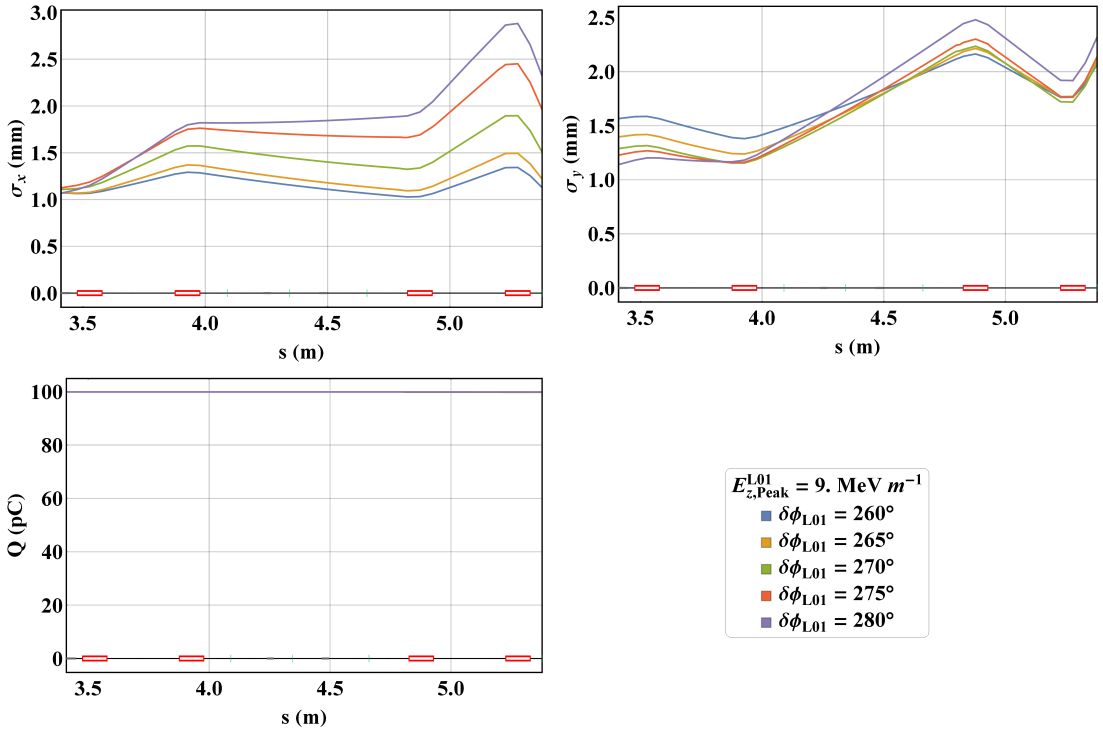

Figure 4.12: Horizontal and vertical beam sizes and bunch charge evolution along the straight section following the injector linac. Bunch dimensions are considerably larger than those seen for conventional accelerating modes due to the low energy space charge in the bunch. The sharp changes seen in the vertical r.m.s bunch size, and to a lesser extent in the horizontal also, arise from charge losses concentrated at large vertical displacements where transverse divergences are also largest.

Beam optics are optimised such as to avoid inversion of the transverse phase space about its abscissa, whilst constraining the bunch's maximum transverse extent over the straight section between the injector linac and the first dogleg dipole. A bunch with a large in-plane transverse size at the entrance of a dipole

is susceptible to bunch-elongation due to geometric effects; a particle entering the dipole with an orbit deviation of δ_x away from the reference orbit will travel along a trajectory of the same curvature as that of a particle on the reference orbit. There is a path length difference, $\Delta l = \rho\Delta\theta$, incurred with respect to the reference orbit due to the different trajectory lengths, where $\Delta\theta$ is the change in the particles horizontal divergence with respect to the reference orbit at the dipole exit. This deviation error can be determined from the 2-dimensional transfer map of a sector magnet in the x-x' plane [147],

$$\begin{pmatrix} \delta_x \\ \Delta\theta \end{pmatrix} = \begin{pmatrix} \cos\theta & \rho\sin\theta \\ -\frac{1}{\rho}\sin\theta & \cos\theta \end{pmatrix} \begin{pmatrix} \delta_x \\ 0 \end{pmatrix},$$

which gives an equivalent path length difference and R_{51} of

$$(\delta_z)_1 = R_{51}\delta_x = -\sin\theta\delta_x. \tag{4.3}$$

Here $(\delta_z)_1$ is the contribution from the R_{51} coupling towards the total change in the longitudinal coordinate. For a Gaussian electron distribution of

$$\sigma_i = \langle\delta_i^2\rangle - \langle\delta_i\rangle^2,$$

where $i = x, y, z$, it can similarly be written that the contribution to the change in r.m.s bunch length due to the R_{51} of the magnet is

$$(\Delta\sigma_z)_1 = \sin\theta\sigma_x.$$

The bend angle of the first dogleg dipole is 45°, meaning that the beam size at the dipole entrance must be kept small ($\sigma_x \ll \sqrt{2}\sigma_z$) to avoid the R_{51} of the

dipole from negating the compression due to velocity bunching. The bunch dimensions seen after optimisation are far larger than those seen in typical CLARA accelerating modes, which are usually less than 1 mm (Figure 4.12), and so this R_{51} coupling is likely to be a significant effect.

For an electron beam with a large correlated momentum spread such as in the CLARA velocity-bunched mode, the presence of a constant magnetic focusing gradient gives rise to a longitudinal correlation in the net focusing experienced along the beam. Filippetto *et. al.* demonstrated in [148] that introducing such correlations between the longitudinal can bring about increases to the projected emittance. This increase in the projected emittance is attributable to cross-terms between individual slice emittances within the electron bunch. For a bunch with longitudinal chirp $\zeta = \frac{d\frac{\Delta p}{p_0}}{dz}$, it is necessary that the individual slice widths satisfy

$$\Delta z \ll \frac{1}{\zeta}$$

to ensure that a given slice can be assumed mono-energetic, which assures that the focusing felt within a given slice is constant. The result of this is that any changes to the divergences and positions of particles within the slice are correlated, and there should be no growth of the individual slice emittance. The total projected emittance can be expressed as

$$\epsilon_u = \sqrt{\langle u^2 \rangle \langle u'^2 \rangle - \langle u u' \rangle^2}, \tag{4.4}$$

where $u \in \{x, y\}$ and $u' \in \{x', y'\}$. A generalised second moment of the bunch in the v-w plane (where $\{v, w\} \in \{x, x', y, y'\}$) can be written in terms to statistical properties of individual slices by recognising that

$$\begin{aligned}
\langle vw \rangle &= \frac{1}{N} \sum_{i=1}^{N} \left(v_i - \bar{v}\right) \left(w_i - \bar{w}\right) \\
&= \frac{1}{N} \sum_{i=1}^{N_s} \sum_{j=1}^{N_i} \left(v_{ij} - \bar{v}\right) \left(w_{ij} - \bar{w}\right) \\
&= \frac{1}{N} \sum_{i=1}^{N_s} \sum_{j=1}^{N_i} \left(\left(v_{ij} - \bar{v}_i\right) + \left(\bar{v}_i - \bar{v}\right)\right) \left(\left(w_{ij} - \bar{w}_i\right) + \left(\bar{w}_i - \bar{w}\right)\right) \\
&= \frac{1}{N} \sum_{i=1}^{N_s} N_i \left(\langle vw \rangle_i + \left(\bar{v}_i - \bar{v}\right)\left(\bar{w}_i - \bar{w}\right)\right),
\end{aligned} \tag{4.5}$$

where N is the population of the bunch, N_s is the number of slices, N_i is the population of the i^{th} slice, and $\bar{\cdot}$ represents the first moment. The operator

$$\langle vw \rangle_i = \frac{1}{N_i} \sum_{j}^{Ni} (v_{ij} - \bar{v}_i)(w_{ij} - \bar{w}_i) = (\sigma_{vw})_i^2,$$

represents the correlation between the coordinates v and w in the i^{th} slice. Application of Equation 4.5 to Equation 4.4 gives rise to three distinct contributions towards the projected emittance, which are attributable to the envelope, the variation in the slice centroids, and the correlation between the slice centroid and size. The first of these,

$$\begin{aligned}
\epsilon_{env,u}^2 &= \frac{1}{N^2} \left[\left(\sum_{i=1}^{N_s} N_i \langle u^2 \rangle_i \right) \left(\sum_{j=1}^{N_s} N_j \langle u'^2 \rangle_j \right) - \left(\sum_{i=1}^{N_s} N_i \langle uu' \rangle_i \right) \left(\sum_{j=1}^{N_s} N_j \langle uu' \rangle_j \right) \right] \\
&= \frac{1}{N^2} \left[\sum_{i=1}^{N_s} N_i^2 \left(\langle u^2 \rangle_i \langle u'^2 \rangle_i - \langle uu' \rangle_i^2 \right) \right. \\
&\left. + \sum_{i=1}^{N_s} \sum_{j=1; j \neq i}^{N_s} N_i N_j \left(\langle u^2 \rangle_i \langle u'^2 \rangle_j - \langle uu' \rangle_i \langle uu' \rangle_j \right) \right],
\end{aligned}$$

consists of a component equivalent to the sum of the individual slice emittances and one equivalent to the mixing of pairs of slices [148]. In a homogeneous beam with no correlations between the longitudinal and transverse coordinates this second term is zero, whereas in the case of a velocity bunched beam passing through a quadrupole the correlation generated due to the focusing gradient along the bunch results in a non-zero contribution from mixing between slices. This serves to generating an emittance increase from the spread in the slice lattice parameters of the bunch. The latter two terms are dependent on the individual centroid offsets for each slice, which is zero for a bunch whose individual slices have the same centroid in the transverse phase space. Should the bunch orbit be altered by correctors or dipole magnets, a correlation between trajectory kick with respect to slice position will be generated, and these terms would also contribute to the overall emittance change.

In the context of the CLARA velocity bunching mode, these chromatic effects are another significant challenge when applying the velocity bunching mode at these high bunch charges. Because of the low-energy space charge-driven expansion of the bunch transversely, the focusing strengths required from the straight section quadrupoles are large. GPT simulations predict large scale variations in the normalised transverse r.m.s emittances of up to ± 16 mm $\cdot$ mrad (Figure 4.13), which can be attributable to the large correlation imparted between the transverse and longitudinal planes by the quadrupole field. Figure 4.13 shows a sharp increase in the transverse beam emittance as the electron beam reaches the final quadrupole, which has a large focusing gradient applied. While these emittance changes can be reversed, this adds an extra constraint when matching transverse distributions.

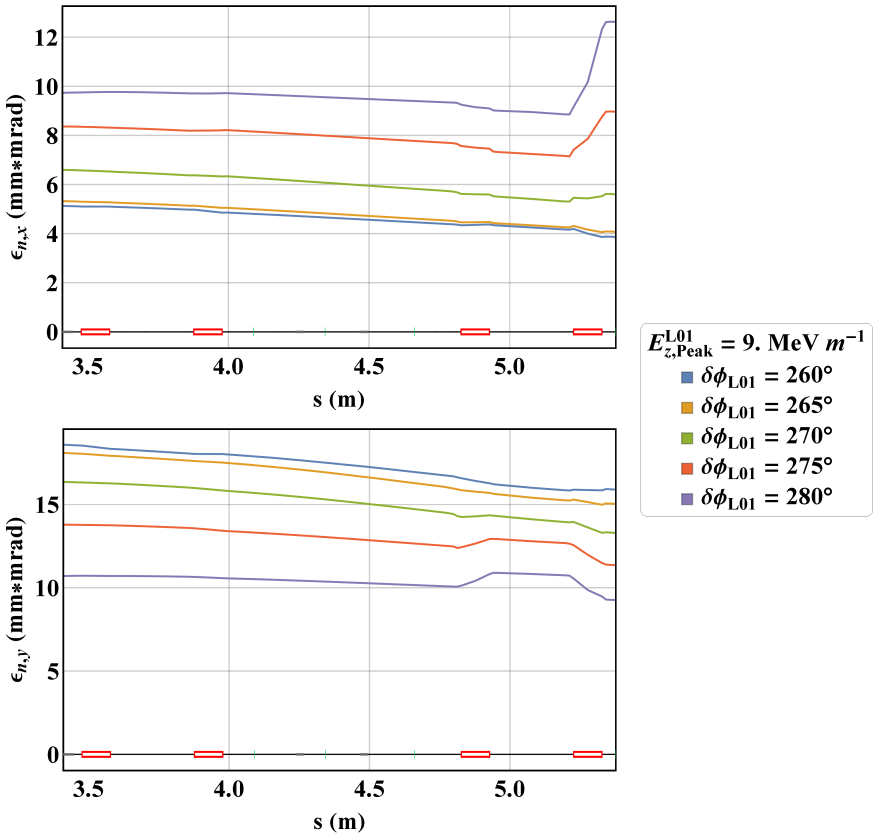

Figure 4.13: Transverse emittance variation in S02 arising from chromatic effects in quadrupoles with large focusing gradients. A large correlated energy spread gives rise to a longitudinal correlation of the individual slice dimensions, which in turn contributes to off-diagonal terms in the full projected transverse emittance.

This scheme is further complicated by the fact that a negative longitudinal energy chirp must be imparted onto the bunch by the accelerating field to enable velocity bunching. Here a negative chirp refers to an electron distribution where particles towards the rear of the bunch (at negative z) have a higher energy than those at the head. However, due to the positive R_{56} of the first dipole on the dogleg transfer line, the velocity bunching effect will compete against the longitudinal dispersion of the bunch in the dogleg. Further to this, the low-energy of the electron beam in velocity-bunching mode will result in a beam that is very

sensitive to the machine optics. This will amplify the effects of the machine jitter.

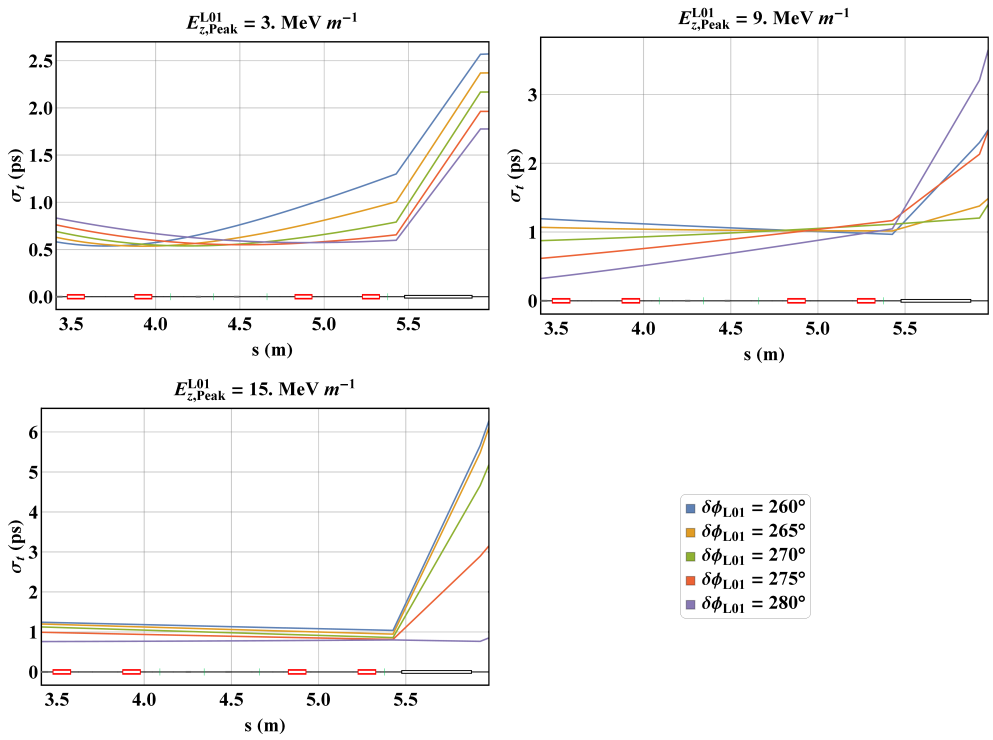

Figure 4.14: Longitudinal elongation the first dogleg dipole for several machine set-ups considered in the VB mode. Large transverse beam sizes, driven by low-energy space charge, give rise to significant bunch elongation due to path length differences for particles at larger horizontal offsets. This works in tandem with the dispersive R_{56} component arising from the dipole to overcome the velocity bunching R_{56} component. Such bunch elongation occurs in all cases considered.

Scanning both the accelerating gradient and phase offset and propagating the beam along a free path in GPT demonstrates that the bunch-length-minimum position could be shifted all the way to the second C2V dogleg dipole in principle (Figure 4.9), however this does not include the effect of dispersion on the bunch length. When the C2V dipole is included in simulations, the bunch elongation due to the negative chirp and R_{51} coupling quickly overcomes any compressive effect arising from the velocity bunching (Figure 4.14). This makes it unsuitable

for sufficiently amplifying the CSR interaction to enable detection of the energy spread change.

4.2.2 Dispersive Compression

The velocity bunching mode has been shown to be ineffective for bunch compression in the CLARA Phase 1 beamline. This is due to a lack of a secondary accelerating structure, which could be used to accelerate the electron bunch to ultra-relativistic energies in order to relativistically reduce the velocity spread within the beam, which would "freeze-in" the bunch compression due to velocity bunching. As such a more conventional method of compression is will be investigated for the CLARA Phase 1 beamline. This compression will exploit the non-zero R_{56} and T_{566} of the dogleg transfer line connecting the CLARA and VELA beamlines by running the injector linac off-crest once again, this time closer to the crest phase. The injector settings used for this compression scheme will mirror the "conventional" BA1 delivery settings (Table 4.2). It is desirable to keep the beam energy constant for the phase scan to minimise the number of experimental variables; as such it is necessary to scale the peak accelerating gradient by a factor of $(\cos\delta\phi_L 01)^{-1}$. The injector linac is capable of sustaining accelerating fields of up to 20 $\mathrm{MeV\,m^{-1}}$, but this is reduced to 15 $\mathrm{MeV\,m^{-1}}$ to allow for sufficient increases of the field magnitude in order to maintain the bunch momentum.

Table 4.2: Summary of injector parameters used in GPT simulations for the dispersive compression mode.

Bunch Generation Parameters	
Laser Pulse Length (FWHM)	2 ps
Bunch Charge	$\leq$100 pC
Number of macroparticles	10^4
Machine Parameters	
Gun Peak Field	71.5 MV m^{-1}
Gun On-Crest Phase	142°
Gun Off-Crest Phase Offset	-5°
Gun Solenoid Peak Field	0.26 T
L01 Peak Field	15 MV m^{-1}
L01 On-Crest Phase	23.5°
L01 Off-Crest Phase Offset	0° $\rightarrow$ 30°
L01 Solenoid 1 Peak Field	0 T
L01 Solenoid 1 Peak Field	0 T

Magnetic bunch compression exploits the path length difference of off-momentum particles in a chirped bunch to bring about changes to the overall r.m.s bunch length. For a particle at (z_i, δ_i) passing through a dipole, the change in the longitudinal coordinate is given by

$$\Delta z = R_{56}\delta_i + T_{566}\delta_i^2 + \mathcal{O}\left(\delta_i^3\right) = R_{56}(\nu z_i + \xi z_i^2) + T_{566}\nu^2 z_i^2 + \mathcal{O}\left(z_i^3\right), \qquad (4.6)$$

where ν and ξ are the first and second order chirp parameters arising from the accelerating field in linac-1. Equation 4.6 demonstrates that for a given value of R_{56} the sign of the 1$^{\text{st}}$-order chirp imparted on the bunch by the off-crest accelerating field determines whether the bunch is compressed or elongated. In the convention adopted here, a positive value of Δz corresponds to a particle advancing head-ward within the bunch; should this occur for a particle to the rear of the bunch (and vice-versa) this would result in a system that results

in bunch compression. As such, for a positively chirped (in 1st-order) electron bunch, a negative R_{56} would result in compression of the electron bunch.

CSR Measurement in the S02SP1 Spectrometer Line

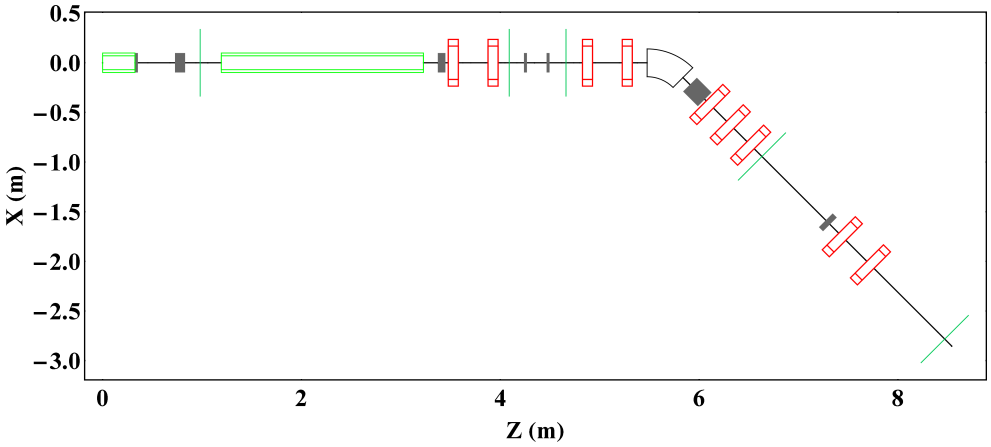

Figure 4.15: CLARA S02SP1 spectrometer line schematic. Accelerating structures in light green, diagnostic screens in dark green, corrector magnets in grey, quadrupoles in red, and dipoles in white.

The S02 spectrometer line (Figure 4.15) is the candidate location for the detection of CSR-induced energy spread, with two screens available for measuring the corresponding variation in the transverse size due to dispersion. As only one dipole is available for compression, the injector linac will need to be set fairly off-crest to achieve significant compression of the electron bunch. As before, the effects of the R_{51} and R_{52} coupling are significant due to the large bending angle (45°), and must be accounted for by keeping the β_x and α_x of the lattice small at the dipole entrance (Figure 4.16).

The S02 optics are matched in `elegant` in order to minimise the in-plane transverse β-function and maximise the dispersion at the screens, resulting in the major contribution to the beam size being the dispersive component (Figure

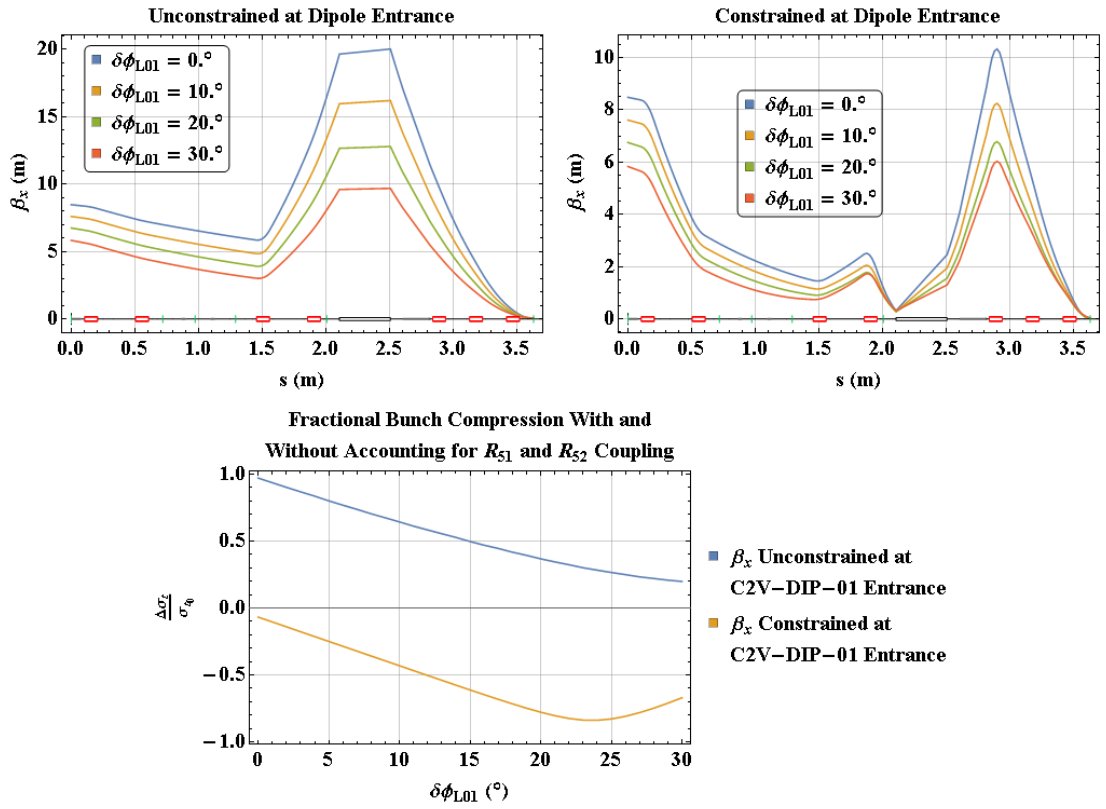

Figure 4.16: Matching with and without accounting for the effect of R_{51} and R_{52} on the electron bunch compression

4.17). Practically this is a non-trivial endeavour on a real machine, where the dispersion of the structure must be measured and set to its desired value before adjusting optics to minimise β_x. The minimisation of β is complicated by several factors, namely a variation of the slice Courant-Snyder parameters throughout the electron bunch as well as difficulties with assuring a β_x-minimisation on a real machine which does not rely entirely on simulation. For both matches shown in Figure 4.17 maximum compression occurred at 24° due to the R_{56} being unchanged between the two matches (Figure 4.18), although the overall magnitude of the compression is slightly shifted by the change in upstream transverse optics between the two set-ups.

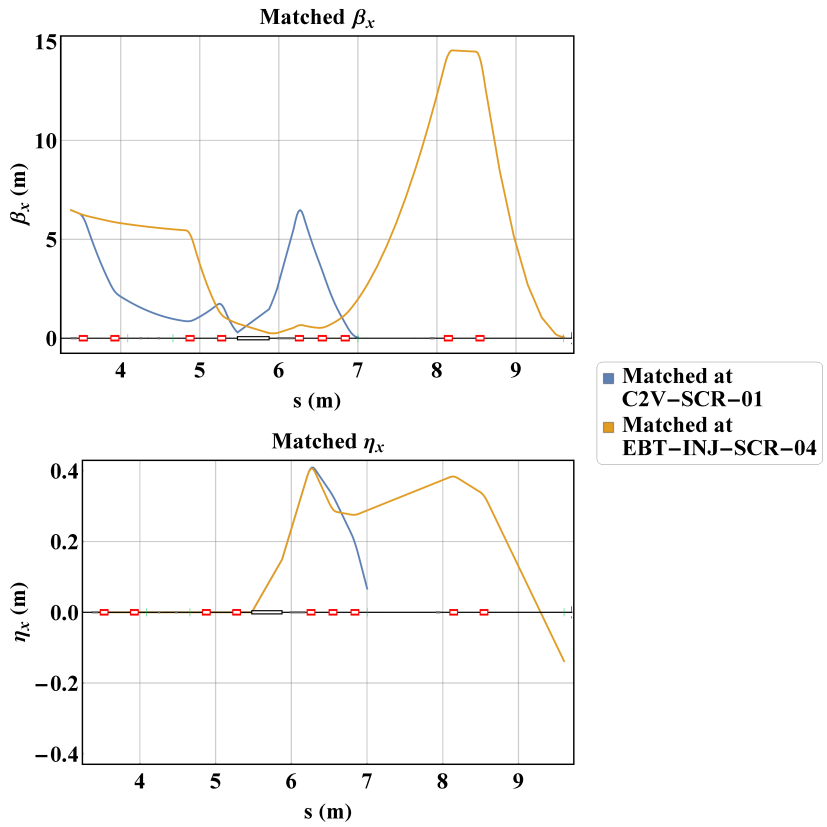

Figure 4.17: Dispersion function and transverse in-plane β-function for potential machine set-ups.

Although convergence of GPT's CSR model is typically only seen for macroparticle numbers $\gtrsim 10^6$ [1], such simulations are computationally intensive. As such, a smaller number of macroparticles is used to determine the viability of the proposed experimental procedure. GPT simulations using 10^4 macroparticles show that the fractional change in the energy spread is on the order of 1% (Figure 4.19). By simulating the beamline with and without the CSR model enabled, it is possible to determine the expected "effective" contribution to the transverse size at the screens due to CSR-induced energy spread.

While the beam size does change with respect to the linac phase, this is almost completely attributable to the varying energy spread imparted by the linac field.

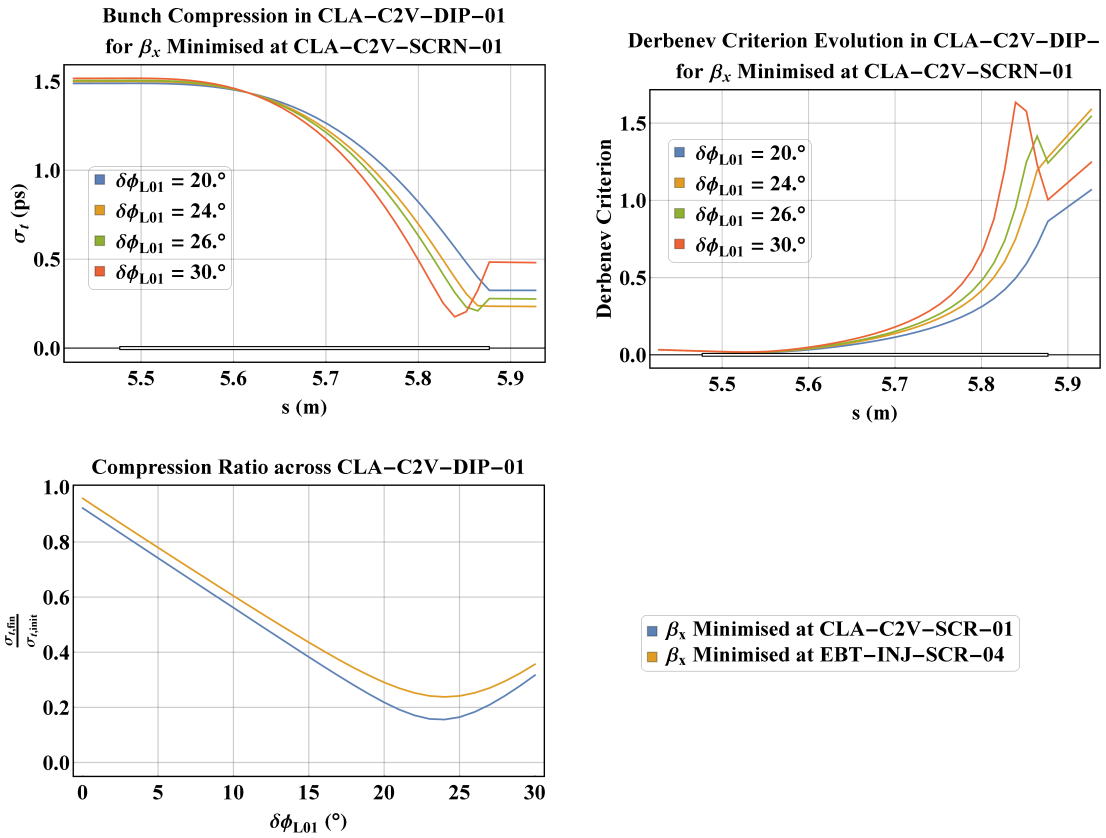

Figure 4.18: Bunch compression and Derbenev parameter across the first dipole of the C2V dogleg (CLA-C2V-DIP-01).

The contribution due to CSR is on the order of $\sim$ 1 µm to $\sim$ 10 µm, and while it appears that the peak change in the beam size approximately coincides with the maximum compression phase in the case where β_x is minimised at EBT-INJ-SCR-04, the same is not echoed in the other set-up. Despite this discrepancy, it can still be assumed that the overall changes in the beam size due to CSR-induced energy spread will be very small compared to the total beam size. The scheme is further complicated by the fact that the energy-redistribution within

the bunch due to CSR is not purely linearly correlated, resulting in coupling to higher-order dispersive terms within the beamline. This increase in the beam size is far too small to be detectable on the resolution of a typical YAG screen at CLARA, especially when considering the effects of the machine jitter. There is a suspected phase jitter of $\sim \pm 1°$, the effect of which is to produce a large centroid and r.m.s beam size jitter in the dispersive C2V dogleg.

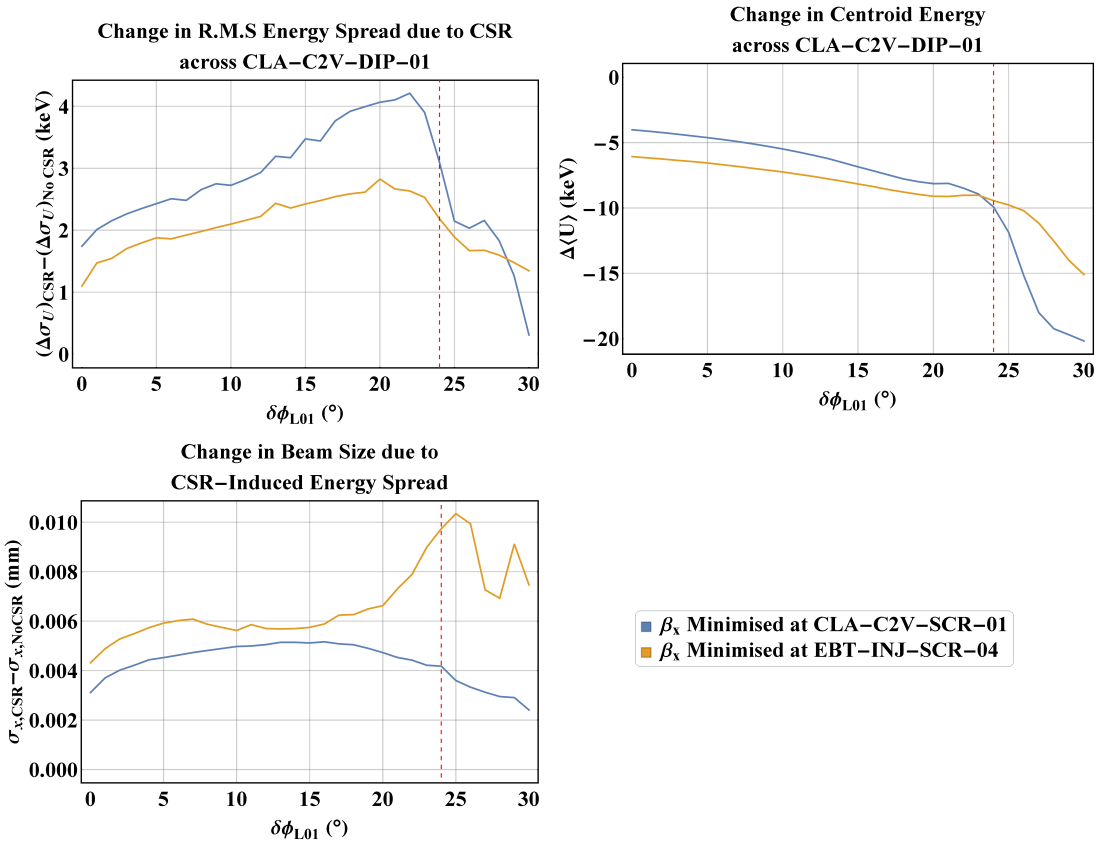

Figure 4.19: Change in r.m.s energy spread across CLA-C2V-DIP-01 (between 5 cm upstream and 5 cm downstream of the dipole) and the corresponding changes in transverse size at CLA-C2V-SCR-01 and EBT-INJ-YAG-04 against linac-1 phase offset. The maximum compression phase is indicated by the red dashed line.

The small change observed in the longitudinal phase space (LPS) is attributable in part to the sharpness of the bunch length minimum (Figure 4.18). As the bunch is compressed very quickly, it also moves through this point and becomes over-compressed quickly. This leads to less time being spent at short-bunch lengths within a dipole, and thus only a small part of the electron bunch's trajectory is spent under the influence of an amplified coherent interaction. This can be seen in part with the fact that neither the largest change in the r.m.s energy spread nor the largest loss in beam energy due to CSR coincide with the maximum compression phase. In the case of the energy loss of the bunch, this can be understood by looking at the averaged "CSR contribution from the bunch length"; in the 1-dimensional approximation of a Gaussian electron current profile, CSR scales according to $\sigma_t^{-4/3}$. As such, by averaging this quantity over the dipole, i.e.

$$\langle \sigma_t^{-4/3} \rangle^{-3/4} = \frac{1}{l_{Dip}} \left(\int_{Dip} \sigma_t(s)^{-4/3} ds \right)^{-3/4}, \tag{4.7}$$

it is possible to better estimate the effect of the constantly changing electron bunch length on the energy loss of the bunch (Figure 4.20). This effect poses a limit on the applicability of CSR-based bunch length monitoring systems in structures which rapidly compress electron bunches. While this effect describes the energy loss of the bunch, the energy-spread change shows a peak in the under-compressed region of the phase-offset scan.

When considering the energy spread evolution through the beamline, the reason for the discrepancy between the phase of maximum compression and the phase of maximum energy spread growth becomes clear (Figure 4.21). While the maximum compression phase does indeed experience the greatest growth in

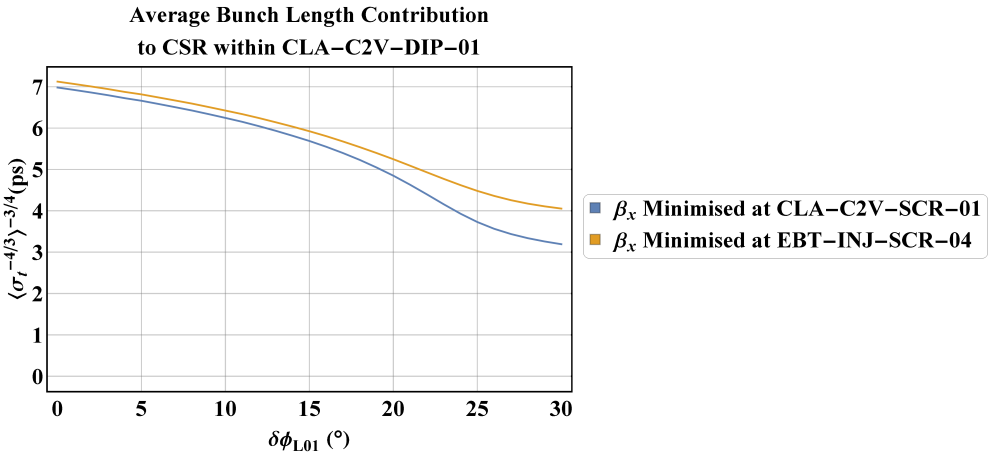

Figure 4.20: Averaged contribution to CSR due to changing bunch length in CLA-C2V-DIP-01, calculated as shown in Equation 4.7

energy spread within the dipole itself, the Coulomb term of the CSR interaction results in a sharp reduction at the dipole fringe. Furthermore, there is a sustained reduction in the subsequent drift section which potentially explains discrepancies between the simulated changes in the beam size at downstream screens and the energy spread growth seen in Figure 4.19. This effect echoes simulation findings on the FERMI beamline presented by Brynes *et al.* in [88], and indicates the possibility of designing bunch compression schemes which are "self-cancelling" in terms of CSR-induced energy spread growth.

Because of the large value of the Derbenev parameter [8] (Figure 4.18), the CSR-interaction would be expected to be suppressed towards the dipole exit; as the effect of dispersion broadens the transverse distribution of the bunch at the same time as the bunch is compressed longitudinally, the coherence of the individual particles synchrotron fields is inhibited. Comparison of the simulated CSR power to the analytical radiative power of a Gaussian charge distribution in the steady-state, 1-dimensional limit (Equation 2.56) shows a clear deviation from

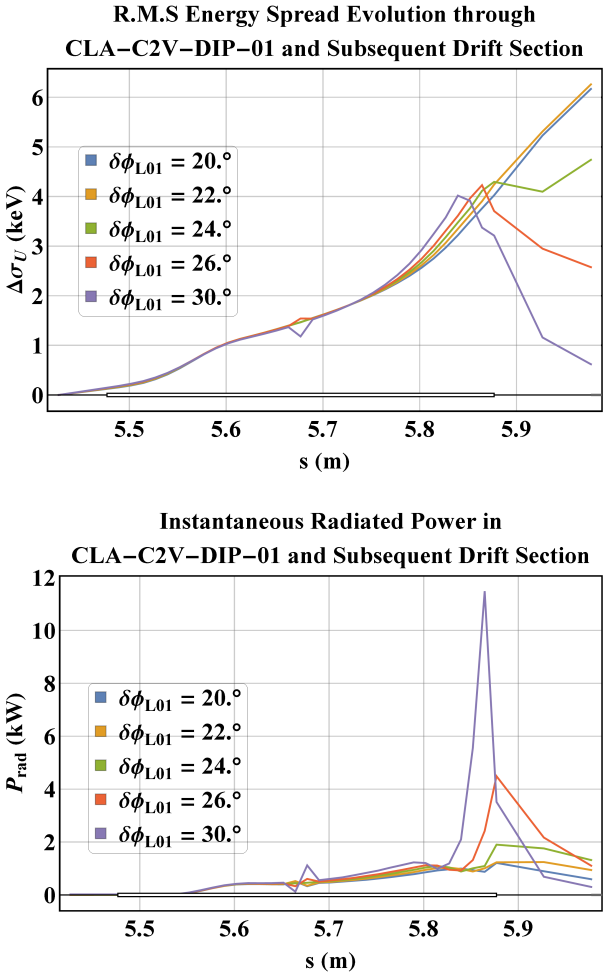

Figure 4.21: Radiated power and energy spread gain through CLA-C2V-DIP-01 and into subsequent drift section. Data shown corresponds to optics matched to minimise β_x at C2V-DIA-SCR-01.

the 1-dimensional case when the Derbenev criterion (Equation 2.65) is violated (Figure 4.22). This effect is especially pronounced due to the relatively small bending radii of the CLARA C2V dipoles. This is a clear demonstration that the GPT CSR model is capturing transverse effects that would otherwise be ignored in the 1-dimensional limit.

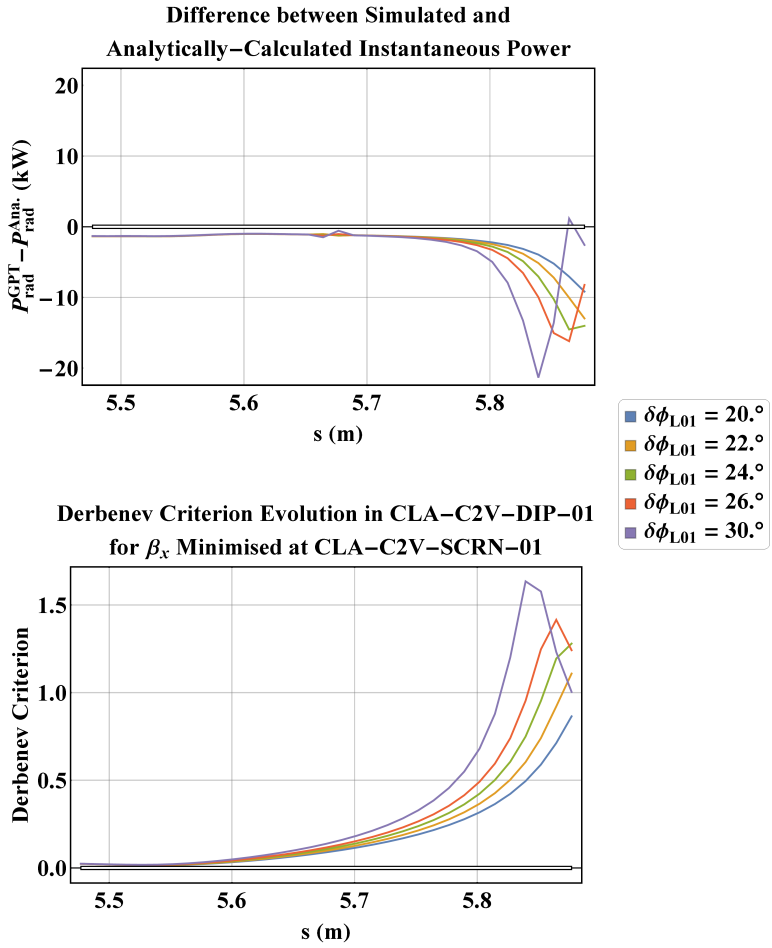

Figure 4.22: Difference between instantaneous powers derived from GPT Simulations and analytical calculations (Equation 2.56) alongside the evolution of the Derbenev parameter.

Analysis of the beam LPS after the dipole exit shows a smearing of the energy redistribution attributable to CSR (Figure 4.23). This arises from the non-zero dispersion within the electron beam introducing a correlation between a particle's horizontal offset and its energy deviation; particles at the extrema experience the most relative longitudinal motion during compression. Because of the slicing mechanism within GPT, this corresponds to particles at large transverse offsets having moved between many slices during tracking, and so experienced a

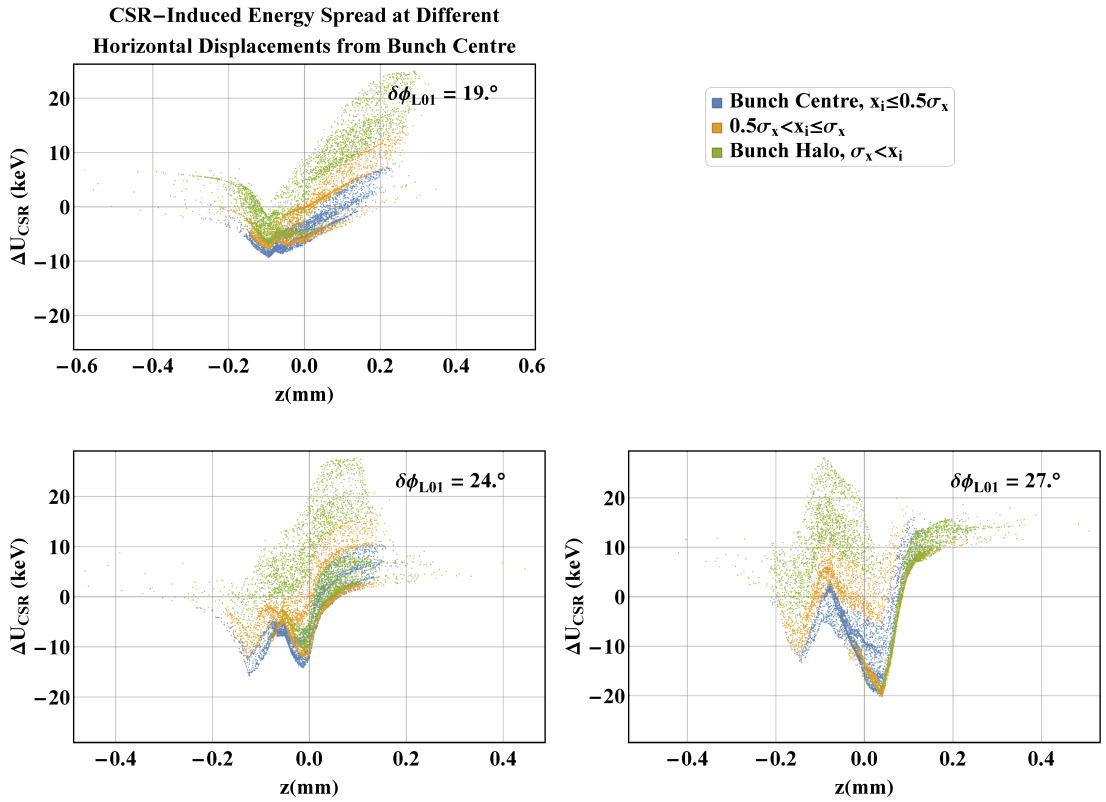

Figure 4.23: CSR-induced component of energy-spread 5 cm from the dipole exit, calculated from the difference between individual particle energies in simulations with and without CSR enabled. Particles within different regions of the horizontal beam profile are shown in different colours for clarity. The smearing of the energy redistribution is attributable to the dispersion within the bunch.

large variation in the strength of the CSR wake. Despite the clear presence of a CSR-induced component within the beam's LPS, it must be stressed that this contribution is dwarfed by the chirp imparted by the linac necessary for bunch compression (Figure 4.24). This is the predominant obstacle when approaching this type of measurement scheme, and renders the method unusable for detection of CSR in the context of CLARA Phase 1.

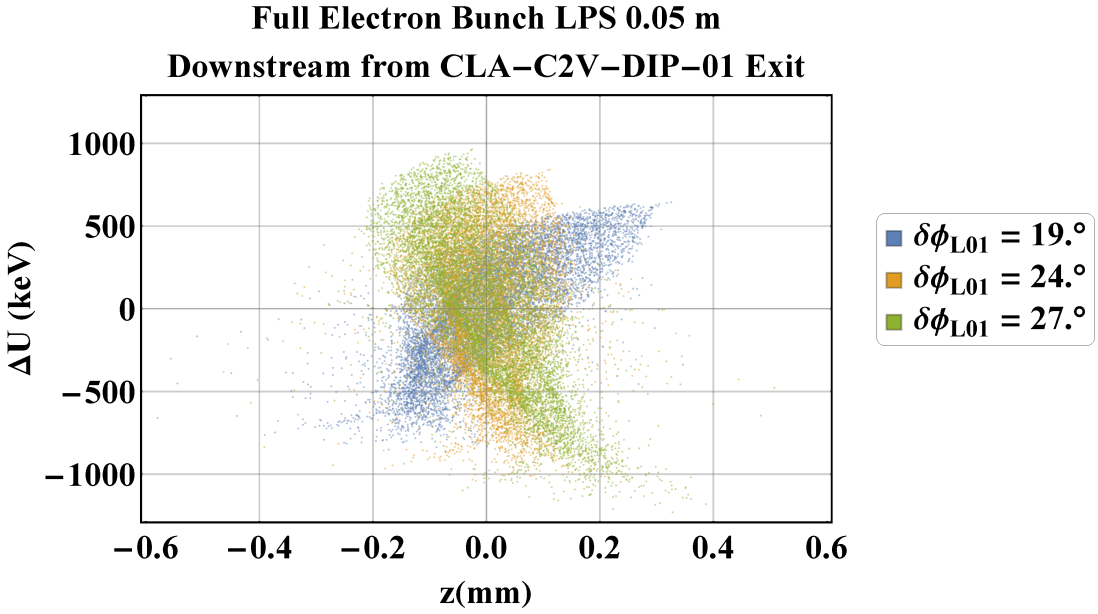

Figure 4.24: Complete LPS of the electron bunch, including energy spectrum due to space charge and the linac-1 phase offset. The combined energy deviations are up to 2 orders of magnitude greater than those attributable to CSR alone.

4.2.3 Conclusions

It has been shown that a beam-based method for the detection of CSR is not viable on the CLARA Phase 1 beamline (Figure 4.19). There are several hindrances to the experimental method when applied to the CLARA Phase 1 beamline. The magnitude of the energy spread induced is very small due to the relative small distances over which the electrons radiate, making detection of its contribution to the transverse size at a dispersive screen unlikely when machine jitter and screen resolution are taken into account. This is compounded by the fact that the dispersive compression method relies on a correlated energy spread imparted by the off-crest linac field. This energy spread is typically 2 orders of magnitude larger than the energy spread induced by the coherent interaction, making any observed changes with respect to linac phase almost wholly attributable to the

linac off-crest phase itself. Another issue arises from the significant variation of the electron bunch length along the trajectory within the C2V dipole. This leads to a discrepancy between the observed maximal energy-spread gain phase and the maximum compression phase, which is complicated further by the effects of the transverse size on the radiative interaction.

Of note from a simulation standpoint is the observed continued variation of the beam energy spread after the bunch has fully exited the bending magnet field (Figure 4.21). For over-compressed bunches, the energy spread induced by the CSR interaction is shown to decrease, implying that bunch compressing beamlines and optics could be designed with the view to completely or partially cancelling out the effects of CSR. This corresponds to observation reported by Brynes *et al.* in [88], wherein the inclusion of the Coulomb term in the Liènard-Wiechert fields used in GPT served to provide this cancellation of the exit transient field. GPT simulations were also shown to predict deviations from the analytically-calculated instantaneous radiated power in regions where the electron bunch violates the Derbenev criterion, demonstrating that effects due to the transverse bunch size can be incorporated by simply employing off-axis sources in the sub-bunch method used in GPT's CSR model. Finally, a smearing of the CSR-induced energy spread has been observed in simulations. This is believed to be attributable to the large variation of the relative longitudinal position of particles with large momentum deviations, and may be a source of additional uncorrelated energy spread not accounted for within bunch compression systems.

Should a beam-based approach be pursued at a later juncture of the CLARA project installation, the best candidate for such a study would be the ultra-short

velocity-bunched regime. This would allow for the bunch to be very strongly compressed and then for the bunch length to be "frozen-in" by subsequent accelerating structures. Although the lower charge required for this operating mode would inhibit the interaction considerably, the short bunch lengths achieved would go some way to mitigating this. Detection would either occur on the screen midway through the planned VBC, exploiting the non-zero first-order dispersion, or on a screen downstream from the VBC, which would require a residual second-order dispersion component. In pursuing this experimental method, it would be necessary to ensure that the energy spread due to the linac-1 crossing phase be compensated by the accelerating fields of linac-2 and linac-3. This would solve multiple issues: eliminating the large energy-spread produced by the off-crest linac field, and maintaining close to constant bunch length throughout the VBC dipoles.

4.3 Photonic Detection Method at CLARA

With a beam-based detection scheme ruled out for the CLARA Phase 1 beamline, an alternative method for the detection of coherent radiation must be developed in order to produce quantitative comparison to the CSR model employed in GPT. Such a study would provide confidence in some of the beam-based effects observed in simulations of the beam-based detection method. While the energy spread induced due to CSR is too small to be inferred from the transverse bunch distribution, the emitted radiation of the whole bunch should be measurable using an appropriate detector, owing in part to the short bunch lengths achievable. The VELA beamline section of CLARA Phase 1 is terminated by a dedicated experimental area, Beam Area 1 (BA1). This section of the beamline

Figure 4.25: Beam Area 1. This experimental area is separated from the rest of the VELA beamline by a 2 m shield wall (back of photo).

can be isolated from the rest of CLARA/VELA by a shutter, which combined with radiation shielding allows for manual work to be carried out whilst VELA is operational (Figure 4.25).

BA1 consists of: a user experimental area hereafter referred to as the "Coffin", which acts as general-purpose testing area for accelerator technologies; a dipole and spectrometer line, terminated with a Faraday cup; and two quadrupole triplets either side of the Coffin, allowing for fine control of the electron beam optics within the Coffin and the spectrometer (Figure 4.26). The BA1 spectrometer dipole (BA1-DIP-01) has three ports available, two of which are potentially viable candidates for the extraction of emitted CSR (Figure 4.27). These ports are positioned tangential to the beam trajectory at the dipole entrance (Port A)

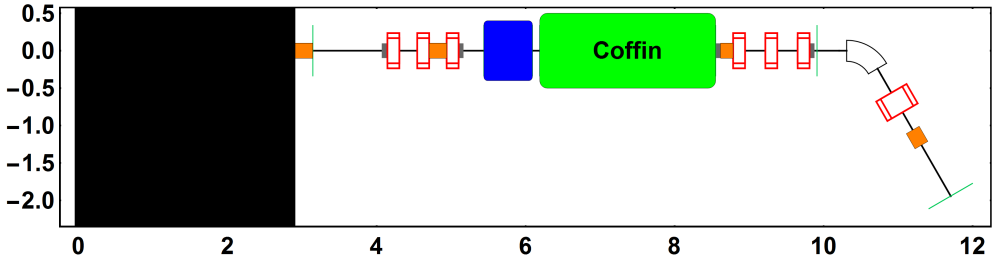

Figure 4.26: Schematic diagram of BA1, including the 2 m shield wall shown in black, with key beamline elements included. Quadrupoles in red, corrector magnets in grey, dipole in white, laser box in blue, and general experimental area in green (labelled "Coffin"). Beam position monitors (BPMs) are shown in orange, and YAG screen positions shown in green. There are three additional YAG screens inside the Coffin.

and at half of the dipole bend angle (Port B).

A YAG screen precedes BA1-DIP-01, allowing for the transverse bunch profile to be measured close to the dipole entrance. This makes Port A a more favourable option than Port B in terms of effective monitoring and control of the transverse properties of the bunch for the portion of its trajectory at which detection of emitted CSR will occur. Alongside this, a CTR detection system located in the Coffin will allow for simultaneous monitoring of the relative compression achieved over the C2V dogleg. As the bunch length will vary due to dispersion in the BA1 dipole, this will not prove as effective a method for determining the bunch length at Port B. However, it is likely that the emitted power at Port A will be considerably lower than at Port B due to the observable trajectory length being low compared to the formation length of the CSR wake; a significant portion of the relevant section of the bunch's trajectory corresponds to only part of the bunch radiating. GPT simulations will be used to inform which port should be used.

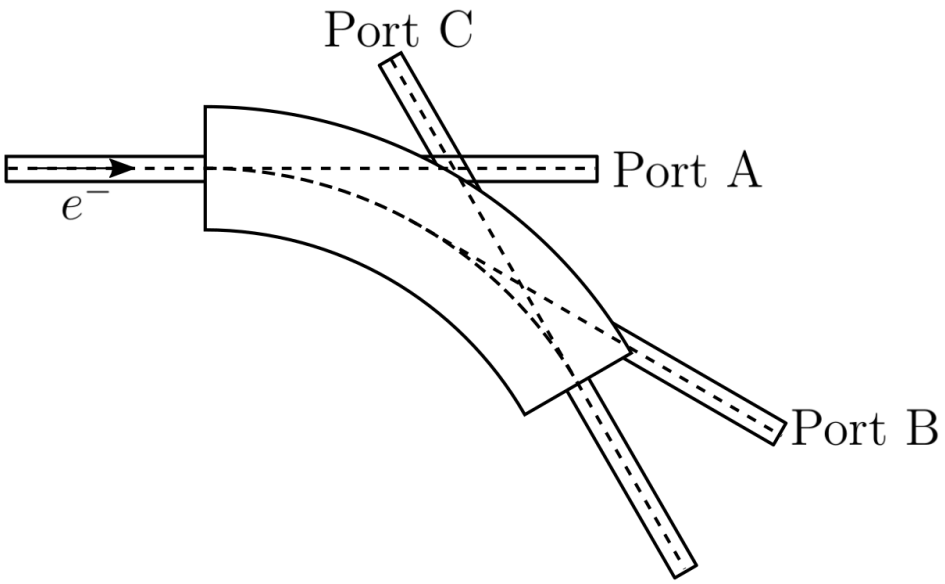

Figure 4.27: The BA1 dipole and its three ports. Port C is clearly not suitable for measurement of coherent radiation, whereas both Port A and Port B are to be investigated as candidate experimental locations.

The study will focus upon verifying the capabilities of GPT CSR in modelling coherent radiation in both a regime where only the longitudinal dimensions of the bunch affect the form of emitted CSR, and in the case where the transverse extent of the bunch plays a significant role in the final emitted CSR power. The former of these involves two areas of investigation: one in which the bunch charge will be varied whilst maintaining the spatial properties of the bunch, and a second which makes use of the linac-1 phase offset to control the bunch length (as detailed in the previous section).

The former of these will entail variation of the photocathode laser attenuation whilst keeping the bunch at a constant length and transverse size. It would be advisable to maintain the bunch close to maximal compression for this study, with the transverse size of the bunch kept small enough so as to satisfy the Derbenev

criterion. A variation in the observed CSR power (inferred from the voltage induced on the PED) which is quadratic with respect to bunch charge is expected, and will serve as confirmation of the observation of coherent radiation.

Following the scan of the bunch charge, the variation of the radiated power with respect to bunch length will be measured. This will again be facilitated through variation of the linac-1 phase offset, as described in the previous section. It is desirable that the electron bunch's transverse dimensions be kept small enough, once again to satisfy the Derbenev criterion. This can only be experimentally assessed reliably if Port A proves to be an appropriate measurement location, and would be carried out using BA1-YAG-02. If Port B proves to be the only viable location for the experiment, then it will be necessary to infer the transverse size using measurement from both BA1-YAG-02 and BA1-YAG-03 as well as simulations.

The final section of the study will focus explicitly on testing the capability of GPT to model the effects of the bunch's transverse distribution on the CSR interaction. By varying the strengths of the quadrupoles in the second triplet in BA1, the beam size at the BA1 dipole can be varied while keeping the bunch length at the measurement location constant. This section of the study becomes more complex if Port B is to be used for extraction of CSR, as transverse beam optics will, once again, have to be inferred from the upstream and downstream YAG screens. Furthermore, a large aspect ratio bunch may give rise to a large R_{51} coupling in the dipole, resulting in additional changes to the bunch length alongside those due to the R_{56} coupling. Care must be taken to avoid this in order to avoid changes to the bunch length independent of the injector linac

phase. Further care must be taken to minimise beam losses in the beam pipe due to large transverse dimensions, as this will further skew measurements of the beam's CSR emission. Measurements of the bunch charge can be made in the Faraday cup terminating the BA1 beamline to monitor such losses.

4.3.1 Equipment

CSR emission in the CLARA Phase 1 beamline is expected to peak in the THz region, due to r.m.s bunch lengths on the order of $\sim$0.1 ps expected close to maximal compression. This motivates the use of pyroelectric detectors (PEDs), which possess both the broad frequency response and high sensitivity required for this study. There are two PEDs currently available at Daresbury Laboratory, one of which will be in use for the aforementioned CTR detection system. As such, spectral measurements of the radiation will not be possible given the requirement for two detectors in order to carry out interferometry. Instead, only the radiation power can be measured. This limits the degree at which CSR could be used to characterise the current profile of an electron bunch beyond a rough measurement of the r.m.s bunch length. Any such inferences of the r.m.s bunch length must also make broad assumptions of the nature of the current profile.

Due to competitiveness for beam exploitation time at CLARA Phase 1, it was imperative that this study be simple to carry out in terms of set-up and alignment of equipment, should the allocated time for the experiment be short. It is also important to minimise the cost of the study by making use of materials already available at Daresbury. Only Port A is suitable for proper alignment of the detector system with the beam axis, given its clear line of sight to the coffin where an alignment laser may be positioned. As such, it is proposed that

the PED be mounted on an x-y translation stage so as to minimise alignment requirements should Port B be chosen as the detector location. This will also allow for the angular distribution of the radiation to be imaged. Should this be the case, the only alignment required is that the detector is perpendicular to the port axis, which will be done by-eye should Port B be selected. The stage will be mounted on an optics breadboard, which in turn will be clamped to the dipole girder section (Figure 4.28).

Measurements will be taken in a shot-to-shot manner at 10 Hz. As such, machine jitters may become a significant factor affecting the transverse displacement of the bunch at the relevant emission point. This will in turn affect the shot-to-shot power received by the detector, and may result in the radiation signal disappearing completely on some shots. To account for this, a Winston cone may be mounted to the PED face should the observed signal level be too low. This is a non-imaging collector which serves to increase the effective detector area, reducing the effect of the beam's centroid jitter.

A polyethylene polariser in a rotatable mount can be positioned between the PED and the dipole port, allowing the two orthogonal polarisation modes to be measured independently. Such a measurement would be useful solely to confirm the presence of CSR. If centroid jitters at the emission point are deemed to be sufficiently small, there is a potential to measure some of the angular dependence of the radiation.

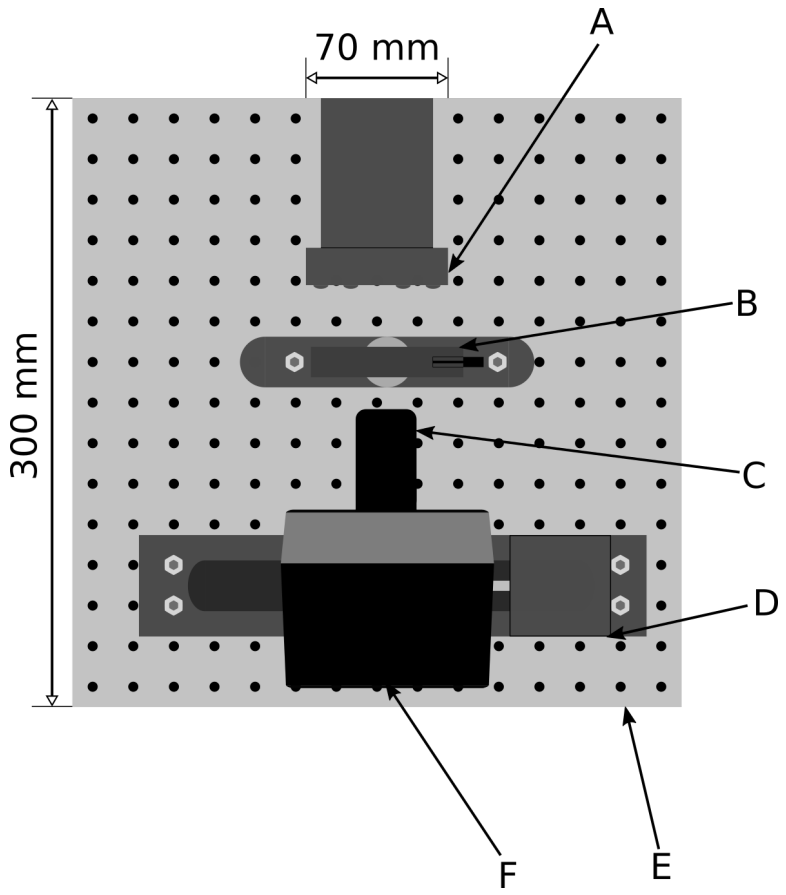

Figure 4.28: Diagram of proposed apparatus: A. port/window; B. rotatable polariser; C. Winston cone; D. x-y translation stage; E. optical breadboard; F. pyroelectric detector.4

Pyroelectric Detectors

PEDs detect voltages induced in a crystal structure as a result of pyroelectricity. Pyroelectricity is somewhat analogous to piezoelectricity, wherein mechanical energy imparted upon a crystal results in changes to the lattice polarisation. However, in pyroelectric crystals it is thermal changes to the crystal which bring about a build-up of surface charge [85], making them ideal for detecting IR radiation. Despite this distinction, all pyroelectric materials are also piezoelectric, and so non-thermal sources of work are also detectable with PEDs. It follows that acoustic sources, such as vacuum pumps, can be major contributors to the

noise detected by the PED.

The polarisation of a pyroelectric crystal is related to the temperature distribution across the lattice. The polarisation of the crystal lattice naturally equilibrates after a characteristic time under constant conditions. As such, a PED signal only measures changes to the incident energy upon the detector surface rather than absolute values. A proper calibration of a PED requires specification of several signal characteristics, namely:

- signal frequency
- signal amplitude
- signal rise-time
- pulse repetition rate and duty cycle

It follows that PEDs can be easily calibrated at optical frequencies (a calibration at a single optical frequency and duty cycle is provided by the vendor, Gentec-eo) using a coherent optical source, but doing so in the THz-region requires a reliable THz-source of known energy and ideally tunable frequency. Furthermore, calibration for duty-cycles comparable to those that would be seen in this experiment (i.e. pseudo-instantaneous pulsed operation) is not possible using table-top sources. Therefore a full calibration cannot be done at the frequencies in question for this experiment; instead of absolute power measurements, ratios of the emitted CSR power against a nominal case will be taken.

4.3.2 Data Acquisition and Conditioning

The PED will be connected to a 400 kHz (aggregate) National Instruments DAQ via a BNC connection. This DAQ is connected to a PC in BA1, positioned below the beam plane to ensure there is no radiation damage. The parameter of interest for this study is the peak voltage (V_{pk}) of the detector signal, which will be taken as a ratio to a "nominal" case. The strength of the source signal, the detector response and the stability of the signal will dictate the time taken for a given acquisition, and this is the dominant time constraint for data acquisition, not including the machine set-up. For each machine setting in the study a scan of the radiation distribution in the vertical opening angle will be carried out, allowing for comparison to the theoretical distribution assumed in the analysis of simulation results.

The detector signal is conditioned using a LabVIEW VI developed in-house at Daresbury Laboratory. The individual shot-to-shot signal may vary significantly, especially in the presence of a weak source strength and large jitters in the beam's position. In order to account for this, each acquisition of the peak-to-peak voltage (V_{Pk}) consists of measurements taken over multiple shots. A low-pass filter is applied to the signal to remove high frequency noise. In order to further reduce the noise, the background acoustic level may be sampled with a second PED placed in close proximity to the active detector. Subtraction of the signals in this manner is very effective, and has been shown to lower the NEP down to sub-nJ level in tests carried out in BA1 using a chopped optical signal, continuously variable neutral-density filter wheel and optical power meter. Due to requirement of the second PED, this noise subtraction cannot be carried out at the same as CTR measurements, which take place $\sim$2 m away from the

detection location. As such, it is advisable to initially characterise a phase scan using the CTR target, before repositioning the second PED for noise subtraction.

A rolling average of the signal for each acquisition is built shot-by-shot for between 50-100 shots, with the V_{Pk} recorded for each shot along with an associated weighting. The V_{Pk} measurement requires a baseline voltage level to be defined. A user-defined offset, related to the signal rise-time, dictates where behind the peak voltage the baseline calculation will begin. A second parameter defines the number of shots used for the averaging calculation. The acquisition continues until the standard deviation of the measured average peak-to-peak voltage is below a user-specified level.

4.3.3 Simulations

Beam Dynamics: Methodology and Optics Matching

Full start-to-end simulation of the CLARA Phase 1 beamline are carried out in GPT. The results of the injector optimisation described previously are used (Section 4.1), with the injector parameters the same as described in Table 4.2. A broad scan of the phase offset applied to linac-1 is carried out, with the electron bunch tracked to the BA1 dipole. As with the phase scan described in Section 4.2.2, the beam momentum is kept constant throughout the phase scan by scaling of the accelerating field. Using the broad scan of the linac phase, an appropriate region of the parameter space is defined corresponding to phases close to the phase of maximum compression at either the BA1 dipole entrance, or the BA1 dipole centre. The injector is then re-simulated around this more focused scan

range.

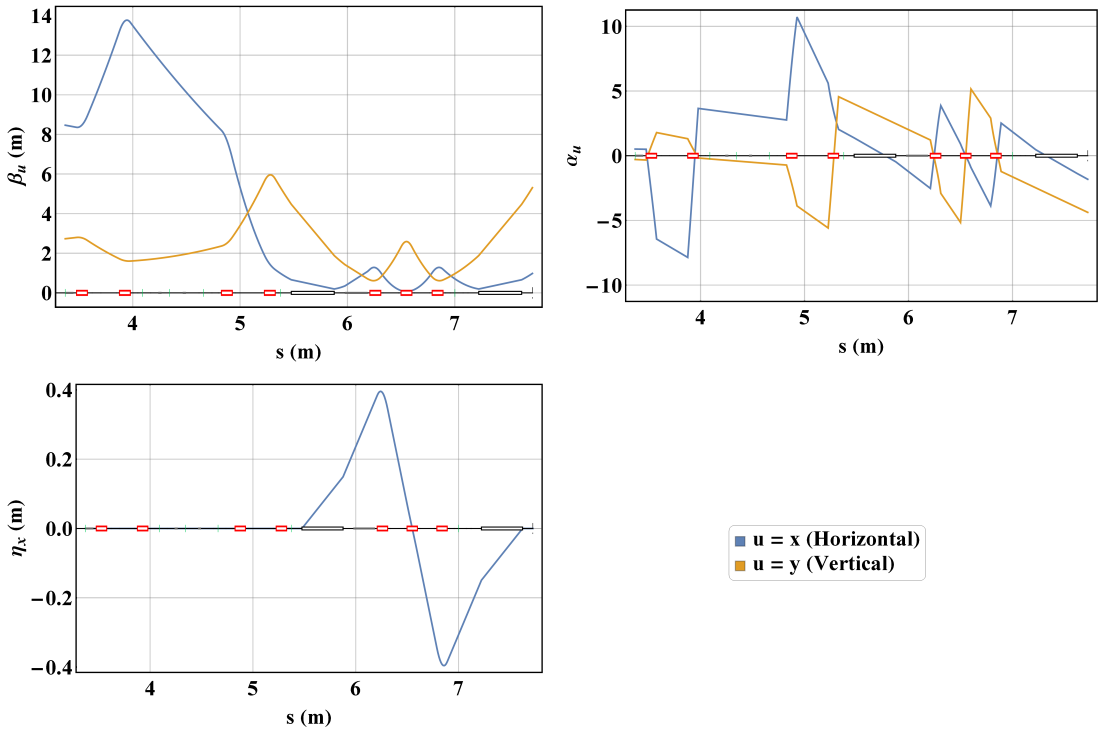

Figure 4.29: Dispersion-minimising optics for the C2V dogleg and preceding beamline section (S02) as matched in tracked in `elegant`. The 1st and 2nd-order dispersion are minimised at the dogleg exit, with the former carried out using the central triplet of the dogleg, and the latter using the preceding S02 quadrupoles to symmetrise the transverse lattice functions across the structure. Due to a lack of 2nd-order optics on the dogleg, the 2nd-order dispersion cannot be eliminated completely.

In order to deliver electron beams along the VELA beamline to BA1, the residual dispersion at the exit of the C2V dogleg must be minimised. This matching is carried out in `elegant`, by first closing the 1st-order dispersion with the dogleg triplet, and subsequently adjusting the S02 quadrupoles (positioned in a "telescope" arrangement) to match the transverse β and α functions at the first dipole entrance (Figure 4.29). Due to the lack of sextupole optics on the C2V dogleg, there is a significant amount of residual 2nd-order dispersion at the dogleg (∼5 m,

Figure 4.30). While this cannot be negated given the CLARA Phase 1 lattice, it can be mitigated by ensuring the transverse lattice functions are symmetric across the dogleg structure.

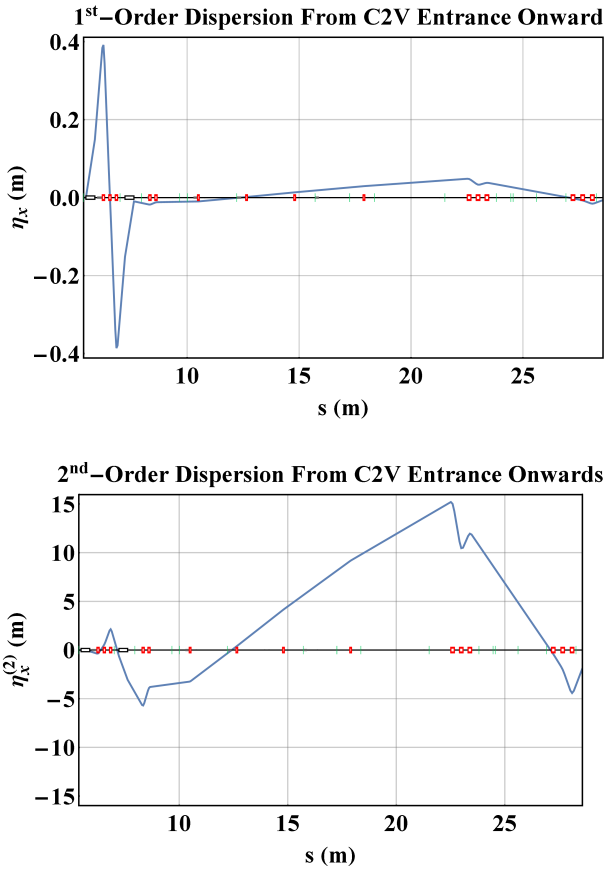

Figure 4.30: Evolution of 1st and 2nd-order residual dispersion functions along VELA-EBT. The residual 2nd-order dispersion drives emittance growth along the VELA beamline.

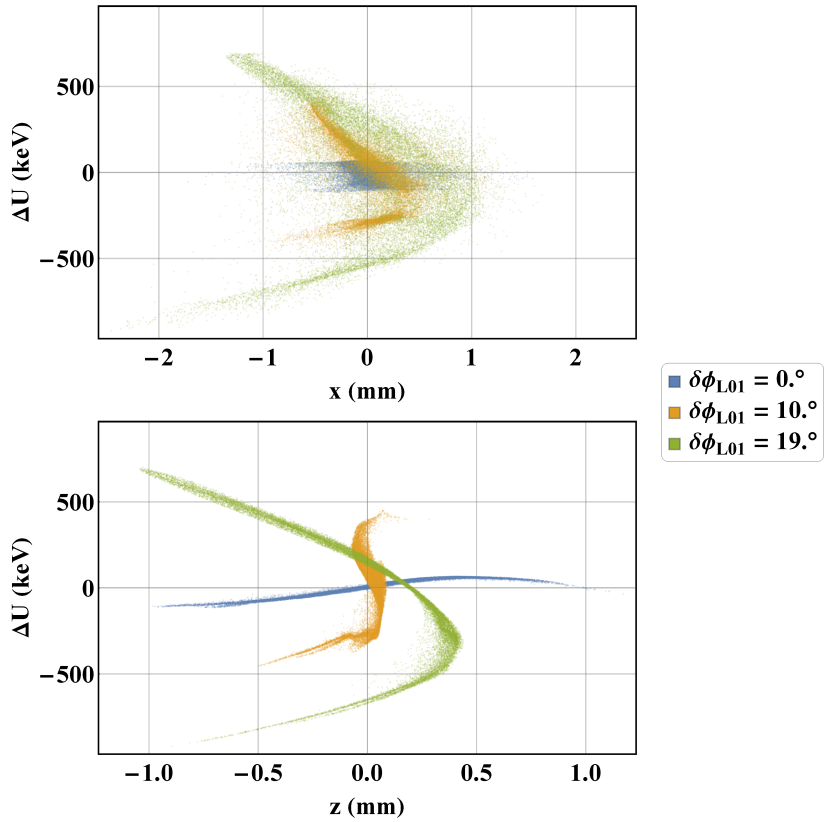

Figure 4.31: x-δ and z-δ phase space at the C2V dogleg exit for several simulated bunches. Clear quadratic correlations can be seen in the x-δ plane, arising from residual 2$^{\text{nd}}$-dispersion.

When using the `elegant`-matched optics in GPT simulations, deviations from the ideal match occur, primarily due to fringe field effects not incorporated into the `elegant` model. This can be seen in the residual 1$^{\text{st}}$-order dispersion present in GPT simulations. The effect of this residual component is small compared to the residual second order dispersion, with the relative contribution to the beam size due to the 1$^{\text{st}}$-order dispersion at most 10% that of the 2$^{\text{nd}}$-order contribution downstream from the C2V dogleg exit.

The residual 2$^{\text{nd}}$-order dispersion of the C2V dogleg (Figure 4.30) results in a 2nd-order correlation in the x-δ phase space at the dogleg exit (Figure 4.31).

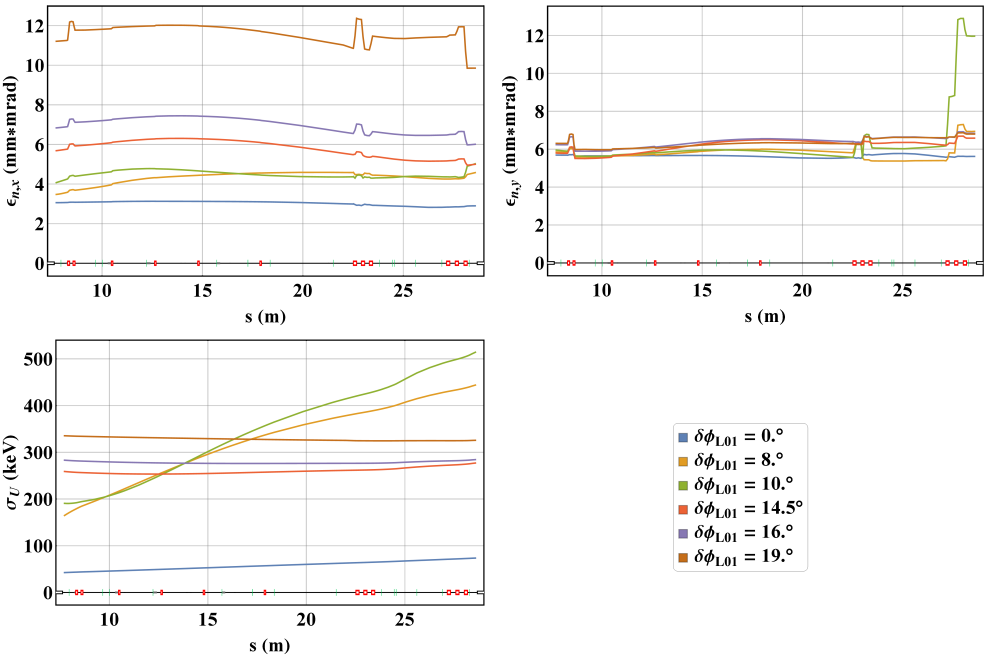

Figure 4.32: R.M.S normalised transverse emittance and energy spread evolution along the VELA beamline following compression in the C2V dogleg. The maximum compression phase lies around $\delta\phi_{L01} = 10°$, as such, the energy spread growth along the VELA beamline is greatest at this phase. The residual 2$^{\text{nd}}$-order dispersion present in the bunch drives projected emittance changes at the quadrupoles, though this is technically reversible due to it being rooted in a correlated phase space as evidenced by both reduction and growth in the emittance. The magnitude of the shifts are both dependent upon the beam energy spread and the quadrupole focusing strength (Figure 4.33).

This dispersion continues to evolve along the length of the beamline. In the case of beams with a large energy spread, such as those accelerated far from the crest phase of linac-1, this correlation results in significant changes to the projected emittance in the downstream quadrupoles (Figure 4.32). Energy spread increases along the dogleg, driven predominantly by longitudinal space charge at short bunch lengths, further increase the heating of the beam. Such an emittance growth is expected to suppress the CSR interaction, and while this effect is

captured within simulation, the degree to which this emittance growth is properly calculated is a potential source of discrepancy between simulations and experimental results. This emittance growth drives increases in the overall beam size as it propagates through the CLARA beamline, and as such relatively large quadrupole fields are required to constrain the beam size (Figure 4.33).

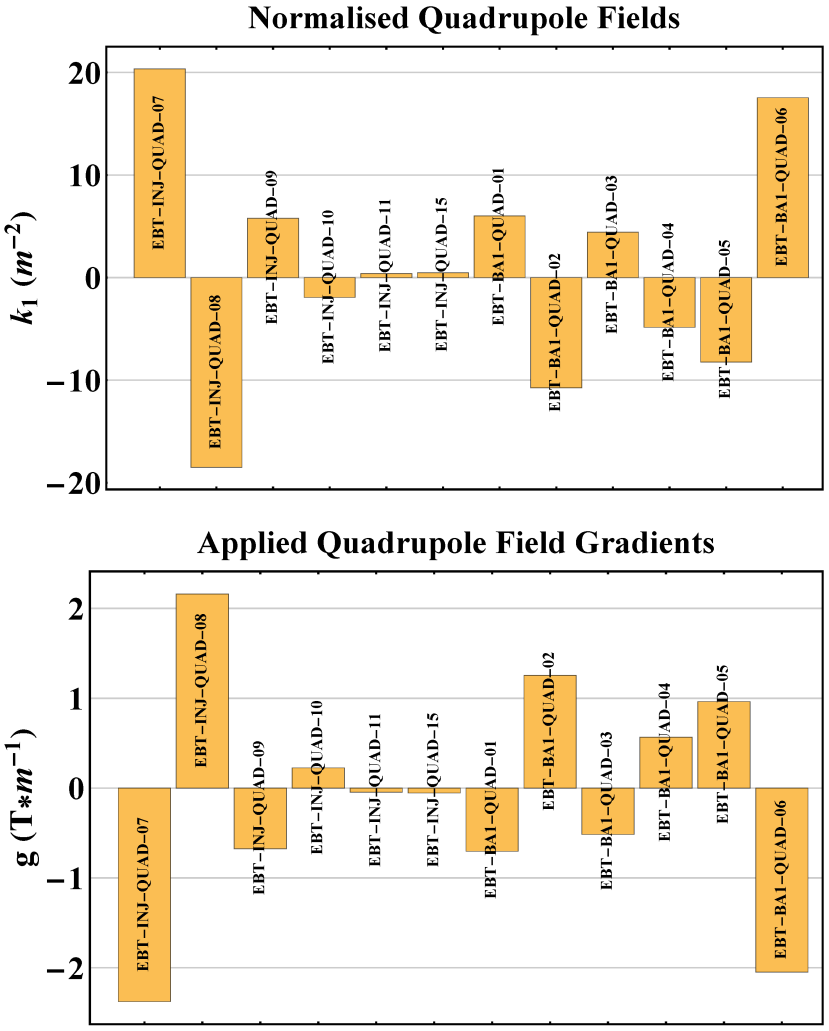

Figure 4.33: Matched quadrupole optics for the VELA-EBT.

Alongside maintaining the transverse beam dimensions it is necessary to focus the beam at the BA1 dipole entrance, to prevent elongation of the electron bunch due to the geometric R_{51} coupling. Furthermore, it is necessary to maintain the beam size to be sufficiently small at the radiating point (Figure 4.34). This is important for the bunch length scan as it will allow the Derbenev parameter to be kept small enough to test the 1-dimensional capabilities of the CSR model.

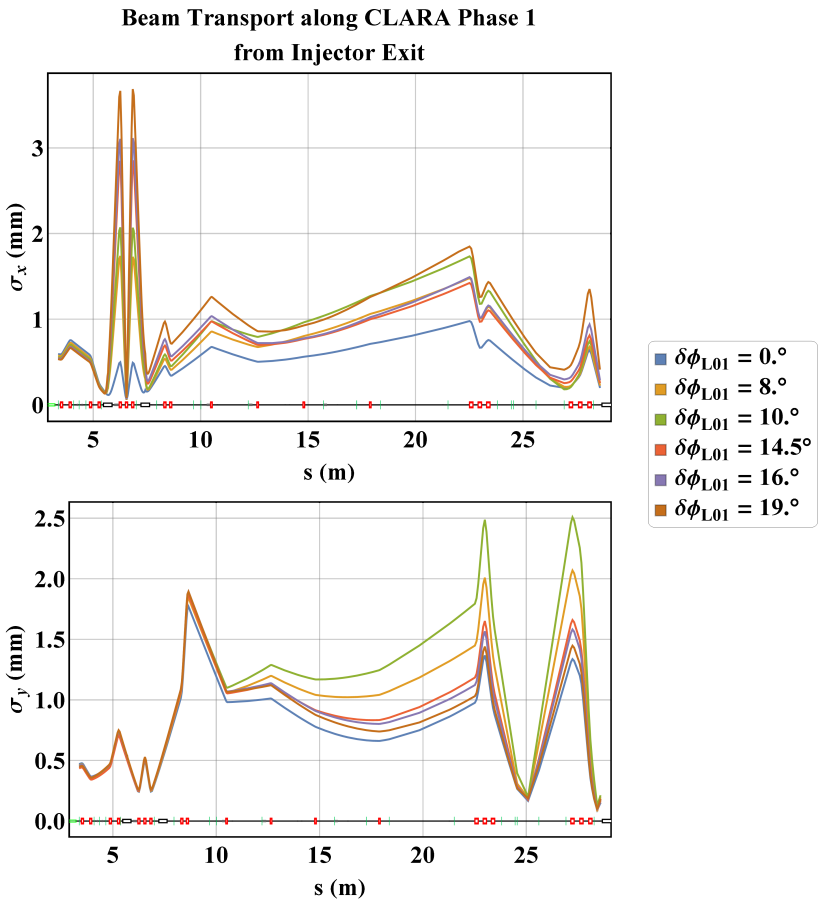

Figure 4.34: Beam transport from linac-1 exit to BA1. Beam sizes are constrained to ensure that the beam's transverse dimensions are sufficiently small to be within a 1-dimensional CSR regime. The beam is matched to be at a focus at the centre of the BA1 dipole, where radiation directed towards Port B is emitted.

It is expected that there will be continued interaction between the electron bunch and radiation emitted at the exit of the final dipole of the C2V dogleg along a considerable proportion of the EBT-S02 beamline. A continuation of the energy redistribution demonstrated in the Section 4.2.2 is expected, however it is unlikely that this will lead to a detectable increase in the beam energy spread given the many orders of magnitude difference between the LPS chirp and the CSR-induced energy spread previously observed. Given the length of the VELA beamline, simulation of this process is very computationally intensive when using 10^6 macroparticles; as stated previously in Section 3.1.5, inclusion of the Coulomb term means that CSR in enabled and calculated throughout the simulation, which results in a recursive reduction of the simulation time step when encountering fringe fields of quadrupoles. With time steps as small as 0.1 fs being used by the Runge-Kutta integrator, this leads to a simulation that is so computationally intensive that it becomes unfeasible. As such, the beamline is separated into four sections simulated separately: the injector, the C2V dogleg, the VELA beamline and BA1, and the BA1 spectrometer dipole. Only the C2V dogleg and the BA1 dipole are simulated with CSR enabled, but in all sections space charge calculations are included. The radiation emitted from the C2V dipole exit is expected to interfere with radiation generated at the BA1 dipole entrance, and the omission of this effect in simulations makes the use of Port B more desirable from an accuracy standpoint.

As stated in Section 3.1.5, it is possible to use either 4 or 16 off-axis emission points for the calculation of CSR in GPT. It is advised to use both, as significant discrepancy is an indicator that the CSR model of GPT is insufficiently capturing the effects of the transverse distribution and is thus not an appropriate model.

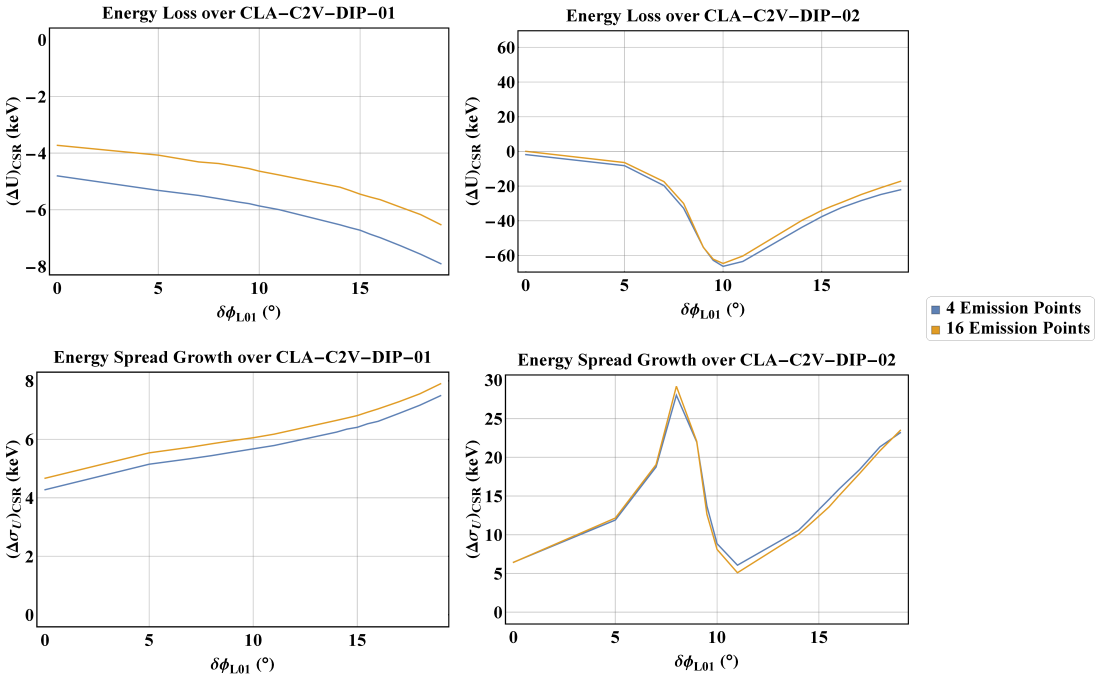

Figure 4.35: Comparison between 4 and 16 source points used for CSR modelling in GPT simulations. Good agreement is seen between the two cases, with the largest relative discrepancy seen in the energy loss over the first C2V dogleg dipole. However, the size of the energy loss observed over the magnet is, in general, small, and so the discrepancy can be deemed inconsequential in the larger scope of full start-to-end simulations.

If little difference is observed, 4 emission points are recommended. This comparison is carried out for the C2V dogleg, which shows that the GPT CSR model is viable for modelling this portion of the CLARA Phase 1 beamline (Figure 4.35).

A second scan will be carried out alongside the linac-1 phase scan; in order to test the capabilities of GPT outside of the 1-dimensional limit, it is necessary to control the transverse size of the electron bunch while keeping the bunch length constant. In the case where Port A is used for THz detection, this is a simple case of adjusting the beam size at the dipole entrance, although the effect of the

transverse size upon the radiation emitted from the dipole edge is expected to be small compared to the effect on the steady-state wake. Coherence in this regime is dominated by the wavelength of the radiation emitted rather than geometric effects like in the case of the Derbenev condition. The 1-dimensional limit for coherent radiation emitted from the dipole fringe can be expressed as [92, 149]

$$\sigma_r \ll \gamma\sigma_z. \tag{4.8}$$

This condition can be rationalised by considering that, in the laboratory frame, each particle's individual field has an opening angle of $1/\gamma$. In order for a 1-dimensional model to be applicable, the majority of the electron bunch should fall within this radiation cone. The overtaking length in the laboratory frame, L_O, for a distance equivalent to the r.m.s bunch length is given by

$$L_O = \frac{\sigma_z}{1-\beta} \approx 2\gamma^2\sigma_z,$$

where the ultra-relativistic approximation has been made. As $\sigma_x/L_O < \gamma^{-1}$ for a 1-dimensional approximation, it follows that the condition on the bunch dimensions for this regime is given by equation 4.8. When applied to the CLARA beam, it is expected that the dipole fringe radiation will only capture transverse effects for transverse sizes on the order of σ $\sim$1 mm. Measurement at Port B requires the electron bunch transverse size to be small at the dipole entrance to avoid elongation of the bunch due to geometric R_{51} coupling (Equation 4.3). The bunch must then experience rapid transverse expansion while within the dipole, requiring a very sharp peak in the β function to occur just prior to the dipole. This is achieved through variation of both quadrupole triplets within GPT. When tracking in GPT, the removal of particles at large transverse offset

results in significant erosion of the bunch charge within quadrupole fields (Figure 4.36). As such, the electron bunch is tracked in `elegant` along the VELA beamline to avoid large losses of charge in the beamline before being passed to GPT for CSR simulations through the BA1 dipole. The BA1 dipole will also experience similar issues regarding particle losses, though to a lesser extent as the beam is convergent at this location.

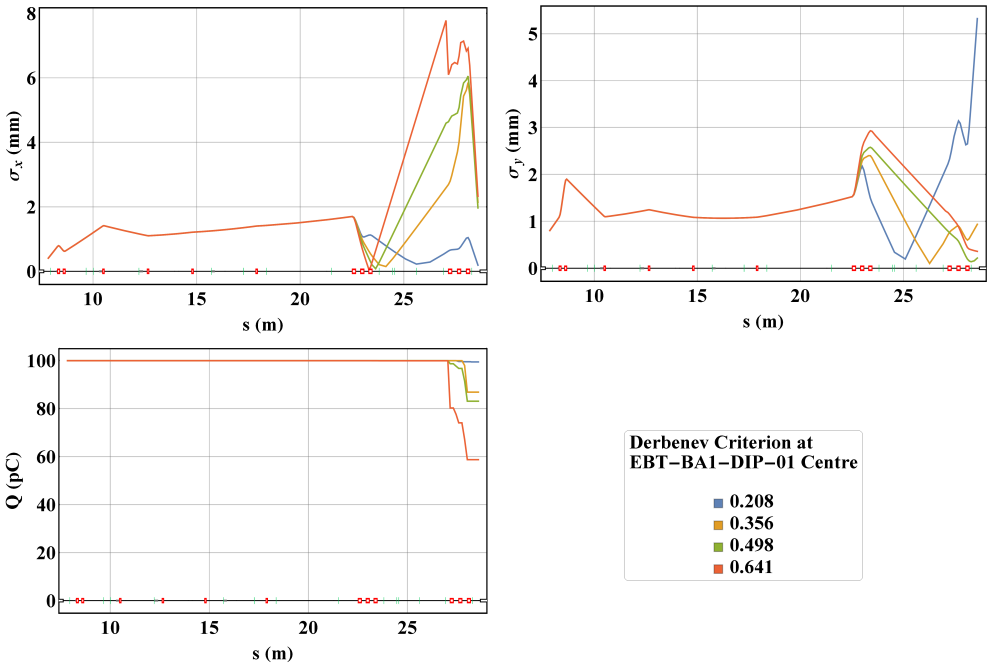

Figure 4.36: Charge loss in GPT due to large transverse beam size. Due to this, `elegant` is used to track the electron bunch from the C2V dogleg exit to 0.1 m upstream of the BA1 dipole entrance. The values shown in the legend correspond to the equivalent value of the Derbenev parameter achieved in `elegant` tracking.

While this method is achievable in simulations where the simulated electron bunch characteristics are visible along the whole beamline, the feasibility of the process may be limited in a real experiment where information about the electron bunch is limited to the available diagnostics. Without a direct method of

measuring the transverse beams size within the dipole, the measurement of lattice functions will need to be carried out either side of the dipole as well as measurements of the downstream dispersion on the BA1 spectrometer. This method will be time consuming, and still requires inference of the beam size at the dipole centre from measured beam distributions elsewhere. Furthermore, set-up of this experiment will likely be time-consuming; reliance on complex and unstable quadrupole optics (Figure 4.37) will require confidence in the modelling of the CLARA beamline in simulations, else excessive tweaking of machine optics will need to occur. Moreover, the erosion of the bunch charge due to large transverse beam size within the last triplet is likely in this method, and the measured CSR emission.

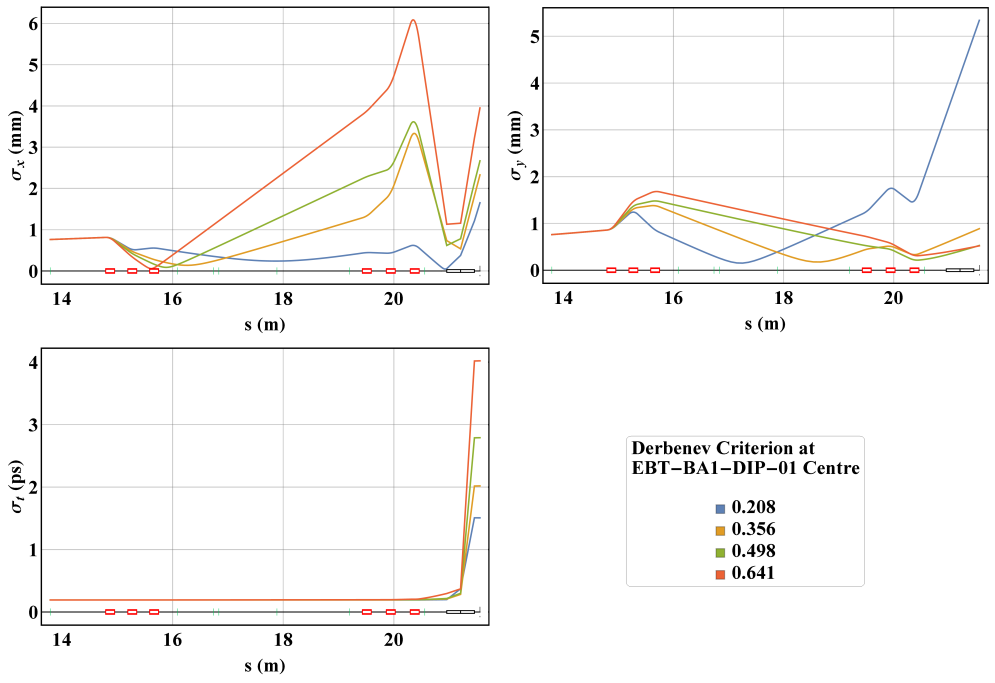

Figure 4.37: Matching of BA1 optics for the quadrupole scanning method. A unique match of the BA1 optics is generated for each value of the Derbenev parameter at the BA1 dipole centre.

Radiation Distribution

As was discussed in Section 3.1.5, the GPT CSR model only deals with the effects of CSR as experiences by the electrons in the beam. As such, the only information about the radiation itself that can be gleaned from GPT is the instantaneous radiated power of the bunch, which is inferred from the energy loss of the bunch centroid. In order to estimate the energy incident upon the PED, and thus the relative detector response, an estimation of the angular distribution is required. This is approached in two separate ways; a 3-dimensional analytical approach as described by Equation 2.67, and using the simulation code SPECTRA.

SPECTRA simulations are carried out using decoupled generalised distributions of the 3 orthogonal phase space planes, x-x', y-y', t-δ. While the SPECTRA algorithm does support simulations modelling the full 6-dimensional phase space through macroparticle distributions, these simulations were found to result in the SPECTRA solver becoming unstable. The use of un-coupled phase space planes will result in simulation errors, especially considering the radiation simulated from a point of non-zero dispersion in the beamline. The electron bunch distribution is considered rigid in SPECTRA simulations, and as such it is necessary to specify the distribution at the measurement location, to maximise the simulation accuracy for the given measurement point.

For each electron bunch simulated (i.e. each phase offset of L01 scanned), a scan of the angular coherent power distribution is generated in SPECTRA. In order to lessen the computational load of SPECTRA simulations, the angular-spectral distribution is not calculated; instead the total spatial power distribution

in the detector plane (approximated to be 40 cm from the radiation point) is calculated. In order to model the angular distribution, a scan over a grid of points in the detector plane is performed. The grid is defined such that it sufficiently captures the entire vertical distribution of the radiation with a resolution equivalent to the PED pixel size. The horizontal extent of the grid corresponds to an angular range within the bending plane equal to the angular separation of points between which the bunch energy loss is determined in GPT, equivalent to ±32.735 mrad.

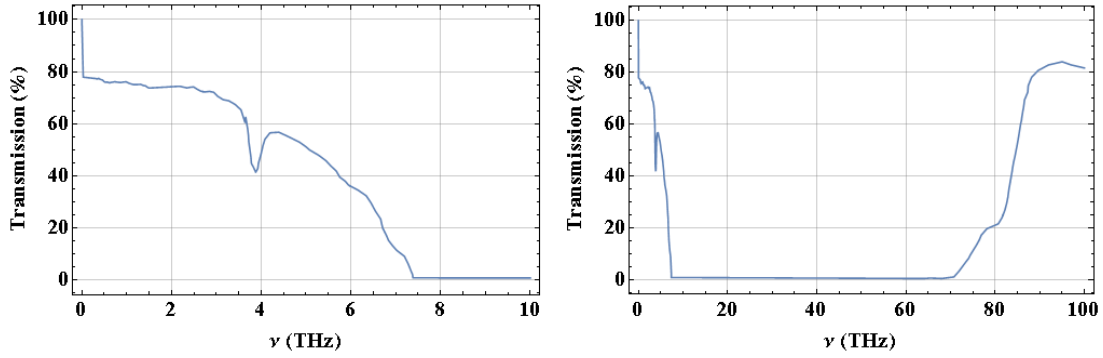

Figure 4.38: Transmission curve of Z-cut quartz provided to SPECTRA for radiation filtering in both the THz region and beyond into the visible range of the spectrum. Data corresponds to measurements with a 1 mm sample of crystal quartz, obtained from [150]. Including are added points for low-frequencies not included in the data used, in which the assumption that the transmission is exactly 100% at infinitely long wavelengths.

In order to determine the fraction of radiation that is transmitted through the Z-cut quartz view port, a custom filter is applied to account for the variation of the Z-cut quartz view port's transmission across the relevant range of frequencies. Data used for the filter is obtained from TYDEX [150] (Figure 4.38) corresponding to a Z-cut quartz window thickness of 1 mm, although this does not include data for frequencies lower than around 0.3 THz, which are still likely

to be relevant for this study. To enable the filter around these wavelengths, the transmission will need to extrapolated and interpolated, though the extrapolation must be restricted such that transmission coefficients >1 do not occur. While the thickness of the Z-cut quartz window will be greater than 1 mm this is not expected to have a significant impact upon the overall transmission, as reflection rather than absorption is the dominant source of in the reduction of the transmission.

In expanding this data set the assumption is made that a radiation of infinitely long wavelength, i.e. 0 eV photons, will be perfectly transmitted through the medium. Cubic spline interpolation with this assumption alone generates a rapid increase at frequencies below the minimum frequency present in the data, which is likely non-physical and may result in a large error in the transmitted power, especially in the case of long electron bunch lengths radiating predominantly in the lower part of the relevant spectrum. As such, a further assumption is made that in the region of the spectrum between to 0.03 THz and 0.3 THz the transmission of the Quartz window behaves similarly as it does in the region immediately around 0.3 THz (i.e. $d_{Win.} < \lambda < 10d_{Win.}$, where λ is the frequency and $d_{Win.}$ is the window thickness). This corresponds to a very slight increase centred around a transmission coefficient of $\sim$0.7. This is implemented by using a moving average to calculate over a 0.25 THz window the average gradient in the data. Using these assumptions, a cubic spline interpolation is performed over the data, which is then re-sampled in the missing data range and appended to the data supplied to SPECTRA. The filter does not factor in attenuation due to atmospheric conditions in BA1 such as humidity. Further reduction of power incident on the detector will occur due to scattering and absorption in air, given

the lack of a vacuum chamber in the apparatus. Water is a significant absorber of radiation between 1.05 and 1.275 THz, and the effects are significant even at low humidities [151]. For practicality this is ignored given the lack data available for atmospheric conditions in BA1, however in practice this is likely to result in some discrepancy between simulations and measurement.

SPECTRA simulations provide both the filtered and unfiltered radiation distributions, allowing for the fraction of radiation surviving transmission through the window to be estimated. Both spatial distributions are integrated to determine the total radiative power and the total detectable power predicted by spectra. The unfiltered distribution is interpolated using a cubic spline interpolation and numerically integrated to get the total power radiated as calculated by SPECTRA. The filtered spatial distribution is then also interpolated in a similar fashion and scaled by the ratio between the integrated power calculated from SPECTRA and the instantaneous power obtained from GPT, such that

$$\left(\frac{d^2P}{dxdy}\right)_{Det.} = \frac{P_{GPT}}{P_{SP}}\left(\frac{d^2P}{dxdy}\right)_{SP,F}, \tag{4.9}$$

where $\left(\frac{d^2P}{dxdy}\right)_{Det.}$ is the power density in the detector plane that has been transmitted through the PED, P_{GPT} is the instantaneous power from GPT, P_{SP} is the total unfiltered power calculated from SPECTRA simulations, and $\left(\frac{d^2P}{dxdy}\right)_{SP,F}$ is the interpolated filtered power density obtained from SPECTRA. Equation 4.9 is then integrated over the effective detector area, with this area scanned over the detector plane to simulate scans using the two-axis translation stage.

The second method used for determining the radiation distribution uses macroparticle data directly to generate a 3-dimensional bunch form factor for use in Equation 2.67. A Cartesian 3-dimensional distribution function is generated from macroparticle data using the "`SmoothKernelDistribution`" function in Mathematica which is then converted to a normalised density function, $S_{3D}(x, y, z)$, such that

$$\int_{-\infty}^{\infty}\int_{-\infty}^{\infty}\int_{-\infty}^{\infty} S_{3D}dxdydz = 1.$$

In order to obtain the form factor $F(\Omega, \omega)$, the Fourier transform of the bunch distribution must be calculated. Direct calculation of the Fourier transform using numerical integration proved too computationally costly, so instead a 3-dimensional discrete Fourier transform (DFT) was performed. The DFT, is calculated according to

$$F(\vec{n}_k \odot \Delta\vec{k}) = \Delta x\Delta y\Delta z \sum_{n_z=0}^{N_z-1}\sum_{n_y=0}^{N_y-1}\sum_{n_x=0}^{N_x-1} S_{3D}(\vec{n}_r \odot \Delta\vec{r} - \frac{1}{2}\vec{X})e^{-i\frac{2\pi\vec{n}_k\cdot\vec{n}_r}{N_xN_yN_z}},$$

where F is the calculated form factor, the vector $\vec{X}$ defines the sampling window, the vector $\vec{n}_k = n_{k_x}\vec{e}_x + n_{k_y}\vec{e}_y + n_{k_z}\vec{e}_z$ defines the harmonic numbers of the wavevector $\vec{k}$, and equivalently the vector $\vec{n}_r = n_x\vec{e}_x + n_y\vec{e}_y + n_z\vec{e}_z$ defines the harmonics of the position vector $\vec{r}$. The symbol $\odot$ is used here to define the diagonal components of the tensor product between the two vectors. These harmonics define the components of their respective vector through the resolution of the sampling in the respective space; the vector $\Delta\vec{r} = \Delta x\vec{e}_x + \Delta y\vec{e}_y + \Delta z\vec{e}_z$ defines the resolution in position space, while the $\Delta\vec{k}$ operates similarly in the reciprocal space. The components of $\Delta\vec{k}$ are defined such than $\Delta k_i = \frac{2\pi}{\Delta r_i}$. The DFT is performed using

an FFT method which permits a relatively large sampling rate of S_{3D}, with 64 sample points used in the transverse dimensions, and 128 used along the longitudinal axis. The sampling window applied along a given axis u is $\pm 3\sigma_u$, where σ_u is the r.m.s size of the beam distribution along the axis. In order to capture the asymmetry of the electron bunch, and the resultant expected asymmetry of the radiation distribution, the spatial harmonics were symmetrised around $\vec{k} = \vec{0}$.

A cubic spline interpolation of F is generated, which is then used to produce a coherent angular spectral density as per Equation 2.67. The DFT method results in a ringing effect for higher frequency harmonics, the amplitude of which is typically very low and thus not a concern in principle, however when interpolation of the form-factor data is carried out this ringing can generate erroneous large values at higher frequencies. In order to suppress these, the DFT is padded with null values around the maximal values of k_i (Figure 4.39). This is justified given that harmonics significantly shorter in wavelength than the bunch dimensions will contribute very little to the overall form factor. In order to incorporate GPT results into this expected radiation spectrum, a similar process of normalisation and re-scaling as with the SPECTRA distribution is carried out. The angular-spectral density is normalised by integration over the full spectrum and the relevant angular range, corresponding to the full vertical angle, and a horizontal (in-plane) angle equivalent to that used in the normalisation of the SPECTRA distribution as described previously. Once again, this distribution is then rescaled with the power calculated from GPT. Finally, this rescaled coherent spectral density is integrated over the full spectral range, whilst modulated by the window transmission curve to produce the detectable angular distribution.

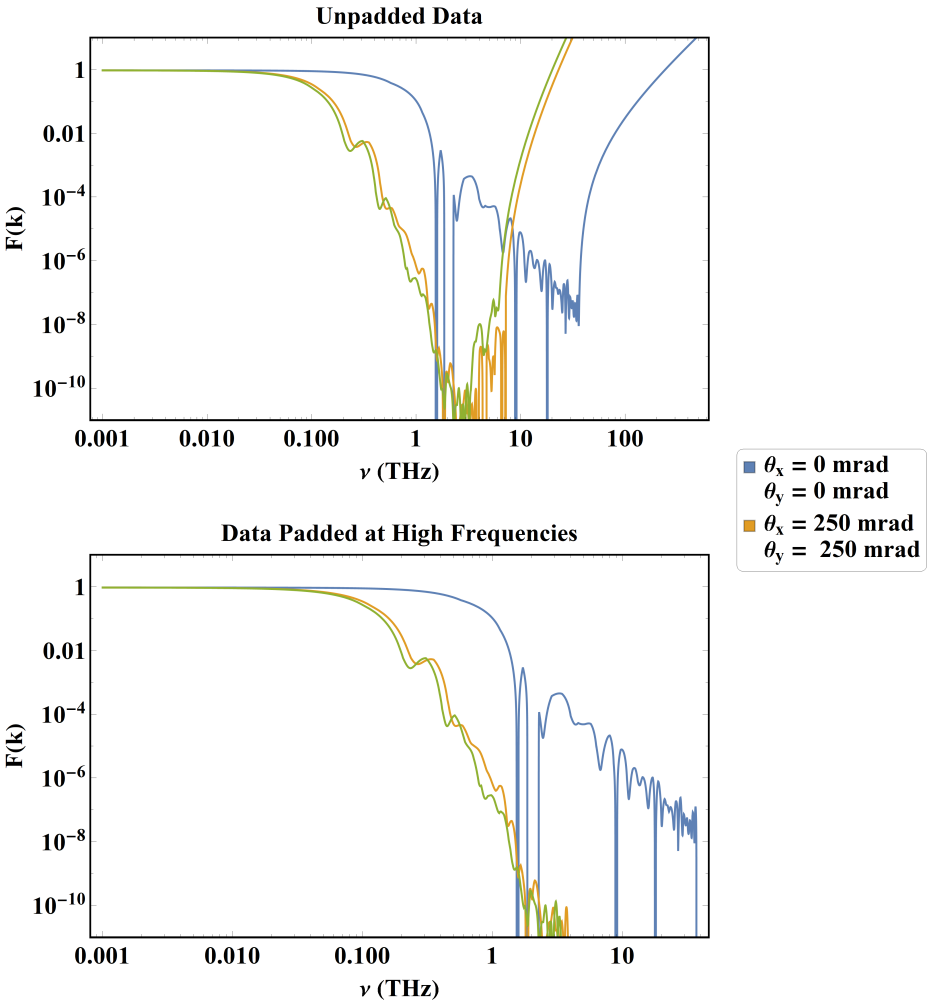

Figure 4.39: Bunch form factor spectrum generated using a DFT operation and then interpolated. The DFT results in significant ringing of the function at high frequency components. These are typically of a very low amplitude, although the highest frequency terms are large enough to be problematic when generating radiation spectra. As such the highest frequency terms are omitted, after which only the low amplitude ringing persists. The spectral range shown is the full spectral range considered in subsequent analysis, as coherent radiation amplification will not occur at frequencies higher than those presented.

Simulation Results - Linac-1 Phase Scan

As with the emission across the C2V dogleg, it is necessary to compare simulation results between cases where 4 and 16 emission points are used. As with the C2V dogleg, there is little observed between the induced energy loss and energy

redistribution, and the 4-point method can be used (Figure 4.40).

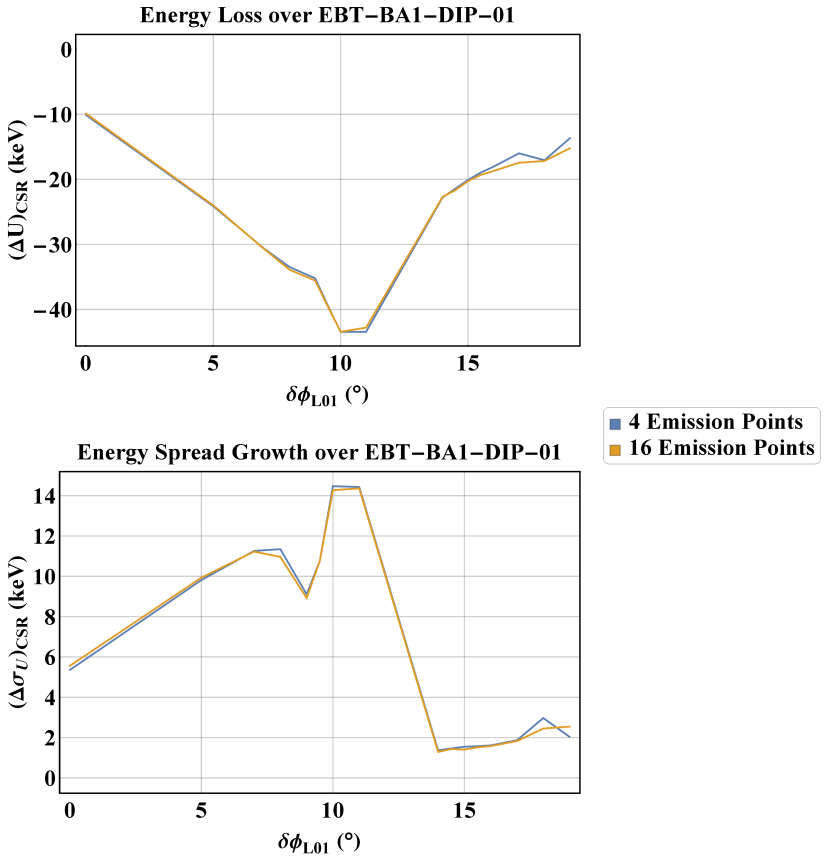

Figure 4.40: Comparison between the 4 and 16 emission point models in GPT. The good convergence between the two is an indicator for the 4-point model's utility in this regime.

Simulations indicate that the energy radiated at both Port A and Port B would be detectable by the PED considering the measured sub-nJ NEP at optical wavelengths (Figure 4.41), although the energy emitted towards Port B is still considerably greater than for Port A. It is worth noting that this refers to the total power radiated; the incident energy upon the detector is expected to be much lower, meaning that while the peak emission may be detected at Port A, the full scan of the linac-1 phase may not be as easily characterised. Taking this

into account alongside the difficulty of capturing interference effects expected at the entrance transient due to radiation emitted from the upstream dipole exit, Port B is the preferable choice for measurement. This is compounded further by the fact that there are pre-existing alignment optics present at Port A, used for alignment of components within the Coffin, and so Port B presents the option with the least impact on other operations currently being carried out in BA1.

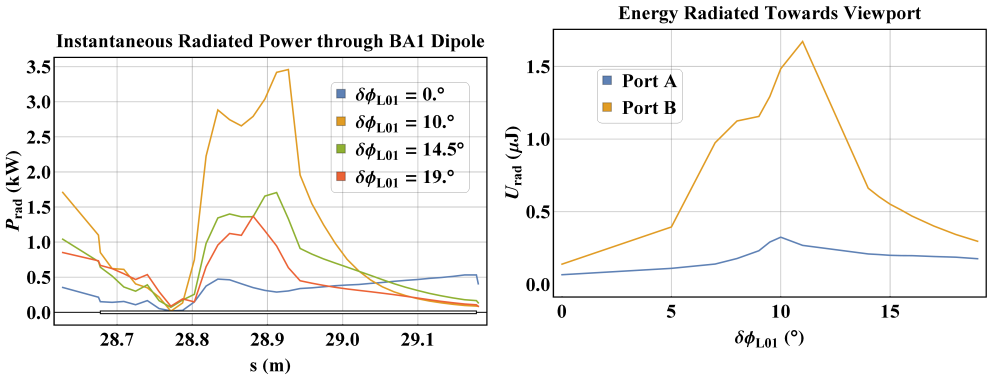

Figure 4.41: Evolution of the instantaneous radiated power alongside a comparison of CSR emission at the two available ports. The emission preceding the dipole entrance arises from radiation generated from the fringe field.

Simulations suggest that significant coherent emission occurs in the fringe region of the dipole magnetic field. This quickly dies away as the bunch enters the dipole proper, as the steady state wake has yet to form. The emission from the fringe region typically bears qualitative characteristics different to those of conventional CSR [149], such as a relatively frequency-independent spectrum at low frequencies and a hollow angular distribution, but is similarly strongly coupled to the bunch length. The radiation emitted in the edge region propagates largely parallel to the initial propagation axis of the beam and does not interact further with the beam as it enters the dipole proper and thus does not contribute to

the CSR wake formation within the dipole, hence the reason behind the drop in the emitted power following the initially strong emission. The peak CSR power occurs at the centre of the dipole, due to the preceding beam optics, which were designed to bring the beam to a focus midway through the dipole. Here the beam is well within the 1-dimensional limit described by Equation 2.65, and thus the emission is not suppressed by de-coherence brought about by a large transverse extent.

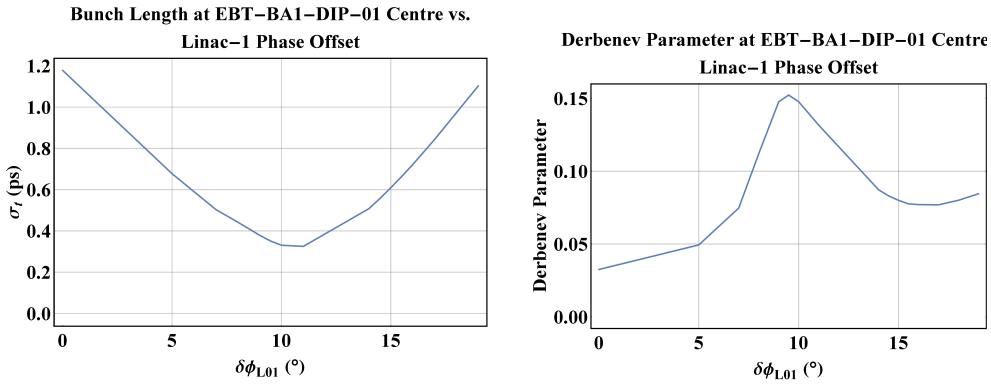

Figure 4.42: R.M.S bunch length and Derbenev parameter at the emission location. The peak in the Derbenev parameter corresponds well to the asymmetry seen in the radiative emission towards Port B (Figure 4.41)

The emission peaks at a linac-1 phase offset of 10°, which as expected coincides with the phase of maximum compression (at the radiating location). It follows that the value of the Derbenev parameter is also maximal close to this phase, although its value is still low (Figure 4.42). Despite this, while the value of the Derbenev parameter is <1, the value is not so small that the transverse size is not impacting the overall emission rate at all as described by the Derbenev criterion (Equation 2.65). However, comparison of GPT-simulated energy loss against the power expected from a 1-dimensional Gaussian electron pulse shows

little deviation (Figure 4.43). A 3-dimensional bunch analysis (in the manner discussed in Section 4.3.3) follows some of the qualitative features of the radiated power's variation with respect to the linac-1 phase offset, such as a small dip in the emission at $\delta\phi_{L01} = 9°$, however significantly underestimates the emission. Similarly, integrated SPECTRA radiation distributions underestimate the radiated energy considerably, however do not echo the general trend of the emitted power's variation as well as the 3-dimensional semi-analytic method. The qualitative agreement between the 3-dimensional semi-analytic analysis and GPT simulations implies that this will be an effective method for calculating the radiation distribution when re-normalised, although the stark difference in magnitude indicates significant sources of uncertainty.

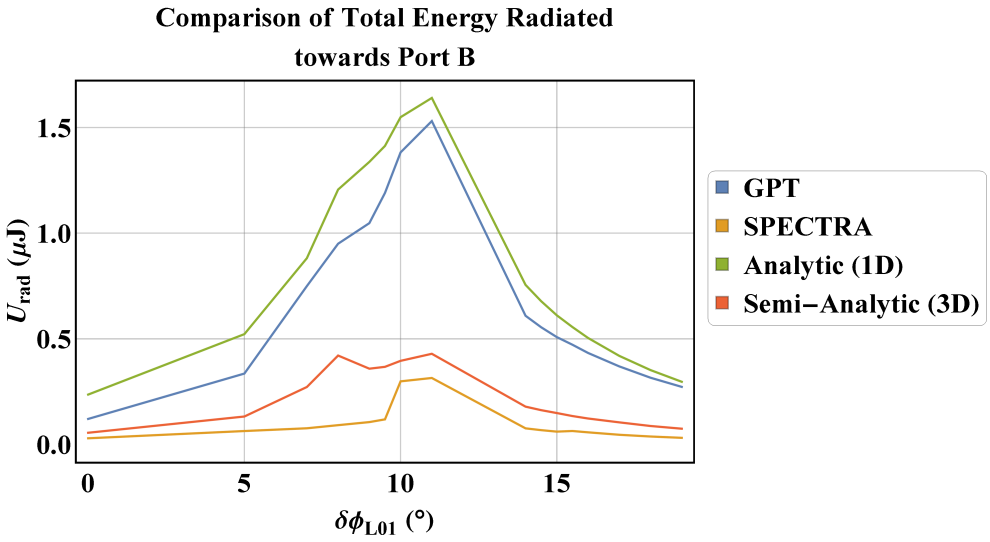

Figure 4.43: Comparison of predicted energy radiated towards Port B. Good agreement is shown between 1-dimensional analytic modelling and GPT simulations. The 3-dimensional semi-analytical model predicts a similar drop in the emitted energy as GPT simulations, implying this is an effect due to the electron bunch distribution. In terms of the total power radiated, both the 3-dimensional semi-analytic and SPECTRA simulation results deviate considerably from measurements.

Inspection of the bunch current profile (Figure 4.44) demonstrates a potential cause for the small drop in the peak power close to maximum compression. Rather than being attributable to drop in the emission solely, it may be a combination of a drop in the emitted power at $\delta\phi_{L01} = 9°$ and $\delta\phi_{L01} = 9.5°$, likely caused by the broadening and semi-bifurcation of the longitudinal current profile, and a second peak at $\delta\phi_{L01} = 8°$ as evidenced by the large central current spike in this case. The maximally compressed case at $\delta\phi_{L01} = 10°$ shows a considerably lower peak current than the $\delta\phi_{L01} = 8°$ bunch, yet still results in the greatest emitted energy. This can be attributed to the lack of low density tails in this bunch current profile, resulting in a bunch core with a high average current density.

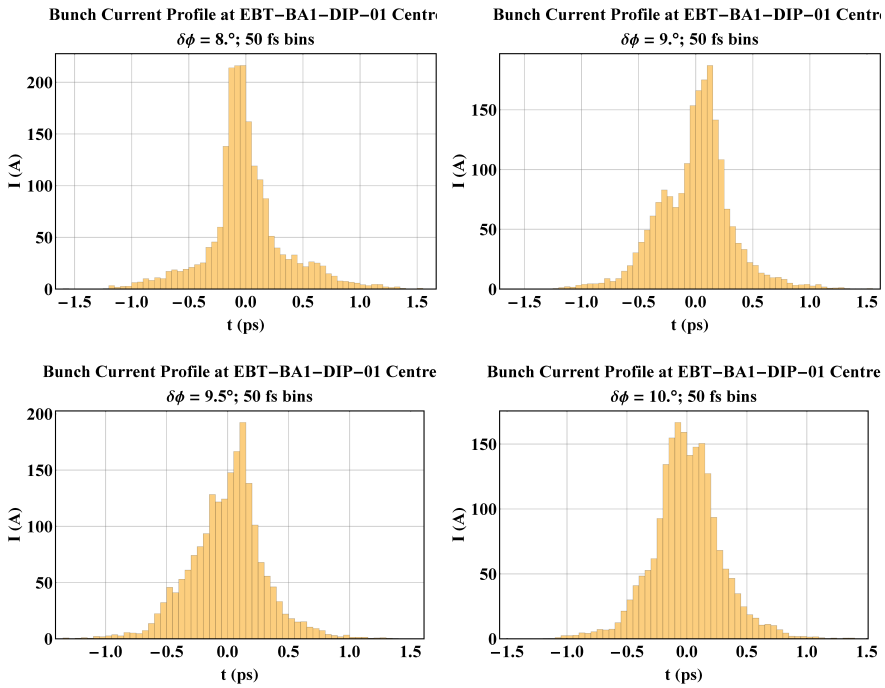

Figure 4.44: Comparison of bunch current profiles close to maximum compression ($\delta\phi_{L01} = 10°$). The head of the bunch is towards the left on all plots.

The energy redistribution due to CSR (Figure 4.45) is considerably larger than that observed in the C2V dogleg at between 5%-10% of the total energy spread (Figure 4.44). Despite this increase, the effects of beam jitter, typically on the order of ∼1 mm at the BA1 spectrometer screen, are still likely too large to make the effect of this measurable.

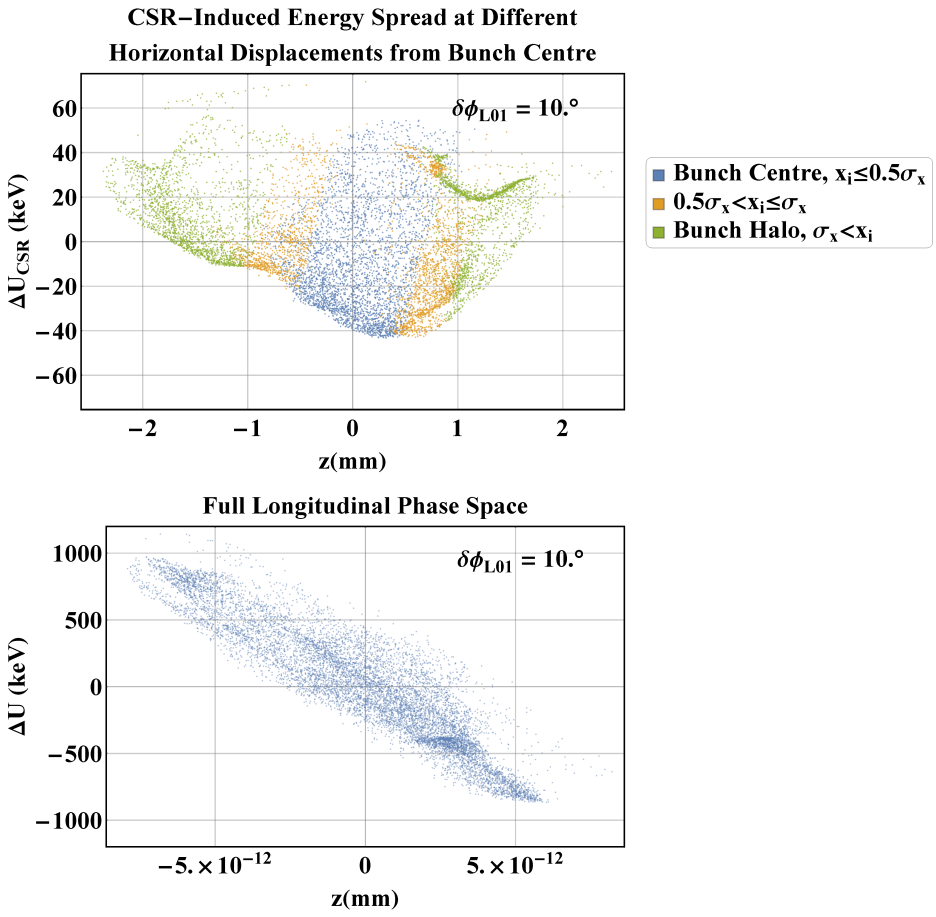

Figure 4.45: Energy redistribution within the bunch due to CSR compared to the full LPS at the BA1 dipole exit. Both plots correspond to the bunch at the maximal compression phase of linac-1. The plots shown correspond to the energy redistribution within the bunch only, with the centroid energy shift having been removed.

Despite what would be expected from an electron bunch within the 1-dimensional limit, the non-trivial discrepancies can be seen in the higher-frequency portion of the spectra generated from 1-dimensional and 3-dimensional models (Figure 4.46). This is a likely cause for the relatively low total power resultant from the 3-dimensional analysis and is potentially caused by the resolution of the DFT method used in generating the 3-dimensional bunch form factor. The effect of the Z-cut quartz window's transmission curve is to marginally reduce the overall emission in both cases, implying that the radiation surviving propagation to the detector plane will still be both measurable and that phase scan measurements should not display any significant error close to maximum compression arising from suppression of higher frequency spectral components by the view port.

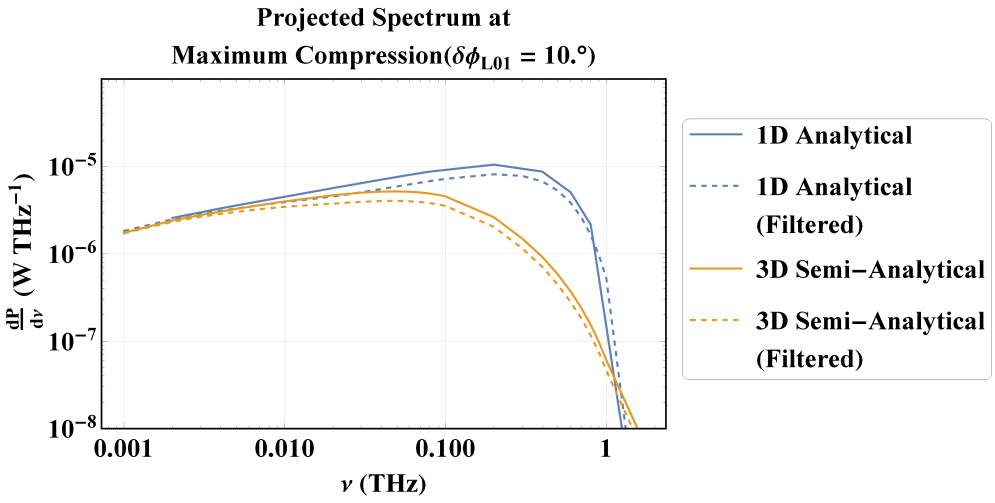

Figure 4.46: Predicted radiation spectra from 1-dimensional and 3-dimensional models of the electron bunch. Discrepancies between the two are likely due to the resolution of the DFT employed in generating a 3-dimensional form factor. The effect of including a filter from the transmission curve of the Z-cut quartz window is very small.

The angular radiation distributions generated in SPECTRA and from the 3-dimensional analytic spectral-angular density (Equation 2.67) show broadly

similar features: both signals show the same vertical opening angle and both have the characteristic double-hump with a local central minimum arising from the π polarisation mode (Figure 4.47). However, the separation and breadth of these peaks is notably different between the two cases. Should these features be measurable with the PED in BA1, this would be a convincing comparison for evaluation of SPECTRA's ability to model low-frequency (i.e. THz) radiation.

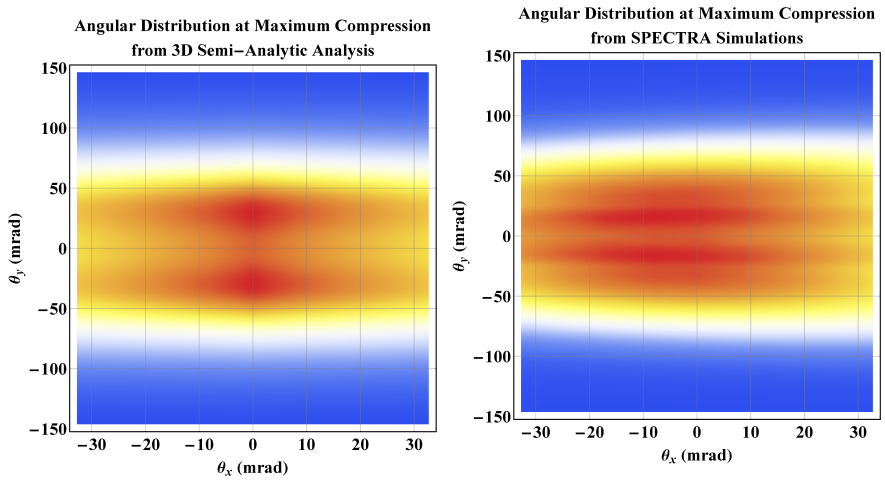

Figure 4.47: Angular power distribution for the CSR emission of the maximally compressed bunch predicted in both SPECTRA and by 3-dimensional analysis of the electron bunch form-factor.

Integration of the spectrum-filtered distribution across the detector area confirms that the emission should be detectable, with a typical energy incident upon the PED pixel of several nJ at the centre of the distribution for most of the bunches considered (Figure 4.48). Furthermore, it should be feasible to characterise the radiation distribution allowing for quantitative evaluation of the methods for estimating the simulated distribution. The ability to characterise the distribution will be limited further away from maximum compression however,

where the incident energy upon the pixel approaches the NEP of the PED. As the radiation distribution only varies weakly with the horizontal detector position, a search for the signal maximum at the centre of the view port (along the horizontal axis) need not be exhaustive.

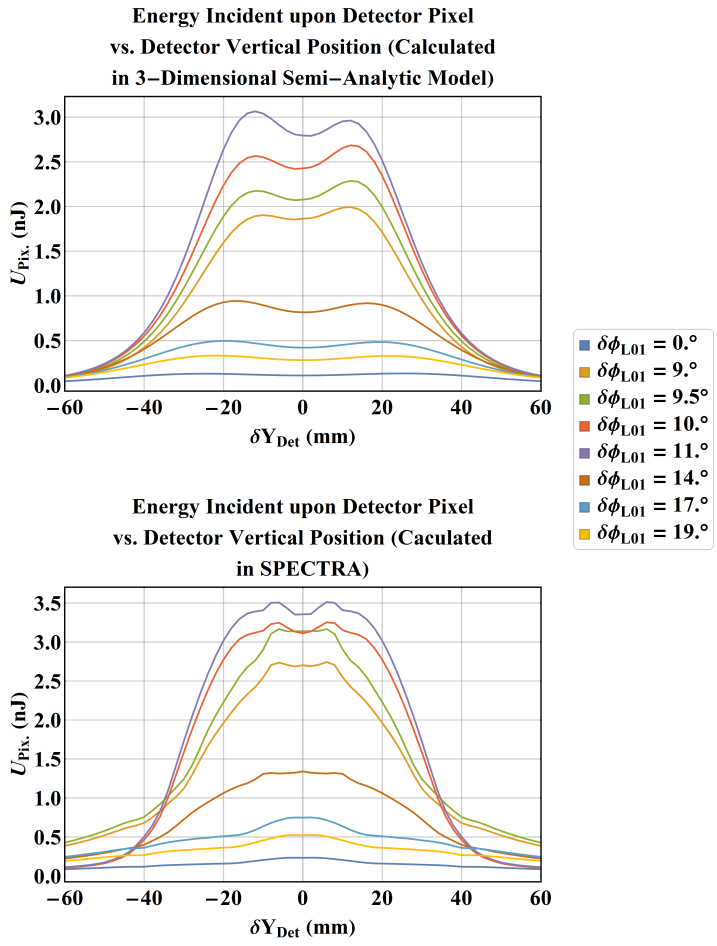

Figure 4.48: Energy incident upon the PED pixel as a function of the pixel vertical displacement from the centre of the beam axis. The filtered spectral-angular distribution is integrated over the 2 mm×2 mm pixel area, with the pixel considered positioned at the centre of the distribution along the horizontal axis. The pixel is moved in 2 mm steps.

Due to the unknown spectral response of the PED, relative measurements will be used to compare against simulations. This analysis will be approached in two different ways: by comparison of the peak voltage in a scan of the detector's vertical position to those at other linac-1 phase offsets, and by comparison of the total integrated voltage of the scan of the detector position to that at other linac-1 phase offsets. In the case of the latter, if the detector is stepped at increments equivalent to the detector pixel, this can be simply be the sum of all voltages detected over the range, normalised to the scan range.

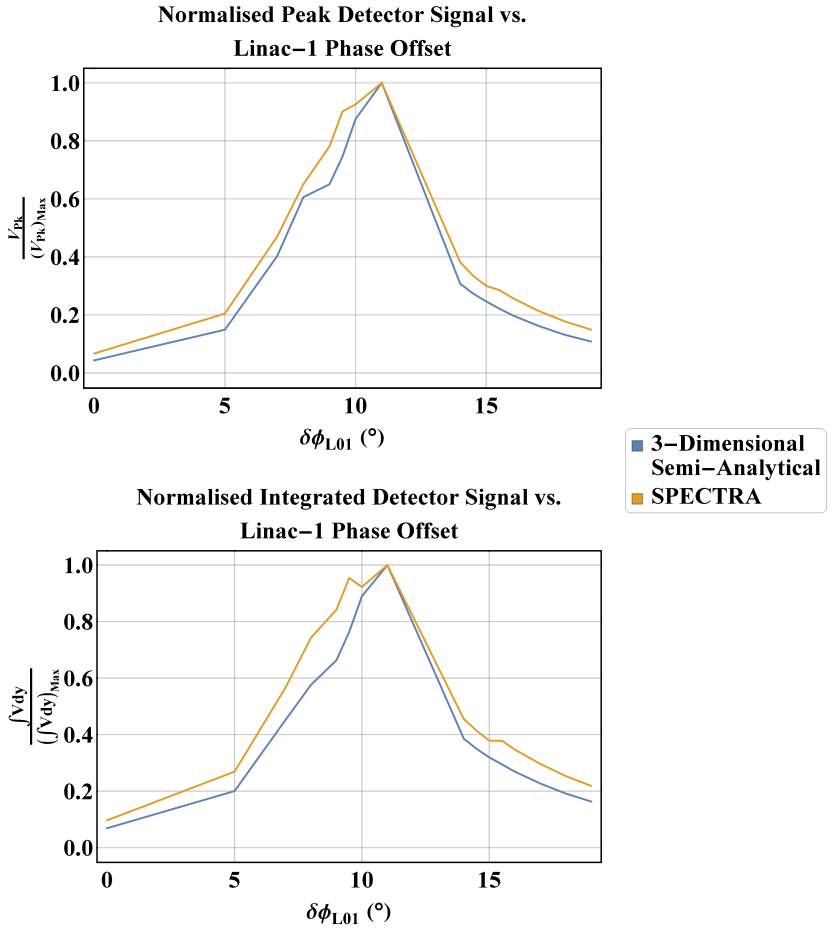

Figure 4.49: Normalised peak voltage and integrated voltage over the scan of linac-1.

Because of the low value of the expected incident energy far from the signal centre and far from crest, the former method is likely to be the most accurate as the latter may be erroneously biased such that the emission at maximum compression seems greater than it should when compared to far away from maximum compression. Both methods show a clear peak corresponding with the maximal compression and emission phase (Figure 4.49), providing a clear demonstration of the measurement principle as well as the usage of the system as a relative bunch length monitor.

Simulation Results - Quadrupole Scan

A scan of the quadrupole focusing strength of the quadrupole immediately upstream from the BA1 dipole is used to investigate the effects of the transverse beam size on the CSR emission process. Exaggerated transverse effects are expected in the quadrupole scan, and as such the 4- and 16-source point methods must once again be compared (Figure 4.50). There is very good agreement observed between the two models, providing some confidence that significant transverse effects are not being omitted by the 4-point model.

First inspection of the overall centroid energy and r.m.s energy spread changes due to full transport through the BA1 dipole in the quadrupole scanning regime highlight a potentially interesting effect; namely that for all bunches with an appreciably large value of the Derbenev parameter, the energy spread actually decreases. In order to confirm that this effect is indeed a product of the modelled CSR interaction within the bunch, these results are compared against simulations of the same beamline geometry and bunches with CSR disabled (Figure 4.51). The sign of the energy spread change across the BA1 dipole is echoed in

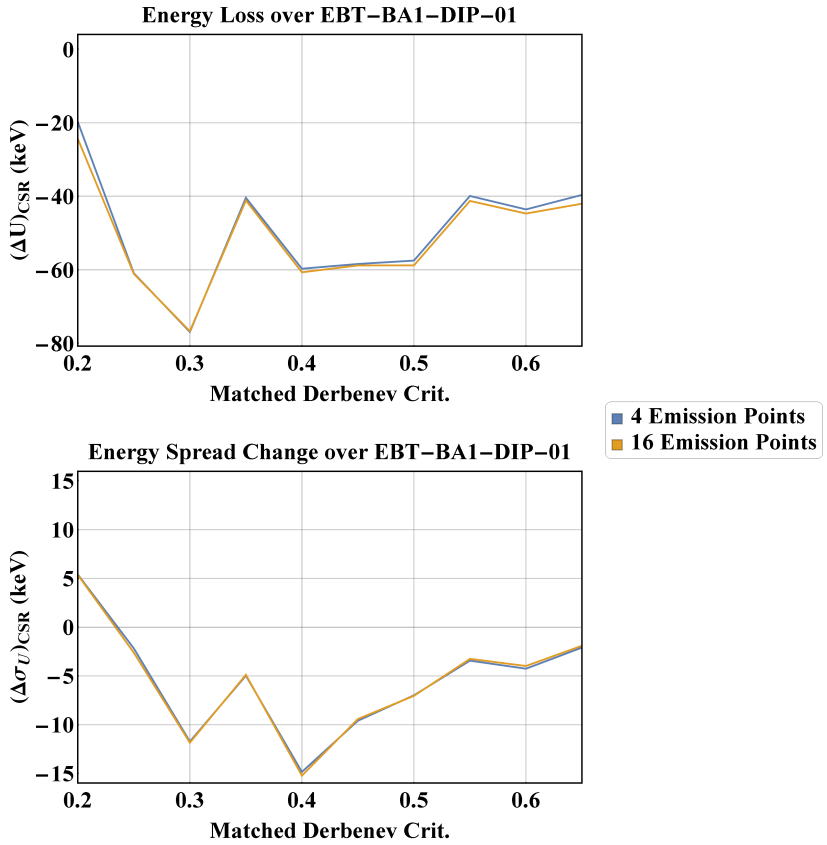

Figure 4.50: Comparison between 4- and 16-source point methods for GPT CSR in the quadrupole scan. The abscissa corresponds to the target Derbenev parameter at the dipole centre used in the `elegant` matching procedure for a given BA1 optics set-up. As such, this typically does not correspond to the actual Derbenev parameter at the bunch centre as simulated in GPT.

all quadrupole set-ups by the space charge-only simulations. However, the overall strength of the effect is far greater in the case of both models being used.

The bunch charge stays constant throughout the BA1 dipole in all but one case, which shows a maximum loss of 5 pC, which excludes the loss of particles with high momentum deviation as an explanation for the reduction of the beam energy spread (Figure 4.52). Observation of the evolution of the bunch's r.m.s energy spread shows that the majority of the energy spread reduction occurs in

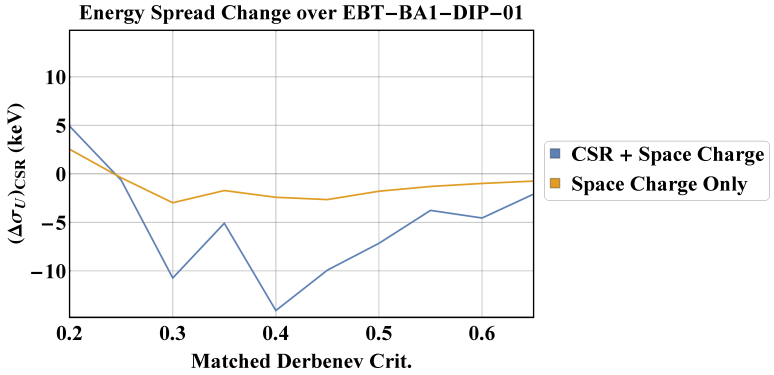

Figure 4.51: Energy spread change for simulations of the BA1 dipole carried out in GPT using both space charge and CSR or space charge alone. Both simulations show reductions in the r.m.s energy spread, however the reduction is far more pronounced in simulations using CSR.

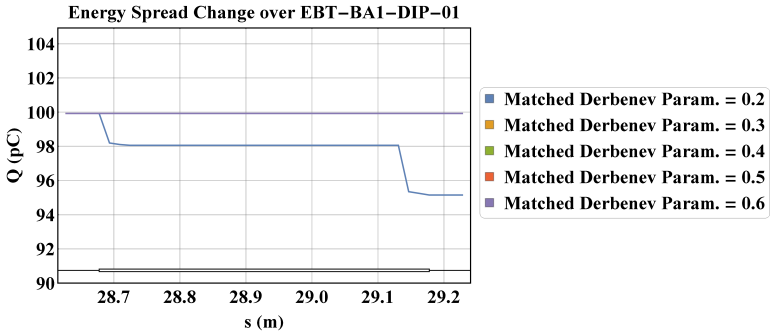

Figure 4.52: Bunch charge through the BA1 dipole. Losses only occur for the set-up where the Derbenev parameter was matched to a value of 0.2 in `elegant`.

the dipole proper as opposed to the fringe regions (Figure 4.53) as seen in Section 4.2.2. It should be noted that the reduction in the energy spread only occurs in cases where the beam is transversely convergent at the dipole entrance. Furthermore, the magnitude of the reduction does still appear to be dependant upon the longitudinal beam size, as shown by the curve corresponding to a matched Derbenev parameter of 0.65.

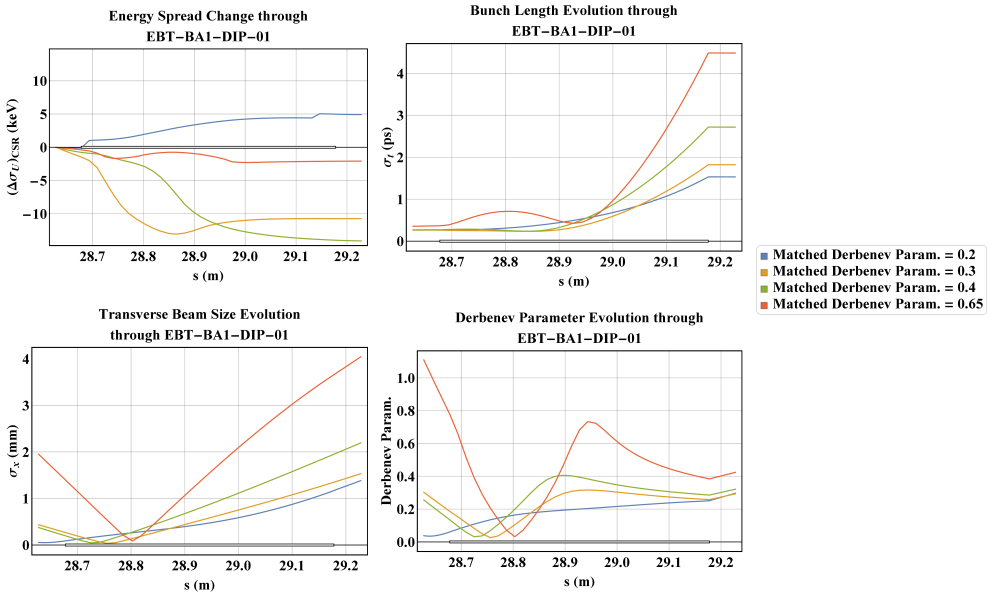

Figure 4.53: Plots of r.m.s energy spread, r.m.s bunch length, and Derbenev parameter evolution through the BA1 dipole for a selection of the tracked bunches.

The dynamics responsible for this loss of beam energy spread can not be clearly explained in terms of statistical bunch properties alone. The residual dispersion due to the C2V dogleg results in correlations in the $x - \delta_U$ and longitudinal phase-spaces (Figure 4.54). Taking the example of the optics set-up which maximises the energy spread reduction across the dipole it can be seen that this correlation occurs such that the higher energy particles occur more commonly at positive horizontal displacements from the bunch centre, with the opposite occurring for lower energy particles. The LPS shows the maximally compressed bunch, whereby the distribution is weakly non-linearly correlated, with a bimodal energy distribution towards the rear of the electron bunch.

As the bunch is focused by the preceding quadrupole and travels through the dipole, the lower energy particles both move closer to the centre transversely,

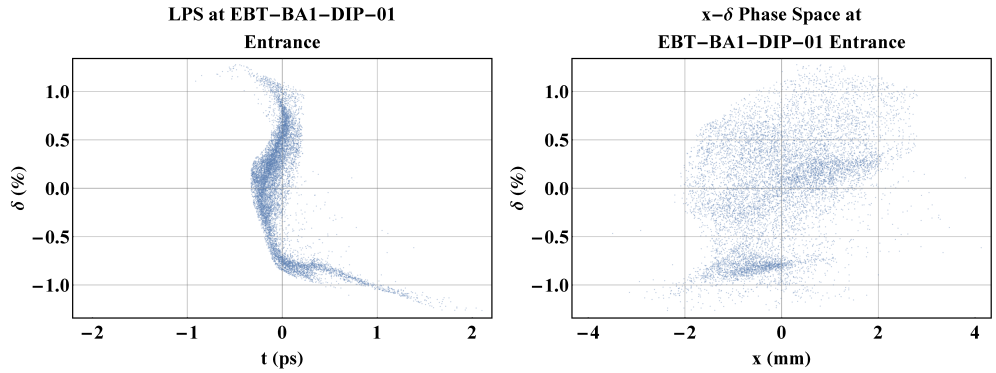

Figure 4.54: LPS and x-δ phase space at the BA1 dipole entrance. The bunch head is to the left of the LPS plot.

and move forward relative to the bunch centre. The higher energy particles move rearward in the bunch whilst also moving towards to bunch centre. This can be clarified by inspection of the dipole transfer matrix elements R_{51} and R_{52} [56]:

$$R_{51} = -\sin\theta$$

$$R_{52} = \rho(\cos\theta - 1).$$

These matrix elements refer to the 1$^{\text{st}}$-order transfer matrix for a single sector dipole. The first order matrix is defined in the same way as described in the first term of Equation 1.2. In a right handed coordinate system, the bending angle of the BA1 dipole is of negative sign; resulting in the R_{51} being positive, and R_{52} being negative. At positive transverse offsets, particles tend to have a higher energy and negative divergence; as such the contribution arising from R_{51} and R_{52} are both positive, and higher energy particles move rearward to the decelerative region of the CSR field. The converse then occurs for lower energy particles. This can be shown in the projection of the bunch spatial distribution in the t-x plane

(Figure 4.55). Following this, the electron bunch lengthens, weakening the CSR wake and "freezing-in" the energy redistribution.

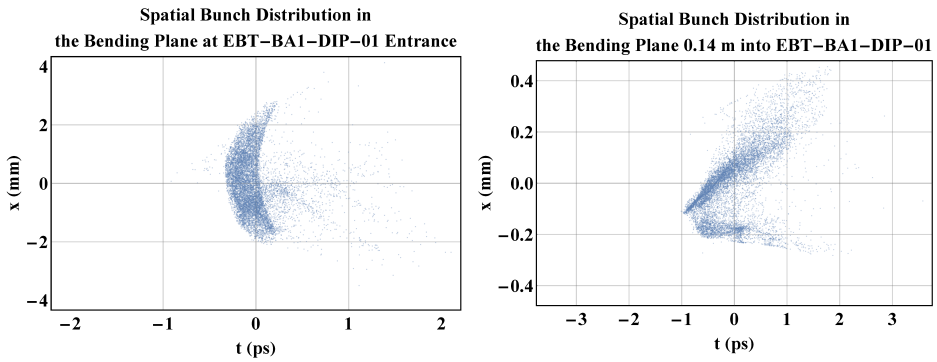

Figure 4.55: Projection of the bunch spatial distribution onto the t-x plane at the BA1 dipole entrance and at the location where the energy spread is minimised. The head of the bunch is to the left. Lower energy particles at negative transverse offset move forward in the bunch, resulting in a reduction of their energy deviation from the centroid energy. The opposite occurs for higher energy particles at positive transverse offsets. The effect of this is amplified by the focusing of the electron bunch, which forces particles towards the transverse bunch centre where the CSR wake is strongest.

The Derbenev parameter at the radiating location in GPT corresponds well to the target parameter used for matching, exceeding the matching target in some cases (Figure 4.56). Conversely, whereas `elegant` matching was carried out with the condition to maintain a constant bunch length, this has not been achieved in GPT simulations. The power emitted by the electron bunch at the dipole centre does not show a monotonic decrease with respect to increasing Derbenev parameter as would be expected and this can be partly explained with the variation in bunch length at the radiating location, with increases in the radiated energy corresponding with decreases in the bunch length. While the maximal value of the Derbenev parameter is still < 1, at a value of $\sim$0.7 this does not fulfil the

criterion set out in Equation 2.65 and effects from the transverse size would still be expected.

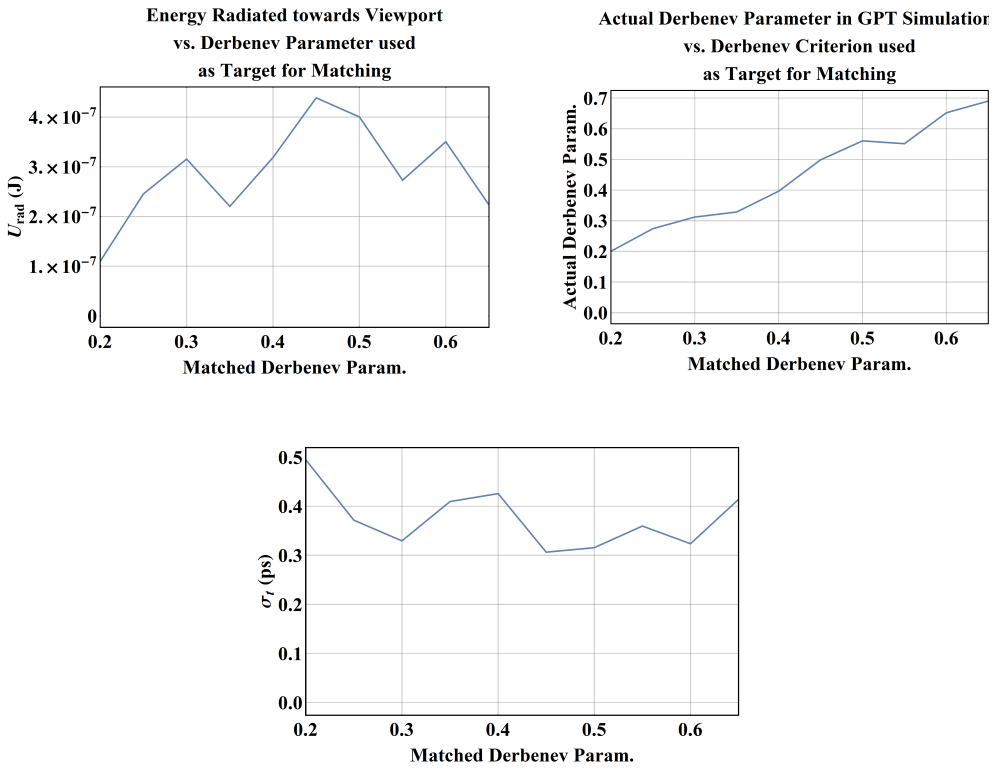

Figure 4.56: Radiated energy, bunch length and Derbenev parameter vs. target Derbenev parameter used in matching as simulated in GPT. Despite the large value of the Derbenev parameter for some bunches simulated, variations in the power appear to be completely described by the bunch length.

Comparison of the GPT-simulated energy loss with SPECTRA simulations, the analytic 1-dimensional model, and semi-analytic 3-dimensional model shows limitations with both SPECTRA simulations and the 3-dimensional semi-analytical model, which do not echo GPT simulations qualitatively. Conversely to the phase scan, these models do result in total emitted energy of a comparable magnitude.

Little difference is observed between the 1-dimensional analytical result for the total power and GPT simulations, implying that despite the relatively large value of the Derbenev parameter at the extreme of the scan the electron bunch is still well modelled in a 1-dimensional framework. Alternatively this could be an indication that GPT is not capturing some of the transverse effects of the bunch; the electron bunch is maximally compressed and the LPS rolls over as it transits the dipole. As stated previously in Section 3.1.5, the GPT algorithm has difficulty in modelling such bunches due to bimodal energy, position, and velocity distributions within a given longitudinal slice (Figure 3.2) and this could be responsible for the lack of transverse effect captured in simulations (Figure 4.55).

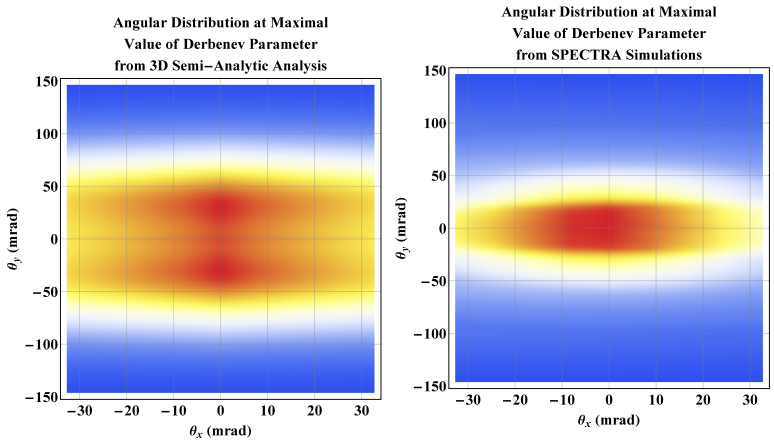

Figure 4.57: Angular distribution of unfiltered radiation as calculated in two different modelling methods. Both methods display a significant departure from one another.

The radiation distributions calculated from the 3-dimensional semi-analytical analysis and SPECTRA show considerable qualitative differences to one another (Figure 4.57). As they both show a further discrepancy to the results from GPT

simulations (Figure 4.58), it is difficult to determine which is a better reflection of the true expected radiation distribution if at all.

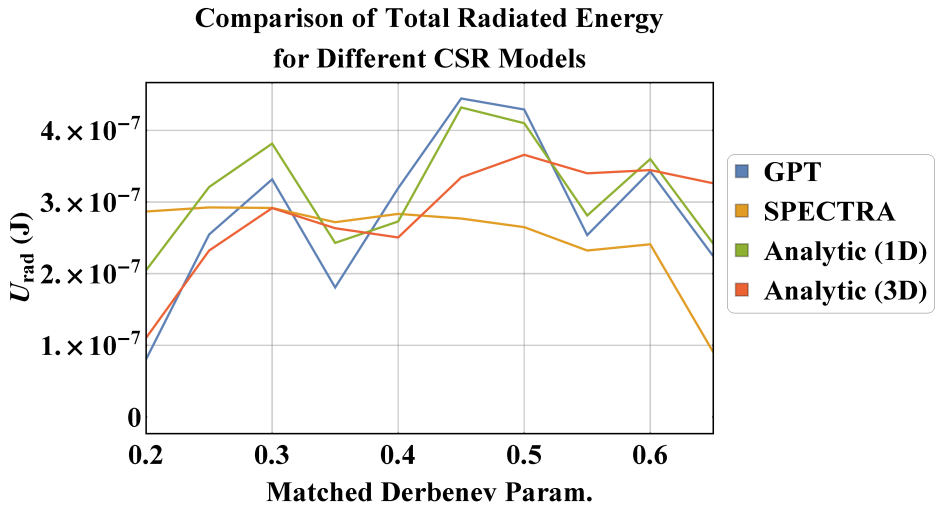

Figure 4.58: Total radiated energy across the Derbenev parameter scan for different CSR modelling methods. The close agreement between GPT and the 1-dimensional analytical model implies that either GPT is limited in its capabilities to model in this particular bunch regime (i.e. a rolled over LPS), or that the electron bunch is still well-described by the 1-dimensional model. The maximal value of the Derbenev parameter shown is the largest achievable by the matching procedure used, with greater transverse sizes resulting in excessive elongation of the electron bunch.

Discrepancies in the 3-dimensional analysis likely arise either from a low resolution in the DFT algorithm for a bunch displaying significant substructure, or from the fact that the electron bunch is considered in the steady state insomuch as the calculation uses the distribution at the centre of the dipole only when in fact this is a constantly changing function. As the electron bunch is considered rigid along its longitudinal axis in SPECTRA, a similar issue may arise in the SPECTRA-generated angular distribution. Furthermore, as can be seen in Figures 4.54 and 4.55, the electron bunch distribution at the radiating location is

certainly not well approximated by a Gaussian distribution as is used in SPECTRA calculations.

The typical energy incident upon the PED pixel is much smaller in the scan of the Derbenev parameter (Figure 4.59) than in the linac-1 phase scan (Figure 4.48). The DFT analysis of the electron bunch yields a broader angular distribution than that calculated by SPECTRA, and as such the energy density is lower. In the case that the true radiation distribution echoes this more closely, it will only be feasible to characterise the distribution up to a maximum angle of $\sim$75 mrad, corresponding to a detector vertical offset of $\sim$30 mm. Furthermore, identification of a peak energy density will not likely be possible in the case of the most weakly-radiating bunch considered.

The SPECTRA-generated distribution presents a narrower, denser radiation pattern at the detector plane. As such, it is likely that quantitative measurements can be taken for all bunches considered if this reflects the true radiation distribution. The angular extent which can be characterised is comparable to that of the 3-dimensional semi-analytical model. However, considering the unknown factor of water vapour absorption in BA1 the radiation may be undetectable. To minimise this effect, the PED should be positioned as close as possible to the window. Characterisation of the polarisation components will not be possible if this is the case, although it is likely that only the dominant σ-mode would be detectable.

Considering the fact that large portions of the radiation distribution would deliver insufficient energy to the overcome the PED pixels NEP, it is unlikely that

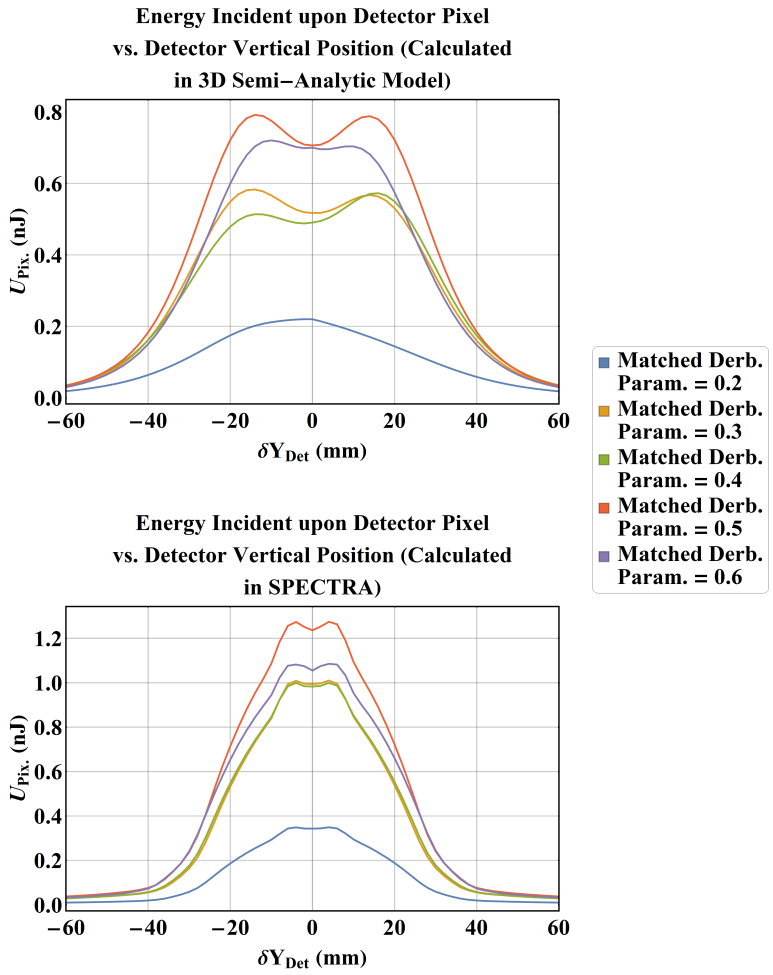

Figure 4.59: Dependence of detectable incident energy upon the PED pixel with respect to the pixel's vertical offset from the centre of the beam axis. The low incident energy-per-pulse is likely to limit the ability to both fully characterise the angular distribution with the PED and prevent detection of the peak signal in the case of heavily suppressed radiation.

the integrated signal would be an accurate reflection of the true radiative output of the electron bunch. In the idealised scenario presented (Figure 4.60), both methods echo the simulated radiated energy (Figure 4.56) well, though given the signals have been rescaled to the GPT simulated power this is unsurprising.

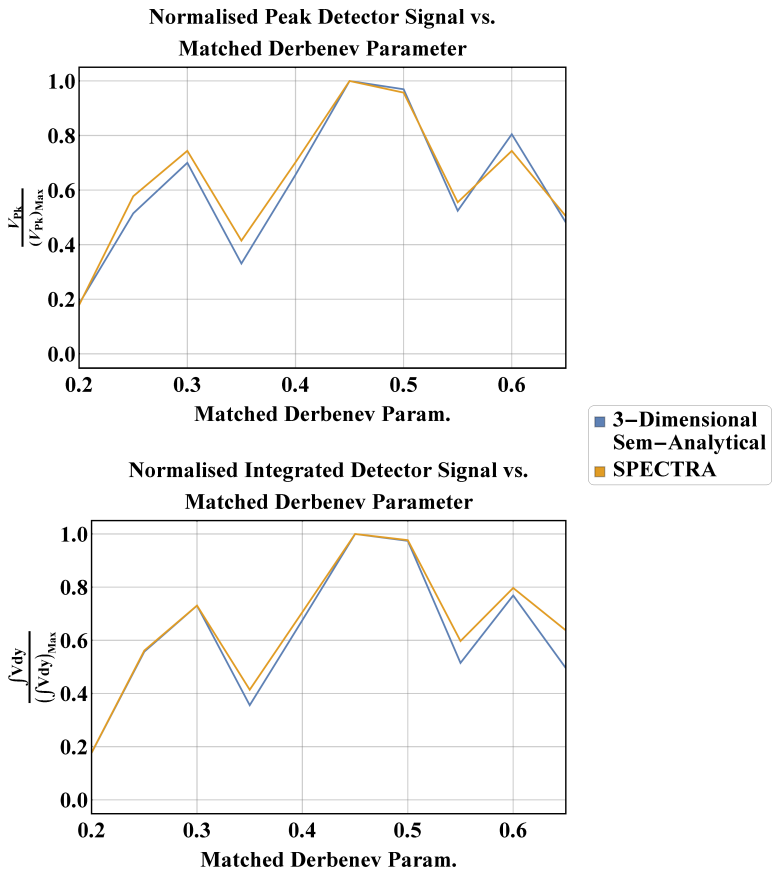

Figure 4.60: Normalised peak detector response and integrated detector response (with respect to the vertical detector offset) for all bunches considered in the scan of the Derbenev parameter. There is little difference between the two methods, though because of large regions of the radiation distribution delivering energy below the NEP of the PED the peak voltage method is preferable.

4.3.4 Conclusions

An experimental procedure based upon the detection of radiation in the THz region has been demonstrated for comparison with the new GPT CSR model. A model of the entire CLARA Phase 1 beamline has been developed in GPT, with optimisation of the CLARA lattice, including the Phase 1 injector, carried out using both GPT and `elegant`. Start-to-end simulations have been used

to design full-machine optics of the CLARA Phase 1 beamline, from the photocathode through to the user experimental area BA1, and for tracking of an electron bunch to the experimental location in order to incorporate space charge and upstream CSR effects in the 6-dimensional phase space of the electron bunch.

A phase scan has been demonstrated as an effective method for determining the capabilities of GPT in modelling of conventional 1-dimensional CSR emitted in the BA1 spectrometer dipole, through control of the electron bunch length via a variable LPS chirp and subsequent magnetic bunch compression. In this regime, the expected energy incident upon a PED pixel is sufficient to allow for characterisation of the spatial distribution of a radiation pulse without the requirement for focusing optics. Furthermore, relative power measurements can be used to effectively describe the relationship between the emitted power and linac phase offset.

Variation of machine optics preceding the BA1 dipole with the view to controlling th Derbenev parameter at the measurement location have highlighted interesting beam-based effects. The combination of strong focusing and slight bunch elongation of the initially maximally compressed electron beam in the presence of residual of 1^{st}- and 2^{nd}-order dispersion has been shown to reduce the r.m.s energy spread of the electron beam in GPT simulations. As this energy spread reduction occurs within the first portion of the dipole, it highlights the potential for design of energy spread reduction methods using short dipoles and quadrupole magnets.

Due to the effects of bunch elongation due to R_{51} coupling, measurements

of CSR in the regime of a large Derbenev criterion are not believed to be feasible. GPT simulations have not demonstrated significant deviations from the 1-dimensional model of CSR for values of the Derbenev parameter ≤ 0.7, and achieving larger values of the Derbenev parameter has been shown to be infeasible without significant lengthening of the electron bunch and subsequent reduction of the total emitted energy. While this may be an underlying issue with the method of modelling CSR employed by GPT in the context of highly compressed and "rolled-over" electron bunches, given the complex transverse distribution expected within longitudinal slices which is ignored in the CSR calculation. Moreover, the expected incident energy upon the PED pixel has been shown to be likely below the NEP of the PED in this regime. This measurement scheme is further hampered by the need to tailor machine optics for a given value of the Derbenev parameter, as such reliance on simulations will require extensive testing of the model of CLARA implemented in GPT. In the absence of pre-existing bunch length diagnostics at the measurement location, the bunch length evolution would need to be inferred from simulations alone.

Chapter 5

Coherent Radiation Detection at MAX IV

Towards the end of this project, an opportunity was presented to conduct a similar photonic study of coherent radiation at the MAX IV beamline in Lund, Sweden. This experiment was to be conducted alongside development of a CTR bunch monitoring system after the second bunch compressor of the MAX IV beamline, with a secondary aim to inform on the degree of CSR-pollution present in the CTR signal. The radiative power emitted from the final bunch compressor dipole exit was measured with a pyroelectric detector in order to provide data to compare to GPT simulations and to characterise the nature of coherent radiation emitted in the transient regime of a bending magnet for electron bunch distributions outside of the 1-dimensional analytic limit. These measurements are compared to the GPT CSR model, and will present a quantitative assessment to the modelling technique in the regime where the Coulomb term of the Lièнard-Wiechert field is believed to have significant effects upon the bunch energy spread. This comparison to results will strive to validate the model, and provide weight to some

of the conclusions derived from simulations on the CLARA Phase 1 beamline in the previous section.

A preliminary investigation was carried out in October 2018, with the aim to use a Spiricon Pyrocam III pyroelectric camera to characterise the full 2-dimensional distribution of the bunch. However, the camera was a borrowed item that was over a decade old, and was found to be non-operational; preliminary bench-tests carried out at Daresbury Laboratory with a broad-band thermal source showed no-response to infra-red radiation but this was attributed to a lack of power in the THz band and it being an old piece of equipment. However, thorough testing on the MAX IV beamline demonstrated that the pyroelectric camera was completely unusable for THz radiation detection, and it is believed that prior users have damaged the pyroelectric layer through un-filtered exposure to optical laser light. Fortunately, a backup Gentec-eo single-pixel detector (the same as was planned for experiments at CLARA) was also available. This setback proved significant, as the nature of the detection system required the single-pixel pyroelectric detector to be mounted on 3-axis translation for focusing and signal-hunting due to beam jitter and variable optics, and the time taken to capture a 2-dimensional radiation profile was increased by a factor of around $\sim$200. Furthermore, the resolution of the single-pixel detector system was a factor of $\sim$500 times lower (86 µm vs. 2 mm pixel dimension). As such, the experiment became merely a proof-of-principle for the measurement system as well as an opportunity to develop measurement techniques rather than a thorough quantitative study to compare against GPT simulations.

A second experimental period was carried out in late February and early

March 2019. For this experimental period a 1-dimensional linear pyroelectric array (DIAS Pyrosens) was used, which allowed for much faster data acquisition and better resolution. The increased speed at which the radiation profile could be measured meant that thorough machine parameter scans could be carried out. The results of these parameter scans are presented in this chapter.

5.1 The MAX IV Linac and Beam

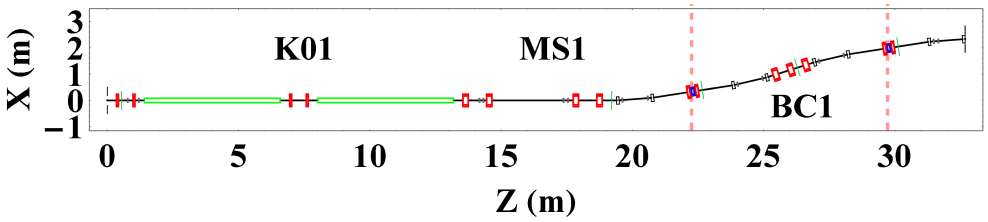

Figure 5.1: Schematic of the first MAX IV beamline section, comprised of: the first accelerating structure, K01, which accelerates the electron bunch from ∼100 MeV to ∼240 MeV; a matching section, MS1, used to control the machine optics going into the bunch compressor; and the first bunch compressor, BC1, which longitudinally compresses electron bunches down to sub-ps r.m.s bunch lengths. Dipole magnets are indicated in white, quadrupoles are in red, sextupoles are in blue, and accelerating structures are shown in green. The green markers correspond to screen locations. Sextupoles varied in one of the parameter scans carried out in the MAX IV CSR experiment are highlighted with dashed red lines.

The first acceleration stage of the MAX IV linac is carried out in a structure henceforth referred to as K01. The K01 structure consists of two individual units, which are controlled by the same linac phase offset (Figure 5.1). The electron bunch used at the start of the MAX IV accelerator in simulations has a transverse normalised emittance of 0.371 mm · mrad and 0.408 mm · mrad in the horizontal and vertical planes respectively; the true emittance of the injected MAX IV beam

has not been measured, but is expected to be significantly larger given the idealised cylindrically-symmetric initial bunch distribution supplied to the `elegant` lattice. In order to prevent the creation of a transverse energy correlation due to the off-axis accelerating field in K01, the electron beam size must be constrained within the K01 units. Because the initial β-function of the injected distribution is large and the beam is divergent, the first two quadrupoles preceding K01 have a relatively large field gradient ($|k_1| \sim 10\ \mathrm{m}^{-2}$) to ensure constantly convergent β-functions in both transverse planes throughout the accelerating structure (Figure 5.2).

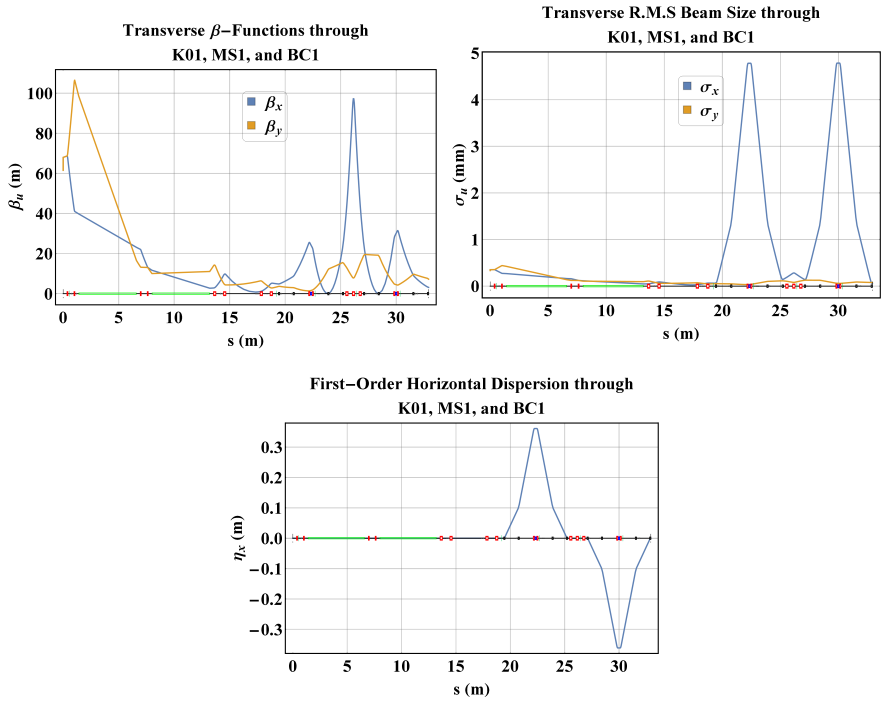

Figure 5.2: Transverse β-functions and corresponding r.m.s transverse beam sizes from the injector exit through to the exit of the first bunch compressor, BC1. The injected bunch is strongly focused by the quadrupole doublet preceding the first unit of K01 in order to prevent transverse beam blow-up within the K01 units. Dispersion control within BC1 is facilitated by the quadrupole component of the BC1 dipoles and the quadrupole doublets at the centres of the two BC1 achromat structures.

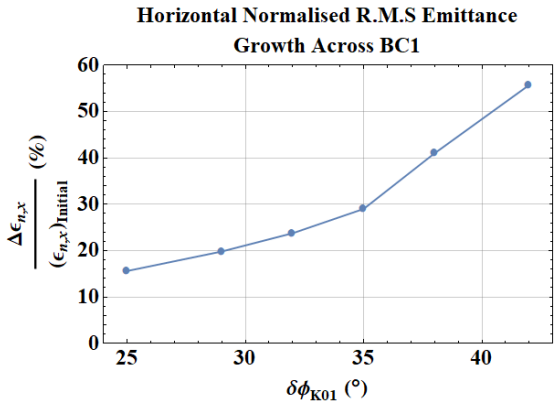

Figure 5.3: Emittance growth across the BC1 dogleg with respect to the phase offset applied to the K01 accelerating field. As the bunch is compressed, the horizontal and longitudinal planes become coupled, permitting an exchange of longitudinal beam emittance to the transverse plane.

Dispersion control through BC1 is facilitated using the quadrupole doublets within the two achromat structures of BC1. Because the dipoles of BC1 are combined function, their quadrupole component provides an additional component to this dispersion minimisation (Figure 5.2). 2^{nd}-order dispersion correction is carried out by the sextupoles situated at the achromat centres. The matching section preceding BC1, MS1, is used to symmetrise the transverse lattice functions across the bunch compressor and further minimise the second-order dispersion. The sextupoles also perform the function of linearising the electron bunch's longitudinal phase space (LPS), although the degree to which this is achieved is dependent upon the phase offset applied to the K01 accelerating field. This linearisation control forms the basis of one of the parameter scans conducted in the MAX IV experiment. Significant increases in the horizontal beam emittance are observed due to compression in BC1, with the emittance growth increasing monotonically with respect to an increasing positive phase offset (Figure 5.3).

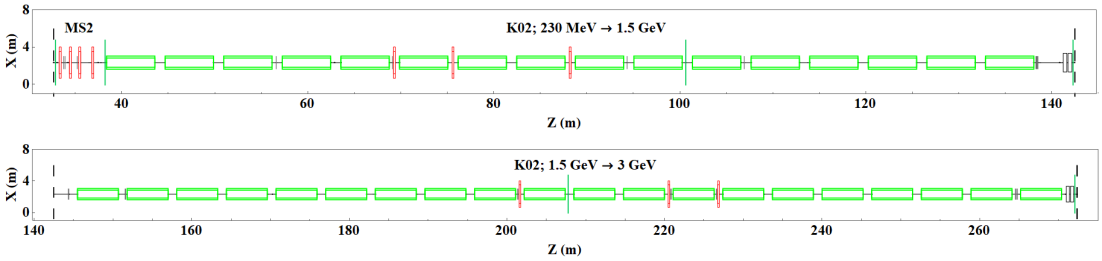

Figure 5.4: Schematic of the second accelerating structure of the MAX IV linac, K02. The preceding matching section facilitates optics control through the 232 m long structure to prevent transverse beam beam blow-up. K02 is split into two separate sections, with final beam energies of 1.5 GeV and 3 GeV. Between these is a straight section and dipole used for extraction of the beam to the two synchrotron rings. Both of these dipoles are switched off during SPF operation. Dipole magnets are indicated in white, quadrupoles are in red, and accelerating structures are shown in green, with green markers corresponding to screen locations.

Bunches compressed within BC1 then continue into the second matching section of the MAX IV lattice, after which they are accelerated to 3 GeV across two main sections. The first of these accelerates to 1.5 GeV through 16 individual accelerating units, and the second accelerates to 3 GeV through a further 20 units. Here, the transverse beam sizes are once again constrained to prevent the electron beam's transverse size from growing too large and thus incurring transverse energy correlations (Figure 5.5). This optics control is carried out using a preceding matching section, MS2, and several quadrupole magnets interspersed between the individual accelerating units of K02 (Figure 5.4).

A third matching section, MS3, follows K02, used to control the optics across the second bunch compressor, BC2. The quadrupoles in this section were altered from the matched "reference" lattice in an attempt to recreate the transverse distribution seen on screens at the BC2 entrance, centre, and exit. The design of BC2 is similar to that of BC1, with achromat sections at the start and

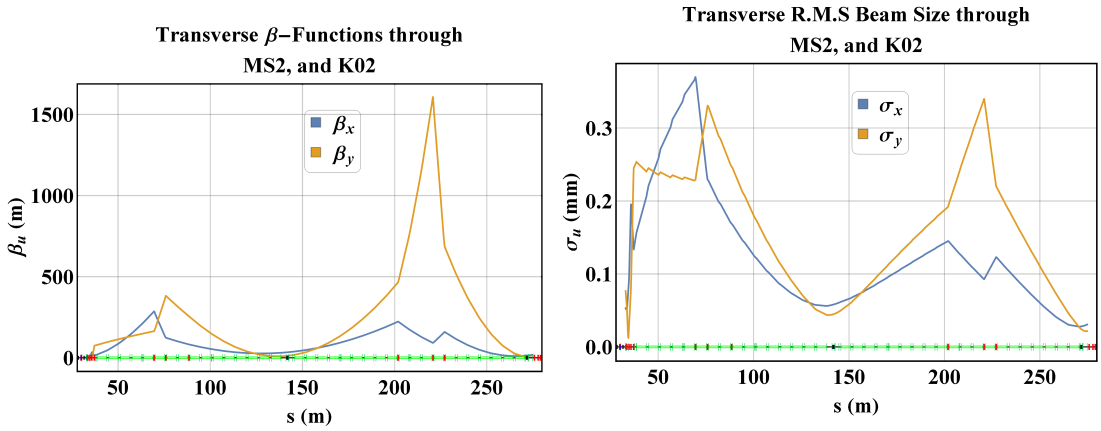

Figure 5.5: Transverse β-functions and corresponding r.m.s transverse beam sizes from the exit of BC1 through to the exit of K02. The large values seen in the β-function arise from decreases in the r.m.s emittance due to the increase in γ.

end to minimise dispersion across the structure (Figure 5.6). As with BC1, at the centre of each achromat is a quadrupole doublet and a sextupole for 2_{nd}-order dispersion control, and the BC2 dipoles are also combined function to aid in dispersion minimisation. A dispersion-free section in the dogleg contains a quadrupole triplet used for symmetrising of lattice functions across BC2 (Figure 5.7). These quadrupoles were also varied from their "matched" values to recreate transverse beam distributions seen during the experiment.

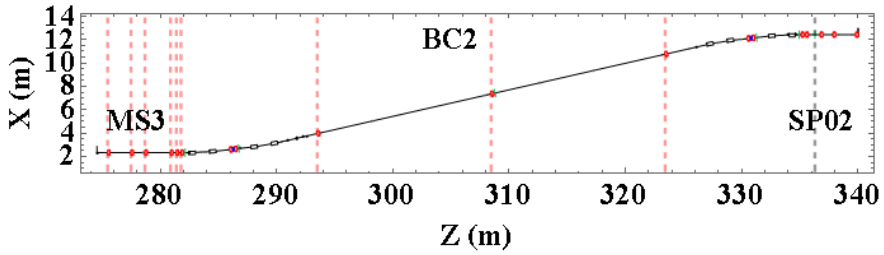

Figure 5.6: Schematic of the MAX IV SPF beamline, from the exit of K02 up to the measurement location. Dipole magnets are indicated in white, quadrupoles are in red, and sextupoles are in blue. The green markers correspond to screen locations. The dashed red lines indicate the location of quadrupoles varied in re-matching the lattice to measured screen images from the experiment. The dashed grey line indicates the location of the CSR detection system.

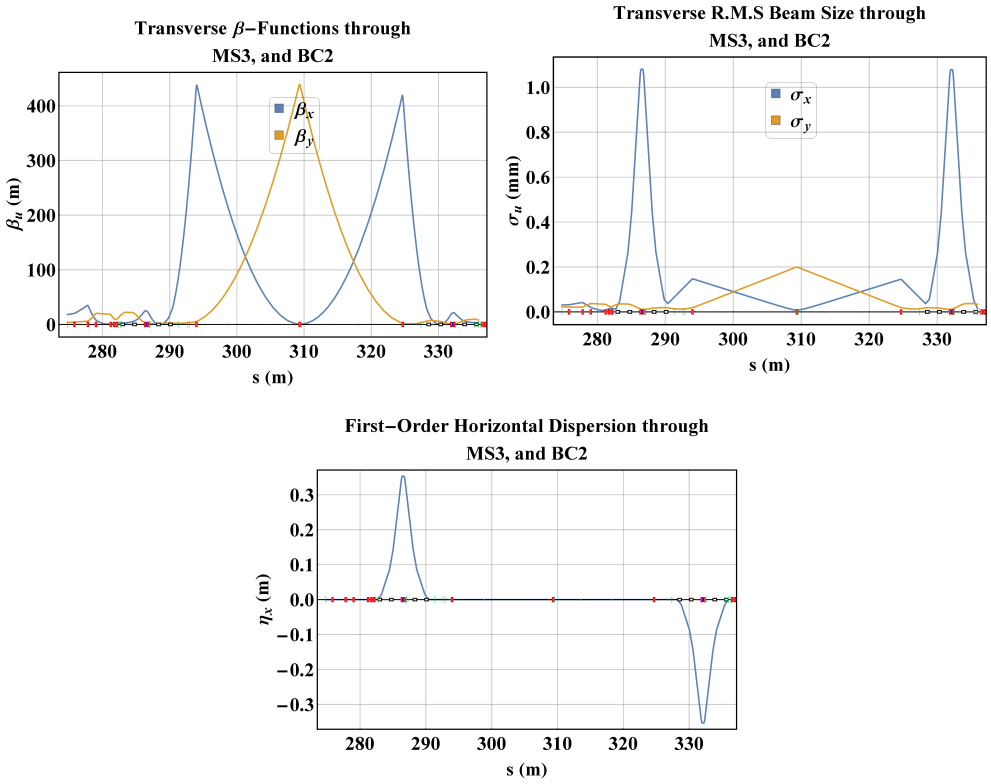

Figure 5.7: Transverse β-functions, corresponding r.m.s transverse beam sizes, and horizontal dispersion from the exit of K02 through to the exit of BC2. As with BC1, the preceding matching section optics and dispersion free optics at the compressor centre are used to symmetrise the transverse lattice function, aiding in 2$^{\text{nd}}$-order dispersion correction.

Similarly to BC1, significant transverse emittance growth is observed across BC2 due to the compression process, with the horizontal emittance more than doubling across the structure at maximal compression (Figure 5.8). Downstream from BC2 is the SP02 beamline, which delivers highly compressed electron bunches to the FemtoMAX experiment. The experimental apparatus used for CSR measurements is installed on this beamline, 1.67825 m downstream from the final bunch compressor dipole (Figure 5.6). The expected beam parameters at the exit of BC2 are summarised in Table 5.1.

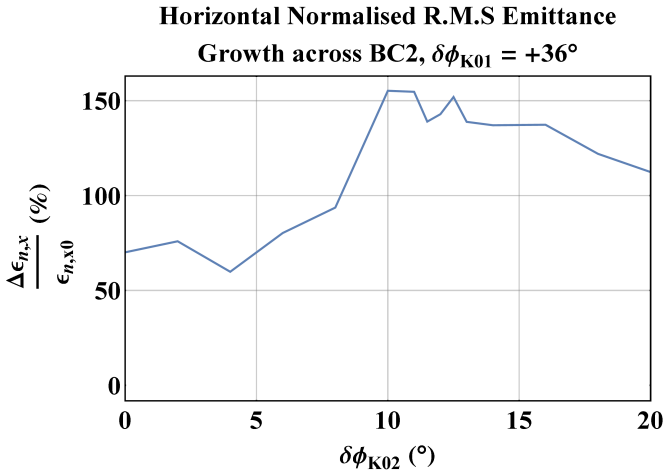

Figure 5.8: Emittance growth across BC2 with respect to the phase offset applied to K02. The phase offset applied to K01 in this case is close to the maximal compression phase.

Table 5.1: Summary of statistical beam parameters from `elegant` simulations at the exit of BC2. The bunch charge stated has been taken from charge measurements carried out in the experimental period.

Beam Parameters	
Bunch Centroid Energy	3 GeV
Bunch Charge	∼80 pC-100 pC
Bunch R.M.S Energy Spread	∼1 MeV-13 MeV (0.05%-0.4%)
Bunch R.M.S Bunch Length	∼10 fs-400 fs
Bunch R.M.S Horizontal Size	∼15 µm-40 µm
Bunch R.M.S Vertical Size	∼30 µm-35 µm
Bunch R.M.S Normalised Horizontal Emittance	∼0.5 mm · mrad-3.2 mm · mrad
Bunch R.M.S Normalised Vertical Emittance	∼0.5 mm · mrad-0.6 mm · mrad

5.2 CSR Detection System

The detection system was installed in the SPF hall of the MAX IV facility, which houses the last half of the second bunch compressor and the SP02 beamline, which is terminated by a beam dump dipole (Figure 5.6). A gold-plated target installed 1.678 m downstream from the exit of the final bunch compressor dipole was designed to facilitate the generation of CTR, but also functioned as a mirror for the radiation generated by the beam as it left the bending magnet. This shall henceforth be referred to as the mirror (Figure 5.9). The mirror is angled at 45° to the beam propagation axis, which is the preferential angle for CTR generation and emission perpendicular to the beamline axis but also enables reflection of CSR along a perpendicular path, and is gold-plated in order to facilitate reflection of THz radiation. The mirror is flat to a tolerance of 633 nm, which is well below that required for effective imaging of THz radiation. Actuators enable the mirror to be raised partially or fully out of the beam path from the MAX IV control room. The proximity of the detector system to the final bunch compressor dipole mandated the use of lead shielding to block X-ray synchrotron emission,

which would otherwise pollute data and cause damage to some of the system components.

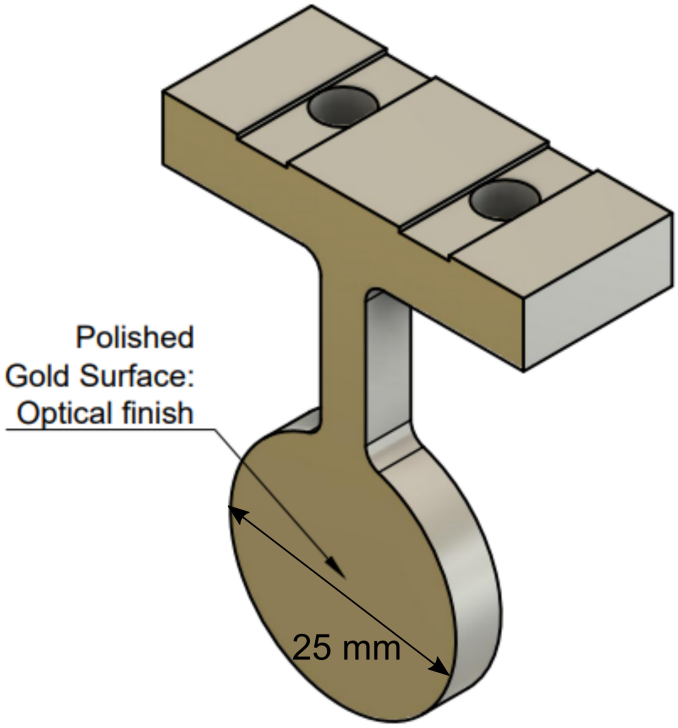

Figure 5.9: Target designed for the generation of CTR and capture of CSR emitted from the final BC2 dipole fringe field. Gold plating was selected to permit reflection of THz radiation. Image courtesy of Thomas Pacey [152].

A Z-cut quartz view port with a window thickness of 3.5 mm is situated at the mirror location. As before, this permits transmission of both optical and THz frequencies (Figure 4.38), but once again the data available corresponds to the transmission through a thinner sample than was used in the view port. Despite the relatively high transmission coefficient within the THz band, a reduction in the total signal power of anywhere between 20% and 50% is expected due to the window, with the fraction dependent upon the spectrum of the incident radiation.

As before, reflection is assumed the dominant source in the loss of transmission through the 3.5 mm window.

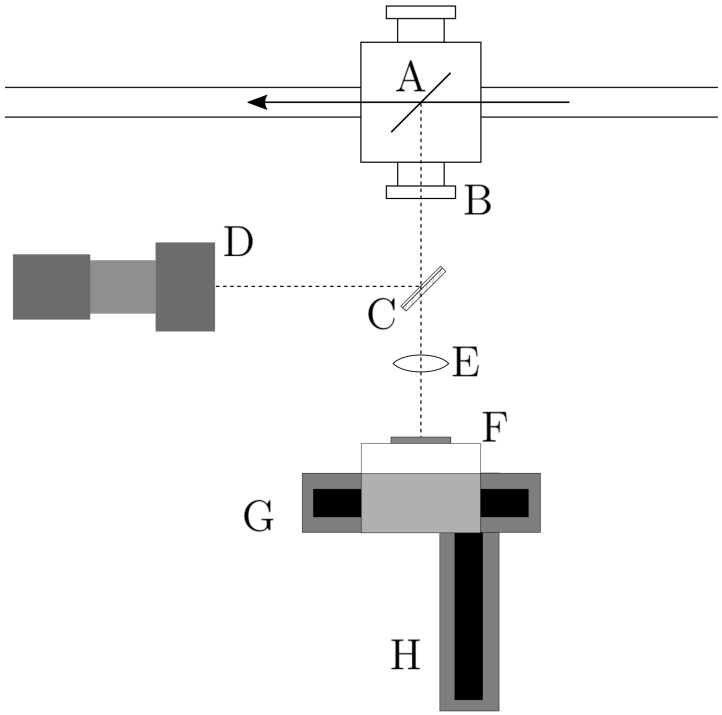

Figure 5.10: Schematic layout of the THz detection system: A - Gold-plated mirror; B - Z-cut quartz view port; C - Pellicle beamsplitter; D - CCD fitted with macro lens; E - TPX lens; F - Pyroelectric pixel array and mounting; G - Transverse alignment stage; H - Longitudinal focusing stage.

The detection system consisted of two optical axes, one for the detection of optical radiation, and the other for THz. A 5 µm beamsplitter is used to isolate optical wavelengths, which were measured using a CMOS detector fitted with a macro lens (Figure 5.10); radiation wavelengths significantly larger than the beamsplitter thickness passed through the element unaffected, thus maximising the THz power available along the THz-detection axis. This part of the system was used for imaging of OTR generated by the mirror, ensuring that the beam

was either fully hitting the mirror for CTR measurements or that conversely no OTR generation is observed for CSR measurements (Figure 5.11).

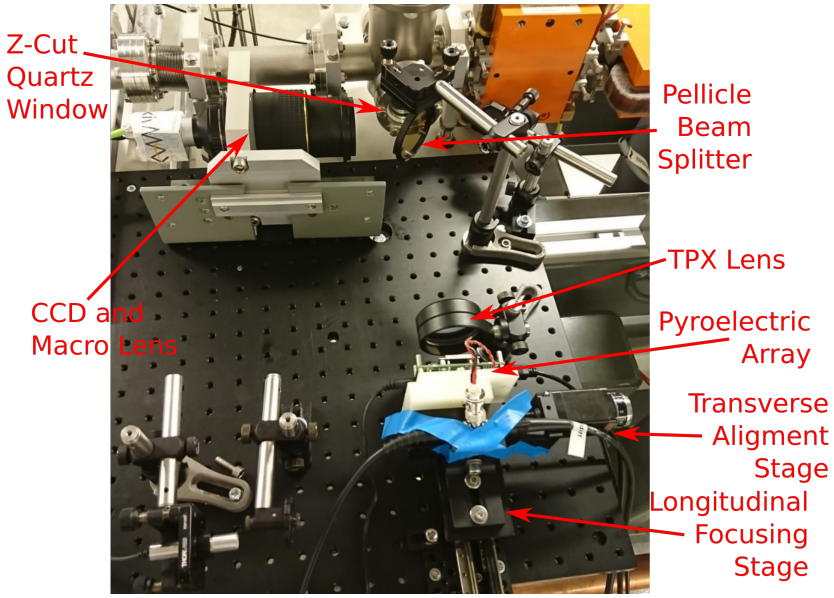

Figure 5.11: Top-down view of THz detection system. In the bottom right is the pyroelectric array mounted onto the bi-axial translation system. Positioned right in front of the detector is the 50 mm TPX lens. The large CCD and macro lens assembly is seen in the top left, while top-right shows the Z-cut quartz view port and pellicle beamsplitter.

The DIAS linear array consisted of 256 42 µm×100 µm pixels. Between each pixel was a laser-etched groove which suppressed thermal cross-talk between individual pixels, which results in a total pixel pitch of 50 µm. The pyroelectric crystal layer is 5 µm thick, and is mounted upon a CMOS multiplexer array to enable fast readout of pixel voltages to an evaluation board. Such a thin layer of pyroelectric crystal is easily eroded by optical wavelength, including both HeNe alignment laser light and typical electronic ambient lightning. As such, all pyroelectric arrays are fitted with a window (hereafter referred to as the detector

window) to filter out short wavelength radiation, with the detector window material selected according to the requirements of the application. The selection of appropriate detector window materials is limited to materials which can be easily machined into sufficiently thin wafers to be fitted onto the detector head; a high-resistivity float-zone silicon (HRFZ-Si) was selected for this application [153] given its broad spectral transmission region ($\lambda \gtrsim 1$ µm). Permitted wavelengths are typically attenuated by ∼55% for the TYDEX wafers sourced [153] for the detector window material.

As has been previously stated, pyroelectric crystals are typically more sensitive to THz radiation than more conventional infra-red cameras, especially for the radiation pulse energies expected in this experiment. However, the small size of the individual pyroelectric pixels used in the linear detector array means that a low-density radiation distribution may struggle to overcome the natural noise level on the individual pixels. This is further compounded by the approximately-known attenuation brought about by both the Z-cut quartz and HRFZ-Si windows, reducing the detectable power by anywhere between ∼55%-75%. As such, focusing elements are required to achieve the signal strength necessary for reliable detection of THz radiation on the detector. In the case of both CTR and CSR, the expected radiation spectrum is very broadband up to wavelengths on the order of the bunch length, and it follows that any optical elements used in the detection system must have both good transmission in the THz region of the electromagnetic spectrum, and have a refractive index relatively independent of the wavelength of the incident radiation to avoid chromatic aberrations in the detected radiation distribution. As such polymethylpentene (PMP), or TPX, a trade name by which it is more commonly referred, lenses were used in the optical

set-up; the refractive index of TPX is approximately invariant with respect to frequency, varying by around 0.001 (≈0.07%) [154, 155] between 1 THz and 4 THz. The power absorption coefficient at THz-wavelengths varies more strongly with respect to frequency, varying by between ∼0.75 cm^{-1} [155] to ∼1.8 cm^{-1} [154] in the same frequency range. Because of this lower frequency harmonics (sub-THz) are expected to be heavily attenuated by the lens, though these are believed to be below the peak wavelengths of the emission spectrum.

Further reduction of power incident on the detector will occur due to scattering and absorption in air, given the lack of a vacuum chamber in the apparatus. Water is a significant absorber of radiation between 1.05 and 1.275 THz, and the effects are significant even at low humidities [151]. Given that the view port transmission is suppressed for frequencies greater than 6 THz, the water vapour absorbs a small but non-trivial proportion of the otherwise detectable spectrum. However, in this study this effect will be ignored due to a lack of data on the ambient conditions within the SPF at the time of measurement. The total loss of transmitted power through the three media in use (discounting air) results in a net ∼40% of the emitted power transmitted to the pyroelectric array pixels, with significantly less transmission at higher frequencies.

Alignment of the system was carried out in order to ensure that both the TPX lens and pixel array were perpendicular to the primary optical axis. By extension, it was required that the focusing stage axis was parallel to the optical axis, in order to prevent transversal drift of the radiation distribution when focusing. At the opposite side of the beam pipe to the Z-cut quartz view port was a second view port (though one not suited for THz-transmission, hereafter referred to as

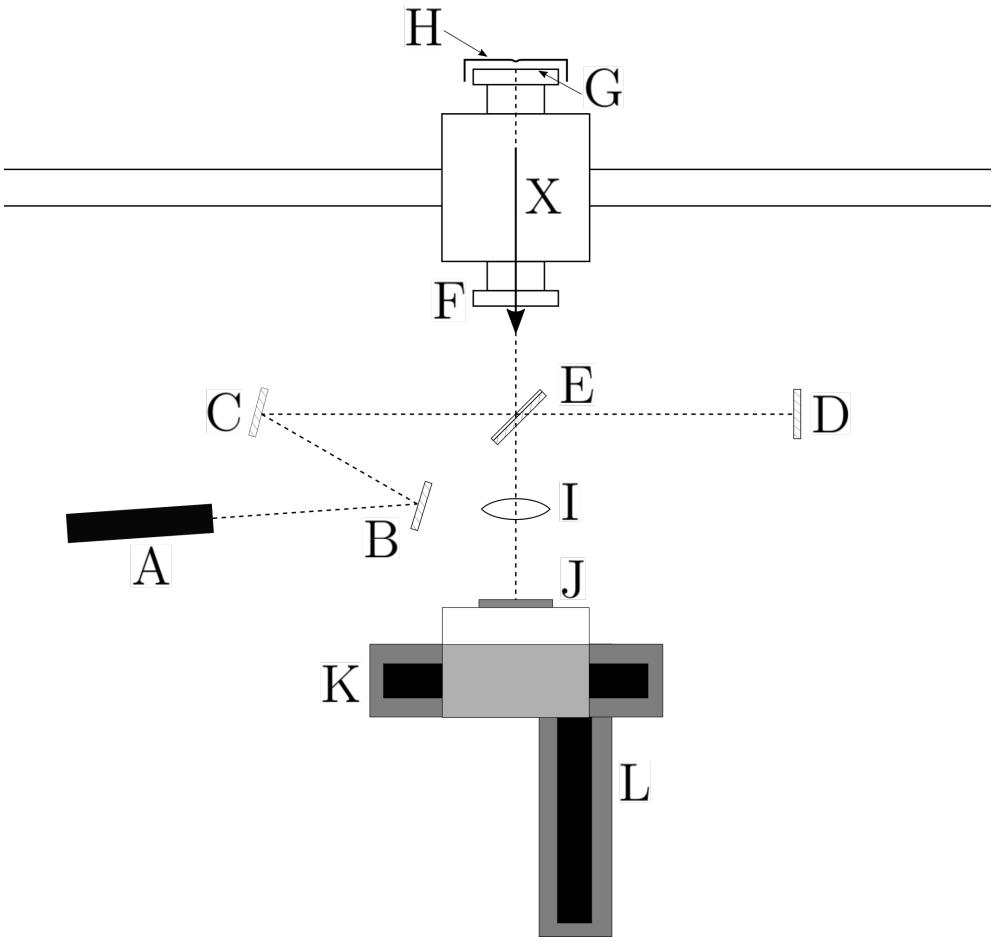

Figure 5.12: Schematic diagram of the detector alignment system: A - HeNe alignment laser; B, C, D - alignment mirrors on manual tip-tilt mounts; E - pellicle beamsplitter; F, G - view ports; H - view port cap; I - TPX lens; J - pyroelectric array and mount; K, L - translation stages (alignment and focusing respectively), X - primary optical axis.

the rearward view port. The centre points of these view ports were considered to be the fiducial in the alignment procedure. The centre was identified with the aid of a translucent cap which could be fitted over the rearward view port (Figure 5.12). The cap had a small mark at the centre, and so this could be used to define the centre point using a HeNe laser. A fundamental assumption of the alignment procedure was that the axis joining the centre points was perpendicular to the beam axis, and lay completely in the plane corresponding to

the beam pipe centre (vertically). The alignment laser was held in a V-mount, and it was necessary to ensure that the laser beam propagated within central vertical plane of the detector system, i.e. at $y = 0$. The vertical alignment was carried out simply by shining the laser directly at the view ports, using the laser spot reflected from the view ports back to the laser front face as a guide for the angular alignment and using the incident laser spot upon the translucent cap as a guide for the positional alignment of the laser. The laser was then clamped into its aligned position and angle.

The alignment laser was then moved to the side, and alignment mirrors were positioned (Figure 5.12). Each mirror was situated upon a manual tip-tilt mount, with the axis of rotation aligned to the post permitting rotation of the mirror without translation of the mirror's centre through space. The dogleg mirrors (B and C in Figure 5.12) were aligned directly to the laser in turn, followed by alignment with mirror D. A beam splitter was inserted between C and D and positioned approximately central on the primary optical axis and orientated at approximately 45°. The angle of the pellicle was then adjusted until the beam reflected from the pellicle towards the view ports and the beam re-reflected back towards the pellicle were coincident. This then establishes that the alignment laser bath is parallel to the primary optical axis. The positional alignment in the horizontal plane of the laser was not critical, given the horizontal translation stage upon which the detector was mounted. Furthermore, while effort was made at this stage to make the laser path between C and D perpendicular to the primary optical axis, this was also not essential.

After attaining a parallel laser axis, the detector and translation stage assembly was mounted to the optical board. The focusing stage was then stepped forward and backward and the transversal drift of the alignment laser spot was assessed. Appropriate corrections were then applied to the assembly until the drift was minimised, thus ensuring that the focusing stage was parallel to the primary optical axis. Following this, a 150 mm TPX lens was placed just behind the pellicle (relative to the beamline), with the laser spot approximately centred upon the lens. Once again the focusing stage was stepped forward and backwards to assure the angular alignment of the lens, with adjustments made as required.

Initial tests with the pyroelectric array showed no signal being measured with the detector. Initially, this was believed to be an issue arising from the settings of the evaluation kit itself; the user is required to adjust internal clock settings for the evaluation kit, determining when various filters and voltage integrations occurred over the detection cycle. The pyroelectric array is AC-coupled, which means that the temporal evolution of the pixel voltage typically experiences a rebound for a chopped signal of a low duty-cycle, whereby a similar voltage pulse of opposite polarity is generated across the pyroelectric crystal after the incident radiation is removed [156]. As such, too great an integration time on the evaluation kit circuit would result in the net voltage read out by the CMOS being significantly reduced. It was later determined that while this was a factor, the main issue arose from the significant reduction in the incident radiation brought about by the Z-cut quartz window. This lead to such a low energy density incident upon the individual pixels of the pyroelectric array that the detector NEP was not overcome. In order to mitigate this issue, a different optical arrangement was installed with the view to reducing the magnification of the radiation in the focal plane and thus increasing the incident energy density. As such, the

150 mm focal length TPX lens was replaced with a 50 mm focal length lens and the magnification of the system was reduced to 1/3.

5.3 Experimental Procedure

5.3.1 SLEDs

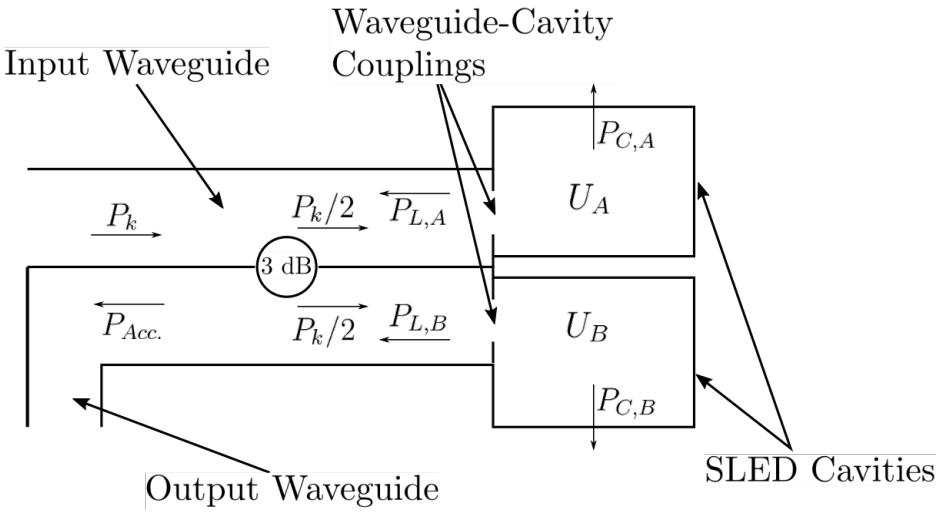

Figure 5.13: A schematic diagram of a SLED RF network. Here, P_k is the power delivered from the klystron, $P_{L,A}$ and $P_{L,B}$ are the net powers redirected back along the waveguide from cavities A and B respectively, $P_{C,A}$ and $P_{C,B}$ are the power losses from the cavity walls of A and B respectively, $U_{C,A}$ and $U_{C,B}$ are the energies stored within A and B respectively, and $P_{Acc.}$ is the power delivered from the SLED to the accelerator. The circle with the label "3 dB" represents the 3 dB directional coupling between the two waveguides.

In order to maintain the electron beam energy throughout the experimental study, it was necessary to vary the accelerating gradient within the accelerating sections of the MAX IV Linac. The large accelerating gradient of the two structures at MAX IV is sustained using SLAC Energy Doublers (SLEDs) [157]. A SLED consists of 2 high-Q resonant cavities terminating parallel wave-guides, one

leading from the klystron and one leading to the linac (Figure 5.13). The waveguides are connected by a 3 dB coupler, a four port waveguide coupling which equally distributes power from from a given input port to the two opposite ports while preventing any power flow to the off-axis port on the same side [158]. The 3 dB coupler additionally imparts a path length difference to the wave entering the translated (off-axis) output port such that the wave is $\frac{\pi}{2}$ out of phase with the on-axis output (Figure 5.14).

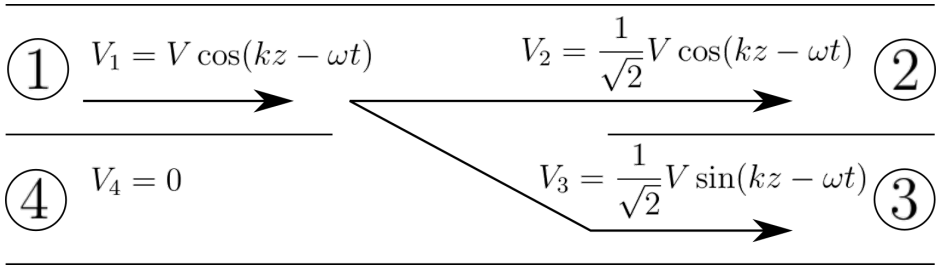

Figure 5.14: A 3 dB directional coupler schematic. Input power from port 1 is split equally between ports 2 and 3, with no power directed towards port 4. The path length difference between the output waves of port 3 and 2 results in a $\frac{\pi}{2}$ phase difference between the outputted waves. The factor of $\frac{1}{\sqrt{2}}$ arises from the fact that the power, $P \propto V^2$.

RF power is transported from the klystron along the input waveguide towards the SLED network, with half of the power directed towards each cavity by the 3 dB coupler. As the incoming electric field hits the waveguide-cavity coupling, the majority of it is reflected back, such that

$$E_R = \frac{1}{\sqrt{2}} R E_k,$$

where R is the reflection coefficient, E_k is the electric field entering the SLED (prior to being divided by the 3 dB coupler), and E_R is the reflected wave. The factor of $\sqrt{2}$ arises from the fact that the electric field $E \propto \sqrt{P}$, where P is the power. In practice the reflection is almost total by design, and henceforth the

assumption that $R = 1$ will be made [159]; the consequence of this total reflection is that the reflected wave is π out of phase with the incoming wave. A small part of the RF power enters the cavity, increasing the energy stored within. As it does, the cavity loses energy both to the cavity walls and through field emission back through the waveguide-cavity coupling. By conservation of power [159],

$$\frac{P_k}{2} = P_L + P_w + \frac{dU}{dt}, \tag{5.1}$$

where P_k is the power output from the klystron, P_L is the net output from the waveguide-cavity coupling (the reflected wave and the emitted), P_w is the power lost to the cavity walls, U is the energy stored in the cavity. By writing the power of a given wave as proportional to the square of the field, with the constant of proportionality being represented by ξ, Equation 5.1 becomes

$$\frac{\xi E_k^2}{2} = \xi(E_e - \frac{E_k}{\sqrt{2}})^2 + P_w + \frac{dU}{dt}, \tag{5.2}$$

where E_e is the electric field of the emitted wave. The minus sign in the term representing the total cavity output arises from the π phase difference between the emitted and reflected components. The stored energy is related to the dissipated power by

$$P_w = \frac{\omega U}{Q_0},$$

where *omega* is the resonant frequency of the SLED and Q_0 is the Q-factor of the cavity. The ratio between the power emitted from the coupling and the power dissipated in the cavity walls is defined by the cavity coupling coefficient β [160, 161], such that $\xi E_e^2 = \beta P_w$. Using these relations in combination with Equation 5.2 yields the differential equation

$$\tau_c \dot{E}_e + E_e = \alpha \frac{E_k}{\sqrt{2}},$$

where $\tau_c = \frac{2Q_0}{\omega(1+\beta)}$ is the cavity time constant, $\alpha = \frac{2\beta}{1+\beta}$, and the dot operator represents the time-derivative. The SLED operation cycle consists of three phases. The first phase is the filling phase, wherein the initially empty cavity is filled with energy up to the time t_1, known as the SLED fill time. During this phase, the net output field of from the waveguide-cavity coupling is given by [159]

$$E_L = \frac{E_k}{\sqrt{2}} \left[\alpha(1 - e^{-t/\tau_c}) - 1) \right].$$

Here, the first term corresponds to the field emitted from the waveguide-cavity coupler due to the energy contained in the SLED cavity, and the second term corresponds to the electric field reflected from the coupler itself. The assumption has been made that the klystron output field's polarity is positive in the filling phase.

An important design consideration of the SLED is that the two SLED cavities are identical, resulting in $E_{out,A} = E_{out,B}$, where the labels A and B refer to the cavities on and off-axis relative to the input wave from the klystron respectively (Figure 5.13). The output field from cavity B going back towards the klystron undergoes two $\frac{\pi}{2}$ phase shifts relative to that from cavity A, meaning that the two output fields are π out of phase with one another. This results in no net field being directed back towards the klystron (and thus no power), preventing damage to the klystron. Instead all output power from the SLED network is directed towards the accelerating cavities, corresponding to $P_{Acc.} = \xi(2E_L)^2$. During the

filling phase, in the limit of infinite filling time, the output field changes polarity exponentially until the SLED cavity fields are saturated. During this phase, the magnitude of the output power is always less than the power output of the klystron itself.

The second phase ($t_1 \leq t$) of the SLED cycle is initiated by applying a π phase shift to the klystron field rapidly. By once again solving Equation 5.3.1 for the appropriate boundary conditions, the total field supplied by a single SLED cavity to the accelerator is

$$E_L = \frac{E_k}{\sqrt{2}} \left[\gamma e^{-(t-t_1)/\tau_c} - \alpha + 1\right], \tag{5.3}$$

where $\gamma = \alpha \left(2 - e^{-t_1/\tau_c}\right)$. Upon inspection of Equation 5.3, the output of the SLED network at $t = t_1$, in the limit of $\tau_c \ll t_1$, is amplified by a factor of $1 + \alpha$ relative to the klystron output. For large values of β $\alpha \approx 2$, and in this regime the SLED effectively triples the power supplied to the accelerating cavity for a small fraction of the full SLED cycle, which permits the high field gradients used for electron acceleration.

During the final phase of the SLED cycle ($t_2 \leq t$) the klystron is switched off, following which the output field from each of the cavities is governed by an exponential decay, such that

$$E_L = \alpha \frac{E_k}{\sqrt{2}} \left[\gamma e^{-(t_2-t_1)/\tau_c} - 1\right] e^{-(t-t_2)/\tau_c}.$$

The SLED network at MAX IV uses a variable fill time between 2.5-4 µs, which permits a 5 MeV m^{-1} margin above the nominal accelerating gradient of

15 MeV m^{-1}. The nominal klystron output power is 35 MW with a full RF pulse length of 4.5 µs [162]. The SLED system employed at MAX IV permits a factor of 6 increase in the instantaneous power supplied to the linac following the klystron phase shift.

5.3.2 Parameter Scans

Following the optimisation of the THz-detection system, scans of machine parameters were carried out. The linacs K01 and K02 control the compression in the first and second bunch compressors (BC1 and BC2) respectively via the linac field phase offset, and initially both of these parameters were varied to provide a broad characterisation of the bunch length variation. In order to perform this scan, the crest phases of both structures must be determined. While the crest was found to be fairly stable, this measurement was carried out at the start of each set of measurements to account for any drift of the crest. Measurement of the crest was carried out manually, by using screen images in BC1 and BC2 to measure the centroid offset variation with respect to crossing phase in a dispersive region.

The diffusivity of the beam's transverse profile in the dispersive region as well as visible non-linearities in the screen image (potentially arising from kinks or hooks at the head and tail of the longitudinal phase space) give rise to a potential uncertainty when determining the location of the centroid within the beam profile. This in turn will lead to uncertainty in the measurement of the crest phases of both K01 and K02. While scanning the two phases, the energy was maintained by increasing the SLED fill time for each of the structures (thus raising the field peak-gradient). This was informed by the bunch trajectory through

each bunch compressor, which showed little deviation from the central axis when the beam was at nominal energy.

A more focused scan of $\delta\phi_{K02}$ was carried out following the broad characterisation of the machine parameter-space. In this scan, the phase of K02 was kept constant at $+35^\circ$ from the crest phase. K02 was chosen over K01 for this fine scan due to practicalities in the accelerator operation; variation of K01's phase offset required significant adjustment of the MAX IV linac optics to maintain good beam transport through K02, whereas variation of the K02 phase offset required little to no adjustment of the optics in the downstream beamline. Further to this, K01 typically operates far away from crest; at these phase offsets, a large increase in the field amplitude is required to compensate for the momentum loss. The SLED fill time was typically maximised at around $\delta\phi_{K01} = 32^\circ$ when accelerating a beam to 250 MeV. Beyond this point it was necessary to adjust all downstream optics, and compensate for the energy loss by further increasing the K02 SLED fill time in order to accelerate the electron bunch to 3 GeV. As K02 typically operates considerably closer to the crest phase, it proved far more time-efficient to simply vary the compression in the BC2.

Variation of the linac phase offsets necessitated orbit correction in order to centre the beam on the mirror, typically indicated by the image upon the OTR camera. In order to determine the optimum detector position, the CTR signal was measured (mirror fully inserted) whilst stepping through the detector's horizontal translation. A typical CTR signal is annular and cylindrically symmetric, resulting in a symmetric double-peak signal when incident upon the linear array; the detector was assumed correctly aligned (i.e. perpendicular to the THz-axis)

when the CTR signal displayed symmetric peaks. Furthermore, the detector was assumed centred on the radiation distribution when the CTR peaks were maximally separated.

Measurement of the CSR signal was carried out by partial extraction of the mirror, typically around halfway ($\delta y_{mirror} = 13$ mm). At the same time, vertical corrector magnets were used to kick the beam beneath the target. In order to verify the lack of CTR generation, an optical fibre beam-loss monitor was used to follow the electron shower generated by the 3 GeV hitting the mirror. When the signal from the shower dropped to zero, the beam was assumed to be completely passing beneath the mirror (Figure 5.15).

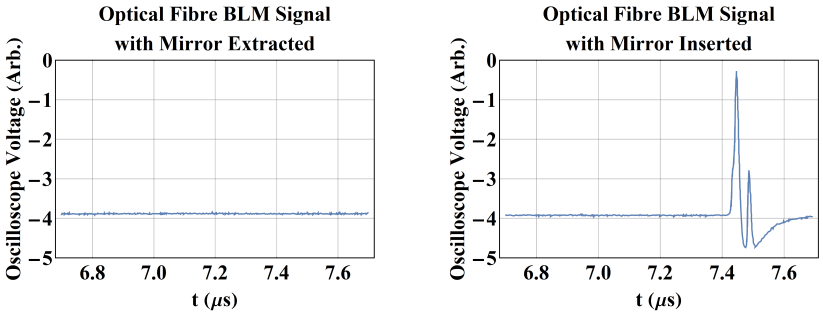

Figure 5.15: Optical fibre BLM readout with the mirror fully extracted and inserted. When no signal was observed the beam was assumed to be fully passing beneath the mirror edge.

Coherent diffraction radiation (CDR) is expected to be generated at the bottom edge of the mirror. A conventional model for a CDR detection system is the ceramic gap, which consists of a short ceramic section of beam pipe. The change in medium between the metal and ceramic beam pipe results in radiative emission at the media boundaries. This has been modelled by Veronese *et al.* in

[163], which uses an analysis based on a semi-infinite waveguide model set out in [164] that treats the ceramic gap a such wave-guides separated by a free-space gap of length l. Using this model in the limit of radiation wavelengths significantly smaller than the beam pipe, the angular-spectral energy distribution of the radiation emitted from the ceramic-conductor boundary by the passage of a single electron can be analytically approximated as [163]

$$\left(\frac{d^2W}{d\Omega d\omega}\right)_{DR} = \frac{\beta q^2}{4\pi^2 c}\frac{\sin^2\theta J_0^2\left(\frac{\omega}{c}a\sin\theta\right)}{(1-\beta\cos\theta)^2 I_0^2\left(\frac{\omega a}{\beta c\gamma}\right)}\left|\sqrt{\frac{1-\beta}{1-\cos\theta}}e^{i\frac{\omega l(1-\beta\cos\theta)}{\beta c}}\right. \\ \left. +i\sqrt{\frac{1+\beta}{1+\cos\theta}}e^{-i\frac{\omega l(1-\beta\cos\theta)}{\beta c}}\right|^2. \tag{5.4}$$

CDR is analogous to CSR, insomuch as the single-particle angular-spectral density is modulated by a form-factor equivalent to the Fourier-transformed normalised current distribution (Equation 2.60). As such, the CDR angular-spectral density for a Gaussian longitudinal current profile, in the limit where the beam's transverse size $\sigma_r \ll a$, is given by

$$\left(\frac{d^2W}{d\Omega d\omega}\right)_{CDR} = \left(\frac{d^2W}{d\Omega d\omega}\right)_{DR}(N + N(N-1)|F(\omega)|^2) \tag{5.5}$$

$$= \left(\frac{d^2W}{d\Omega d\omega}\right)_{DR}(N + N(N-1)e^{-\left(\frac{\omega\sigma_z}{c}\right)^2}). \tag{5.6}$$

The generation of CDR from the bottom edge of the mirror is of course significantly different from the idealised waveguide-gap model. Because the cylindrical symmetry of the ideal case is not preserved in the conditions being discussed it is reasonable to assume that the CDR emission will be comparatively suppressed,

and so calculations for an idealised ceramic-gap pose an upper limit on the expected strength of the CDR emission in the MAX IV detection apparatus. As it happens, using approximations to the beam-mirror distance as a value for a and half the mirror thickness for values of l in Equation 5.4, numerical integration of Equation 5.6 yields a typical total energy-per-pulse of $\sim 10^{-13}$ J, which is around a factor of 10^{-6} less than the energy per-pulse emitted from the final dipole exit predicted by GPT simulations. As such, the effects of CDR can be ignored in the context of this experiment.

Although a pair of orthogonal corrector magnets are situated just upstream of the mirror, the rigidity of the 3 GeV beam was too great for these to have a significant effect upon the beam's vertical position at the mirror. Instead the final vertical corrector of BC2, 6.86 m upstream from the final dipole exit, is used resulting in a significant vertical offset in the beam at source position. This is in contention with the methodology of isolating the CSR signal, results in only a fraction of the CSR signal captured by the mirror. As such, each measurement consisted of iterative adjustment of the mirror height and the current supplied to the corrector to maximise the incident signal upon the detector without generating CTR. A scan of the signal with respect to the mirror extraction was carried out to qualitatively describe the transition between combined CTR and CSR and partial capture of the CSR (Figure 5.16).

When properly configured, the response of the pyroelectric array was very clear, requiring $\lesssim 20$ shots to achieve statistical confidence when the radiation source was strong i.e. close to bunch length minimum (Figure 5.17). Further away from the maximum compression phase, a greater number of shots was taken.

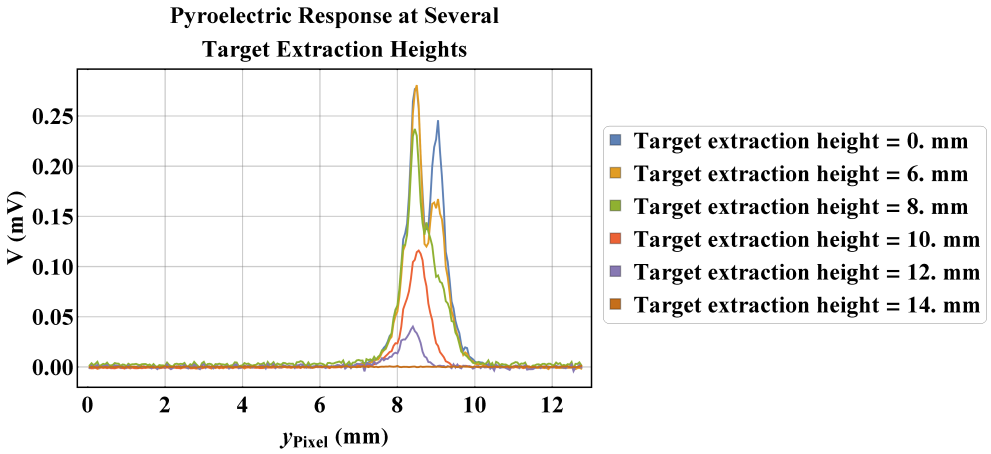

Figure 5.16: Pyroelectric detector signal at various target extraction heights. Initially, the peaks become asymmetric, as the full CTR distribution remains due to the electron beam impacting the target fully while half of the CSR emitted upstream is cut off. As the target is drawn out further, the CTR signal decreases, until only the upper lobe of the fringe field radiation remains.

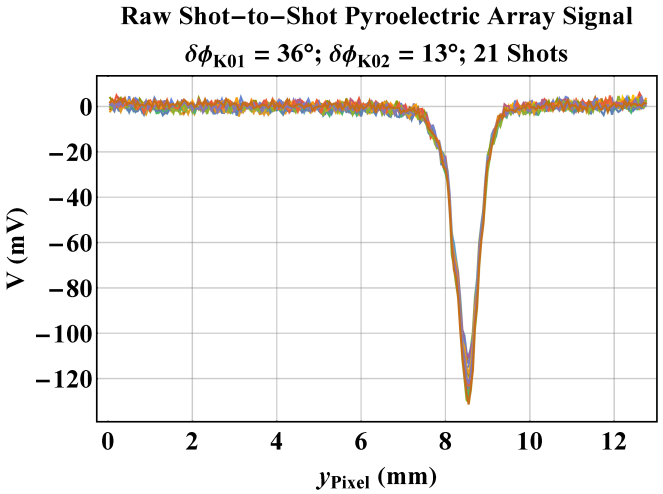

Figure 5.17: Raw shot-to-shot signal of the pyroelectric array close to maximal compression. Little variation is observed, meaning that a relatively low number of shots is required.

Alongside the phase scan of K01 and K02, a scan of the current supplied to sextupole magnets in BC1 was carried out. The compression ratio in BC1 is very high, with the phase offset applied to K01 typically in the range of 25°-35°.

As such, significant curvature is generated in the LPS of the electron bunch due to this large phase offset. As such, sextupole magnets in the BC1 structure are used to aid in the linearisation of the LPS in BC1. This linearisation has a direct impact upon the bunch profile downstream in the accelerator, which in turn leads to a variation in the emission of CSR in the bunch compressor dipoles through changes to the bunch form-factor.

In order to reconstruct the experimental conditions in simulations, for each value of both the phase scans and the sextupole scan quadrupole currents were saved for the entire MAX IV linac lattice. This was done both using the MAX IV online model (at the time in-development), as well as direct evaluation using the currents supplied to magnets and the corresponding calibration data. Alongside this, energy estimates were carried out using the online model. In order to test the ability of `elegant` to recreate the electron bunch, screen images were obtained for all set-ups from screens positioned at the start, middle, and exit of BC2. Images were also acquired of the YAG screen background, i.e. in the absence of the electron beam, for later image processing. Charge measurements are continuously acquired throughout the experimental period on a downstream current transformer.

5.4 CSR Simulations for the MAX IV Experiment

In order to recreate the experimentally observed electron bunches at the exit of BA1, normalised magnetic multipole strengths were obtained from both the online model and directly from the currents supplied to magnets in the lattice.

However, use these in the `elegant` model of the MAX IV lattice, proved unsuccessful with tracking through the linac proving unstable. This instability has been attributed to a mismatch between the real injected beam and the simulated idealised beam supplied to `elegant`.

Given the time-scale requirements for this study injector simulations with the view to recreating the real injected bunch's transverse phase space were infeasible, and the decision was made to forego recreation of the machine state during the experiment and instead approximate the bunch at the radiating location through matching to the screen images taken on BC2. This methodology assumes that the longitudinal distribution can be recreated using the matched "reference" lattice with the appropriate phase offsets applied to K01 and K02. This essentially is dependent upon three assumptions. Firstly that, while clear quantitative differences occur between the optics applied to the real machine versus optics which occur in the reference lattice, these optics essentially result in a similar bunch at key points in the accelerator. Secondly, that direct longitudinal manipulation of the bunch, i.e. linac phase offsets, bunch compressor R_{56}, and sextupole linearisation of the LPS, is reflected in the `elegant` model sufficiently accurately so as to properly recreate the bunch current profile. Finally, it must be assumed that LPS of the electron distribution used as an input to the `elegant` lattice reflects the true LPS of the electron beam at the MAX IV injector exit.

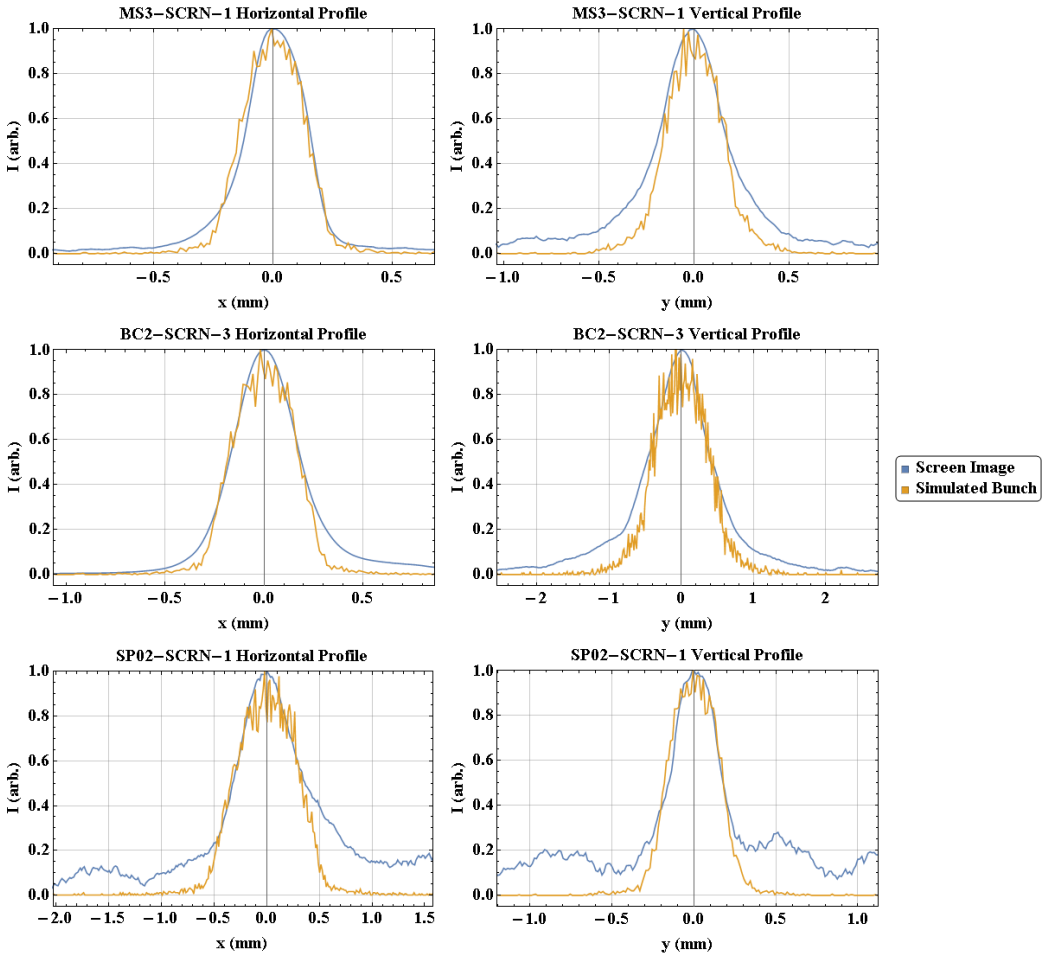

Figure 5.18: Matched profiles at screens located at the entrance (MS3-SCRN-1), middle (BC2-SCRN-3) and exit (SP02-SCRN-1) of BC2 for a bunch in the broad scan of the phase offset of K01 and K02 ($\delta\phi_{K01}$ =35°; $\delta\phi_{K02}$ =15°). While not exact, matching to the FWHM derived from screen images reproduces the transverse profile with reasonable accuracy.

The corresponding background is subtracted from each screen image taken, and then the distribution is projected onto both the x and y axes. The full-width at half maximum (FWHM) of these projected distributions is then calculated, after which the approximate r.m.s beam size is derived according to the relation for a Gaussian function, i.e.

$$(\mathrm{FWHM})_u = 2\sqrt{2\ln 2}\,\sigma_u.$$

While the transverse distribution observed is not equivalent to a Gaussian, it does form a reasonable approximation (Figure 5.18). Matching was carried out using the quadrupole triplet in the dispersion-free centre of the BC2 dogleg, and the six quadrupoles in the preceding matching section. Further to this, a TWISS element was used at the start of the preceding matching section to further allow control of the transverse bunch profile at the screen locations. The transverse r.m.s beam sizes are well matched to screen image measurements using this method, with reasonable agreement also seen in the transverse distribution shape (Figure 5.19).

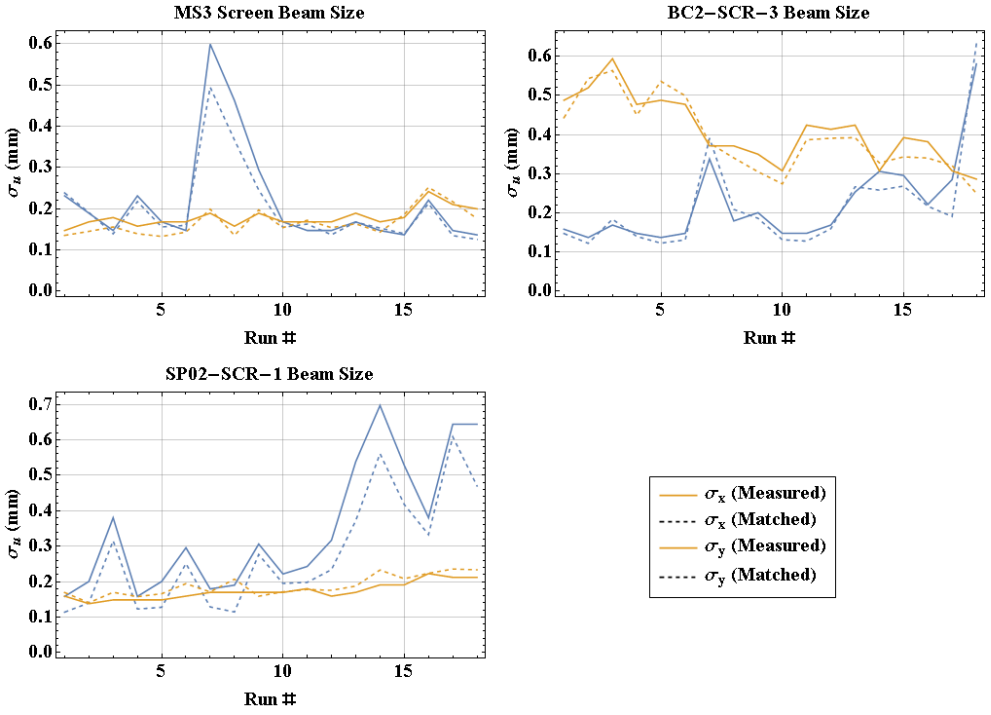

Figure 5.19: Summary of matching process for the broad scan of $\delta\phi_{K01}$ and $\delta\phi_{K02}$.

While matching to the screen images in `elegant` was successful, it yields very large non-physical emittances ($\sim 10^3$ mm $\cdot$ mrad)) across the BC2 dogleg in the case of the phase scans. It is believed that the TWISS element is primarily

responsible for this, as it was not employed in the sextupole scan which does not exhibit this emittance growth. This stems from the fact that the matched electron beam in the "reference" MAX IV `elegant` lattice has a very low emittance and transverse dimensions; increasing those dimensions to those of the realistic beam results in lattice parameters that are not well matched, which drives emittance growth across the BC2 structure arising from chromatic and dispersive effects. The emittance growth at a quadrupole due to chromaticity can be approximated by [165]

$$(\Delta\epsilon_u)_{Chrom.} \approx \frac{\epsilon}{2}(\beta_u k_1 l_q \sigma_\delta)^2,$$

where ϵ_u is the r.m.s emittance ($u = x, y$), β_u is the transverse beta function, k_1 is the normalised quadrupole focusing strength, l_q is the quadrupole length, and σ_δ is the r.m.s fractional momentum deviation. The effect of a large emittance and β-function at a quadrupole with a large focusing gradient is a significant increase in the beam emittance. As such, each parameter scan was simulated with and without this transverse matching. Both of these methods are expected to produce inaccuracy in reproducing the real electron bunch and the coherent emission; the large emittances produced by matching will suppress the CSR interaction due to the incoherent spread in transverse particle velocities and positions, while the effects of the transverse size will be neglected entirely when the matching is omitted.

The electron bunch charge is determined using archive data acquired by a downstream integrating current transformer (ICT). This archive data consists of continuous measurements taken over the course of the entire experimental period alongside the respective time of measurement for each point. The steps between

each data point are non-constant. In order to obtain a value for the charge for a given point in a parameter scan, the file date of a given data file generated by the pyroelectric array is attributed to a corresponding range within the ICT data, taken to be ±5 min from the specific file's creation date. The raw charge data contains many variations from the true bunch charge, namely arising from periods where an upstream screen is inserted, resulting in no charge measured at all; top-up periods for the MAX IV storage rings, which again result in no beam delivered to the ICT; and periods where the mirror is fully inserted, which results in a charge shower that raises the measured bunch charge. In order to isolate the correct charge delivered to the SP02 beamline, the low-charge readings are removed and the remaining charge values are binned. The result is a bimodal distribution, the lower mode of which is identified as the actual bunch charge. The average is then taken of the lower mode over the full time scale considered to produce the typical bunch charge for a scan point (Figure 5.20).

The electron bunch is extracted from `elegant` simulations 0.05 m upstream from the final dipole of BC2, and is then passed to GPT simulations for CSR calculations. As discussed in Section 3.2, the implementation of the BC2 dipole is incomplete; the BC2 dipoles are combined function, and minimising the BC2 dispersion in the final achromat requires the quadrupole moment of the dipole field to be included. This can be modelled in GPT without issue, as can the fringe fields for the multipolar magnetic field, however the BC2 dipoles are also rectangular rather than sector magnets. GPT currently does not have edge angles included for its multipolar bending magnet element, and the omission of these edge angles will have an impact on the focusing due to the dipole field, and the nature of the radiation emitted from the fringe. It is deemed most important for

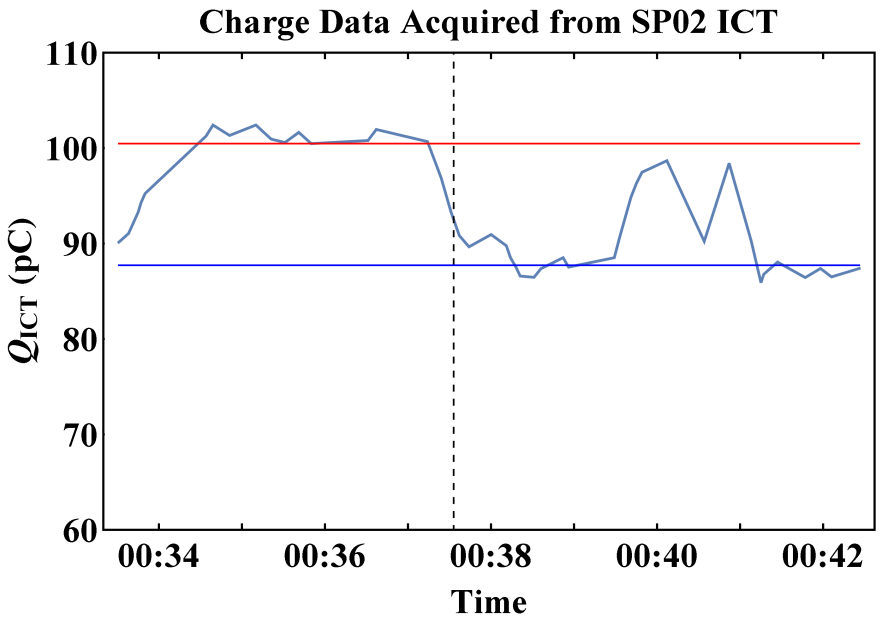

Figure 5.20: Example of the charge data acquired from a downstream integrating current transformer (ICT). The high charge level, indicated by the red line, corresponds to the charge when additional electrons are generated from the beam impacting upon the mirror. The low charge level (blue) corresponds to the actual bunch charge. The dashed vertical line indicates the time at which data was saved to a file for this particular acquisition.

the BC2 dipole to minimise the dispersion correctly in GPT simulations, and so the bending magnet's quadrupole component is optimised to do so. As a result, the projected transverse beam distribution deviates from experimental observations and `elegant` matching at the BC2 exit (Figure 5.21).

The electron bunch at the dipole exit is used to generate distributions of the x-x', y-y', and t-δ phase spaces. These distributions are then used in SPECTRA simulations to generate an expected angular distribution at the mirror location. In some cases, these distributions generate instabilities in the SPECTRA solver, and idealised Gaussian bunches needed to be employed instead, wherein the electron bunch is assumed Gaussian in all planes and is defined completely by

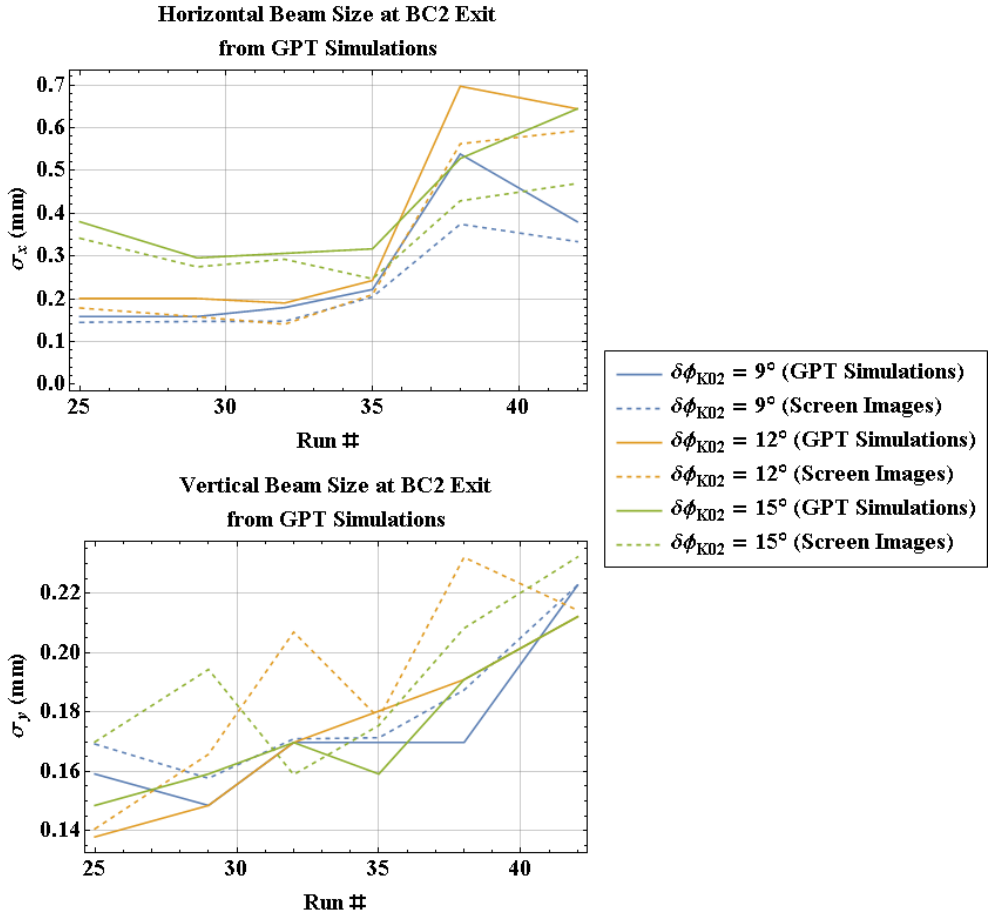

Figure 5.21: Beam size at the exit of BC2 from GPT simulations compared to measured beam profiles from screen images. The mismatch is brought about by the lack of a rectangular combined-function dipole implemented in GPT.

- its r.m.s energy spread, bunch length, and r.m.s emittance
- the centroid energy
- the bunch charge
- the lattice functions at the location where the beam is specified
- the first order dispersion and its slope where the beam is specified.

This method of course contributes to the error for some values within a given scan. A combined spectral filter is applied to the calculation, corresponding to

the net transmission due to the Z-cut quartz window, the TPX lens, and the HRFZ-Si window fitted to the pyroelectric array (Figure 5.22). The angular distribution calculated by SPECTRA is then offset according to the bunch centroid offsets observed in screen images at the BC2 exit. Centroid offsets are calculated under the assumption that the screen image is centred upon the beam pipe centre, however there is no reference marker to confirm this assumption. Only radiation that would hit the target (taking into account the target extraction height) is propagated to the lens plane. The method of propagating from the mirror location to the lens plane does not account for diffraction, and the resultant simulated angular distribution is hard-edged when compared to measurements due to the cut-off from the mirror edge.

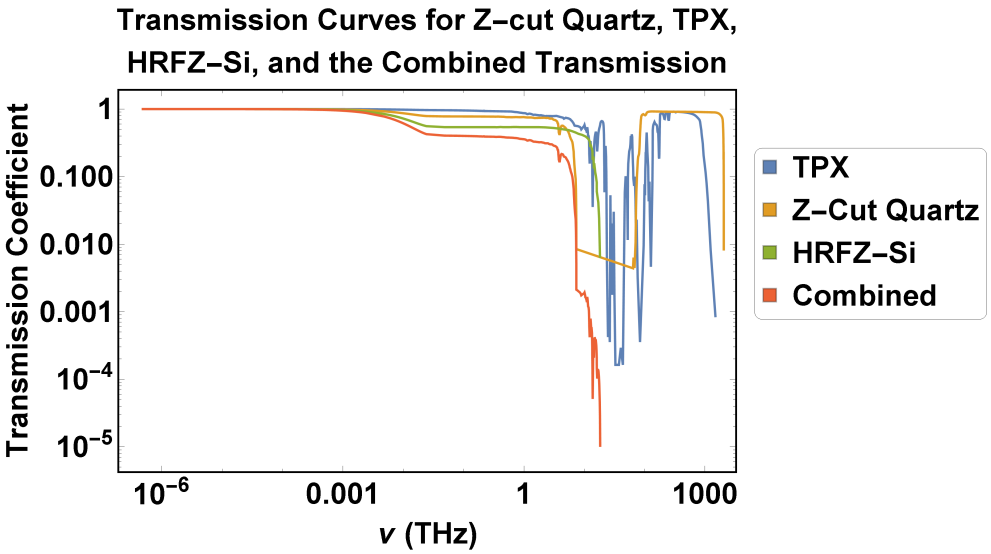

Figure 5.22: Combined spectral filter of Z-cut quartz, TPX, and HRFZ-Si. The upper limit of the detectable band is set by the Z-cut quartz transmission. The increase in the transmission at lower frequencies is a product of the interpolation used to fill in the lower frequency region of the transmission data.

In order to determine the approximate radiation distribution at the lens plane a method similar to that described in [92, 93] is adopted. The high coherence of the fringe field CSR along with its narrow opening angle results in a laser like beam incident upon the target. While the radiation is broadband, the high value of γ at the measurement location ensures $\gamma^2 \lambda \gg L$ for all relevant wavelengths, where L is the drift length distance between the dipole edge and the mirror. In this regime, the formation length of radiation emitted at the dipole fringe $L_f = L$. This distance can be likened to the Rayleigh zone of a laser, wherein the beam can be approximated by plane wave-fronts at a given longitudinal position. It follows that $L = L_f$ can be considered analogous to the Rayleigh length of the beam, which defines the mirror location as coincident with the beam waist. Propagation of the reflected radiation can then be carried out using [166]

$$\frac{w(z)}{w_0} = \sqrt{1 + \left(\frac{z}{z_R}\right)^2},$$

whereby the spatial distribution of the reflected radiation is scaled by this quantity. Here, w_0 and $w(z)$ corresponds to the beam width at the waist and at z respectively, z is the distance to the waist, and z_R is the Rayleigh length, which in this case corresponds to the distance between the dipole fringe and the mirror. The TPX lens is then modelled as a thin lens in order to generate the radiation distribution in the detector plane. This is another source of simulation error, insomuch as the TPX lens is poorly approximated as thin, however the lack of an alternative given the scant information about the electromagnetic fields involved at this location necessitate this choice. Simulations carried out by Joseph Wolfenden in Zeemax indicate that the image produced by the TPX lens is ∼6-7× larger than that produced with an ideal lens of equivalent focal length at

the same object distance [167]. This is consistent with the radiation distribution predicted at the target in SPECTRA simulations, and this scaling is applied to the simulated radiation distribution accordingly. GPT simulation results are incorporated into this radiation distribution in a similar manner as described in Section 4.3.3, in which the SPECTRA-generated distribution is normalised and then scaled by the energy loss predicted by GPT.

5.5 Results

In this section, the measurements of CSR emission from fringe fields taken on the MAX IV SP02 beamline will be discussed and compared to GPT simulations of the experiment. A broad phase scan characterising the parameter space of both accelerating linacs is discussed as well as a finer scan of the K02 phase close to the maximum compression phase of K01. Beyond this, results of a sextupole scan are compared to simulations and will highlight limitations in the methodology presented.

Signals from the pyroelectric array typically feature a background. This background is not a virtue of noise alone, but rather slight persistent biases on each pixel of the array. As such, averaging of the signal does not remove this background, and instead a baseline measurement must be carried out and subtracted from each acquisition. Noise is still present in the signal, and the array readout is averaged over as many shots as were acquired. An error is assigned to each pixel voltage, corresponding to the r.m.s variation in that pixels voltage reading for a particular set of acquisitions. The r.m.s error of the baseline reading is also accounted for in this. The data is then smoothed using a 9-point moving average,

with the weighted error attributed to each pixel. A residual baseline offset still remains in the data, likely from insufficient sampling of the baseline, or possible drift in the baseline over the course of experimentation. This is accounted for by sampling the region of the smoothed detector signal where there is clearly minimal CSR; this region is then averages to find a final baseline which is subtracted once again from the signal as a whole. An error is associated with this second baseline measurement, which is again accounted for in the final error attributed to a given pixel (Figure 5.23).

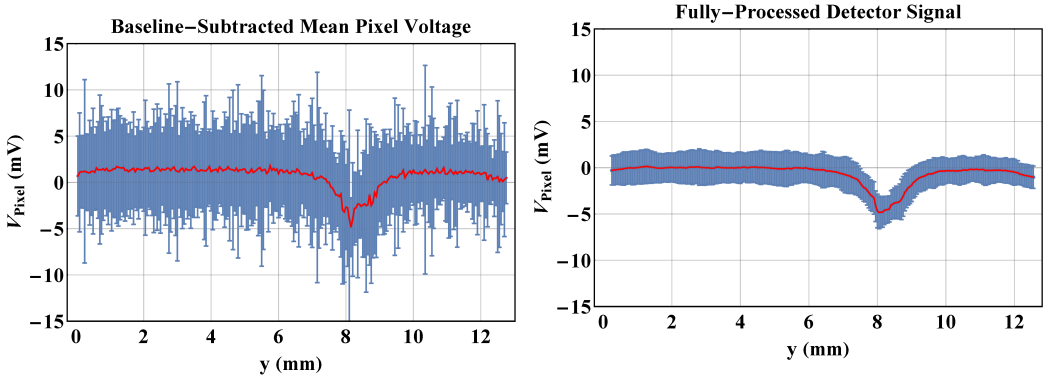

Figure 5.23: Signal processing for data taken with the pyroelectric array. A measured baseline is determined to minimise the effects of "hot pixels", which possess an inherent, non-noisy voltage bias. This is subtracted from each shot-to-shot acquisition of the THz signal which is then average to produce the signal on the left. Further smoothing is then carried out, which serves to reduce the individual pixel error, as well as a second baseline subtraction to negate the DC-offset seen in the detector voltage. The final conditioned signal is shown on the right.

All comparisons to the pyroelectric signal are relative, as is mandated by the unknown spectral response of the detector and thus lack of complete calibration. When comparing the signal to the emitted energy simulated in GPT, both the total integrated signal response and the peak detector voltage will be considered. It is expected that the integrated signal voltage will provide better reliability for comparison, due to a smaller error incurred from signal offsets. This can be visualised by considering the far-field approximation of single-particle fringe field radiation from a single dipole edge [92]

$$\frac{d^2W}{d\Omega d\omega} = \left(\frac{q}{4\pi\epsilon_0}\right)^2 \frac{1}{c\pi^2} \frac{\gamma^4\theta^2}{\left(\gamma^2\theta^2+1\right)^2},$$

where θ is the divergence angle relative to the central direction of radiation propagation. While this expression is not strictly valid for the MAX IV experiment, given the experiment was carried out in the near-field limit of the bending magnet radiation, it provides a useful analytical description of the radiation for the purposes of this explanation. By considering this signal in the detector plane, with a cut-off corresponding to the mirrors edge, the error in both comparative methods due to a signal offset can be approximated. The typical variance of the bunch centroid position at the dipole exit in the vertical plane is $\sim \pm 0.25$ mm, corresponding to an angular offset of the signal at the mirror location of $\sim \pm 0.15$ mrad. From Figure 5.24, it can be seen that the integrated signal method performs far better in the limit of a small angular offset of the signal that is not accounted for in the analysis. That being said, an error of around $\sim$20% is still expectable from this method of determining relative signal strengths (and thus relative energy losses of the electron bunch).

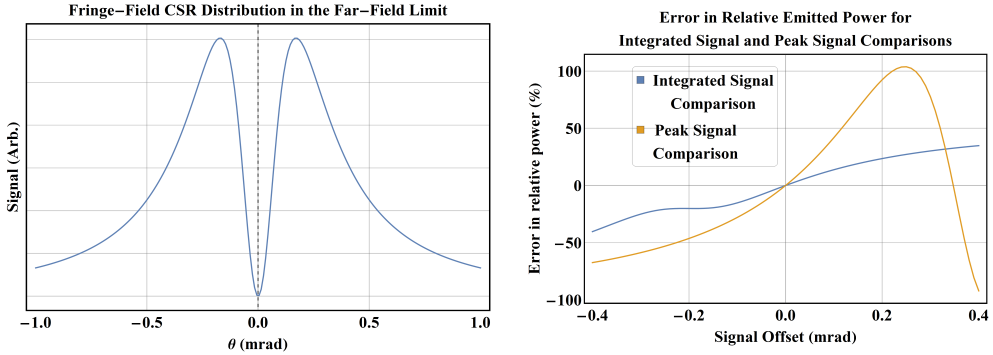

Figure 5.24: The error induced when assuming the relative radiative output from the BC2 dipole fringe field with two different comparative methods. The plot on the left shows the signal used, which is the far-field limit of the single particle radiation distribution for a single dipole fringe. The dashed line represents the cut-off assumed due to the mirrors edge; while selection of the value for this cut-off is somewhat arbitrary, the general conclusions remain regardless. On the right shows the comparative error in the two methods considered as a function of an unaccounted-for signal offset within the detector plane. The integrated signal method clearly performs better, especially in the region where the signal error is small.

5.5.1 Direct Comparisons to GPT

While there is no detail of the resultant radiation provided by GPT, the energy radiated towards the mirror can be inferred from the energy loss of the bunch centroid. It is important to caveat this with the fact that the energy loss predicted by GPT close to maximal compression relative to that at lower compression factors will likely be over-estimated when compared to the measured signal. This arises from the spectral filtering due to the Z-cut quartz view port, TPX lens, and HRFZ-Si window fitted to the detector resulting in only a fraction of the electron beam's radiative emission being incident upon the detector. The minimum value is also often unsuitable as the "nominal" case, due to the signal commonly being barely above the noise level in the data in this case. As such the associated error at this point is too large, and impacts upon the presentation of the data

as a whole due to the uncertainty being carried though to each data point. This then requires the candidate "nominal" case to be somewhere in between, and this choice is somewhat arbitrary, barring the requirement for the expected emitted radiation to be within the non-negligible transmission region of the radiation transport system and the requirement that the overall signal level is sufficiently large compared to the noise inherent in the signal. It is chosen that the "nominal" measurement will correspond to the smallest peak voltage that is at least twice as large as its corresponding pixel voltage uncertainty. This of course means that there is a fixed point at which simulations and data are guaranteed to intersect, being this nominal case.

Direct comparison of the broad phase scan of the phase offsets on K01 and K02 shows a significant under-estimation of the radiated energy, specifically at larger compression, when compared to data (Figure 5.25). Furthermore, there is a clear discrepancy between the phases at which maximal compression appears to occur. This can be explained by comparing the bunch length at the exit of BC2 in GPT simulations for the cases where the "re-matched" lattice and "reference" lattices are used. Here, the "re-matched" lattice refers to simulations where the non-dispersion controlling quadrupoles in BC2 and the preceding matching section, MS3, have been altered to force the beam size to match screen image measurements along with the inclusion of a TWISS element at the start of MS3. The "reference" lattice refers to simulations where only the linac phase offsets have been altered, effectively ignoring the transverse distribution observed during the experiment entirely. These simulations predict a similar phase of maximum compression, although the degree to which the electron beam is compressed varies significantly around the maximal compression point (Figure 5.26).

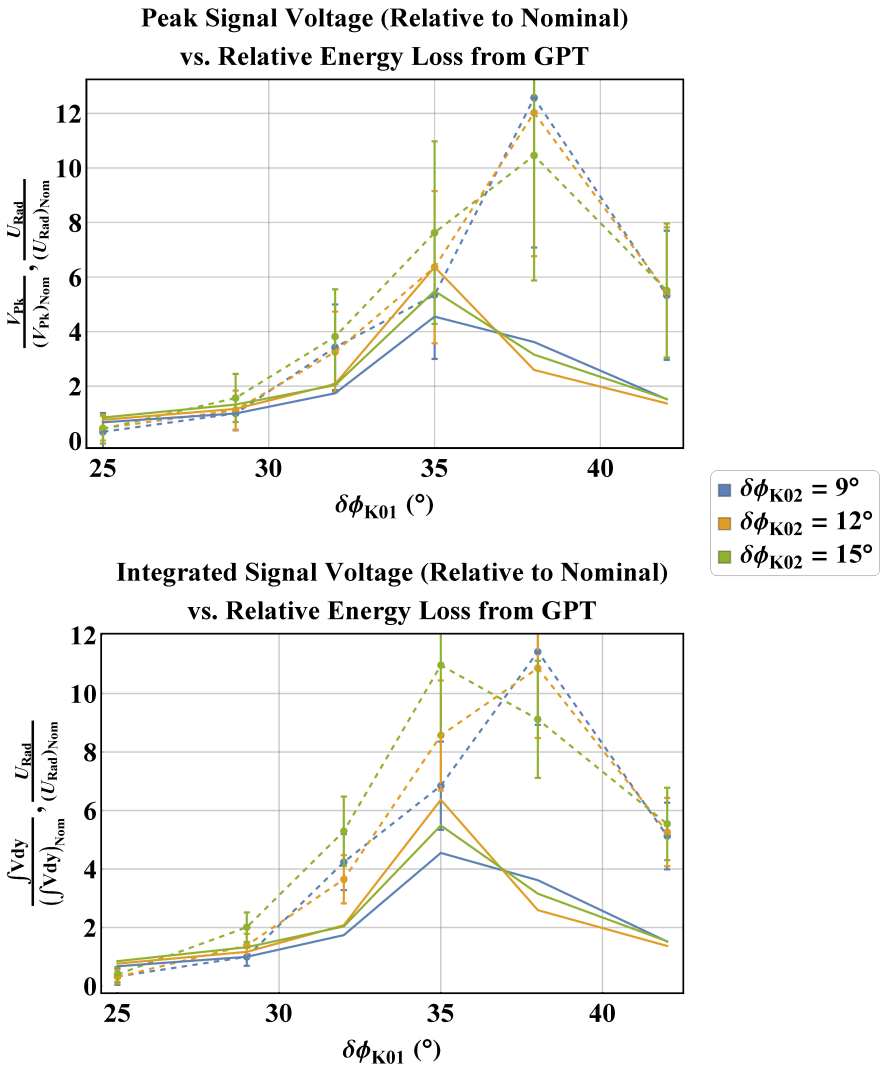

Figure 5.25: Comparison between the energy loss simulated in GPT (solid lines) and the measured detector signal (dashed lines with error bars) in the broad phase scan. Relative peak pixel voltages and integrated detector voltages are compared, with the overall magnitudes presented relative to the "nominal" case, in this scan taken to correspond to the $\delta\phi_{K01} = 29°$, $\delta\phi_{K02} = 9°$ measurement. The same relative scaling is carried out for the simulated energy loss for the same "nominal" case. In both comparative methods presented, the energy loss is significantly under-estimated when compared to measurements.

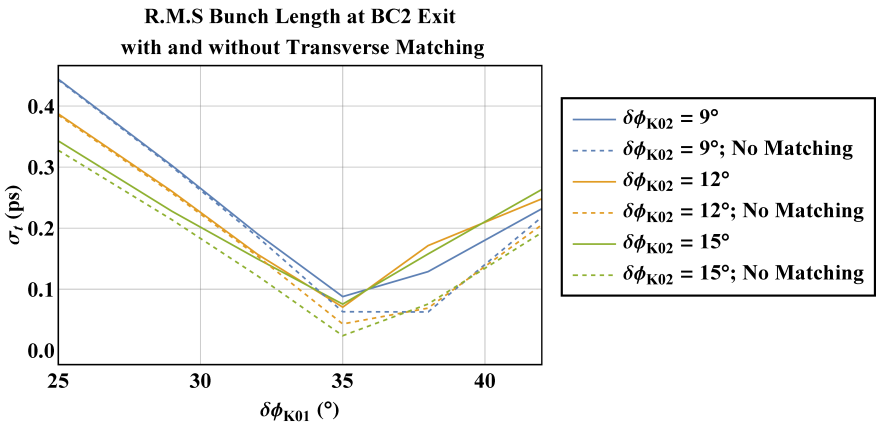

Figure 5.26: R.m.s electron bunch length at the exit of BC2, with and without matching of transverse lattice functions to screen images. The minimum bunch length observed when transverse matching is carried out is significantly larger close to maximal compression than the case where the transverse matching is ignored.

Because the BC2 dipoles are rectangular, this can not be attributed to the geometric path length difference incurred due to large particle offsets (Equation 4.3). The beam emittance grows significantly over the dogleg, driven by very large non-physical β functions at the dipoles which were necessitated in order to increase the beam's transverse size at the screen location to match screen observations (Figure 5.27). This large transverse emittance generated within the BC2 dipoles and quadrupoles due to the poorly matched beam is then transferred to the longitudinal bunch distribution during compression, which increases the minimum attainable bunch length.

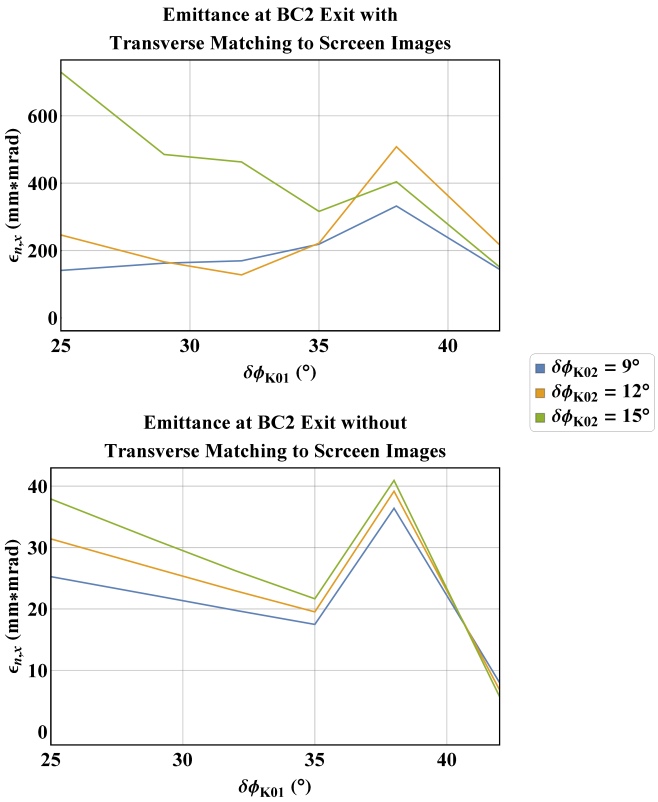

Figure 5.27: Final beam emittance at the BC2 dogleg exit with transverse matching carried out. By forcing the beam size to be much larger than the natural "reference" beam through large transverse lattice functions, the transverse normalised emittance becomes un-physically large. This has the effect of suppressing the CSR interaction.

The effect of this emittance growth and bunch compression suppression is observed in the radiated energy of the electron bunch at the dogleg exit. The emission from the dipole exit is an order of magnitude lower than the case where the "reference" lattice is used (Figure 5.28). Typically, transverse effects are expected to play a role in the fringe field emission's coherence when the condition described in Equation 4.8 is violated. In the case of the 3 GeV MAX IV beam, this corresponds to transverse sizes on the order of ∼10cm, which of course are not observed. Given this fact, the suppression must be a product of the beam

emittance instead, and it follows that in this regime of un-physically large transverse emittances the calculated energy loss at the fringe depends predominantly upon the beam emittance rather than the electron bunch length. As the beam emittance was not measured, this is an unquantifiable effect when comparing to measurement, however it can be assumed that the emittance for the "reference" lattice more closely corresponds to the beam emittance than the case where transverse matching has occurred. It should be noted however, that the normalised transverse r.m.s emittance predicted by GPT at the dogleg exit is still orders of magnitude larger for the "reference" lattice than that expected when only `elegant` is used to simulate the MAX IV linac (Table 5.1).

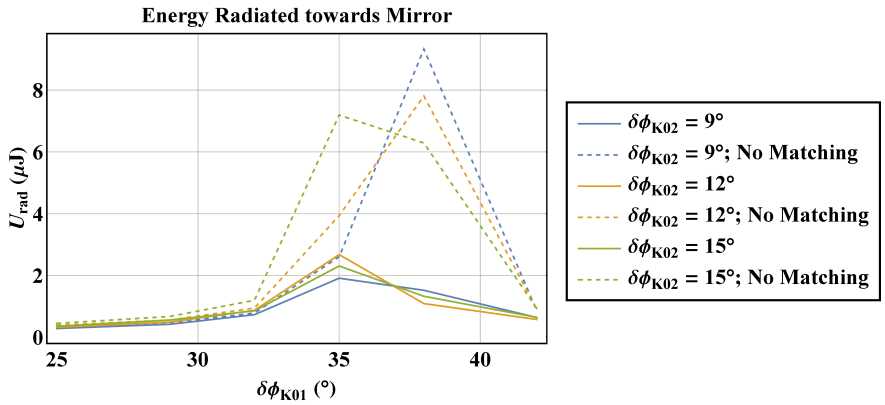

Figure 5.28: Energy radiated towards the mirror as calculated in GPT. Because of the large emittance growth occurring in the BC2 dogleg, the CSR emission is heavily suppressed. Because of this, the electron beam's emission is likely to be more strongly dependent upon the beam emittance as opposed to the bunch length, which is not believed to reflect the measurements taken.

A clear transition in the instantaneous power radiated by the electron bunch is seen at the dipole exit for both the matched and un-matched cases (Figure 5.29). In the case where matching has been carried out for the transverse bunch profile, a small increase is seen in the radiated power as the electron bunch moves

into the fringe region. This echoes predictions from the model laid out in [88], wherein it is stated that there is a spike in the CSR field expected as the electron bunch transitions between the curved and straight trajectories. This spike arises from the velocity term of the Lièнard-Wiechert field, which is compressed into a thin disk around the particle due to relativistic effects. From the point of view of a witness particle, the velocity field appears to arise from a "virtual" source, that has the velocity of the source particle at the retarded time t_r. The position of this virtual source is equivalent to the source particle's position if it were to have continued along it's instantaneous trajectory at t_r. The field lines from this virtual source appear to be aligned with the field at the retarded location. If the bunch is following a curved trajectory, this results in the virtual source's velocity field lying ahead of the observer electron provided the instantaneous separation between the two electrons on the curvilinear trajectory is sufficiently small. As the particles transition into a straight trajectory, the virtual source location moves backwards relative to the observer particle, resulting in a point where the observer moves through the dense region of field lines, thus creating a sharp spike in the CSR field [88]. As the electron bunch moves away from the dipole fringe, the radiated power seems to decay exponentially, which is consistent with approach taken in `elegant` for CSR in drifts [103]. This increase in the radiated power is not seen in the case using the "reference" lattice due to the strength of the CSR wake built up in the dipole proper.

Because of the stark difference the total radiated energy and final transverse emittances observed between the "reference" and "re-matched" cases, as well as the poor agreement between the "re-matched" simulations and the measured detector signal, it can be concluded that the transverse matching procedure is not

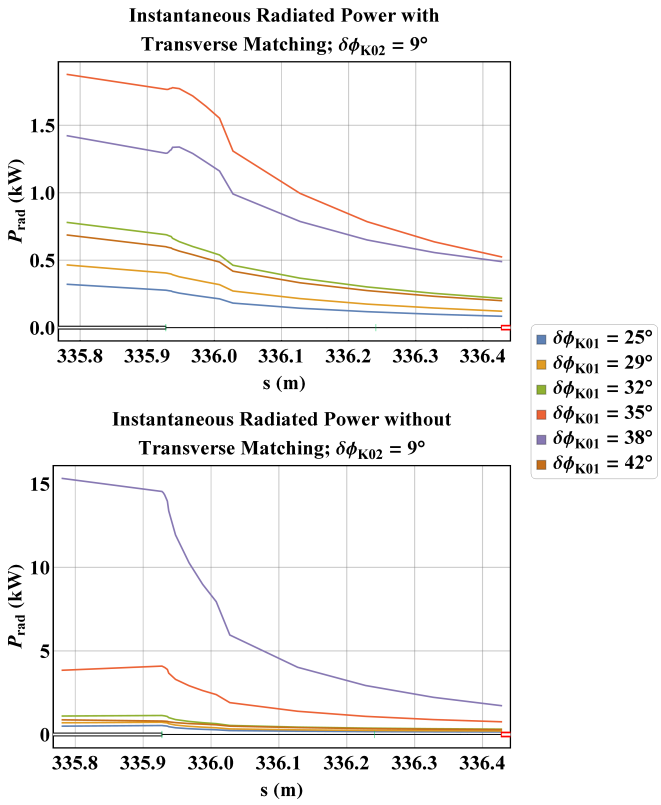

Figure 5.29: Instantaneous radiated power with and without transverse matching. The total emission is heavily suppressed by the large transverse emittance of the electron bunch in the case where matching to screen images has been carried out. The CSR emission in the region close to the dipole exit exhibits differences to the exponential decay adopted in 1-dimensional analytical models such as that employed in `elegant` [103].

a viable method of re-creating the electron bunch distribution. While this denies the experimental method's ability to capture transverse effects and compare them to GPT's CSR model, this is no great loss given the large transverse beam sizes to violate the condition set out in Equation 4.8. Furthermore, the method still presents the opportunity to provide quantitative comparisons to the GPT CSR model's ability to simulate the CSR interaction in a dipole fringe field. As such, henceforth all simulations will make use of the "reference" lattice. Comparison of measured data to the energy loss calculated by GPT in this regime shows a better qualitative correspondence altogether with crest phases now in better agreement

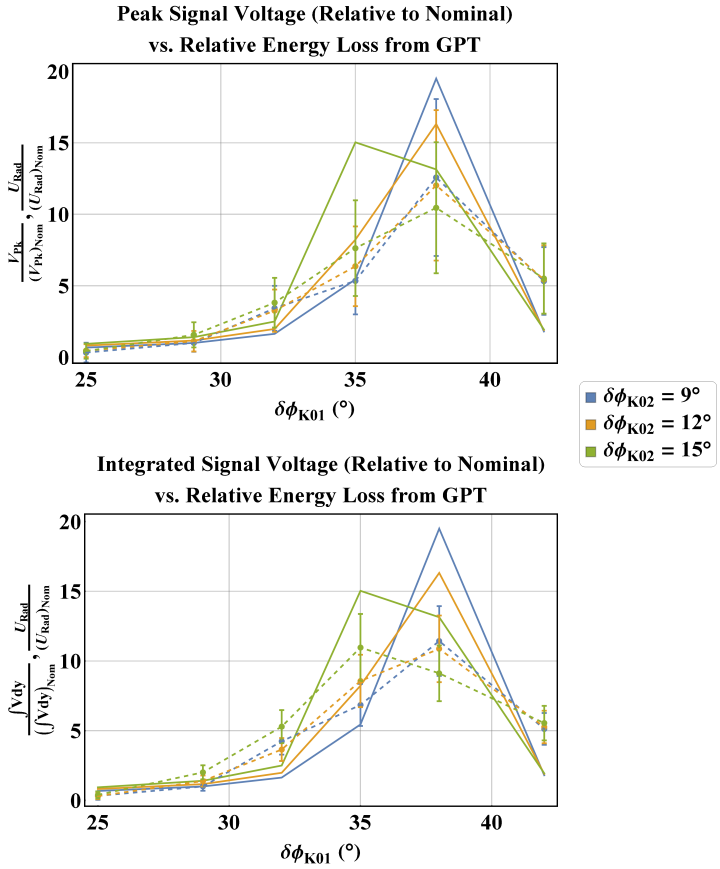

Figure 5.30: Comparison between the energy loss simulated in GPT (solid lines) and the measured detector signal (dashed lines with error bars) for simulations using the "reference" lattice. The "nominal" case in this scan corresponds to the $\delta\phi_{K01} = 29°$, $\delta\phi_{K02} = 9°$ measurement and simulated energy loss. GPT now shows a considerably larger energy loss close to maximum compression than measurement; this is expected given the lack of spectral filtering.

(Figure 5.30), especially in the case where the integrated signal is compared to simulations. The better accuracy observed in the integrated signal comparison corroborates with the predictions depicted in Figure 5.24. Quantitatively the signals still do not agree, specifically in the region of the maximal compression phase. Once again, this is expected due to the lack of spectral filtering in the GPT calculated energy loss when compared to the spectral filter found due to the combined transmission curve of Z-cut quartz, TPX, and HRFZ-Si.

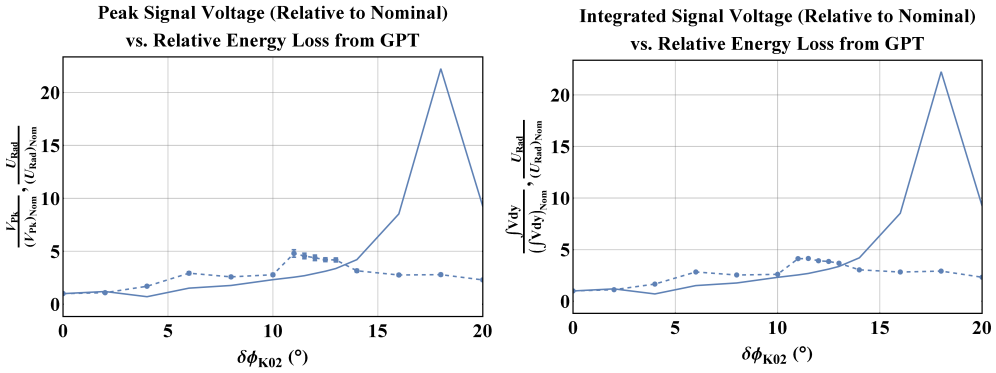

Figure 5.31: Plots of peak pixel voltage and integrated detector signal (dashed lines) against the simulated energy loss for the fine phase scan (solid line). The clear peak in simulations is offset from the peak in measured data in both cases. This indicates a phase error in the simulations which can be attributed to an incorrectly measured crest phase.

A finer scan was carried out varying solely the phase offset of K02. In this scan, the phase offset of K01 was chosen to be close to the maximal compression phase observed in the broad phase scan, i.e $\delta\phi_{K01} = 35°$. A direct comparison between the energy loss calculated in GPT and the measured CSR signal shows no correspondence between simulations and measurement (Figure 5.31). There is a clear peak in the simulated energy loss, though it occurs at a different phase offset to that seen in the data. This peak coincides with the simulated minimum bunch length, conforming to expectations. It can thus be concluded that there is an error in the assumed phase offset at which measurements were carried out upon; this undoubtedly stems from an incorrectly determined crest phase.

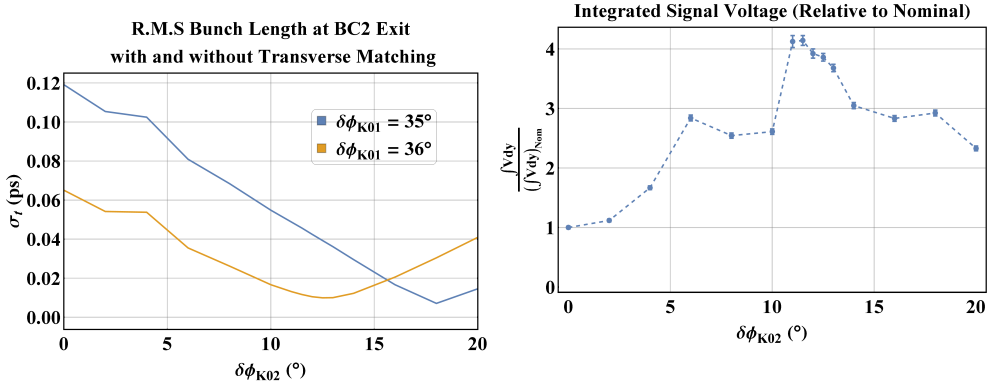

Figure 5.32: Measured integrated detector signal and simulated r.m.s bunch length with and without application of 1° phase error applied to the K01 phase offset. The resolution of the maximum compression phase offset implies that the measured crest phase of K01 was incorrectly measured, with the true value being closer to 36°.

A phase error on the order of ∼1° is possible for the manual crest measurement procedure, however the simulated crest phase occurs around +7° further relative to the crest of K02 than the apparent crest in measurement. As such, it must be concluded that the error is present in the measurement of the K01 crest phase as opposed to K02; as the bunch is compressed significantly over BC1, the bunch length is much more sensitive to variations in the K01 phase. Simulations incorporating a span of phase errors on K01 indicate that a shift in the K01 phase offset of +1°, i.e. a measurement error of -1° on the crest phase determined for K01, results in a better correspondence between the simulated and measured maximum compression phases (Figure 5.32). As the crest was determines at the start of the second day of measurements, this phase error must be applied to both the fine phase scan, and the sextupole current scan.

The nominal phase in this scan also corresponds to the minimum signal level in

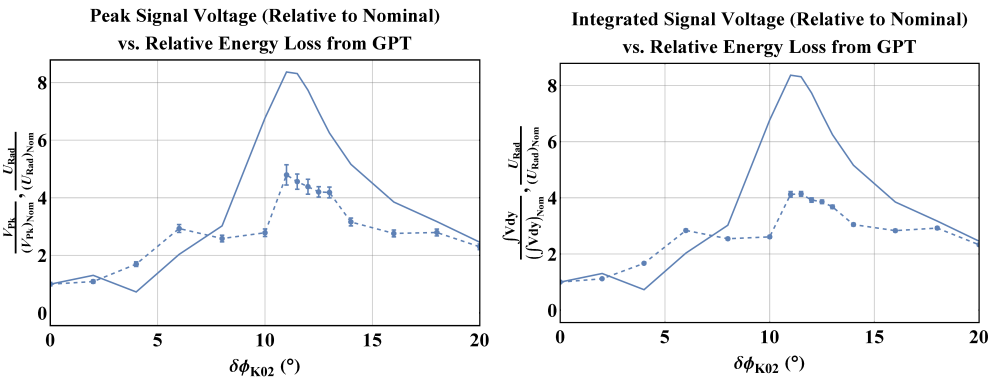

Figure 5.33: Measured integrated detector signal and peak signal voltage (dashed lines) and simulated bunch energy loss (solid lines) for the fine phase scan of K02 after application of a 1° phase error. Identifying the incorrectly measured crest phase of K01 results in a better alignment of the peak energy loss and measure peak signal voltage.

the measurement, which occurs at $\delta\phi_{K02} = 0°$. When this shift in the crest phase of K01 is applied, the maximal emission predicted by GPT and the maximum peak and integrated signals coincide with respect to $\delta\phi_{K02}$ (Figure 5.33). However, similarly to the broad phase scan, the energy emitted in GPT simulations is considerably larger relative to the nominal case than seen in measurement. As before, this is attributed to the full spectrum of radiation not being imaged by the detector, the effect of which is more pronounced at smaller bunch lengths.

The current supplied to the BC1 sextupoles was varied over the entire possible range permitted by the MAX IV control system. This corresponded to a range from 0 A to 9.6 A, where the ideal matched current corresponds to 6.2 A. The MAX IV sextupoles compensate for the over-correction to the LPS curvature induced by the dogleg's natural T_{566} [44], and as such a mismatch in these value will result in a quadratic correlation of variable size in the bunch LPS (Figure 5.34).

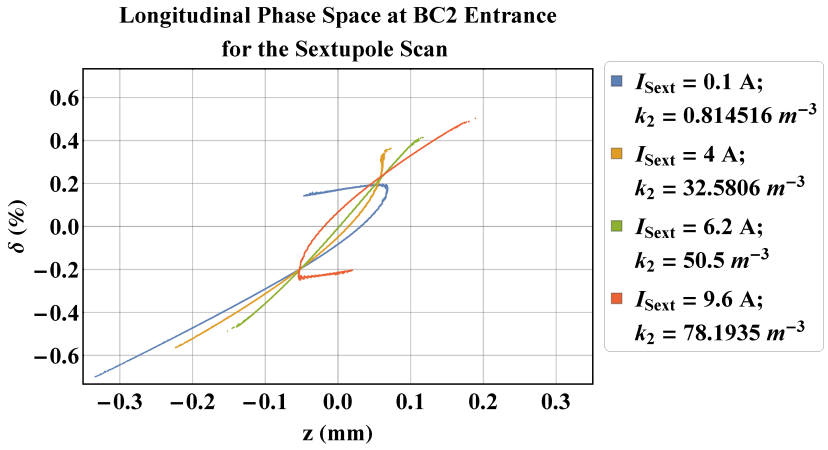

Figure 5.34: Longitudinal phase space at the entrance to BC2 in the sextupole scan. The effect of the BC1 T_{566} matrix element is clearly seen in the phase space curvature.

The quadratic LPS curvature brought about by the dogleg's T_{566} opposes the linear compression in the dogleg, as the quadratic dependence upon the particle energy results in the same path length difference through the dogleg for particles of momentum deviations of opposite sign but similar magnitude. Significant curvature remains in the bunch LPS at the exit of BC2 for some bunches considered in the sextupole current scan; this is expected to pose a limitation in the GPT CSR model's ability to accurately calculate the process as discussed in Section 3.1.5. The method of varying the sextupole strength does present an alternative method of varying the overall compression in the MAX IV linac (Figure 5.35).

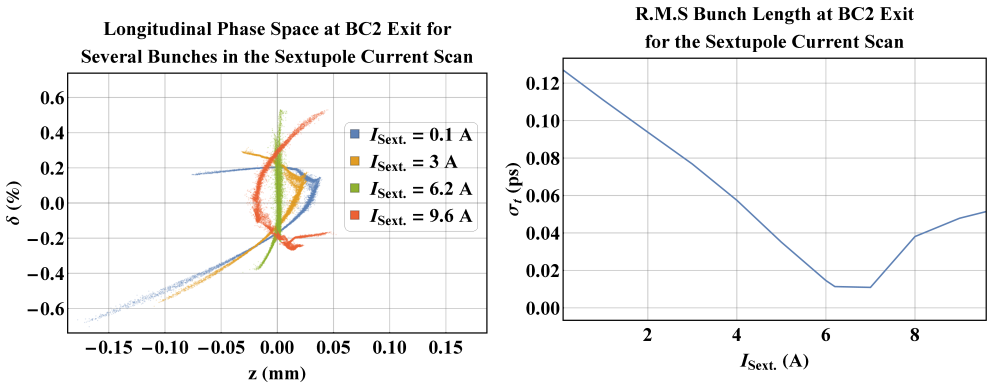

Figure 5.35: Electron bunch LPS and r.m.s bunch length at the BC2 exit. The sextupole current scan poses an effective alternative method to scanning the phases of K01 and K02 for controlling the electron bunch length.

Once again, the contrast between the maximal emission and minimal emission seen in simulations is much larger than that measured (Figure 5.36). The consistency of this pattern across all three parameter scans suggests a constant cause, that being the lack of a spectral filter. As such, further conclusions cannot be drawn without inclusion of this factor into the analysis. It is noted that significantly larger measurement errors are observed for the broad phase scan than for the other parameter scans. This can be attributed to the considerably lower signal level observed in data for this scan.

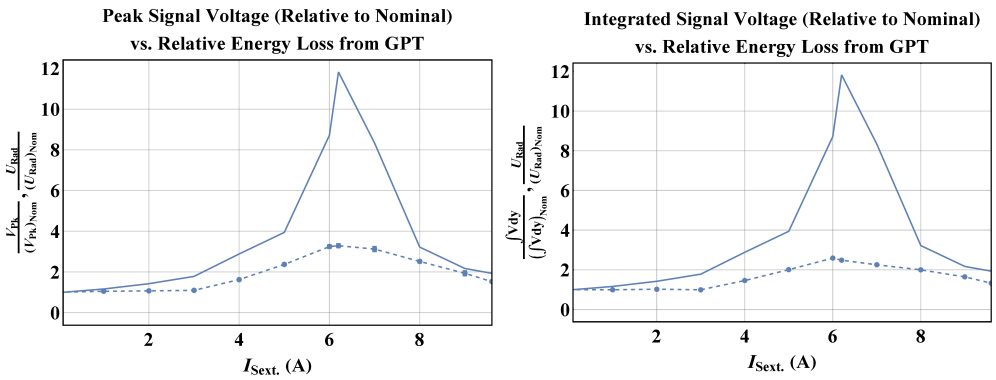

Figure 5.36: Measured integrated detector signal and peak pixel voltages (dashed lines) and simulated energy loss (solid) for the sextupole scan.

5.5.2 Incorporating Spectral Filtering

Two different approaches are used for applying a spectral filter to the energy loss from GPT. The first of these uses the results of SPECTRA simulations, wherein the electron bunch distribution is used to generate the coherent radiation distributions both with and without the spectral filtering arising from the various media through which the radiative emission is transported. Integration of the resultant radiation distributions with and without the spectral filter is used to generate scaling factors for the energy loss predicted from GPT simulations. The SPECTRA distributions are expected to be more accurate for the broad phase scan as opposed to the finer phase scan and the sextupole scan. This is due to the use of un-coupled phase space distributions for the broad phase scan simulations.

Because of instabilities encountered in the SPECTRA solver for the finer phase scan and the sextupole current scan, simple Gaussian bunch distributions based on the r.m.s beam dimensions and the transverse lattice functions were

used instead. This is a significant departure from the true bunch distribution observed at the exit of BC2, hence the likelihood of worse correspondence to data for these scans.

An alternative method adopts the DFT method of generating a form factor discussed in Section 4.3.3. This analysis exploits the fact that the low-frequency region of the fringe field spectrum is approximately frequency-independent [149]. The majority of the emitted radiation is within this low-frequency region, and as such the detectable fraction of the emitted radiation, $R_{Spec.}$, can be determined from

$$\begin{aligned} R_{Spec.} &= \frac{\int_0^\infty \left(\frac{d^2W}{d\Omega d\omega}\right)_{Filt.} d\omega}{\int_0^\infty \left(\frac{d^2W}{d\Omega d\omega}\right)_{Full} d\omega} \\ &= \frac{\left(\frac{d^2W}{d\Omega d\omega}\right)_1 \int_0^\infty N(N-1)|F(\omega)|^2 T(\omega) d\omega}{\left(\frac{d^2W}{d\Omega d\omega}\right)_1 \int_0^\infty N(N-1)|F(\omega)|^2 d\omega} \\ &= \frac{\int_0^\infty |F(\omega)|^2 T(\omega) d\omega}{\int_0^\infty |F(\omega)|^2 d\omega}, \end{aligned}$$

where $T(\omega)$ is the spectral transmission of the radiation transport system and $\left(\frac{d^2W}{d\Omega d\omega}\right)_1$, $\left(\frac{d^2W}{d\Omega d\omega}\right)_{Filt.}$, and $\left(\frac{d^2W}{d\Omega d\omega}\right)_{Full}$ are the single-particle, spectrally filtered coherent, and full coherent angular-spectral energy distributions respectively. This fraction is then used to scale the simulated beam energy loss for comparison to data. As transverse effects can be largely ignored, due to the condition set about in Equation 4.8, the form factor is 1-dimensional.

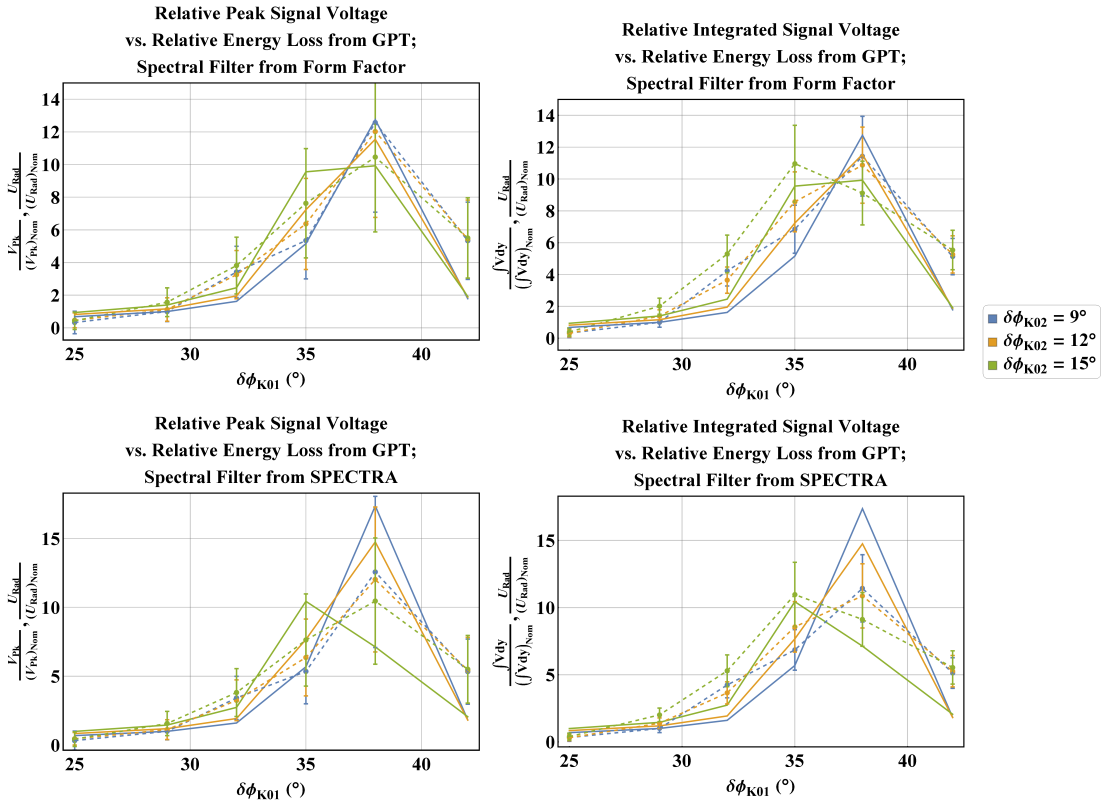

Figure 5.37: Comparison of data (dashed lines) to GPT calculated centroid energy loss (solid lines) in the broad phase scan, with spectral filtering accounted for. A much improved correspondence is seen between simulations and measurement here, with especially good agreement observed in the case where the spectral filtering is sourced from the form factor.

Inclusion of the spectral filter results in a significantly improved comparison between measurement and GPT simulations for the broad phase scan, specifically in the case where a form factor calculated directly from the electron bunch provides spectral filtering of the calculated energy loss (Figure 5.37). Despite the expected better accuracy predicted with the integrated signal as opposed to the peak pixel voltage (Figure 5.24), the best agreement is seen in the comparison between simulation and the peak pixel voltages. At over-compressed phases

($\delta\phi_{K01} = 42°$), the agreement is worse between the GPT model and measurements, and this can be attributed to the difficulties encountered within the GPT model when dealing with a rolled-over bunch LPS.

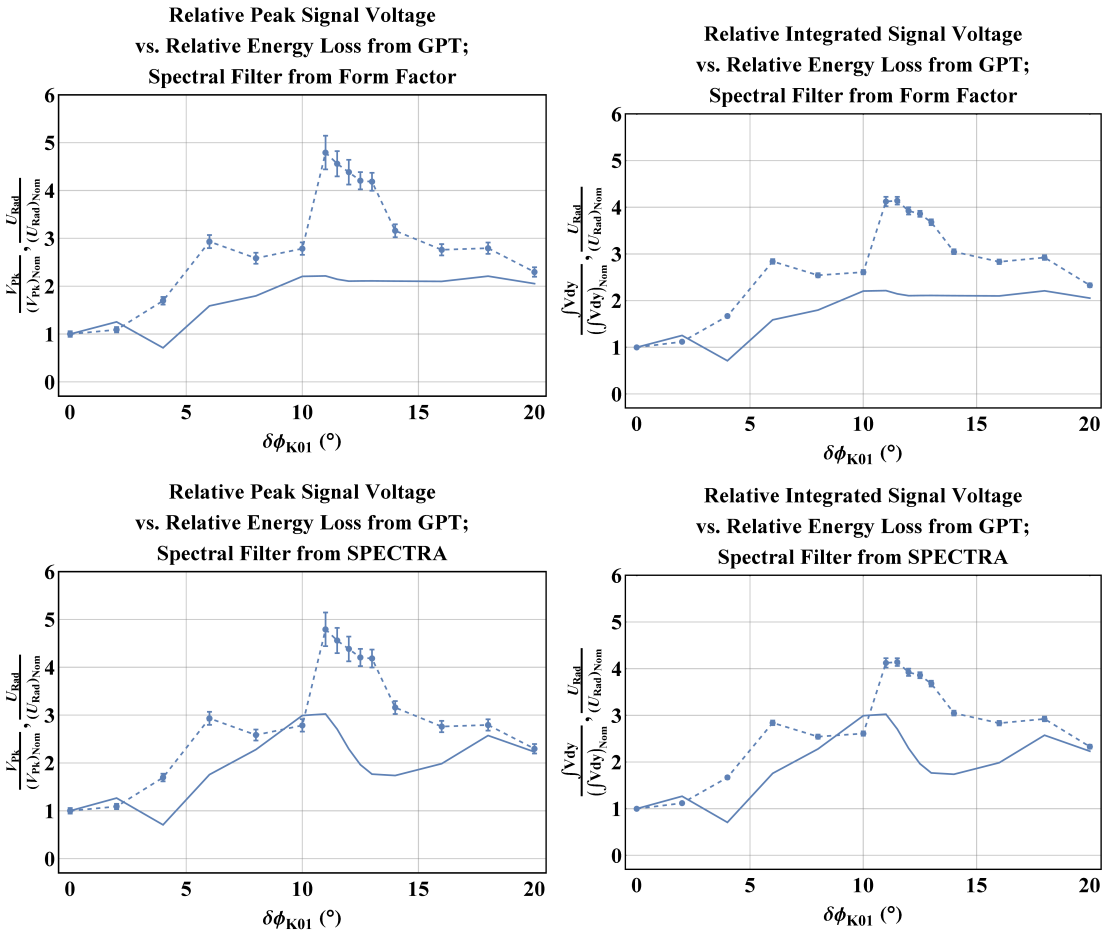

Figure 5.38: Comparison of measured data (dashed lines) to GPT calculated centroid energy loss (solid lines) in the fine phase scan, with spectral filtering included. The measurement and simulations remain in poor agreement for this scan. This may be attributable to a further phase error on the measurement of the K02 crest phase which is not accounted for in simulations, or an incorrectly defined phase error on the crest phase of K01.

Little agreement is seen in any methods considered for the fine phase scan (Figure 5.38). This may arise from an additional phase error on the crest phase measurement for the scanned phase on K02; the case where SPECTRA filtering is applied appears to suffer from a similar systematic offset in the phase relationship, although the size of this offset is much greater than would be reasonable to attribute to the error on this measurement. As such it may also be the case that the 1° phase error applied to the crest phase of K01 may not be fully accurate given the sensitivity of the $\delta\phi_{K02}$-σ_z relationship with respect to $\delta\phi_{K01}$, where a 1° phase error on K01 is seen to shift the maximal compression phase of K02 by $\sim$5° (Figure 5.32). Further to this, it was noted that when conducting the fine phase scan the orbit correction used to kick the electron beam below the mirror's lower edge was varied considerably. This may result in significantly varying portions of the radiation distribution hitting the mirror, thus suppressing a clear relationship between the measured CSR signal and the phase of K02. Despite this, the considerable difference between the magnitudes of the maximal measured signals and the maximal simulated energy losses implies that the phase error is the more likely cause.

Much better agreement is observed for the sextupole scan in the comparison between the peak pixel voltage and simulations which have been scaled by a spectral filter derived from a DFT-generated form factor (Figure 5.39). The deviations that are observed in this corresponding to bunches with a high degree of curvature in the LPS, which once again conforms with expectations that the GPT CSR model would be unsuitable for such electron bunch distributions. While there may still be an incorrectly identified crest phase error applied to K01 in this scan, as well as an unaccounted for error in the K02 crest phase, the

effect of this is considerably less pronounced in the sextupole current scan. This is expected considering the maximum bunch compression is predicted to occur at or close to the matched sextupole current value, 6.2 A.

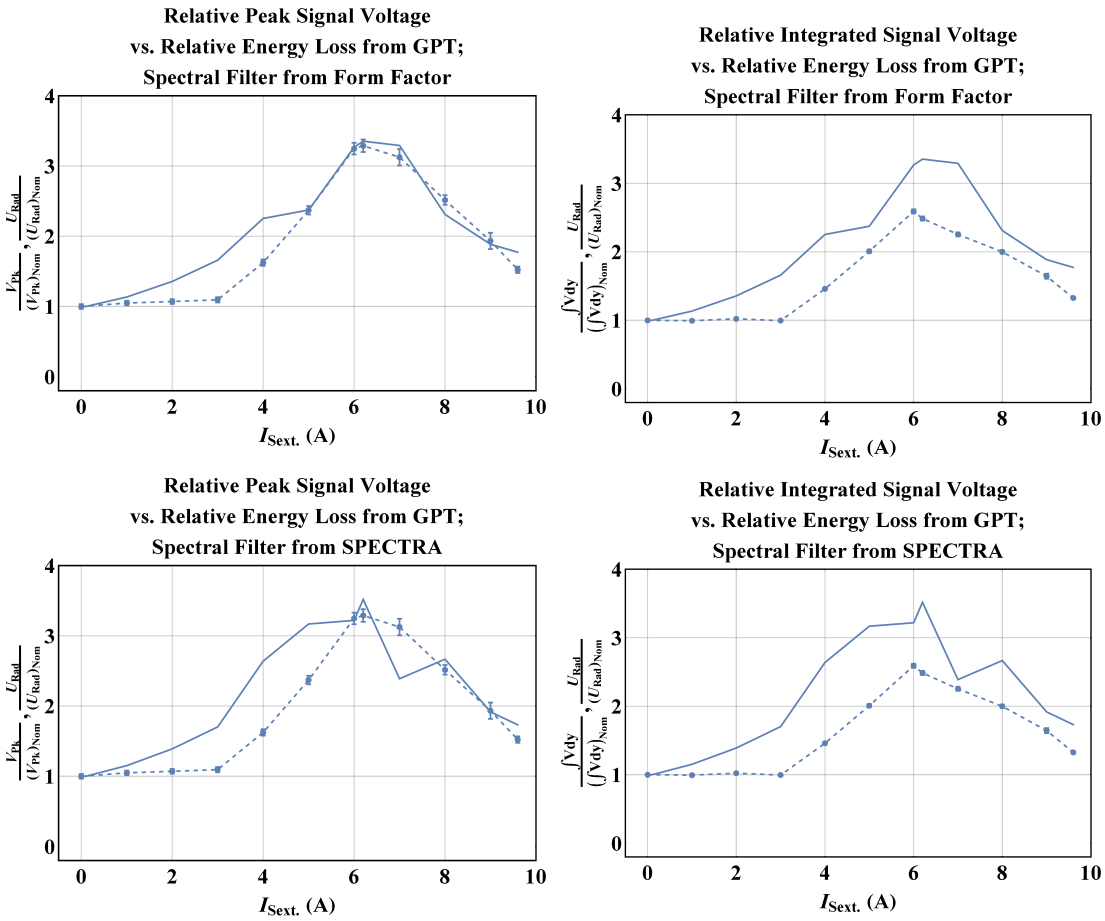

Figure 5.39: Comparison of measured data (dashed lines) to GPT calculated centroid energy loss (solid lines) for the scan of the BC1 sextupole current, with spectral filtering included. A considerably improved agreement is seen in this case due to the spectral filtering applied, with the biggest improvement on comparison once again observed for the DFT-generated form factor method of spectral filtering.

5.5.3 Propagation of Radiation to the Detector Plane

In this section of the analysis, the radiation distribution predicted by SPECTRA simulations, normalised and scaled to the energy loss calculated in GPT, is propagated through the THz detection system. In order to properly estimate the region of the angular distribution incident upon the mirror, the centroid offset of the bunch at the dipole exit is taken into consideration. The divergence angle of the electron bunch is not, and this may be a source of error in the analysis. A further source of error may arise from the lack of a reference marker on screen images corresponding to the beam pipe centre. All analysis is thus carried out under the assumption that the centre of the screen image corresponds to the centre of the beam pipe. Misalignments of the pyroelectric array are considered, with an error in the vertical detector position of half the separation between the pixel centres and an error in the horizontal alignment on the order of 50 µm. As the spectral filtering calculated from the bunch form factor has been shown to be more reliable than that from SPECTRA, this frequency scaling method will be applied in this section.

The broad phase scan once again shows good agreement when comparing the simulated peak pixel irradiance to the peak pixel voltage (Figure 5.40), however the agreement is once again not seen in the integrated signal comparison. The $\delta\phi_{K02} = 15°$ case shows the greatest discrepancy in the comparison between simulations and measurement, as is the case in all of the analysis carried out. This discrepancy may be due to the longitudinal current distribution generated by the `elegant` model of the MAX IV linac not accurately reflecting the true current profile of the MAX IV beam in this case. Once again, the over-compressed electron bunches show the greatest deviation.

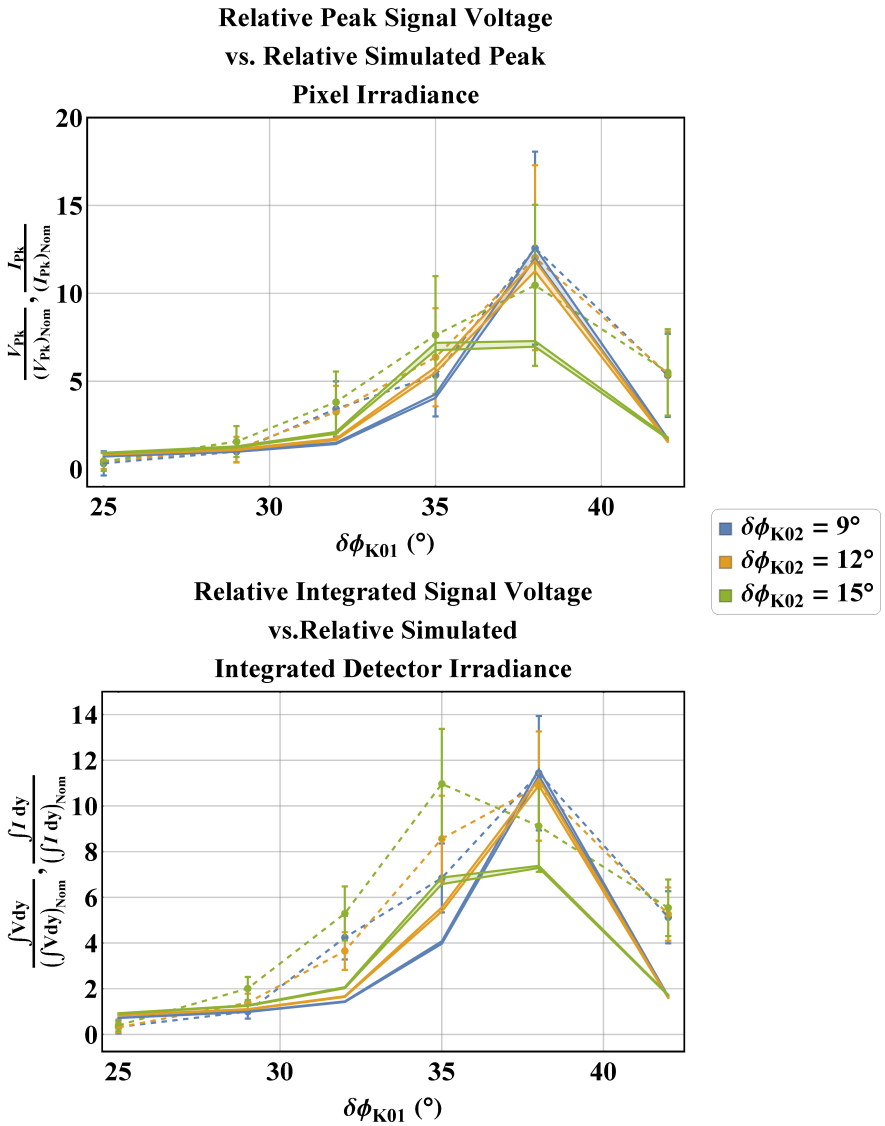

Figure 5.40: Comparison of the simulated detector signal (solid lines) to the measured detector signal (dashed lines) for the broad phase scan. Reasonably good agreement is seen once again for the peak pixel voltage comparison as opposed to the integrated signal comparison. The coloured region corresponds to the signal variation with respect to a detector misalignment.

The simulated detector irradiance for the fine phase scan show little agreement to the measured signal (Figure 5.41). This is attributable to the calculated

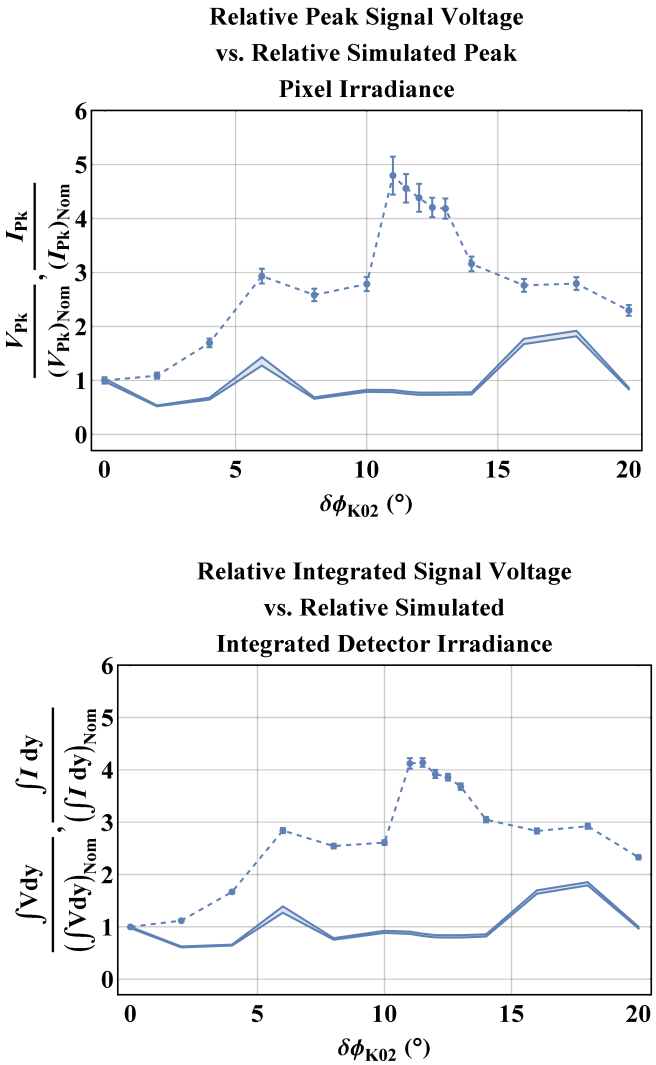

Figure 5.41: Comparison of the simulated detector signal (solid lines) to the measured detector signal (dashed lines) for the fine phase scan. The lack of agreement shown is attributable to the use of Gaussian bunch profiles as opposed to custom phase-space distributions. Beyond this, the issues with the fine phase scan observed in the direct energy loss comparison are likely present in this method of analysis also.

spectral filtering in the case of the fine phase scan, as seen previously in the direct energy loss comparison. The use of a Gaussian bunch profile in SPECTRA simulations may also be responsible for the disagreement seen in the fine phase scan.

The sextupole scan shows reasonable agreement between simulations and measurement (Figure 5.42), this time in the integrated signal comparison, which conforms with expectations outlined in Figure 5.24. Once again, far away from the matched sextupole current value the resultant rolled-over LPS leads to an overestimation of the calculated detector irradiance. The degree of correspondence between measurement and simulations is worse in the case of where the simulated radiation has been propagated to the detector plane than that seen when directly comparing to the energy loss predicted by GPT.

The general conclusion of the radiation propagation method is that, while it has produced some agreement for the broad phase scan and the sextupole scan, the use of a SPECTRA code to estimate the radiation distribution is not particularly effective in improving comparisons to data. Because of the number of potential points of failure when transferring between codes, such as inconsistencies between the electron bunch distribution supplied to SPECTRA and that found in GPT simulations, there are many potential sources of simulation error unaccounted for. Furthermore, the analysis is further complicated by the highly asymmetric experimental geometry, such as the partially extracted mirror and the beam centroid offsets. The beam's centroid divergence is not accounted for, which results in another unknown quantity that is likely significant when considering the radiation propagation. Finally, the approximations used to propagate from the mirror to the detector plane will likely be a further limitation to this analytical method, especially when considering the poor approximation of the TPX lens with an ideal lens. In the case of the TPX lens, while TPX is in principle free of chromatic aberrations, the same cannot be said for geometric aberrations.

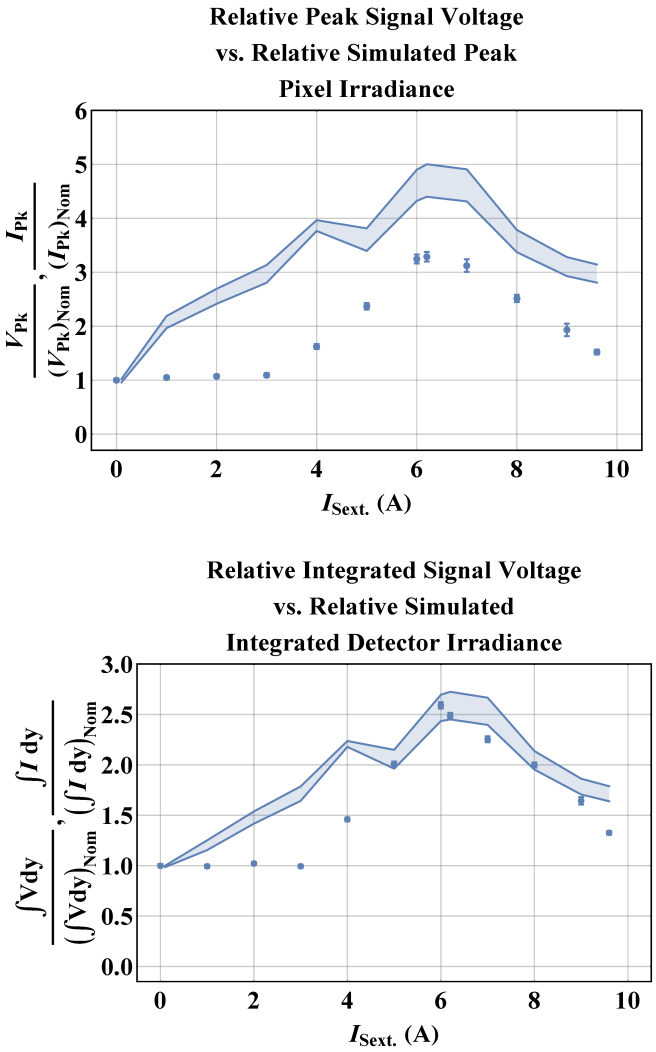

Figure 5.42: Comparison of the simulated detector signal (solid lines) to the measured detector signal (dashed lines) for the sextupole scan. As with the fine phase scan, the poor comparison between measurement and simulations is primary attributable to the use of Gaussian bunch profiles as opposed to custom phase-space distributions.

5.6 Conclusions

Experimental comparisons to GPT's CSR model are required to provide confidence to the findings from CSR simulations of the CLARA beamline. Measurement of coherent radiation has been carried out in the MAX IV SPF using a pyroelectric array positioned downstream from the final dipole of the second

bunch compressor, BC2, with the view to comparing the detected radiation to the predicted energy loss of the electron bunch centroid. Achieving a good comparison between the measured signal and simulated energy loss provides confidence in GPT's ability to model the CSR process in the fringe field region of a dipole, as well as the overall implementation of the general CSR model. A method for isolating CSR emitted from a dipole fringe without generation of CTR using a partially extracted mirror has been explored. Scans of the phase offset applied to the accelerating field of both of the MAX IV accelerating structures, K01 and K02, have been conducted with the aim of controlling the electron bunch length. Accompanying these phase scans, an alternative method of bunch length control was explored, by scanning the current supplied to the sextupoles in the first bunch compressor, BC1. Alongside providing compensation for 2^{nd}-order dispersion within BC1, these sextupole optics aid in the linearisation of the electron bunch LPS. As such, variation of the currents supplied to these magnets results in a quadratic correlation in the bunch LPS, which directly impacts the bunch compression in both BC1 and BC2.

Measurements have then been compared to simulations of CSR carried out in GPT. Two comparative methods have been used for the measured detector signal, with both the integrated detector signal and the peak pixel voltage investigated. These values are taken as relative intensities with respect to a chosen "nominal" case. The criterion for this nominal case was the lowest peak pixel voltage that is at least twice the r.m.s uncertainty on the same pixel voltage, which typically, but not universally, corresponded to the minimum peak signal voltage observed for a given scan. GPT simulations have been solely conducted for the final dipole of BC2, with the rest of the upstream accelerator modelled in

`elegant` using the pre-existing MAX IV lattice. Several methods for re-creation of the 6-dimensional phase space of the electron bunches used in the experiment have been explored, but discrepancies between the true electron bunch injected into the MAX IV linac and the electron bunch provided to `elegant` simulations have meant that this was not possible. As such, only the longitudinal bunch distribution has been modelled by tracking in `elegant`.

In a direct comparison between the simulated energy loss and measured pyroelectric response methods of spectral filtering have been explored in an attempt to emulate transmission losses due to the THz transport through the detection system. A method using the transmission curve and a bunch form factor calculated using a DFT method has been shown to be the most effective in reproducing the observed loss in radiated energy due to reflections from media used in the detector system. When this spectral filtering is included in analysis, a very good agreement is shown between the peak pixel voltage seen in the processed pyroelectric signal and the energy loss calculated by GPT for the broad phase scan and the sextupole scan (Figures 5.37 and 5.39). The most pronounced discrepancies seen in these parameter scans occur for electron bunches with significant curvature in their LPS, either from a large sextupole mismatch or over-compression. This conforms with the previously stated limitations of the GPT CSR model, illustrated in Figure 3.2. The peak pixel voltage proved to be a better variable for the comparisons presented, which is contrary to expectation; the error incurred due to unaccounted-for signal offsets is expected to be less pronounced for the integrated signal than the peak pixel voltage, as described by Figure 5.24. In the case of the finer phase scan of K02 significant deviations are observed between

simulations and measurements, and it is most likely that this is caused by an unaccounted for error in the measurement of the K02 crest phase. While this would have also been present in the sextupole current scan, the effect of this is not seen due to the fixed phase offset applied to both K01 and K02 in this parameter scan.

A method of propagating the angular radiation distribution to the detector plane has been attempted using the SPECTRA code in conjunction with measured centroid offsets obtained from screen images. Where possible, un-coupled phase space distributions of the electron bunch determined from GPT simulations have been used to generate the radiation distribution in SPECTRA, but instabilities encountered within the SPECTRA solver have mandated the use of simple Gaussian electron bunch profiles for some simulations. In order to further propagate radiation through the detection system, a method based on a Gaussian beam approximation outlined in [93] has been adopted. The spectral filtering calculated from the bunch form factor was used to scale simulation results in this analytical method, given its demonstrated superiority to the spectral filtering calculated in SPECTRA. Reasonably good agreement for this analytical method is seen for both the broad phase scan and the sextupole current scan, though it is a considerably worse correspondence than in the direct comparison between the simulated energy loss and peak measured pixel voltage. The lack of correspondence between simulations and measurements for the fine phase scan in all cases indicates that the quality of the data collected for this scan is the primary source of error.

The detection of THz emission from a dipole fringe field has been shown to produce a good quantitative comparison to the CSR-induced energy loss calculated

by GPT in the fringe region, providing some weight to novel effects uncovered in GPT simulations of the CLARA Phase beamline. A method for propagating the simulated radiation distribution has been compared to data and, while incorporating additional experimental detail, has been shown to provide a poor comparison to data. This is generally attributable to the number of approximations made when moving between simulation codes and incorporating results from both GPT simulations and SPECTRA simulations into the analysis. This essentially forms multiple points of failure in the analysis, whereby unaccounted for complexities incur inaccuracies in the analytical method. This is compounded by the asymmetry of the experimental set-up, such as the partially extracted mirror and the necessity to induce a large vertical kick to the electron bunch in order to inhibit the generation of CTR. While a quantitative comparison has been shown successful, it is recommended that future work be carried out that is focused upon the beam-based effects of CSR, such as emittance growth and energy spread changes induced in bunch compression structures.

Chapter 6

Conclusions

The latest version of the GPT code includes a new method for the calculation of CSR effects. This new model presents several advantages over comparable general-purpose codes:

- The use of a sub-bunch method results in much faster calculation when compared to fully 3-dimensional models, and does not require assumption to be made about the electron bunch trajectory.

- The use of off-axis source points for the CSR field captures effects due to the transverse size of the bunch.

- Integration into a general particle tracking code allows for simulation of CSR in concert with other collective effects such as wakefields and space charge.

- Inclusion of the velocity term into the Liènard-Wiechert field allows for novel effects to be captured in the upstream and downstream drift sections, as well as fringe regions

- Tracking through finite fringe fields permits more detailed modelling of the CSR process in complex transient regions.

These advantages present GPT as an attractive tool for future FEL driver design, wherein start-to-end simulations can capture adverse effects on the bunch distribution due to collective effects upstream from the lasing section of the FEL. Furthermore, as bunch lengths used in FELs become ever smaller, the transverse effects become more relevant. Both a beam-based method, analysing and measuring the effects of CSR on the bunch energy spread, and a photonic method, inferring the centroid energy loss brought about CSR interaction through the detection of THz radiation, have been investigated. In the case of the latter, comparisons have been made with measurements taken on the MAX IV linac and a good agreement has been observed between the simulated energy loss of the electron bunch and the observed response of a pyroelectric array. Simulations carried out for the CLARA Phase 1 beamline have demonstrated novel beam-based effects arising from the CSR interaction. Simulations have indicated that an energy spread reduction can be expected in the drift sections downstream from a dipole, arising from the velocity term of the Liènard-Wiechert field. Alongside this, a scheme employing strong quadrupole focusing in the presence of non-zero higher order dispersion has been shown in simulation to produce an reduction in the beam's r.m.s energy spread due to the CSR effect in a subsequent dipole.

Start-to-end simulations of the CLARA Phase 1 beamline have been carried out in GPT for design of experiments to compare against the new CSR model employed in GPT. Simulations of the beam-based method focused on inference of the energy spread change arising from CSR through measurements of the transverse beam size in a region of non-zero dispersion. The experiment was proposed

for the C2V dogleg on the CLARA Phase 1 beamline. The beam based method was shown to not be feasible, due to the small changes in the r.m.s energy spread relative to the linear chirp applied to the electron bunch's LPS by the accelerating linac field which facilitates bunch compression. The low magnitude of the energy spread change was exacerbated by the rapid compression and subsequent elongation due within the dipole. Despite this, simulations have highlighted effects arising from the velocity field in the downstream drift from the first dipole of the C2V dogleg transfer line. In this region of the beamline, the sign change in the longitudinal electric field arising from a significant contribution from the velocity component of the Liènard-Wiechert field serves to decrease the r.m.s energy spread, which indicates potential bunch compressor designs wherein the CSR-induced energy spread is self cancelling. Such a bunch compressor design would be of significant use in the design of future linac-driven FELs, where low energy spread is a priority. These findings are consistent with those reported by Brynes *et al.* in [88]. Further to this, deviations from the 1-dimensional model employed in the general-purpose beamline design code `elegant` have been demonstrated in GPT simulations.

Simulations of the photonic measurement technique demonstrated the viability of detection of CSR using pyroelectric detectors in the context of a phase scan, with a clear relationship predicted between the applied LPS chirp and corresponding CSR emission at the measurement location in BA1. A scan of the transverse size at the measurement location was found to be limited in its practical ability; changes to the transverse size at the radiating location invariably lead to elongation of the bunch unless unique optics settings were determined for each point in the scan. Such heavy reliance on simulated optics matching is likely

to become a time consuming process of lattice parameter measurement for each point of the scan. Even with optics matching to constrain the bunch length at the measurement location, the extent to which the transverse size could be altered was limited, with maximum values of the Derbenev parameter being $\sim$0.7. At this extreme, the deviations between 1-dimensional and 3-dimensional CSR calculations were negligible, and so such a scan would not be viable for testing GPT's ability to incorporate transverse effects into CSR modelling. Interesting beam-based effects were observed in simulations from this scan, namely a reversal in the CSR-induced energy spread from the beam's own CSR field. It was found that a correlation in the x-δ plane brought about by residual 2^{nd}-order dispersion within the electron bunch could be exploited through strong focusing of the electron bunch close to the dipole entrance. Particles at high energies relative to the centroid positioned at positive transverse offsets take a longer path through the dipole than those at negative transverse offsets, which have negative momentum deviations. This arises from geometric effects described by the R_{51} and R_{52} elements of the sector dipole transfer map [56]. The result is that the high energy particles move rearwards in the bunch, towards the decelerative region of the CSR wake, while conversely the low energy particles move towards the accelerative portion of the wake. Once again, this has further significant implications for the design of energy-spread reducing machine optics in bunch compressors.

As beam time was not allocated for this study in the CLARA Phase 1 Beam Exploitation Programme, only simulations pertaining to the experimental design have been presented. Future work on this topic is suggested for future phases of the CLARA installation. Specifically, the use of the velocity bunching mode is argued to be an effective method to facilitate bunch compression, with the

correlated energy spread imparted by the CLARA injector linac compensated by subsequent accelerating structures. The compressed bunch with low r.m.s energy spread could then be passed through the planned variable bunch compressor, from which energy spread and emittance growth measurements related to CSR can be measured in a downstream spectrometer line. This scheme would allow for testing of some of the novel beam-based effects highlighted in GPT simulations in this thesis.

In order to provide some confidence in the GPT CSR model and the novel beam-based effects determined in simulations for the CLARA Phase 1 beamline a similar photonic measurement scheme was conducted in the MAX IV SPF. Using a mirror positioned downstream from the final dipole of the MAX IV linac second bunch compressor, BC2, radiation emitted from the fringe field region of the dipole was measured using a pyroelectric array. Scans of the phase offset for the two accelerating structures of the MAX IV linac were carried out to vary the compression of the electron bunch, as well as scans of upstream sextupole field strengths which controlled the linearisation of the longitudinal phase space. These measurements have been presented against simulations of the parameter scans conducted. Simulations made use of the pre-existing `elegant` lattice used for the MAX IV beamline design, with electron bunches passed to GPT simulations for the final BC2 dipole. Given the unknown spectral response of the pyroelectric array, the measurements presented are taken as relative intensities normalised to a "nominal" case, typically corresponding to the minimum measured peak pixel voltage, for both measurements and simulations. In order to account for the spectral filtering brought about by media present in the THz detection system, a DFT method was employed to produce a bunch form factor

which was used in conjunction with spectral transmission data [150, 153, 155] to generate a scale factor. Further analysis attempted to estimate the radiation distribution at the detector location. SPECTRA simulations were used to this end, alongside the aforementioned spectral filtering method. The resultant radiation distributions were then normalised and re-scaled to the energy loss calculated by GPT in order to incorporate GPT's predictions into the comparison to measurements.

Good quantitative agreement has been demonstrated for a broad scan of the phase offsets applied to the two accelerating structures on the MAX IV linac, and for a scan of the currents supplied to sextupoles on the first MAX IV bunch compressor. This agreement was seen predominantly in the case where the energy loss calculated by GPT was compared to the measured peak pixel voltage of the pyroelectric array. This improves confidence in conclusions drawn from GPT simulations, although should be treated tentatively; GPT does not provide details of the radiation itself, and so inference of the radiation from beam parameters was required. Further beam based studies should be carried out to provide a more direct comparison to beam-based effects outlined by GPT simulation results, such as energy spread decreases. Attempts to estimate the radiation distribution incident upon the pyroelectric array were less successful, only showing moderate agreement with measured data. This can be attributed to multiple factors, the foremost of which is that the complexity of the analysis required for this reproduction of the detector signal, and the highly asymmetric experimental geometry necessitated to avoid the generation of CTR, leaves the method open to numerous sources of error that cannot be easily accounted for without extensive studies using the MAX IV beam. Because of the poor comparison between simulations

and measurement for all analytical methods attempted, it can be concluded that the data set for the fine phase scan is of poor quality.

The results of the research discussed in this thesis have implications for the future design of compression systems, wherein novel simulation tools can aid in the design of bunch compressors and bunch compressor optics which have intrinsic reduction of the bunch r.m.s energy spread. Such a design would be of great use in future FEL development, where there is increasing demand for shorter electron bunches with very low energy spread and transverse emittance.

Bibliography

[1] S. B. van der Geer, M. de Loos, I. D. Setija, P. W. Smorenburg, P. H. Williams, and A. D. Brynes, "GPT-CSR : A New Simulation Code for CSR Effects," in *Proceedings of IPAC2018*, Vancouver, 2018, p. THPAK078.

[2] E. M. Rowe, R. A. Otte, C. H. Pruett, and J. D. Steben, "Operation and Performance of the University of Wisconsin Physical Sciences Laboratory Electron Storage Ring," *IEEE Transactions on Nuclear Science*, vol. 16, pp. 159–164, 1969.

[3] E. M. Rowe and F. E. Mills, "Tantalus I: A Dedicated Storage Ring Synchrotron Radiation Source." *Particle Accelerators*, vol. 4, pp. 211–227, 1973.

[4] S. L. Hubert and G. P. Williams, "Vacuum Ultraviolet Spectroscopy," in *Synchrotron Radiation Sources*. ACADEMIC PRESS, 2000, pp. 1–25.

[5] D. S. Yang, "Photoelectron Spectroscopy," in *Comprehensive Coordination Chemistry II*, 2003, pp. 189–196.

[6] K. R. Lea and I. H. Munro, "The synchrotron radiation source at daresbury laboratory," 1979.

[7] H. Winick, "Fourth Generation Light Sources," in *Proceedings of the IEEE Particle Accelerator Conference*, 1997, pp. 37–41.

[8] Y. S. Derbenev, J. Rossbach, E. L. Saldin, and V. D. Shiltsev, "Microbunch Radiative Tail-Head Interaction," TESLA FEL, Tech. Rep., 1995.

[9] A. Tremaine *et al.*, "Observation of self-amplified spontaneous-emission-induced electron-beam microbunching using coherent transition radiation," *Phys. Rev. Lett.*, vol. 81, no. 26, pp. 5816–5819, 1998.

[10] S.-Y. Lee, *Accelerator Physics*, 2nd ed. World Scientific, 2004, p. 498.

[11] E. Allaria *et al.*, "Tunability experiments at the FERMI@Elettra free-electron laser," *New Journal of Physics*, vol. 14, p. 113009, 2012.

[12] M. Cornacchia, "Requirements and Limitations on Beam Quality in Synchrotron Radiation Sources," SLAC, Stanford, CA, Tech. Rep., 1989.

[13] Z. Huang, "Brightness and coherence of synchrotron radiation and fels," SLAC, Tech. Rep., 2013.

[14] S. Reiche, "Compensation of FEL gain reduction by emittance effects in a strong focusing lattice," *Nuclear Instruments and Methods in Physics Research, Section A: Accelerators, Spectrometers, Detectors and Associated Equipment*, vol. 445, no. 1-3, pp. 90–94, 2000.

[15] J. Bengtsson, "Ultra low emittance light sources," in *Proceedings of EPAC08*, Genoa, Italy, 2008, pp. 988–992.

[16] M. W. Guetg, B. Beutner, E. Prat, and S. Reiche, "Optimization of free electron laser performance by dispersion-based beam-tilt correction," *Physical Review Special Topics - Accelerators and Beams*, vol. 18, p. 030701, 2015.

[17] J. Choi, H. S. Kang, and T. Y. Lee, "Energy spread effects in the PAL XFEL," *Journal of the Korean Physical Society*, vol. 48, no. 4, pp. 801–805, 2006.

[18] R. L. Kwang-Je Kim, Zhirong Huang, *Synchrotron Radiation and Free-Electro Lasers*. Cambridge University Press, 2017, pp. 76–78.

[19] I. Davidyuk, O. A. Shevchenko, V. G. Tcheskidov, and N. A. Vinokurov, "Modeling and designing of variable-period and variable-pole-number undulator," *Physical Review Accelerators and Beams*, vol. 19, no. 2, 2016.

[20] I. V. Davidyuk, O. A. Shevchenko, V. G. Tcheskidov, N. A. Vinokurov, B. Inp, and S. B. Ras, "VARIABLE-PERIOD VARIABLE-POLE NUMBER HYBRID UNDULATOR DESIGN FOR NOVOSIBIRSK THz FEL," in *Proceedings FEL 2019*, Hamburg, Germany, 2019, pp. 531–534.

[21] N. R. Thompson *et al.*, "First lasing of the ALICE infra-red Free-Electron Laser," *Nuclear Instruments and Methods in Physics Research, Section A: Accelerators, Spectrometers, Detectors and Associated Equipment*, vol. 680, pp. 117–123, 2012.

[22] B. W. McNeil, "A simple model of the free-electron-laser oscillator from low into high gain," *Nuclear Inst. and Methods in Physics Research, A*, pp. 388–393, 1990.

[23] G. R. Neil *et al.*, "The JLab high power ERL light source," *Nuclear Instruments and Methods in Physics Research, Section A: Accelerators, Spectrometers, Detectors and Associated Equipment*, vol. 557, no. 1, pp. 9–15, 2006.

[24] B. Dunham *et al.*, "First tests of the Cornell university ERL injector," in *Proceedings of LINAC08*, 2009, pp. 699–703.

[25] S. Benson *et al.*, "High power operation of the JLab IR FEL driver accelerator," in *Proceedings of the IEEE Particle Accelerator Conference*, 2007, pp. 79–81.

[26] V. A. Goryashko and V. Zhaunerchyk, "Conceptual Design of an Stockholm- Uppsala THz FEL Oscillator," Swedish FEL Center, Uppsala, Sweden, Tech. Rep. May, 2013.

[27] G. N. Kulipanov *et al.*, "Novosibirsk high-power THz FEL facility," *IEEE Transactions on Terahertz Science and Technology*, vol. 5, no. 5, pp. 798—-809, 2015.

[28] L. Merminga, "Energy Recovery Linacs," in *Proceedings of the IEEE Particle Accelerator Conference*, 2007, pp. 22–26.

[29] J. Feldhaus, J. Arthur, and J. B. Hastings, "X-ray free-electron lasers," SLAC, Stanford, CA, Tech. Rep., 2005.

[30] A. He, L. Yang, and L. Yu, *High-Gain FEL Theory, Introduction.* Springer International Publishing, 2016, pp. 1–37.

[31] F. Parmigiani and D. Ratner, "Seeded Free-Electron Lasers and Free-Electron Laser Applications," *Synchrotron Radiation News*, vol. 29, no. 3, pp. 2–3, 2016.

[32] C. Lechner *et al.*, "Concept for a seeded FEL at FLASH2," in *Proceedings FEL 2017*, 2017, p. MOP003.

[33] Z. T. Zhao *et al.*, "First lasing of an echo-enabled harmonic generation free-electron laser," *Nature Photonics*, vol. 6, pp. 360–363, 2012.

[34] J. Bahrdt, B. Faatz, R. Treusch, V. Miltchev, and R. Reininger, "The properties of the FEL output for self seeding," in *28th International Free Electron Laser Conference, FEL 2006*, 2006, pp. 150–153.

[35] G. Margaritondo and P. Rebernik Ribic, "A simplified description of X-ray free-electron lasers," *Journal of Synchrotron Radiation*, vol. 18, no. 2, pp. 101–108, 2011.

[36] V. Ayvazyan *et al.*, "A new powerful source for coherent VUV radiation: Demonstration of exponential growth and saturation at the TTF free-electron laser," *European Physical Journal D*, vol. 20, pp. 149–156, 2002.

[37] R. Sheffield, "Progress in photoinjectors for linacs," in *Proceedings of 1990 Linear Accelerator Conference*, Albuquerque, New Mexico, 1990, pp. LA–UR–90–3296.

[38] P. J. Feibelman, "Self-consistent calculation of the surface photoelectric effect," *Phys. Rev. Lett.*, vol. 34, no. 17, pp. 1092–1095, 1975.

[39] P. W. Smith, "Mode-Locking of Lasers," *Proceedings of the IEEE*, vol. 58, no. 9, pp. 1342–1357, 1970.

[40] E. P. Ippen, C. V. Shank, and A. Dienes, "Passive mode locking of the cw dye laser," *Applied Physics Letters*, vol. 21, pp. 348—-350, 1972.

[41] J. C. Gallardo, "Control of Non-Linear Space-Charge Emittance Growth," Brookhaven National Laboratory, Tech. Rep., 1990.

[42] S. Di Mitri, "Bunch-length Compressors," in *Proceedings of the CAS–CERN Accelerator School: Free Electron Lasers and Energy Recovery Linacs*, vol. 1, 2018, pp. 363–380.

[43] D. Z. Khan and T. O. Raubenheimer, "LCLS-II bunch compressor study: 5-bend chicane," in *Proceedings of the 36th International Free Electron Laser Conference, FEL 2014*, 2014, pp. 755–762.

[44] S. Thorin *et al.*, "THE MAX IV LINAC," in *Proceedings of LINAC2014*, 2014, p. TUIOA03.

[45] L. S. Cowie *et al.*, "AN X-BAND LINEARISER FOR THE CLARA FEL," in *Proceedings of IPAC2018*, 2018, pp. 3848–3851.

[46] J. A. Clarke *et al.*, "CLARA conceptual design report," *JINST*, vol. 9, no. T05001, p. 16, 2014.

[47] J. A. Clarke *et al.*, "CLARA conceptual design report," *JINST*, vol. 9, no. T05001, p. 20, 2014.

[48] J. A. Clarke *et al.*, "CLARA conceptual design report," *JINST*, vol. 9, no. T05001, p. 38, 2014.

[49] S.-Y. Lee, *Accelerator Physics*, 2nd ed. World Scientific, 2004, pp. 504–507.

[50] D. Angal-kalinin *et al.*, "Commisioning of front end of CLARA facility at Daresbury Laboratory COMMISSIONING OF FRONT END OF CLARA FACILITY AT," in *Proceedings of IPAC2018*, no. May, Vancouver, Canada, 2018, p. THPMK059.

[51] F. Tavares *et al.*, "THE MAX IV SYNCHROTRON LIGHT SOURCE," in *Proceedings of IPAC2011*, 2011, p. THPC058.

[52] U. Johansson, U. Vogt, and A. Mikkelsen, "NanoMAX: A hard x-ray nanoprobe beamline at MAX-IV," in *Proceeding of SPIE Optical Engineering and Applications*, 2013, p. 88510L.

[53] M. M. G. M. Thunnissen *et al.*, "BioMAX : The Future Macromolecular Crystallography Beamline at MAX IV," in *Proceedings of SRI 2012*, 2013, p. 072012.

[54] H. Enquist *et al.*, "FemtoMAX – an X-ray beamline for structural dynamics at the short-pulse facility of MAX IV," *Journal of Synchrotron Radiation*, vol. 25, pp. 570–579, 2018.

[55] S. Werin, S. Thorin, M. Eriksson, and J. Larsson, "Short pulse facility for MAX-lab," *Nuclear Instruments and Methods in Physics Research A*, vol. 601, pp. 98–107, 2009.

[56] Y. Sun, "Second-order achromat design based on FODO cell," *Physical Review Accelerators and Beams*, vol. 14, p. 060703, 2011.

[57] J. McKenzie, "Longitudinal beam characterisation on vela using a transverse deflecting cavity," Ph.D. dissertation, University of Liverpool, 2018.

[58] M. Borland *et al.*, "Start-to-end simulation of self-amplified spontaneous emission free electron lasers from the gun through the undulator," *Nuclear Instruments and Methods in Physics Research, Section A: Accelerators, Spectrometers, Detectors and Associated Equipment*, vol. 483, no. 1-2, pp. 268–272, 2002.

[59] J. Schwinger, "On the radiation by electrons in a betatron," 1945, unpublished pre-print.

[60] E. L. Saldin, E. A. Schneidmiller, and M. B. Yurkov, "On the coherent radiation of and electron bunch moving in the arc of a circle," *Nucl. Instrum. Methods Phys. Res. A*, vol. 398, pp. 373–394, 1997.

[61] Y. Jing, Y. Hao, and V. N. Litvinenko, "Compensating effect of the coherent synchrotron radiation in bunch compressors," *Physical Review Special Topics - Accelerators and Beams*, vol. 16, p. 060704, 2013.

[62] H. S. Kang, S. H. Nam, I. S. Ko, C. Yi, and M. H. Cho, "Three bunch compressor scheme for SASE FEL," in *FEL 2011 - 33rd International Free Electron Laser Conference*, 2011, pp. 447–450.

[63] Z. Zhang *et al.*, "Microbunching-instability-induced sidebands in a seeded free-electron laser," *Physical Review Accelerators and Beams*, vol. 19, p. 050701, 2016.

[64] J. Qiang *et al.*, "Start-to-end simulation of the shot-noise driven microbunching instability experiment at the Linac Coherent Light Source," *Physical Review Accelerators and Beams*, vol. 20, p. 054402, 2017.

[65] D. Ratner, Z. Huang, and G. Stupakov, "Analysis of shot noise suppression for electron beams," SLAC, Tech. Rep., 2015.

[66] E. L. Saldin, E. A. Schneidmiller, and M. V. Yurkov, "Longitudinal space charge-driven microbunching instability in the TESLA Test Facility linac," *Nuclear Instruments and Methods in Physics Research, Section A: Accelerators, Spectrometers, Detectors and Associated Equipment*, vol. 528, no. 1-2, pp. 355–359, 2004.

[67] C. Behrens, Z. Huang, and D. Xiang, "Reversible electron beam heating for

suppression of microbunching instabilities at free-electron lasers," *Physical Review Special Topics - Accelerators and Beams*, vol. 15, p. 022802, 2012.

[68] C. Tennant, S. Benson, D. Douglas, R. Li, and C.-Y. Tsai, "STUDIES OF CSR AND MICROBUNCHING AT THE JEFFERSON LABORATORY ERLS," in *Proceedings of ERL2017*, Geneva, Switzerland, 2017, pp. 59–64.

[69] A. Hofmann, *The Physics of Synchrotron Radiation.* Cambridge University Press, 2004, pp. 10–18.

[70] L. I. Schiff, "Production of particle energies beyond 200 mev," *Rev. Sci. Inst.*, vol. 17, pp. 6–14, 1946.

[71] F. R. Elder, A. M. Gurewitsch, R. V. Langmuir, and H. C. Pollock, "Radiation from electrons in a synchroton," *Phys. Rev.*, vol. 71, pp. 829–830, 1947.

[72] D. J. Griffiths, *Introduction to Electrodynamics*, 3rd ed. Prentice-Hall, 1999, pp. 536–542.

[73] J. D. Jackson, *Classical Electrodynamics*, 3rd ed. John Wiley and Sons, 1962, pp. 464–466.

[74] J. D. Jackson, *Classical Electrodynamics*, 3rd ed. John Wiley and Sons, 1962, pp. 468–471.

[75] S.-Y. Lee, *Accelerator Physics*, 2nd ed. World Scientific, 2004, pp. 426–430.

[76] A. Hofmann, *The Physics of Synchrotron Radiation.* Cambridge University Press, 2004, p. 43.

[77] A. Hofmann, *The Physics of Synchrotron Radiation.* Cambridge University Press, 2004, pp. 57–65.

[78] J. D. Jackson, *Classical Electrodynamics*, 3rd ed. John Wiley and Sons, 1962, pp. 479–484.

[79] A. Hofmann, *The Physics of Synchrotron Radiation.* Cambridge University Press, 2004, pp. 35–36.

[80] A. Hofmann, *The Physics of Synchrotron Radiation.* Cambridge University Press, 2004, p. 51.

[81] A. Hofmann, *The Physics of Synchrotron Radiation.* Cambridge University Press, 2004, pp. 92–94.

[82] J. Murphy, S. Krinsky, and R. Gluckstern, "Longitudinal wakefield for synchrotron radiation," in *Proceedings of PAC 1995: Dallas, USA*, 1995, pp. 2980–2982.

[83] C. Mayes and G. Hoffstaetter, "Exact 1D model for coherent synchrotron radiation with shielding and bunch compression," *Physical Review Special Topics - Accelerators and Beams*, vol. 12, p. 024401, 2009.

[84] L. V. Iogansen and M. S. Rabinovich, "COHERENT ELECTRON RADIATION IN THE SYNCHROTRON. II." *Soviet Physics JETP*, vol. 37, no. 1, pp. 83–87, 1960.

[85] C. Behrens, "Detection and spectral measurements of coherent synchrotron radiation at FLASH," Master's thesis, Institut für Experimentalphysik, Universität Hamburg, 2008.

[86] O. Grimm, "PRINCIPLES OF LONGITUDINAL BEAM DIAGNOSTICS WITH COHERENT RADIATION," in *Proceedings of EPAC06*, 2006, pp. 1040–1042.

[87] D. J. Griffiths, *Introduction to Electrodynamics*, 3rd ed. Prentice-Hall, 1999, pp. 427–428.

[88] A. D. Brynes *et al.*, "Beyond the limits of 1D coherent synchrotron radiation," *New Journal of Physics*, vol. 20, p. 073035, Jul 2018. [Online]. Available: https://iopscience.iop.org/article/10.1088/1367-2630/aad21d

[89] O. Grimm, H. Delsim-Hashemi, J. Rossbach, V. Balandin, and N. Golubeva, "Transverse electron beam size effect on the bunch profile determination with coherent radiation diagnostics," in *Proceedings, EPAC08: Genoa, Italy, May 2014*, 2014, p. TUPC030.

[90] A. A. Vorob'ev *et al.*, "The SIRIUS electron synchrotron at Tomsk Polytechnical Institute," *Soviet Physics Journal*, vol. 10, no. 2, p. 88, 1967.

[91] M. M. Nikitin, A. F. Medvedev, M. B. Moiseev, and V. Y. Épp, "Interference of synchrotron radiation," *Soviet Physics JETP*, vol. 53, no. 3, pp. 338–394, 1980.

[92] G. Geloni, V. Kocharyan, E. Saldin, E. Schneidmiller, and M. Yurkov, "A Theory of edge radiation . Part I : Foundations and basic applications," *Nuclear Instruments and Methods in Physics Research, Section A: Accelerators, Spectrometers, Detectors and Associated Equipment*, vol. 605, pp. 409–429, 2009.

[93] G. Geloni, V. Kocharyan, E. Saldin, E. Schneidmiller, and M. Yurkov,

"Theory of edge radiation . Part II : Advanced applications," *Nuclear Inst. and Methods in Physics Research, A*, vol. 607, pp. 470–487, 2009.

[94] V. L. Ginzburg and I. M. Frank, "Radiation of a uniformly moving electron due to its transition from one medium into another," *J. Phys.(USSR)*, vol. 9, pp. 353–362, 1945.

[95] B. E. Carlsten and T. O. Raubenheimer, "Emittance growth of bunched beams in bends," *Physical Review E*, vol. 51, no. 2, pp. 1453–1470, 1995.

[96] P. Emma and R. Brinkmann, "Emittance dilution through coherent energy spread generation in bending systems," in *Proceedings of PAC 1997*, 1997, pp. 1679–1681.

[97] M. Dohlus and T. Limberg, "Emittance growth due to wake fields on curved bunch trajectories," *Nuclear Instruments and Methods in Physics Research, Section A: Accelerators, Spectrometers, Detectors and Associated Equipment*, vol. 393, no. 1-3, pp. 494–499, 1997.

[98] S. Di Mitri, M. Cornacchia, and S. Spampinati, "Cancellation of coherent synchrotron radiation kicks with optics balance," *Phys. Rev. Lett.*, vol. 110, p. 014801, 2013.

[99] M. Dohlus and T. Limberg, "Impact of optics on CSR-related emittance growth in bunch compressor chicanes," in *Proceedings of the 2005 Particle Accelerator Conference*, 2005, pp. 1015–1017.

[100] Y. Jiao, X. Cui, X. Huang, and G. Xu, "Generic conditions for suppressing the coherent synchrotron radiation induced emittance growth in a two-dipole achromat," *Physical Review Special Topics - Accelerators and Beams*, vol. 17, no. 6, pp. 1–11, 2014.

[101] C. Mitchell, J. Qiang, and P. Emma, "Longitudinal pulse shaping for the suppression of coherent synchrotron radiation-induced emittance growth," *Physical Review Special Topics - Accelerators and Beams*, vol. 16, p. 060703, 2013.

[102] M. Borland, "elegant: A Flexible SDDS-Compliant Code for Accelerator Simulation," in *Proceedings of ICAP2000*, Darmstadt, Germany, 2000, pp. 1–11.

[103] M. Borland, *User's Manual for elegant*, Advanced Photon Source, April 2004, program Version 15.1.1.

[104] Z. Huang *et al.*, "Suppression of microbunching instability in the linac coherent light source," *Physical Review Special Topics - Accelerators and Beams*, vol. 7, p. 074401, 2004.

[105] M. Borland, "Simple method for particle tracking with coherent synchrotron radiation," *Physical Review Special Topics - Accelerators and Beams*, vol. 4, p. 070701, 2001.

[106] G. Stupakov and P. Emma, "CSR wake for a short magnet in ultrarelativistic limit," SLAC, Stanford, Tech. Rep., 2002.

[107] M. Borland, "Coherent Synchrotron Radiation and Microbunching in Bunch Compressors," in *Proceedings of LINAC2002*, Gyeongju, Korea, 2002, pp. 11–15.

[108] Y. S. Derbenev and V. D. Shiltsev, "Transverse Effects of Microbunch Radiative Interaction," SLAC, Stanford, CA, Tech. Rep., 1996.

[109] K. L. Bane *et al.*, "Measurements and modeling of coherent synchrotron radiation and its impact on the Linac Coherent Light Source electron beam," *Physical Review Special Topics - Accelerators and Beams*, vol. 12, p. 030704, 2009.

[110] G. Bassi *et al.*, "Overview of CSR codes," *Nuclear Instruments and Methods in Physics Research, Section A: Accelerators, Spectrometers, Detectors and Associated Equipment*, vol. 557, no. 1, pp. 189–204, 2006.

[111] A. Kabel, M. Dohlus, and T. Limberg, "Numerical Calculation of Coherent Synchrotron Radiation Effects Using TraFiC4," SLAC, Stanford, CA, Tech. Rep., 2000.

[112] A. Kabel, M. Dohlus, and T. Limberg, "Using TraFiC4 to calculate and minimize emittance growth due to coherent synchrotron radiation," *Nuclear Instruments and Methods in Physics Research, Section A: Accelerators, Spectrometers, Detectors and Associated Equipment*, vol. 455, pp. 185–189, 2000.

[113] M. Dohlus, A. Kabel, and T. Limberg, "Efficient field calculation of 3D bunches on general trajectories," *Nuclear Instruments and Methods in Physics Research, Section A: Accelerators, Spectrometers, Detectors and Associated Equipment*, vol. 445, no. 1-3, pp. 338–342, 2000.

[114] M. Dohlus and T. Limberg, "CSRtrack: Faster Calculation of 3D CSR effects," in *Proceedings FEL 2004*, 2004, pp. 18–21.

[115] H. Braun, S. Dobert, L. Groening, M. Borland, and A. Kabel, "Recent experiments on the effect of coherent synchrotron radiation on the electron

beam of CTF II," in *Proceedings of PAC 2001*, Chicago, USA, 2001, pp. 164–166.

[116] T. Limberg, P. Piot, and E. A. Schneidmiller, "An analysis of longitudinal phase space fragmentation at the TESLA test facility," *Nuclear Instruments and Methods in Physics Research, Section A: Accelerators, Spectrometers, Detectors and Associated Equipment*, vol. 475, no. 1-3, pp. 353–356, 2001.

[117] M. Dohlus and T. Limberg, *CSRTrack User's Manual*, Advanced Photon Source, program Version 1.2.

[118] M. Dohlus, "Modelling of Space Charge and CSR Effects in Bunch Compression Systems," in *Proceedings of EPAC06*, Edinburgh, Scotland, 2006, pp. 1897–1901.

[119] R. P. Fliller, H. Edwards, G. Kazakevich, R. M. Thurman-Keup, J. Ruan, and T. Koeth, "INVESTIGATION OF POSSIBLE CSR INDUCED ENERGY SPREAD EFFECTS WITH THE A0 PHOTOINJECTOR BUNCH COMPRESSOR," in *Proceedings of EPAC08*, Genoa, Italy, 2008, pp. 3005–3007.

[120] K. Floettman, *ASTRA: A Space Charge Tracking Algorithm*, DESY, March 2017, program Version 3.2.

[121] T. Tanaka and H. Kitamura, "SPECTRA : a synchrotron radiation calculation code," *Journal of Synchrotron Radiation*, vol. 8, pp. 1221–1228, 2001.

[122] K. Suzuki, M. Ito, N. Tsuji, H. Adachi, and H. Kawata, "An Experimental System of X-ray Magnetic Diffraction at the Photon Factory," *Japanese Journal of Applied Physics*, vol. 48, p. 056506, 2009.

[123] Y. Ohishi, N. Hirao, N. Sata, K. Hirose, and M. Takata, "Highly intense monochromatic X-ray diffraction facility for high-pressure research at SPring-8," *High Pressure Research*, vol. 28, no. 3, pp. 163—-173, 2008.

[124] R. P. Walker and B. Diviacco, "URGENT - A computer program for calculating undulator radiation spectral , angular , polarization , and power density properties," *Review of Scientific Instruments*, vol. 63, pp. 392–395, 1992.

[125] R. Chubar and P. Elleaume, "Accurate And Efficient Computation Of Synchrotron Radiation In The Near Field Region," in *Proceedings of EPAC98*, 1998, pp. 1177–1179.

[126] T. Shaftan, S. L. Hulbert, and L. Berman, "Comparison of calculated brightness and flux of radiation from a long-period wiggler and a short-period undulator," *Journal of Synchrotron Radiation*, vol. 15, pp. 335–340, 2008.

[127] J. F. W. Mosselmans *et al.*, "I18 – the microfocus spectroscopy beamline at the Diamond Light Source," *Journal of Synchrotron Radiation*, vol. 16, pp. 818–824, 2009.

[128] S. B. van der Geer and M. J. de Loos, *General Particle Tracer User Manual*, Pulsar Physics, program Version 3.35.

[129] "Pulsar physics and general particle tracer code," http://www.pulsar.nl/gpt, accessed: 2019-06-20.

[130] J. Barnes and P. Hut, "A hierarchical O(N logN) force-calculation algorithm," *Nature*, vol. 324, pp. 446–449, 1986.

[131] G. Pöplau, U. van Rienen, B. van der Geer, and M. de Loos, "Multigrid Algorithms for the Fast Calculation of Space-Charge Effects in Accelerator Design," *IEEE Transactions on Magnetics*, vol. 40, no. 2, pp. 714–717, 2004.

[132] S. van der Geer, O. Luiten, M. de Loos, G. Pöplau, and U. van Rienen, "3d space-charge model for gpt simulations of high-brightness electron bunches," in *Computational Accelerator physics 2002 : Proceedings of the Seventh International Conference on Computational Accelerator Physics*, ser. Institute of Physics Conference Series, M. Berz and K. Makino, Eds. Institute of Physics, 2005, pp. 101–110.

[133] G. Pöplau, U. van Rienen, S. B. van der Geer, and M. J. de Loos, "A Fast 3D Multigrid Based Space – Charge Routine in the GPT Code," in *Proceedings of EPAC02*, Paris, 2002, pp. 1658–1660.

[134] F. Kesting and G. Franchetti, "Propagation of numerical noise in particle-in-cell tracking," *Physical Review Special Topics - Accelerators and Beams*, vol. 18, p. 114201, 2015.

[135] I. V. Bazarov and T. Miyajima, "CALCULATION OF COHERENT SYNCHROTRON RADIATION IN GENERAL PARTICLE TRACER," in *Proceedings of EPAC08*, 2008, pp. 118–120.

[136] D. Sagan, "An Efficient Formalism for Simulating the Longitudinal Kick From Coherent Synchrotron Radiation," in *Proceedings of EPAC06*, 2006, pp. 2829–2831.

[137] N. R. Neveu *et al.*, "Benchmark of RF Photoinjector and Dipole Using ASTRA, GPT, and OPAL," in *Proceedings, 2nd North American*

Particle Accelerator Conference (NAPAC2016), Chicago, USA, 2016, pp. 1194–1196. [Online]. Available: http://accelconf.web.cern.ch/AccelConf/napac2016/papers/thpoa46.pdf

[138] G. Ha, J. G. Power, M. Conde, D. S. Doran, and W. Gai, "Preparations for Installation of the Double Emittance-Exchange Beamline At the Argonne Wakefield Accelerator Facility," in *Proceedings of FEL2017*, Santa Fe, USA, 2017, pp. 336–339.

[139] R. Akre *et al.*, "Commissioning the Linac Coherent Light Source Injector," *Physical Review Special Topics - Accelerators and Beams*, vol. 11, p. 030703, 2008.

[140] L. Serafini and J. B. Rosenzweig, "Envelope analysis of intense relativistic quasilaminar beams in rf photoinjectors:ma theory of emittance compensation," *Phys. Rev. E*, vol. 55, pp. 7565–7590, Jun 1997.

[141] D. Walsh, private communication.

[142] C. Tollervey, D. A. Walsh, and E. W. Snedden, "Physics of the CLARA Photoinjector Laser System," STFC Daresbury Laboratory, Daresbury, UK, Tech. Rep., 2016.

[143] B. D. Muratori, J. K. Jones, and A. Wolski, "Analytical expressions for fringe fields in multipole magnets," *Physical Review Special Topics - Accelerators and Beams*, vol. 18, p. 064001, 2015.

[144] J. Rosenzweig and E. Colby, "Charge and wavelength scaling of RF photoinjector designs," in *Proceedings, AIP: Fontana, Wisconsin, USA, Jun 1994*, 1994, p. 724.

[145] A. T. Green and Y. M. Shin, "Implementation of quadrupole-scan emittance measurement at Fermilab's Advanced Superconducting Test Accelerator (ASTA)," in *6th International Particle Accelerator Conference, IPAC 2015*, 2015, pp. 669–671.

[146] S.-Y. Lee, *Accelerator Physics*, 2nd ed. World Scientific, 2004, p. 130.

[147] A. Wolski, *Beam Dynamics in High Energy Particle Accelerators*, 1st ed. Imperial College Press, 2014, p. 158.

[148] D. Filippetto *et al.*, "Phase space analysis of velocity bunched beams," *Physical Review Special Topics - Accelerators and Beams*, vol. 14, p. 092804, 2011.

[149] G. Andonian *et al.*, "Observation of coherent terahertz edge radiation from compressed electron beams," *Physical Review Special Topics - Accelerators and Beams*, vol. 121, p. 03070, 2009.

[150] *Sythetic crystal quartz*, Manufacturer Website, TYDEX, St. Petersburg, Ru., accessed 05/08/2019. [Online]. Available: http://www.tydexoptics.com/pdf/Crystal_quartz.pdf

[151] D. M. Slocum, E. J. Slingerland, R. H. Giles, and T. M. Goyette, "Atmospheric absorption of terahertz radiation and water vapor continuum effects," *Journal of Quantitative Spectroscopy and Radiative Transfer*, vol. 127, pp. 49–63, 2013.

[152] T. Pacey, private communication.

[153] *High Resistivity Float Zone Silicon for THz Applications*, Manufacturer Website, TYDEX, St. Petersburg, Ru., accessed

05/08/2019. [Online]. Available: http://www.tydexoptics.com/pdf/HRFZ-Si_for_THz_applications.pdf

[154] A. Podzorov and G. Gallot, "Low-loss polymers for terahertz applications," *Applied optics*, vol. 47, no. 18, pp. 3252–3257, 2008.

[155] J. R. Birch and E. A. Nicol, "THE FIR CONSTANTS OF THE POLYMER TPX," *Infrared Physics*, vol. 24, no. 6, pp. 573–575, 1984.

[156] A. Shaulov and M. Simhony, "Pyroelectric voltage response to rectangular infrared signals in triglycine sulphate and strontium-barium niobate," *Journal of Applied Physics*, vol. 43, no. 4, pp. 1440–1444, 1972.

[157] P. B. Wilson, "SLED: A Method for Doubling SLAC's Energy," SLAC National Accelerator Laboratory, Tech. Rep. SLAC-TN-73-15, 1973.

[158] Z. D. Farkas, "Methods to increase linac efficiency," SLAC, Tech. Rep. SLAC/AP-29, 1984.

[159] Z. D. Farkas, H. A. Hogg, G. A. Loew, and P. B. Wilson, "Recent Progress on the SLED, the SLAC Energy Doubler," SLAC National Accelerator Laboratory, Tech. Rep. SLAC-PUB-1561, 1975.

[160] J. Gao, "Analytical formula for the coupling coefficient β of a cavity-waveguide coupling system," *Nuclear Inst. and Methods in Physics Research, A*, vol. 309, pp. 5–10, 1991.

[161] D. Alesini, "Power coupling," 2011, unpublished report. [Online]. Available: https://arxiv.org/pdf/1112.3201.pdf

[162] "Detailed Design Report on the MAX IV Facility," MAX Lab, Lund, Sweden, Tech. Rep., 2010.

[163] M. Veronese, R. Appio, P. Craievich, and G. Penco, "Absolute bunch length measurement using coherent diffraction radiation," *Phys. Rev. Lett.*, vol. 110, p. 074802, 2013.

[164] L. Palumbo, "RADIATION OF A POINT CHARGE MOVING UNIFORMLY ON THE AXIS OF AN INFINITE CYLINDRICAL PIPE WITH A GAP," CERN, Geneva, Switzerland, Tech. Rep., 1984.

[165] S. D. Mitri *et al.*, "Transverse emittance preservation during bunch compression in the Fermi free electron laser," *Physical Review Special Topics - Accelerators and Beams*, vol. 15, p. 020701, 2012.

[166] D. Meschede, *Optics, Light and Lasers*. Wiley, 2007.

[167] J. Wolfenden, R. B. Fiorito, and C. P. Welsch, "A novel simulation and analysis algorithm for high resolution optical transition radiation imaging," *Optics Express*, vol. 27, no. 3, p. 2988, 2019.

Abbreviations

BA1 Beam Area 1. A user experimental area on the CLARA Phase 1 beamline.

BC1 Bunch compressor 1. The first bunch compressor at MAX IV.

BC2 Bunch compressor 2. The second bunch compressor at MAX IV.

BLM Beam-loss monitor. A diagnostic which detects sources of loss in a particle beam.

BPM Beam position monitor. A diagnostic that determines the transverse centroid position of the particle beam at a given location.

C2V CLARA to VELA. The dogleg transfer line on CLARA Phase 1, which transports electron beams from the CLARA injector to the VELA beamline.

CCD Charge-coupled device. A device commonly used for image acquisition.

CDR Coherent diffraction radiation. A type of coherent radiation produced by an ultra-relativistic particle beam passing close to a material of a different dielectric strength than that which the beam is propagating in.

CLARA Compact Linear Accelerator for Research and Applications. A new FEL under construction at Daresbury Laboratory, UK.

COTR Coherent optical transition radiation. Coherently amplified transition radiation emitted in the optical spectrum.

CSR Coherent synchrotron radiation. The coherent amplification of synchrotron radiation.

CTR Coherent transition radiation. Coherent radiation emitted from a relativistic beam passing between two media of different dielectric strength.

DAQ Data acquisition unit. Samples detector signals and digitises results for further processing.

DFT Discrete Fourier Transform. A method for generating Fourier spectra from discrete data.

DL Daresbury Laboratory. A particle accelerator laboratory in Cheshire, UK.

EBT Electron beam transport. The section of the CLARA Phase 1 accelerator downstream of the C2V dogleg.

ERL Energy-recovery linac. A beamline which, prior to dumping the particle beam, passes the beam through the linac at a decelerative phase to recover the beam energy and improve efficiency.

FEL Free-electron laser. An advanced form of light source that uses ultra-relativistic electron beams as a gain medium.

FFT Fast Fourier transform. A fast method of calculating Fourier components of data.

GPT General Particle Tracer. A general-purpose particle tracking code.

HRFZ-Si High-resistivity float-zone silicon. A type of silicon which transmits THz radiation and reflects visible wavelengths.

ICT Integrating current transformer. A diagnostic for measuring the bunch charge.

IR Infra-red. The region of the electromagnetic spectrum with wavelengths longer than visible light and shorter than microwave radiation (750 nm-1 mm).

ISR Incoherent synchrotron radiation. The single-particle synchrotron radiation emission of an electron bunch that does not depend upon the bunch distribution.

LPS Longitudinal phase space. The distribution of the beam in the z-δ plane, where z is the longitudinal coordinate and δ is the relative momentum deviation. Alternate conventions use some combination of t, the time-displacement within the electron bunch, and p_z, the longitudinal momentum.

LSC Longitudinal space charge. The collective space charge effect observed along the propagation axis of a charged particle beam.

MAX IV A light source facility situated in Lund, Sweden.

MS1 Matching section 1. The first matching section of the MAX IV facility, which precedes the first bunch compressor.

MS2 Matching section 2. The second matching section of the MAX IV facility, which follows the first bunch compressor.

NEP Noise equivalent power. The incident signal power required to overcome the noise level on a detector.

OTR Optical transition radiation. Radiation emitted in the optical spectrum when a particle beam passes through a medium of different dielectric strength.

PC Photocathode. A conducting metal plate which, in combination with a high power laser, acts as an electron source for a particle accelerator.

PED Pyroelectric detector. A single-pixel detector which uses the pyroelectric effect to measure THz radiation.

PI Photo-injector. A charge source for accelerators that uses the photo-electric effect to generate charge from a conducting cathode surface with a high power laser.

PIC Particle-in-cell. A method for evaluating the electromagnetic fields within a charge distribution.

PIL Photo-injector laser. A high-powered laser used to free charge from a conducting cathode surface in a photo-injector.

RF Radio-frequency. Shorthand for both the power systems supplying accelerating cavities in accelerators, and the cavities themselves. So-called because of the frequency bands which the systems operate in.

S02SP1 A spectrometer beamline on the CLARA Phase 1 lattice.

S2E Start-to-end. A type of simulation project which tracks particles from the injector and particle source all the way to the end of the accelerator, usually in the case where the accelerator is terminated by an FEL section.

SASE Self-amplified spontaneous emission. An operational mode of a FEL which uses shot-noise derived modulation within the electron bunch current as the initial seed for the FEL process.

SLED SLAC Energy Doubler. An RF network used to compress the RF pulse produced by a klystron, in order to increase the accelerating field observed by an electron beam.

SP02 The final section of the MAX-IV linac, in which the experiment featured herein was carried out.

SPF Short-pulse facility. Part of the MAX-IV accelerator which delivers ultrashort electron bunches to the FemtoMAX user beamline.

TDC Transverse deflecting cavity. A beamline element used for longitudinal diagnostics. A transverse electric field imparts a longitudinally-correlated kick to an electron bunch, permitting longitudinal imaging.

TPX A polymer with approximately constant refractive index in the THz spectrum.

UV Ultra-violet. The region of the electromagnetic spectrum with wavelengths longer than X-rays and shorter than visible light (10 nm-400 nm).

VBC Variable bunch compressor. The planned bunch compressor chicane for the CLARA accelerator, which has a variable R_{56}.

VC Virtual cathode. A camera image of a photoinjector laser spot, that is produced by transporting the laser along an optical path equivalent to that going to the photocathode surface.

VELA Versatile Electron Linear Accelerator. A low-energy beamline at Daresbury Laboratory, UK.

XUV Extreme ultra-violet. The shortest wavelength region of the UV spectrum.

YAG Yttrium aluminium garnet. A material used for transverse beam diagnostics. YAG screens scintillate when an electron beam passes through, and facilitate imaging of the transverse beam distribution.